

# **New understanding of galaxies, quasars and extra-galactic shock features using optical spectroscopy and low-frequency radio observations**

Author: Marina Arnaudova

Supervised by: Dr Daniel Smith and Professor Martin Hardcastle

Centre for Astrophysics Research  
School of Physics, Astronomy and Mathematics  
University of Hertfordshire

*Submitted to the University of Hertfordshire in partial fulfilment of the requirements of  
the degree of Doctor of Philosophy.*

March 2024

# *Abstract*

The study of Galaxy Formation & Evolution serves as a cornerstone in our quest to unravel the mysteries of the Universe. Galaxies are not only its building blocks, but also the key to understanding its vast complexities. With the advent of new ground-based and space-based facilities, we have acquired multi-wavelength data of millions of galaxies, including active galactic nuclei (AGN), both locally and at higher redshifts, which allow us to trace the evolution of their properties through cosmic time. However, while statistical analyses of large galaxy and AGN samples across different redshifts are invaluable, they are not the sole avenue for exploration. High-quality data of unique objects also play a pivotal role, offering invaluable insights into the underlying physical processes that shape galaxies into the entities that we observe today. In this thesis, we make use of low-frequency radio observations and optical spectroscopy to demonstrate how such studies deepen our understanding of the Universe.

Firstly, we combine 144 MHz observations from the LOFAR Two-metre Sky Survey (LoTSS) and spectroscopic information from the 14th data release of the Sloan Digital Sky Survey (SDSS-DR14) to compile the largest sample of uniformly-selected, spectroscopically-confirmed quasars, the most luminous representations of AGN, and use it to investigate whether radio-loud (RL) and radio-quiet (RQ) quasars are physically distinct populations. Employing the classical definition of radio-loudness,  $R = \log(L_{1.4\text{GHz}}/L_i)$ , we identify 3,697 RL and 111,132 RQ sources at  $0.6 < z < 3.4$ . To study their properties, we develop a new rest-frame spectral stacking algorithm, designed with forthcoming massively-multiplexed spectroscopic surveys in mind, and use it to create high signal-to-noise composite spectra of each class, matched in redshift and absolute  $i$ -band magnitude. We show that RL quasars have redder continuum and enhanced [O II] emission compared to their RQ counterparts. These results persist when additionally matching in black hole mass, suggesting that this parameter is not the defining factor in making a RL QSO. We find that these features are not gradually varying as a function of radio-loudness but are maintained even when probing deeper into the RQ population, indicating that a clear-cut division in radio-loudness is not apparent. Upon examining the star formation rates (SFRs) inferred from the [O II] emission line, with the contribution from AGN removed using the [Ne v] line, we find that RL quasars have a significant excess of star-formation relative to RQ quasars out to  $z = 1.9$  at least. Given our findings, we suggest that RL sources reside in systems which preferably have a rich gas supply and rapidly spinning black holes, or represent an earlier obscured phase of QSO evolution.

We then present a detailed study of Stephan's Quintet (SQ), an interacting nearby group of galaxies which contains a large-scale shock front. This extragalactic shock feature is thought to be the result of an ongoing collision between NGC 7318b and the complex intergalactic medium of SQ, thereby allowing us to study the effects of galaxy mergers and interactions. By combining

the integral field spectroscopy from the first light data of the new William Herschel Telescope Enhanced Area Velocity Explorer (WEAVE) with new 144 MHz observations from LoTSS, plus archival data from the Very Large Array and the *James Webb Space Telescope (JWST)*, we are able to see SQ in a new light. Harnessing WEAVE large integral field unit's (LIFU) field of view ( $90 \times 78 \text{ arcsec}^2$ ), spectral resolution ( $\lambda/\Delta\lambda \sim 2500$ ) and continuous wavelength coverage across the optical band, we perform robust emission line fitting. This allows us to dynamically infer the location of the shock region with higher precision than previously possible. We find that the ionised gas in the shock is of low density ( $n_e < 140 \text{ cm}^{-3}$ ), with a low temperature  $T_e < 14,000 \text{ K}$  and metallicity consistent with the surrounding hot X-ray plasma. The Mach number ( $\mathcal{M} \sim 2.2$ ) of the shock suggests that it is relatively weak and is not efficient in accelerating particles. Instead, it has adiabatically compressed the medium, leading to a boost in the radio emission by a factor of  $\sim 10$ , during which dust has survived the collision event. This is further demonstrated by comparing the extinction distribution seen with WEAVE to the molecular gas and hot dust observed with *JWST*.

Finally, we use the most sensitive low-frequency radio data from the LoTSS Deep Fields and spectroscopic information from the Dark Energy Spectroscopic Instrument (DESI) to classify 2,033 radio sources as star-forming galaxies (SFGs), radio-quiet AGN (RQ AGN), emission-line low-excitation radio galaxies (LINELERGs) and high excitation radio-galaxies (HERGs). This was done by combining two diagnostics: (i) the identification of a radio excess compared to star-forming processes as traced by the Balmer lines, and (ii) the use of emission line ratios to separate sources producing higher ionisation energies than those produced from stellar radiation alone. These spectroscopic classifications allow us to evaluate the performance of recent photometric classifications, created for the same sample of radio sources, by using the deepest wide-field optical, near- and mid-infrared data available. This is important because while optical spectroscopy is widely regarded as a highly reliable method to classify sources, it is not as readily accessible as photometry. Preliminary results show that while photometric classifications can successfully recover the SFG class (above 90 per cent agreement with the spectroscopic classifications), there are some discrepancies involved amongst the three AGN classes, which require further investigation.

# Declaration

I declare that no part of this work is being submitted concurrently for another award of the University or any other awarding body or institution. This thesis contains a substantial body of work that has not previously been submitted successfully for an award of the University or any other awarding body or institution.

The following parts of this submission have been published previously and/or undertaken as part of a previous degree or research programme:

1. Chapter 2: this has been published as Arnaudova et al., 2024, *Monthly Notices of the Royal Astronomical Society*, **528(3)**, 4547.
2. Chapter 3: to be submitted in *Monthly Notices of the Royal Astronomical Society*.

Soumyadeep Das was responsible for the reduction of the radio images, and the subsequent calculations of the spectral indices and the equipartition parameters in Chapter 3.

Except where indicated otherwise in the submission, the submission is my own work and has not previously been submitted successfully for any award.

## *Acknowledgements*

I would like to thank everyone who helped and supported me throughout my PhD experience at the University of Hertfordshire, as well as those who enabled me to progress to this stage. Firstly, I would like to thank my supervisor, Dan Smith, for providing me with the opportunity to embark on this academic journey, for his invaluable guidance and support throughout my research, and for his remarkable patience and unwavering encouragement.

To Alyssa Drake, Soumyadeep Das, and Shravya Shenoy, thank you for being an integral part of my PhD journey. As members of the same science group, you understood my struggles better than anyone else. Thank you for providing your invaluable support and assistance in overcoming them, and for your willingness to lend an ear whenever I needed someone to vent to.

To Calum Morris, Matthew Doherty, and Niall Miller, thank you for being the best office mates one could wish for. You not only helped me with my research by enduring my endless science rants and assisting me with Python and cluster issues, but also for creating a fun and enjoyable work environment. There was never a dull moment in the office. An extension to this office has, of course, always been Kasia Nowak, who further contributed to its liveliness and enjoyment.

I would also like to thank my partner, Ivan Dobrev, for being with me every step of the way. Thank you for your invaluable advice, support, and especially for your understanding and patience. I realise that it must be challenging to live with someone who is at times mentally preoccupied, especially in the past few months, but you have never complained once. (Though, I must admit, I did warn you about the consequences in the beginning!)

Finally, I would like to thank my family, especially my parents, for encouraging me to pursue my dreams and supporting my decision to begin my studies in a new country. Without you, I would have never gotten to where I am today.

# Contents

<b>Abstract</b>	<b>i</b>
<b>Acknowledgements</b>	<b>iv</b>
<b>Contents</b>	<b>v</b>
<b>List of Figures</b>	<b>viii</b>
<b>List of Tables</b>	<b>x</b>
<b>1 Introduction</b>	<b>1</b>
1.1 Galaxies . . . . .	1
1.1.1 Cosmology . . . . .	1
1.1.2 Galaxy Classifications . . . . .	3
1.1.3 Galaxy Mergers . . . . .	5
1.2 Active Galactic Nuclei (AGN) . . . . .	7
1.2.1 Discovery and Unification . . . . .	7
1.2.2 The co-evolution of AGN and their host galaxies . . . . .	10
1.3 Astrophysical shocks . . . . .	12
1.3.1 Different origins of shocks . . . . .	12
1.3.2 The many roles of shocks . . . . .	13
1.4 The Radio Band . . . . .	15
1.4.1 The low-frequency radio population . . . . .	15
1.4.2 The Low Frequency Array . . . . .	17
1.5 Optical Spectroscopy of Distant Sources . . . . .	19
1.5.1 Diagnostics . . . . .	19
1.5.2 Large Scale Spectroscopic Surveys . . . . .	21
1.6 Overview . . . . .	26
<b>2 Exploring the radio-loudness of SDSS quasars with spectral stacking</b>	<b>28</b>
2.1 Introduction . . . . .	28
2.2 Data . . . . .	31
2.2.1 Sloan Digital Sky Survey . . . . .	31
2.2.2 LOFAR Two-metre Sky Survey . . . . .	32
2.2.3 Sample Selection . . . . .	33
2.2.4 The Matching Process . . . . .	35
2.3 The Spectral Stacking Method . . . . .	36

2.3.1	The Stacking Technique . . . . .	36
2.3.2	The Stacking Corrections . . . . .	38
2.3.3	Qualitative Template Comparison . . . . .	39
2.4	Composite Spectra of Quasars . . . . .	42
2.4.1	High S/N Comparison of RL and RQ QSOs . . . . .	42
2.4.2	Black Hole Mass Dependence . . . . .	44
2.4.3	Comparison as a Function of Radio-loudness . . . . .	46
2.5	Spectral Properties of RL and RQ quasars . . . . .	48
2.5.1	The Spectral Fitting Procedure . . . . .	48
2.5.2	Average Emission Line Properties . . . . .	50
2.5.3	Star Formation Rates . . . . .	52
2.6	Discussion . . . . .	54
2.6.1	Could our results be caused by starburst galaxies contaminating our RL sample? . . . . .	54
2.6.2	Could shock excitation be playing a role? . . . . .	55
2.6.3	Possible explanations . . . . .	55
2.7	Summary . . . . .	57
<b>3</b>	<b>WEAVE First Light Observations: Origin and Dynamics of the Shock Front in Stephan's Quintet</b>	<b>60</b>
3.1	Introduction . . . . .	60
3.2	Data . . . . .	64
3.2.1	WEAVE First Light Data . . . . .	64
3.2.2	Radio Data . . . . .	65
3.2.3	Additional Auxiliary Data . . . . .	66
3.3	Spectral Fitting Method . . . . .	66
3.4	General Overview of Stephan's Quintet . . . . .	69
3.4.1	Stephan's Quintet as seen with WEAVE . . . . .	69
3.4.2	Extinction, dust and gas with WEAVE and <i>JWST</i> / <i>MIRI</i> . . . . .	71
3.4.3	Radio morphology of the system . . . . .	73
3.5	Shock properties . . . . .	75
3.5.1	Thermodynamics . . . . .	75
3.5.2	Comparing WEAVE data with theoretical shock models . . . . .	78
3.5.3	The plasma in the shock . . . . .	79
3.5.4	Mach number . . . . .	81
3.5.5	Adiabatic Compression . . . . .	83
3.5.6	Magnetic field strength and shock lifetime . . . . .	84
3.6	Summary . . . . .	85
<b>4</b>	<b>Radio Source Classifications in ELAIS-N1</b>	<b>87</b>
4.1	Introduction . . . . .	87
4.2	Data . . . . .	90
4.2.1	Radio Data . . . . .	90
4.2.2	Spectroscopic Data . . . . .	90
4.2.3	Sample Selection . . . . .	91
4.3	Spectral Fitting Method . . . . .	92
4.4	Spectroscopic Classification Scheme . . . . .	93

---

4.4.1	Radio Excess . . . . .	94
4.4.2	The BPT diagram . . . . .	95
4.5	Results . . . . .	96
4.5.1	Comparison with photometric classifications . . . . .	97
4.5.2	The influence of redshift and optical source size on classification . . . . .	98
4.5.3	Physical properties of the sources by classification . . . . .	102
4.6	Summary . . . . .	104
<b>5</b>	<b>Conclusions and Future Work</b>	<b>106</b>
5.1	The radio-loudness of quasars . . . . .	106
5.2	Stephan's Quintet and Beyond . . . . .	107
5.3	Classifications of the faint radio source population . . . . .	109
5.4	Future Contributions to WEAVE-LOFAR . . . . .	110
5.5	Concluding Remarks . . . . .	111
<b>A</b>	<b>Supplementary Figures for Chapter 2</b>	<b>112</b>
<b>B</b>	<b>Supplementary Figures for Chapter 3</b>	<b>117</b>
	<b>Bibliography</b>	<b>117</b>

# List of Figures

1.1	The Hubble tuning fork diagram . . . . .	4
1.2	The colour-mass diagram. . . . .	5
1.3	Different stages of a galaxy merger. . . . .	6
1.4	Examples of radio galaxies . . . . .	8
1.5	A schematic representation of the AGN Unification model . . . . .	9
1.6	The categorisation of AGN classes into the two fundamental modes. . . . .	10
1.7	The MBH- $\sigma$ relation. . . . .	11
1.8	The cosmic star formation and black hole accretion history. . . . .	12
1.9	Famous examples of astrophysical shocks. . . . .	14
1.10	Different snapshots showing the interaction of a jet with a clumpy ISM. . . . .	15
1.11	The observed radio/FIR spectrum of M82. . . . .	17
1.12	A map of LOFAR stations. . . . .	18
1.13	The three BPT diagnostic diagrams. . . . .	20
1.14	Diagnostics diagrams for separating SFGs and RL AGN. . . . .	22
1.15	A slice through the 3-D map of galaxies from SDSS and DESI. . . . .	24
1.16	The redshift-luminosity plane as sampled by the three tiers of the WEAVE-LOFAR survey. . . . .	25
2.1	Sky coverage of SDSS-DR14Q and LoTSS DR2 . . . . .	33
2.2	The radio-loudness parameter . . . . .	35
2.3	A corner plot summary . . . . .	36
2.4	An example composite spectrum of RQ QSOs . . . . .	38
2.5	A diagnostic plot of a composite spectrum . . . . .	40
2.6	Templates from composite spectra . . . . .	41
2.7	A comparison between the RL and RQ population . . . . .	43
2.8	The black hole mass distribution . . . . .	45
2.9	The redshift - i-band absolute magnitude plane . . . . .	47
2.10	The emission line flux ratio of quasars . . . . .	51
2.11	The SFR of RL and RQ quasars . . . . .	53
2.12	The OIII emission line and 178MHz total radio luminosity relation . . . . .	56
3.1	A composite image of Stephan's Quintet . . . . .	63
3.2	The complex velocity structure in the LSSR . . . . .	67
3.3	The spectral properties of H $\alpha$ . . . . .	70
3.4	The dust properties of the shocked region surrounding NGC 7318a & b . . . . .	73
3.5	Radio observations of Stephan's Quintet . . . . .	74
3.6	The stacked spectrum of the LSSR . . . . .	76
3.7	A BPT diagnostic of the LSSR . . . . .	79

---

3.8	Spectral indices and spectral curvature parameter of SQ . . . . .	82
4.1	The redshift-luminosity plane in ELAIS-N1 . . . . .	92
4.2	Example fits of DESI spectra . . . . .	94
4.3	The spectroscopic classification scheme . . . . .	96
4.4	The photometric classifications along the radio excess and BPT diagnostic. . . . .	99
4.5	The redshift and optical size thresholds. . . . .	101
4.6	The physical properties of the different source classes . . . . .	103
A.1	Results of applying our spectral stacking algorithm to sources according to their location on the BPT-NII diagram. . . . .	112
A.2	A Monte Carlo simulation representing the comparison between RL and RQ quasars under the null hypothesis. . . . .	113
A.3	The comparison between the RL and RQ population matched in $z$ , $M_i$ and $M_{\text{BH}}$ . . . . .	114
A.4	The comparison between the radio-quietest ( $R_1$ ) and more radio-loud ( $R_2$ , $R_3$ and $R_4$ ) parts of the QSO population. . . . .	115
A.5	An example of the spectral fitting procedure with <code>PRQSOFIT</code> . . . . .	116
B.1	The spectra of NGC 7318a/b . . . . .	117
B.2	Example fits of the four Gaussian models at different locations in Stephan's Quintet. . . . .	118

# List of Tables

2.1	The $p$ -values obtained from the null hypothesis test . . . . .	45
2.2	The emission line fitting information . . . . .	50
3.1	Information about the radio images of SQ. . . . .	66
3.2	Emission line flux measurements of the shocked region. . . . .	77
4.1	The total number of a given class per given classification. . . . .	98
4.2	The radio excess diagnostic . . . . .	100
4.3	The BPT diagnostic . . . . .	100
4.4	The change of sample size and level of agreement for B23 and D24. . . . .	102

# Chapter 1

## Introduction

### 1.1 Galaxies

Galaxy Formation & Evolution is an active field of research, as they are key processes that we need to understand to answer the fundamental question of how did the Universe that we observe today come to be. Observations of galaxies are key in addressing this, since due to the large distances involved and the finite speed of light, looking at galaxies at a range of distances is equivalent to looking at the Universe at different epochs. This allows us to study galaxy properties as a function of the age of the Universe, which enables us to statistically identify the relationships between galaxy populations and thus understand their evolutionary tracks.

#### 1.1.1 Cosmology

Studies of Galaxy Formation & Evolution rely on the well-established cosmological framework - the  $\Lambda$ CDM model, which currently provides the best description of the observable Universe (see review by Bull et al. 2016). This model predicts an expanding, spatially-flat universe, consisting of four components: a cosmological constant ( $\Lambda$ ), cold dark matter (CDM), baryonic matter and radiation. The largest contribution comes from  $\Lambda$  ( $\sim 70\%$ ), which is associated with dark (or vacuum) energy, the component responsible for the observed late-time acceleration of the Universe (Riess et al. 1998; Perlmutter et al. 1998). The second largest contribution comes from CDM ( $\sim 26\%$ ), which plays a crucial role in explaining the large-scale structure (e.g. de Lapparent et al. 1986; Shectman et al. 1996; York et al. 2000; Colless et al. 2003; Alam et al.

2017; Ross et al. 2020). The term ‘cold’ refers to the low velocity of dark matter particles compared to the speed of light, which allows for structures to form hierarchically (‘bottom-up’). In this scenario, dark matter particles coalesce due to gravitational instability, forming dark matter halos. Over time, these halos accumulate and condense gas in their centers, resulting in the formation of the first stars and stellar clusters (White and Rees, 1978). These structures evolve to form the first galaxies, followed by the assembly of larger cosmic structures such as groups, clusters, and superclusters of galaxies that we observe today.

This structure formation is ‘seeded’ from the small-scale density perturbations in the distribution of matter, which manifest as over- and under-dense regions. These perturbations are believed to originate from the rapid, exponential expansion of the Universe which immediately followed after the Big Bang, during a phase known as inflation (Guth 1981). Today, these primordial imprints manifest as temperature fluctuations in the Cosmic Microwave Background radiation (the CMB; Penzias and Wilson 1965), a relic from about 380,000 years after the Big Bang. Detailed studies of the CMB not only provide perhaps the strongest evidence for  $\Lambda$ CDM, but also apply stringent limits to fundamental cosmological parameters, such as the abundance of dark matter, baryonic matter, and dark energy, as well as the curvature and expansion rate of the Universe (e.g. Bennett et al. 2003; Spergel et al. 2003; Planck Collaboration et al. 2014; Planck Collaboration et al. 2016).

While the CMB offers a rich source of information about the early universe, studies of the first galaxies provide an equally compelling avenue for understanding its evolution. These early structures are believed to play a crucial role in the re-ionization of the Universe ( $z \gtrsim 6$ ), a process in which neutral hydrogen becomes fully-ionized, when the Universe transitioned from its opaque, neutral state to the transparent, ionized state we observe today (for a recent review see Robertson 2022). However, the duration of this process and the exact source of ionisation remain open questions (e.g. Bunker et al. 2004; Lorenzoni et al. 2011; Lorenzoni et al. 2013; Giallongo et al. 2015; Drake et al. 2017; Finkelstein et al. 2019; Shen et al. 2020; Robertson 2022 and references therein). With the launch of the *James Webb Space Telescope* (*JWST*; Gardner et al. 2023), the prospect of addressing these questions has become attainable. Recent studies have already started to discover galaxies deep into the epoch of re-ionisation ( $z > 10$ ; e.g. Curtis-Lake et al. 2023; Robertson et al. 2023b; Wang et al. 2023), revealing that typical galaxies are metal-poor with small stellar masses of order  $\sim 10^7 - 10^9 M_{\odot}$  and young stellar ages ( $t \sim 10^7 - 10^8 \text{yr}$ ). These galaxies exhibit moderate levels of star formation rate ( $0.2 - 5 M_{\odot} \text{yr}^{-1}$ ), but are compact ( $r \sim 0.1 - 1 \text{kpc}$ ), leading to high star formation surface densities which likely

initiated the re-ionisation process (Robertson et al. 2023b). While such galaxies likely serve as the primary source of ionizing photons throughout the epoch, a new population of faint galaxies with similar stellar masses, but hosting an obscured actively accreting supermassive black hole (Type 2 AGN; see section 1.2), could also play a role in the re-ionisation of the Universe (e.g. Yang et al. 2023; Scholtz et al. 2023).

### 1.1.2 Galaxy Classifications

Galaxies observed today exhibit a broader range of characteristics compared to their earlier counterparts, but amid this diversity, certain shared features become apparent. Recognizing and understanding these similarities underscores the importance of classification schemes. One widely accepted classification system dates back to 1926, when Hubble proposed a sequence diagram resembling a tuning fork, in which galaxies were placed, based on their optical morphology (Hubble, 1926). As can be seen in Figure 1.1, the diagram starts from left to right with the early type (or ellipticals) class, in which galaxies exhibit a smooth and featureless elliptical profile, ordered by ellipticity (with 0 indicating a round elliptical, and 7 corresponding to the flattest one). At the opposite side of the diagram are the so-called late-type galaxies (or spirals). Unlike the ellipticals, these galaxies appear disc-like and contain well defined spiral arms. There are two branches of this class, depending on whether a bar is present at the center (SB) or not (S). In both cases, the galaxies are ordered based on the size of the nucleus (the bulge) and the prominence of the spiral arms (with “a” having a larger bulge and more tightly wound spiral arms, and “c” having a smaller bulge and more loosely wound arms). In between them is the transitional class - the lenticulars (S0 or SB0) in which galaxies exhibit a faint disc but lack prominent spiral arms. Finally, galaxies that do not fall within any of these categories are classified as irregulars (Irr).

Although, this type of classification was initially based solely on visual appearance, it has since become associated with other observable and derivable properties, such as colour (e.g Strateva et al. 2001; Blanton et al. 2003; Kauffmann et al. 2003) and star-formation rate (SFR; e.g Brinchmann et al. 2004; Balogh et al. 2004). This development resulted in the establishment of two overarching galaxy populations, which are most pronounced in the colour – stellar mass diagram as shown in Figure 1.2: passive galaxies, residing in the narrow region known as the ‘red sequence,’ are predominantly associated with early-type galaxies (including lenticulars). They display redder colors and lower levels of star formation, indicative of an older stellar population. Star-forming galaxies, on the other hand, are linked with spirals and irregulars, and populate the

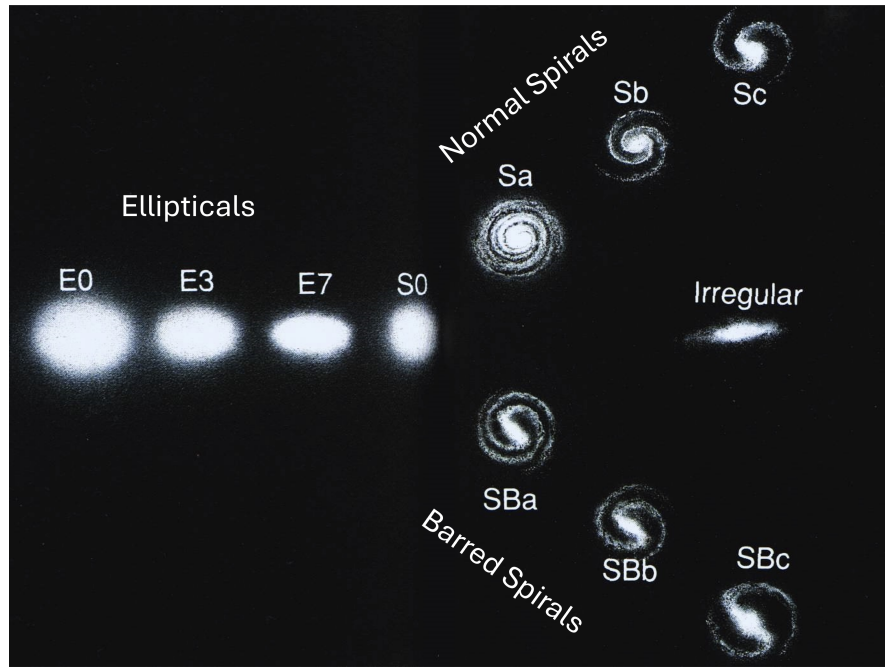


Figure 1.1: The Hubble tuning fork diagram, showing the classification of galaxies based on their optical morphology. Image adapted from Hubble (1958).

more scattered ‘blue cloud.’ These galaxies often appear bluer with higher star formation rates, reflecting the presence of young, hot OB stars. However, it should be noted that both classes are subject to some exceptions (e.g., see Rowlands et al., 2012).

This type of division is present not only in the local Universe, but also at higher redshift (Bell et al. 2004, Williams et al. 2009, Brammer et al. 2009), when the Universe was younger, which allows us to trace the evolution of the two populations individually. In doing so, studies using the number density per given luminosity - the luminosity function (LF; Bell et al. 2004, Willmer et al. 2006, Faber et al. 2007), or per given stellar mass - the stellar mass function (MF; Borch et al. 2006, Ilbert et al. 2010, Ilbert et al. 2013), have discovered that the number density of passive galaxies at low-to-intermediate masses ( $M \lesssim 10^{11} M_{\odot}$ ) grows at  $0 < z < 1$ , whereas that of star-forming galaxies remains nearly constant. Massive red galaxies are found to be already in place at  $z = 1$ , with their number and stellar mass density increasing rapidly from  $z = 3$  to  $z = 1$ , at the same epoch when the star formation rate density reaches its maximum and begins to decline to the present day (Madau and Dickinson 2014; revisited later in section 1.2.2). These results indicate that star formation in galaxies is being suppressed by some sort of mechanism, a process referred to as “quenching”, causing them to migrate from the blue cloud to the red sequence (Faber et al. 2007). However, the nature of this process is still unclear.

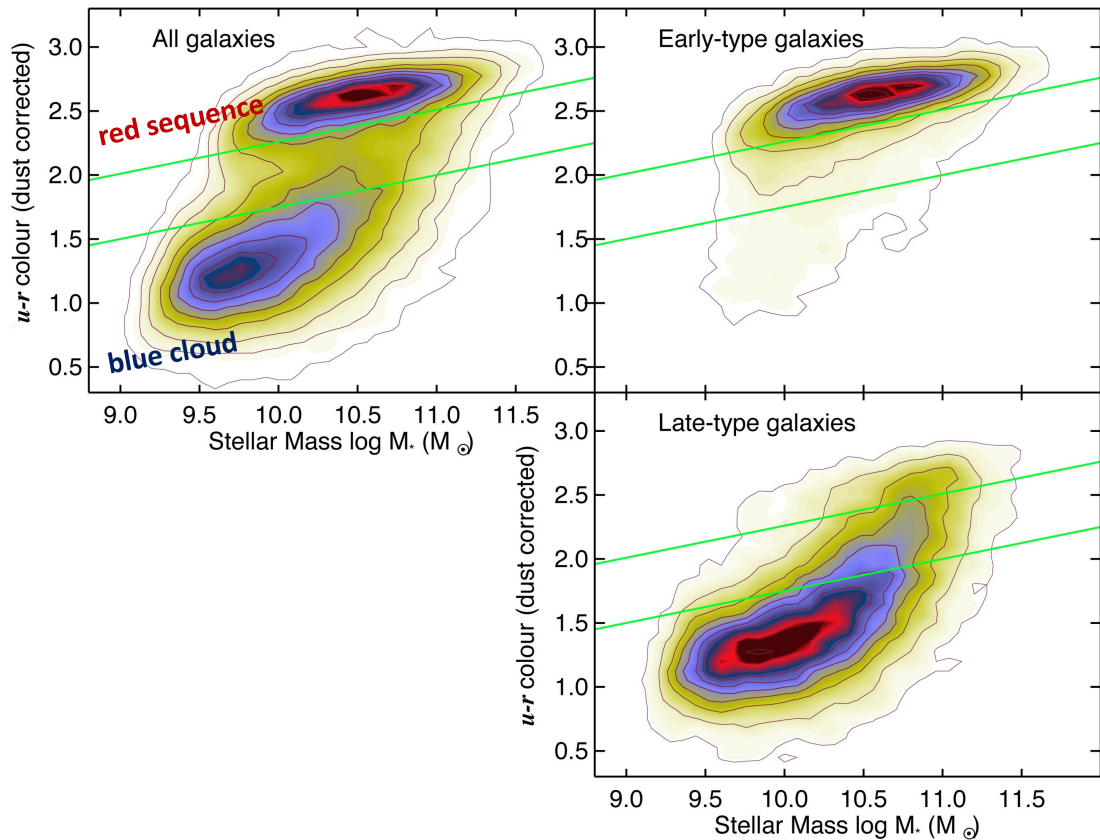


Figure 1.2: The reddening corrected  $u-r$  colour - stellar mass diagram for a sample of galaxies. The top left panel shows the distribution of all galaxies in the sample, while the top right panel depicts only the morphologically classified early-type galaxies and the lower right shows only the late-type. Image adapted from Schawinski et al. (2014).

### 1.1.3 Galaxy Mergers

There is a growing consensus that the transformation of spirals to ellipticals is largely driven by galaxy mergers (e.g. Barnes 1992; Naab and Burkert 2003; Bournaud et al. 2007; Hopkins et al. 2008; Deeley et al. 2017; Martin et al. 2018). The gravitational torque exhibited by major mergers, which involve progenitors of roughly equal mass, is strong enough to disrupt the ordered rotation of material present in spirals into the randomly-oriented, dispersion-dominated motion in elliptical systems, as demonstrated in Figure 1.3. This idea has been supported observationally, where studies into early-type galaxies have found signatures of violent and sudden morphological changes in their stellar populations (e.g. Blake et al. 2004; Wild et al. 2016) and internal dynamics (e.g. Tacconi et al. 2008; Rodrigues et al. 2017), indicative of a past major merger event.

However, minor mergers (i.e. those with unequal progenitor mass ratios) have also been proposed as significant drivers of morphological transformations (e.g. Kaviraj et al. 2009; Kaviraj et al. 2011; Martin et al. 2018), especially at later cosmic epochs ( $z \sim 2$ ). Such merger events could also

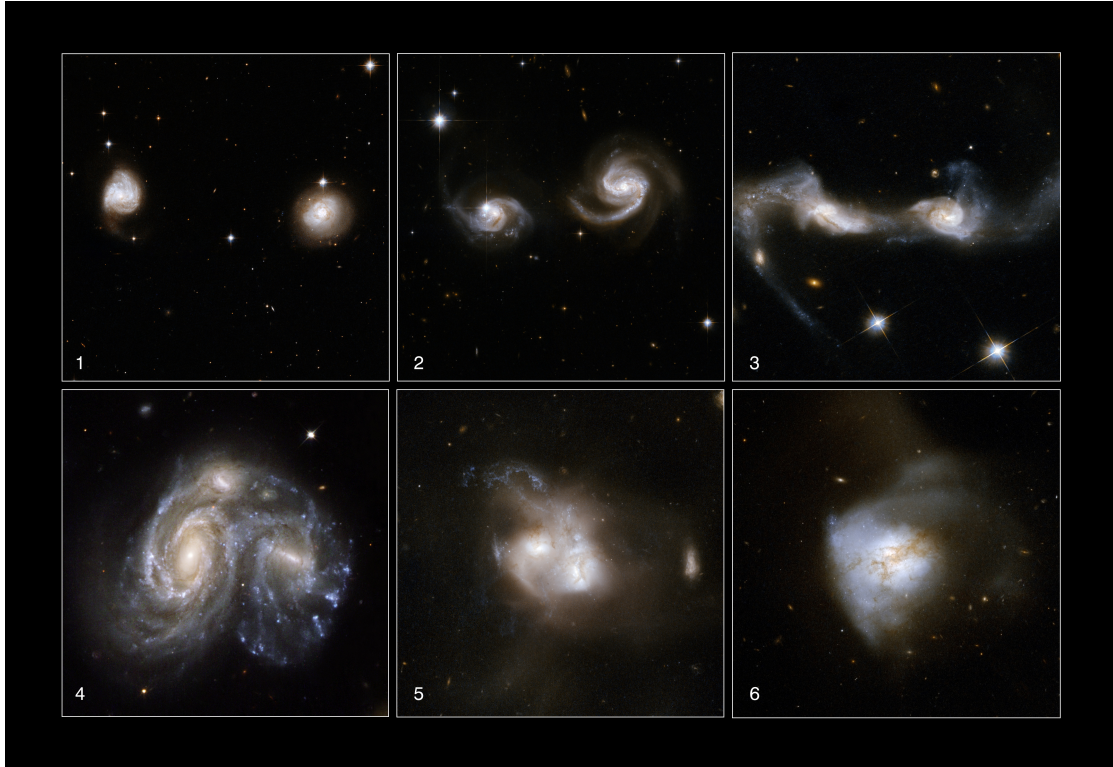


Figure 1.3: Different stages of a galaxy merger event, which last on timescales of Gyrs. Each snapshot represent an actual image, created by combining observations from the Hubble Space Telescope, the Spitzer Space Observatory, the Chandra X-Ray Observatory and Galaxy Evolution Explorer. Image taken from NASA/ESA.

disrupt the ordered rotation of spirals, albeit to a lesser extent, as well as trigger disc instabilities (e.g. Zolotov et al. 2015). Their frequency of occurrence is much higher than major mergers, since low mass galaxies far outnumber their more massive counterparts (as demonstrated by the stellar mass function), making them a crucial part in shaping the evolution of galaxies.

These merger events are also believed to trigger intense outbursts of star-formation (e.g. Barnes 2004; Di Matteo et al. 2007; Kim et al. 2009; Xu et al. 2021). Such shock-induced star formation can rapidly use up all of the available gas, by converting it into stars, and/or increasing the efficiency of stellar feedback in expelling the gas from the galaxy. However, this process may take several gigayears to complete (e.g. Zolotov et al. 2015), whereas observations suggest that galaxies often quench more rapidly (e.g. Schawinski et al. 2014; Barro et al. 2016; Wild et al. 2020). This leads to alternative quenching mechanisms, such as feedback from active galactic nuclei (AGN), fueled by the supermassive black holes (SMBHs; black holes with masses of  $M_{\text{BH}} \sim 10^6\text{--}10^8 M_{\odot}$ ) at the centre of galaxies (e.g. Hopkins et al. 2005; Croton et al. 2006; Fabian 2012; Alexander and Hickox 2012; Heckman and Best 2014; Hardcastle and Croston 2020), which may also be triggered by the merger events.

## 1.2 Active Galactic Nuclei (AGN)

### 1.2.1 Discovery and Unification

AGN are highly energetic sources situated at the centre of galaxies, which produce radiation that cannot be simply explained by stellar processes. Their discovery arguably traces back to 1909, when the first spectroscopic detection of strong emission lines, emanating from the nucleus of NGC 1068, was reported (Fath, 1909). However, it was not until the pioneering work of Carl Seyfert in 1943 that truly led to the recognition of a new class of galaxies. Seyfert noted the presence of broad, high-excitation emission lines associated with a number of bright nuclei in nearby galaxies (Seyfert, 1943), indicating the intense activity and high velocities within these regions. Today, we refer to such galaxies as ‘Seyfert galaxies’ in recognition of his work. But, the term AGN was not used until the development of radio astronomy and the subsequent discovery of quasars or quasi-stellar objects (QSOs). It was these extragalactic sources, characterized by their immense luminosity, which far surpassed that of their host galaxies, and their unusual spectral properties, that prompted the conclusion that AGN result from the accretion of matter onto SMBHs (see Shields 1999 for further details).

AGN display a wide range of characteristics across the electromagnetic spectrum, resulting in their classification into distinct classes. Some key categories include: Seyfert galaxies, which are further divided into Type 1 and Type 2, depending on whether they contain broad permitted lines (with FWHM  $\sim 1000 \text{ km s}^{-1}$ ) in their optical spectrum. Quasars, characterized by a higher bolometric luminosity, which are divided into radio-loud and radio-quiet depending on the ratio of radio-to-optical luminosity. Radio galaxies, featuring relativistic jets and large radio lobes, are classified as broad line and narrow line, based on their optical spectroscopy and as Farnoff-Riley Class I (FRI; brighter in the center) and Class II (FR II; brighter at the edges), as a result of their radio morphology (see Figure 1.4). Blazars, a subtype of radio-loud quasars which are highly variable with timescales varying from hours to days. And finally, Low-Ionisation Nuclear Regions (LINERs), which have a bolometric luminosity much lower than the rest of the classes (see e.g. Beckmann and Shriver 2012 for further details on AGN categorise). However, ongoing debate persists regarding whether all LINERs are truly AGN in nature (see review by Ho 2008).

Much effort has been made to explain the diversity of these classes and to unify them under a common underlying model. The most favoured unification scheme involves the presence of an obscuring optically thick torus that surrounds the black hole and the accretion disc. Initially

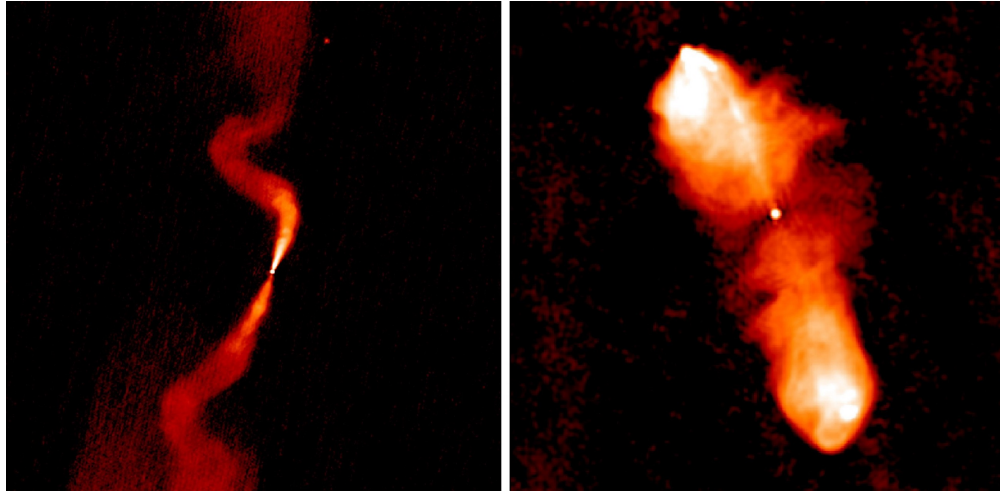


Figure 1.4: Examples of radio galaxies. The left panel presents a radio image of source 3C 31, representing the Fanaroff-Riley Class I, whereas the right panel shows a radio image of 3C 98 representing the Fanaroff-Riley Class II. Image taken from Hardcastle and Croston (2020).

proposed by Antonucci (1993), the existence of such a component would obscure the broad emission lines in Seyfert 2/narrow-line radio galaxies when observed edge-on. In contrast, these emission lines would be visible, as in the case for Seyfert 1/broad-line radio galaxies, when observed face-on. The difference in viewing angles can also explain the difference between radio galaxies, quasars and blazars, depending on the line of sight relative to the jet axis (Urry and Padovani, 1995), as well as the difference between Seyferts and radio-quiet quasars (albeit in the absence of a jet) as indicated in Figure 1.5. However, many challenges remain, particularly in explaining the distinction between radio-loud and radio-quiet AGN (e.g. Kellermann et al. 1989; Ivezić et al. 2002; White et al. 2007; Cirasuolo et al. 2003a,b; Baloković et al. 2012; Gürkan et al. 2019; Macfarlane et al. 2021). This differentiation is governed by the presence or absence of a strong relativistic jet, suggesting underlying physical processes beyond simple orientation effects. Moreover, the current framework fails to describe the differences between FRI and FRII radio galaxies as well as incorporate the less luminous class of AGN, LINERs (e.g. see Netzer 2013 for a discussion).

More recently Best and Heckman (2012) expanded upon this simple orientation model by introducing a new classification scheme, in which AGN are divided into two fundamental modes, depending on the efficiency with which they accrete matter. The first mode is associated with AGN whose primary energy output comes from efficiently converting potential energy from cold, accreted gas into electromagnetic radiation (‘radiatively-efficient’ or ‘quasar-mode’ AGN). Similarly to the orientation model, radiatively-efficient AGN contain a dusty torus, which divides

<sup>1</sup><https://emmaalexander.github.io/resources.html>

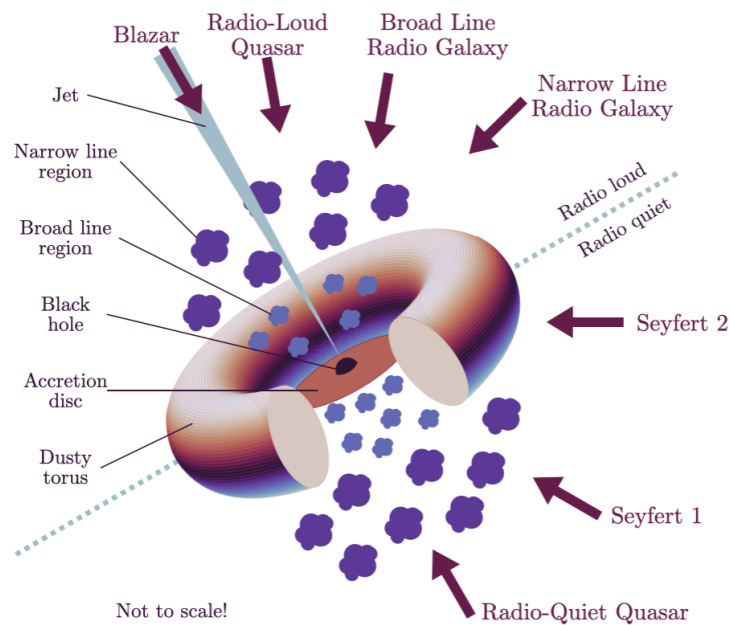


Figure 1.5: A schematic representation of the unified model of AGN, adapted from Urry and Padovani (1995), illustrating how the different type of AGN classes observed can be explained by the viewing angle, as denoted by the arrows, and by the presence or absence of a jet (radio-loud and radio-quiet). Image Credit: Emma Alexander<sup>1</sup>.

them into obscured and unobscured categories, depending on the viewing angle. Additionally, some are found to possess powerful twin radio jets, whereas others lack or are associated with weaker ones (i.e. the previous radio-loud/radio-quiet division). The second mode of AGN, on the other hand, produces very little radiation as a result of hot gas accretion (‘radiatively-inefficient’ or ‘jet-mode’ AGN). Instead, its energy output comes in kinetic form as two-sided, highly-collimated jets of charged particles, which are most easily detected at radio wavelengths via synchrotron radiation. These jets (including those associated with radiatively-efficient AGN) can extend for several megaparsecs, well beyond the stellar body of the host galaxy, and at the highest radio luminosities produce the FRI and FRII classes. At the lowest radio luminosities, however, they are associated with LINERs, as despite their less powerful radiation, radiatively-inefficient AGN can still ionize weak, low-ionization narrow-line regions. Figure 1.6 demonstrates how the various AGN classes fall into these two categories, and provides some information about their properties (for further details see reviews by Heckman and Best 2014; Hardcastle and Croston 2020).

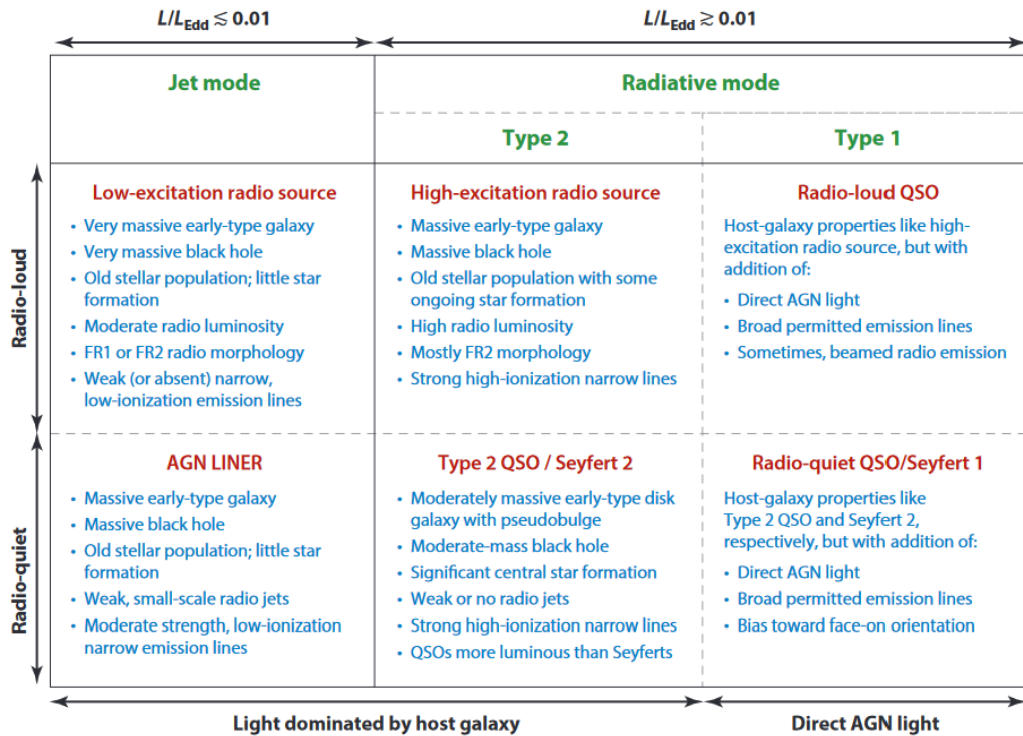


Figure 1.6: The categorisation of AGN classes into the two fundamental modes: radiatively-efficient (radiative mode) and radiatively-inefficient (jet mode), as defined by Heckman and Best (2014), with a description of their typical properties shown in blue, as well as axes denoting the Eddington ratio ( $L/L_{\text{Edd}}$ ), whether they are radio-loud or radio-quiet, and if the light is dominated by the host galaxy (i.e by the star formation processes) or by the AGN. Image taken from Heckman and Best (2014).

## 1.2.2 The co-evolution of AGN and their host galaxies

Understanding the evolution of AGN over cosmic time is crucial, since as previously discussed it is believed to be intrinsically linked to the evolution of their host galaxies. Some of the key evidence supporting this idea include the tight correlation between the mass of the SMBH ( $M_{\text{BH}}$ ) and the stellar velocity dispersion ( $\sigma$ ) of the surrounding galactic bulge (e.g. Ferrarese and Merritt 2000; Gebhardt et al. 2000; Gültekin 2009; Woo et al. 2013; McConnell and Ma 2013; Shen et al. 2015), which can be seen in Figure 1.7. Initially discovered for quiescent galaxies (that is those dominated by an old stellar population) in the local universe, this relationship was found to be more universal; it extends at least to redshift  $z \sim 1$  (e.g. Shen et al. 2015), and applies to galaxies containing an AGN (e.g. Woo et al. 2013; Shankar et al. 2019). Such a relationship is important since  $\sigma$  is a good indicator of the bulge mass ( $M_b \propto L^{5/4} \propto \sigma^5$ ), suggesting that the growth of the black hole is directly proportional to that of the bulge component of the host

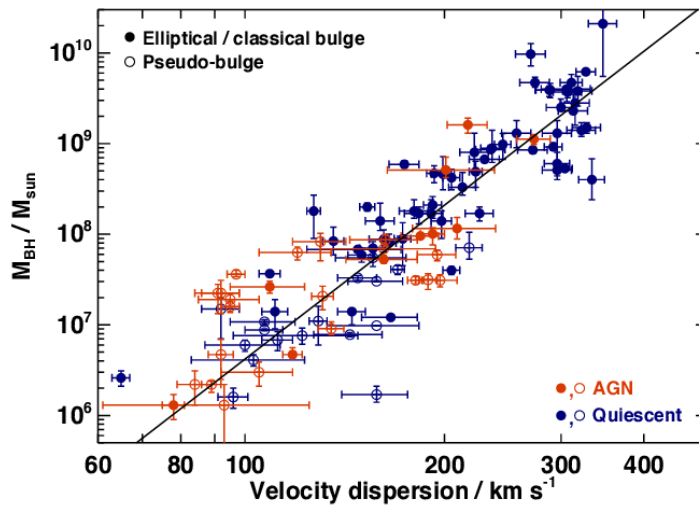


Figure 1.7: The MBH- $\sigma$  relation for quiescent galaxies (red) and AGN (blue; includes both radiative-mode and jet-mode AGNs). The parametric form as denoted by the black solid line is taken from McConnell and Ma (2013). Image taken from Heckman and Best (2014).

galaxy. Therefore, the accretion processes associated with AGNs (that fuel black hole growth) must be related to those affecting the host galaxy, at least up to a few kiloparsecs.

Semi-analytical models and N-body simulations provide additional evidence by highlighting a discrepancy in the LF when comparing theoretical predictions from the hierarchical CDM model to observational data. While feedback from supernovae and stellar winds can explain the fewer faint sources expected per unit volume, a more energetic process is required for the more luminous ones. In this context, the injection of energy from AGN in the form of radio jets has been successful (e.g. Bower et al. 2006; Croton et al. 2006). These radio jets have the capacity to either heat up the surrounding gas or expel it from the galaxy entirely, effectively suppressing star formation and thus the mass buildup of the host, thereby demonstrating the impact of AGN on even larger scales.

Finally, the similarity between the star formation and black hole accretion history highlights the relationship between the AGN and its host through cosmic time (e.g. Boyle and Terlevich 1998; Hopkins et al. 2006; Madau and Dickinson 2014). As shown on Figure 1.8, studies looking at galaxies dominated by star-forming processes (SFGs) have found that the star formation rate density (the black line) has been rising until  $z \sim 2$ , marking the peak of star formation activity (the so-called ‘cosmic noon’), and has been declining to the present day, as previously mentioned. Similarly, observations of AGN indicate a comparable trend in black hole mass growth rate over

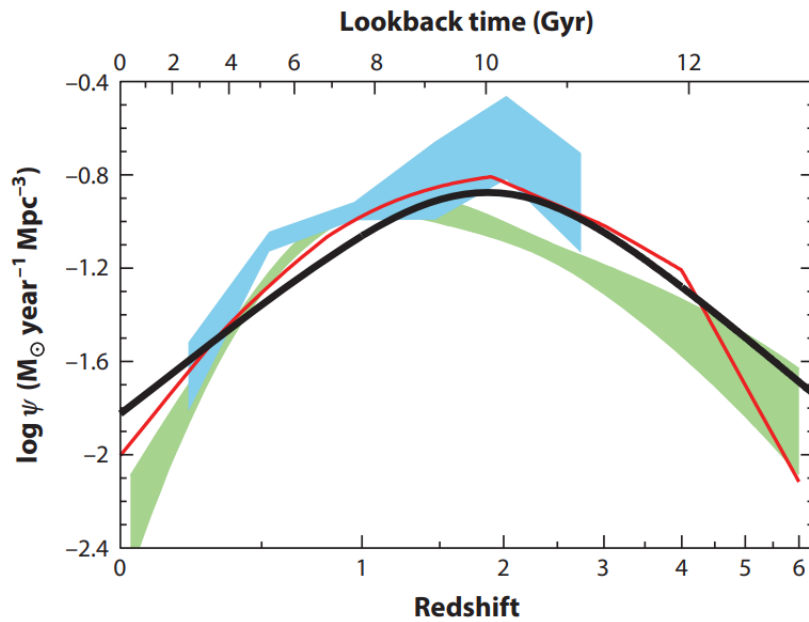


Figure 1.8: The cosmic star formation (SFH) and black hole accretion history (BHAH). The best-fitting function of the SFH (black line), derived from using UV and IR data, is taken from Madau and Dickinson (2014), while that of the BHAH is obtained from Shankar et al. (2009; red line) and Aird et al. (2010; light green shading) using X-rays, and Delvecchio et al. (2014; light blue shading) using IR data. The different shadings, where indicated, represent the  $\pm 1\sigma$  uncertainty ranges. Image taken from Madau and Dickinson (2014).

the corresponding cosmic epochs (e.g. the red line), demonstrating the importance of AGN studies for understanding galaxy evolution.

## 1.3 Astrophysical shocks

### 1.3.1 Different origins of shocks

Shocks in astrophysics originate from a large range of phenomena, including supernovae explosions (e.g. Ellison et al. 1994; Ellison and Cassam-Chenaï 2005; Reach et al. 2019), the activity of radio jets from AGN (e.g. Morganti et al. 2013, 2021, Tamhane et al. 2023), and collisions between galaxies and galaxy clusters (e.g. Moles et al. 1997; Markevitch et al. 2002; Ha et al. 2018). These events release immense amounts of energy, generating shock waves that propagate through the interstellar (ISM), intergalactic (IGM) or intra-cluster medium (ICM).

Supernovae (SNe) create shock waves as the expanding shell of ejected material from the star collides with the surrounding gas and dust, thereby compressing and heating the medium on galactic scales. This process is illustrated in Figure 1.9, where the famous SN remnant, the

Crab Nebula (e.g. Kennel and Coroniti 1984) is shown. Such supernova-driven shocks are quite common during the lifetime of a galaxy (about 3 SNe per century for a Milky Way-like galaxy; e.g. van den Bergh and Tammann 1991), such that they can have a substantial impact on the ISM (see section 1.3.2).

Similarly, high-speed radio jets from AGN produce powerful shock waves as they collide with the surrounding gas, influencing the dynamics and distribution of matter in galaxies on larger scales, as demonstrated by the snapshots in Figure 1.10, taken from the simulation by Wagner and Bicknell (2011). These shocks waves can also extend their impact to affect the IGM or ICM, depending whether the galaxy is in a group or a cluster (reaching up to  $\sim 100$  kpc; e.g. Heckman and Best 2014; Hardcastle and Croston 2020; Tamhane et al. 2023).

Additionally, collisions between galaxies and galaxy clusters generate shock waves as the closing speed between neighboring systems is supersonic in the IGM or ICM, effectively trapping gas within. These collisions compress and heat the gas within and in between galaxies, leading to the formation of large-scale shock fronts (e.g. Moles et al. 1997; Markevitch and Vikhlinin 2007a; Russell et al. 2022). Examples such as the Bullet Cluster (1E 0657-56; e.g. Markevitch et al. 2002), as seen in Figure 1.9, showcase clear evidence of their existence and their impact on the ICM - which is prominent in the X-rays due to the high temperatures of the medium.

### **1.3.2 The many roles of shocks**

Astrophysical shocks play important roles in the evolution of galaxies, particularly in regulating their star formation. As previously discussed in section 1.2.2, stellar feedback from SNe, that is shock waves produced by them, is thought to be sufficient to suppress star formation in low-mass galaxies ( $\lesssim 10^{10} M_{\odot}$ ; e.g. Silk 2011), while the corresponding role in more massive galaxies is often attributed to AGN activity. However, jet-induced star-formation has also been proposed in a number of studies (e.g. Silk 2005; Kalfountzou et al. 2012; Gaibler et al. 2012; Silk 2013; Kalfountzou et al. 2017), in which jets propagating through the ISM can compress the gas, leading to the birth of new stars. Moreover, shocks induced by galaxy interactions or mergers have also been found to be associated with intense bursts of star formation, particularly observed in ultraluminous and luminous infrared galaxies (e.g., Rich et al. 2011, 2015).

These shocks also impact the distribution of dust, which is a fundamental part that regulates the temperature and density of the ISM (Draine 2011). While the ejecta of SNe are a favoured

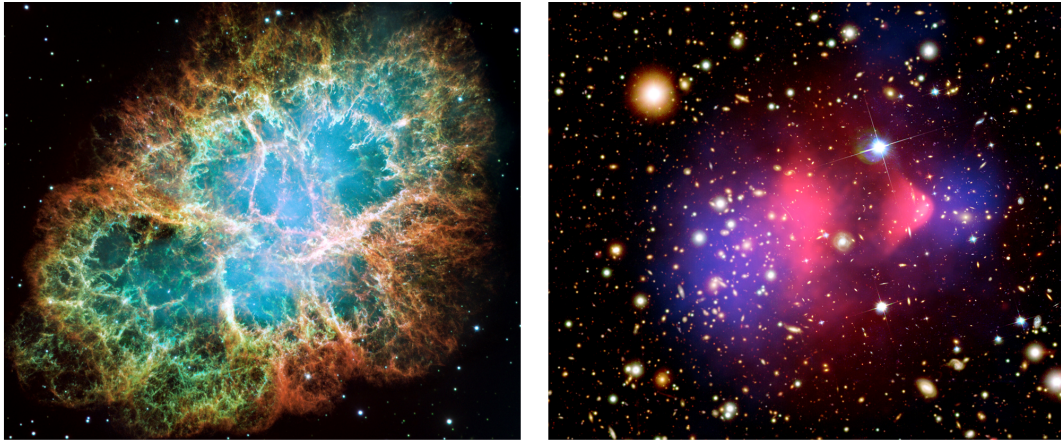


Figure 1.9: Famous examples of astrophysical shocks. The left panel shows the Crab Nebula, demonstrating an expanding shock wave, along with a rapidly spinning neutron star in the center (in blue), both of which are the products of a supernova explosion. This is a composite image made with the F502N, F631N and F673N filters of Hubble’s Wide Field Planetary Camera 2, such that the colours represent different elements that were expelled during the explosion, where red denotes [O III], blue (in the outer part) is associated with [O I] and green indicates [S II]. Image Credit: NASA, ESA, J. Hester and A. Loll (Arizona State University). The right panel highlights the shock wave generated by the high-speed, head-on collision between galaxy clusters in the Bullet Cluster. In addition, this image showcases the spatial offset from normal matter as traced by X-rays (pink) and the concentration of the total matter as calculated from gravitational lensing (blue), revealing the spatial separation between the shock-emitting gas and dark matter. Image Credit: NASA/CXC/CfA/M.Markevitch, NASA/STScI, Magellan/U.Arizona/D.Clowe, and ESO WFI.

scenario for dust production (e.g. Gall et al. 2011), the subsequent fast shocks generated by them can destroy the dust grains by the process of sputtering (e.g. Draine and Salpeter 1979; Jones et al. 1994; Jones and Nuth 2011; Zhu et al. 2019).

Furthermore, shocks can enhance the radio emission by accelerating charged particles to relativistic speeds in the galaxy’s magnetic field, leading to synchrotron radiation (e.g. Blandford and Eichler 1987; Kang and Ryu 2011; Caprioli 2012). This phenomenon, as we will discuss further in section 1.4.1, makes the radio band a good tracer of jet activity and supernovae, which in turn serves as a recent star formation indicator (e.g. Condon 1992). Additionally, weaker shocks that are unable to produce significant particle acceleration can instead compress the surrounding medium, increasing the density of magnetic fields and charged particles, which would also lead to a boost in the radio emission (e.g. Enßlin and Gopal-Krishna 2001; Markevitch et al. 2005; Colafrancesco et al. 2017), as we will see in Chapter 3.

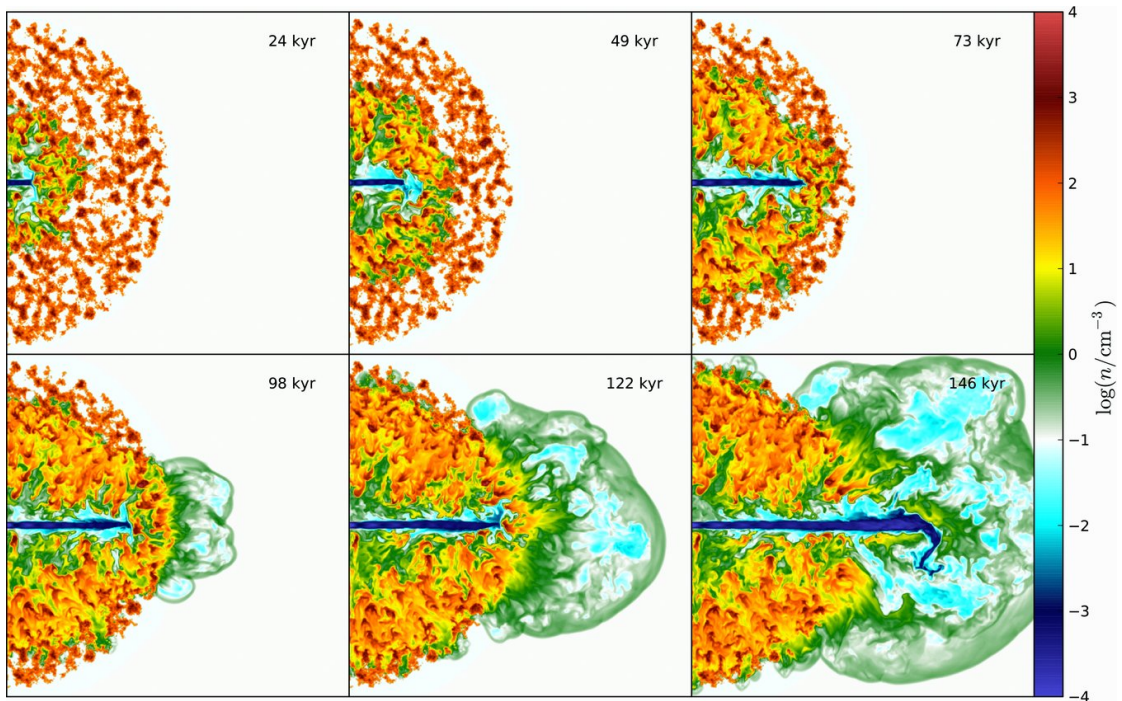


Figure 1.10: Different snapshots showing the interaction of a jet with a clumpy ISM, based on the simulation from Wagner and Bicknell (2011). The dimensions of each panel are 1 kpc in width and height, the time at each snapshot is denoted in the upper right corner and the colourbar denotes the density of the warm gas. Image taken from Wagner and Bicknell (2011).

## 1.4 The Radio Band

### 1.4.1 The low-frequency radio population

In the past decade, significant advancements in the sensitivity of upgraded radio interferometers such as the Karl G. Jansky Very Large Array (VLA; Kellermann et al. 1989) and of the new generation radio telescopes such as the South African MeerKAT (Jonas and MeerKAT Team 2016), the Australian Square Kilometre Array Pathfinder (ASKAP; Hotan et al. 2021), and the Low-Frequency Array (LOFAR; van Haarlem et al. 2013), have placed radio surveys at the forefront of studying galaxy evolution. This is attributed to the shift in composition of radio sources: while radio-loud AGN dominate the radio sky at higher 150 MHz flux densities ( $S_{150\text{MHz}}$ ), the radio source count is found to be increasingly dominated by SFGs at the sub-mJy regime, with a turning point at 150MHz around  $S_{150\text{MHz}} \approx 1.5\text{mJy}$  (e.g. Padovani 2016; Smolčić et al. 2017; Algera et al. 2020; Best et al. 2023; Das et al. *subm*). This indicates that radio observations are valuable not only for studying AGN, which as discussed is an important driver for galaxy evolution, but also for probing star formation processes.

As we saw in the previous sections, the SFR of a galaxy also plays a vital role in its evolution, therefore tracing it across cosmic time is essential. SFR is not a directly measurable quantity, but it can be inferred by the luminosity measured in different wavebands (for further details see Kennicutt, 1998). The near-ultraviolet (UV) emission directly traces the photospheric emission of young stars and is thus one of the most direct tracers of recent SFR (over the past 10–200 Myr; Kennicutt and Evans 2012). Although, UV studies have been able to reach up to  $z \sim 10$  (Oesch et al. 2018; Bouwens et al. 2021), and more recently even up to  $z \sim 15$  with *JWST* (e.g. Donnan et al. 2023; Bouwens et al. 2023; Robertson et al. 2023a; Donnan et al. 2024), during the first few hundred million years after the Big Bang, they are significantly affected by dust and potentially lead to the underestimation of dust-obscured star formation. In the presence of dust, starlight is absorbed and re-emitted in the infrared (IR), making the addition of IR measurements essential for deriving a complete history of star formation. In fact, obscured star formation is found to dominate the cosmic star formation history for the past  $\sim 12$  billion years (Zavala et al., 2021). On the other hand, radio observations offer a unique advantage in that they can provide information on both obscured and unobscured regions simultaneously. As can be seen in Figure 1.11, nearly all radio emission (below a few GHz) comes from synchrotron radiation generated from relativistic electrons spiralling in the magnetic field of a galaxy (Condon 1992; Yun et al. 2001; Kennicutt and Evans 2012; Padovani et al. 2017). In the absence of AGN, such electrons are accelerated to such high speeds by shock waves from supernovae remnants (SNRs), the product of Type Ib and Type II supernovae. Only the most massive stars with  $M \sim 8M_{\odot}$  can lead to these types of supernovae, making the stellar population responsible for radio emission no older than  $\sim 10^8$  yrs (Condon 1992; Kennicutt and Evans 2012).

In the presence of AGN, the majority of synchrotron emission is powered by relativistic jets (Begelman et al., 1984). However, as we move to lower flux densities, where SFGs become more prevalent, these RL (or ‘jetted’) AGN become progressively outnumbered by RQ (or ‘non-jetted’) AGN. Such sources exhibit clear signatures of AGN activity at non-radio wavelengths (e.g., X-ray, mid-IR, and optical), but lack observable large-scale radio jets, making their much weaker radio emission a subject of some debate (e.g. Miller et al. 1993; Cirasuolo et al. 2003a; Kimball et al. 2011; Condon et al. 2013; White et al. 2015; White et al. 2017). This in turn raises the question of whether they are a separate population from the RL AGN (e.g. Kellermann et al. 1989; Ivezić et al. 2002; Cirasuolo et al. 2003a,b; Baloković et al. 2012; Gürkan et al. 2019; Macfarlane et al. 2021), a possibility that will be discussed in Chapter 2. Proposed mechanisms for generating such radio emission in RQ AGN include star formation in the host

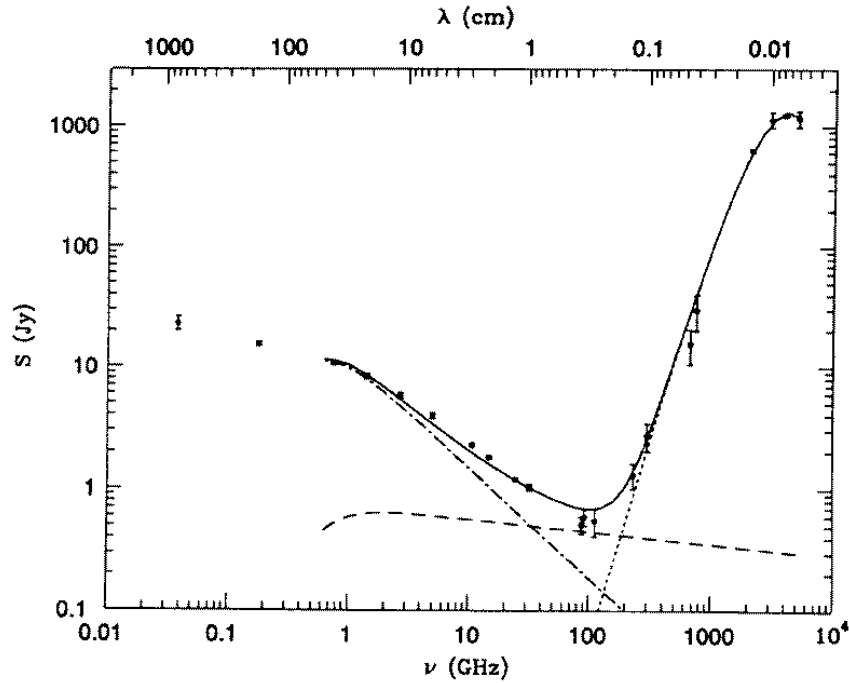


Figure 1.11: The observed radio/FIR spectrum of M82, modelled by the sum (solid line) of synchrotron (dot-dash line), free-free (dashed line), and dust (dotted line) components. This model demonstrates that below  $\sim 30$  GHz, synchrotron emission dominates the radio emission. Image taken from Condon (1992).

galaxies, a scaled-down version of powerful jets, winds associated with the accretion disc of AGN, or the presence of a hot ( $\sim 10^8$  K) corona in its vicinity (e.g. for a review see Panessa et al. 2019). To disentangle which mechanism or combination thereof is responsible requires not only large statistical samples at fainter flux densities, but also observations at higher angular resolution needed to resolve the underlying radio structures.

## 1.4.2 The Low Frequency Array

LOFAR is well equipped to help surveys address these requirements. This innovative radio telescope consists of an interferometric array of dipole antenna stations, primarily situated in the Netherlands, but also extending across Europe as seen in Figure 1.12. Its use of dipole antennas instead of traditional radio dishes, along with its geographical distribution and sophisticated signal processing techniques, have made significant advancement in radio survey capabilities. This design not only dramatically increases the speed of radio surveys, but also offers unparalleled angular resolution, capable of resolving structures down to sub-arcsecond levels, and exceptional sensitivity reaching an order of a few tens of  $\mu$ Jy (for a more detailed description, refer to van Haarlem et al. 2013).

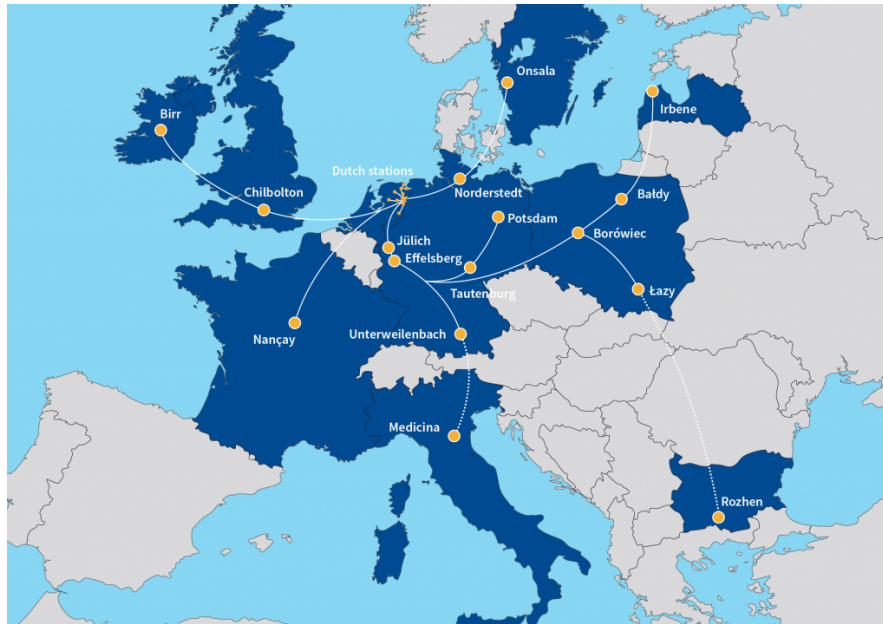


Figure 1.12: A map of LOFAR stations displaying the current stations in the Netherlands, Germany, Poland, France, Sweden, United Kingdom, Ireland and Latvia, alongside future expansions in Medicina, Italy and Rozhen, Bulgaria. Image taken from LOFAR-BG.

In addition, LOFAR probes the largely unexplored low-frequency range of 10–240 MHz. This frequency range is sensitive not only to synchrotron radiation (making it ideal for studying SFGs and AGN), but is also less affected by thermal emission, which as seen in Figure 1.11 can be significant at a few GHz, the frequency range of the VLA. When combined with the capabilities of other interferometers operating at higher frequencies (e.g. the VLA), LOFAR’s ability to capture older, more diffuse emission complements their sensitivity to younger, more compact structures (e.g. Miskolczi et al. 2019; Ignesti et al. 2022; Jones et al. 2023; Bruno et al. 2023). This synergy enables comprehensive studies across different spatial scales, facilitating deeper understanding of astrophysical processes, as will be demonstrated in Chapter 3.

One survey that leverages the unique capabilities of LOFAR is the LOFAR Two-metre Sky Survey (LoTSS; Shimwell et al. 2017), which uses a tiered strategy within the frequency range of 120–168 MHz. In its wide area tier (LoTSS wide area), the survey aims to cover the entire northern hemisphere at an angular resolution of  $\sim 6''$  (using only the Dutch stations), reaching a sensitivity below  $100\mu\text{Jy}/\text{beam}$ , surpassing the sensitivity of the high-resolution sky survey, the Faint Images of the Radio Sky at Twenty-cm survey (FIRST; Becker et al. 1995), by a factor of 10. By making use of the international stations, LoTSS has further started surveying the northern sky at a resolution of 0.3 arcsec, whilst maintaining its sensitivity (Morabito et al. 2022; Jackson et al. 2022a; Sweijen et al. 2022). The deep tier (LoTSS deep fields; Tasse et al. 2021; Sabater et al.

2021), on the other hand, focuses on well-studied several-degree scale regions, containing the highest quality multi-wavelength datasets available across a broad range of the electromagnetic spectrum. Current deep fields include Boötes, ELAIS-N1 and Lockman Hole, reaching a depth of 20-35  $\mu\text{Jy}/\text{beam}$  in the central regions (albeit with sensitivity that varies with locations due to the nature of the facility). However, additional fields and deeper observations (aiming to reach  $\sim 10\mu\text{Jy}/\text{beam}$ ) are underway. This survey will thus provide us with large statistical samples of both the rarest bright (i.e. RL AGN) and numerous faint (i.e. RQ AGN and SFGs) sources. However, differentiating between SFGs and AGN, as well as between the various classes of AGN requires a multi-wavelength approach, with optical spectroscopy being at the forefront of the field.

## 1.5 Optical Spectroscopy of Distant Sources

### 1.5.1 Diagnostics

Optical spectroscopy has revolutionised our understanding of Galaxy Formation & Evolution, providing us with a wealth of information about galaxy properties and dynamics. A galaxy's spectrum not only provides us with an accurate distance measurement (i.e. redshift), but also allows us to determine its chemical abundance (e.g. Kewley and Dopita 2002; Marino et al. 2013; Dopita et al. 2013, 2016; Curti et al. 2017), assess the amount of dust present (e.g. Momcheva et al. 2013; Domínguez et al. 2013), measure the electron density and temperature (e.g. Osterbrock and Ferland 2006; Proxauf et al. 2014; Luridiana et al. 2015), estimate the age of the stellar population (e.g. Bruzual and Charlot 2003; Kauffmann et al. 2003; Hathi et al. 2009; Haines et al. 2017), quantify the rate of star formation (e.g. Kennicutt 1998; Kewley et al. 2004; Kennicutt and Evans 2012; Madau and Dickinson 2014) and more importantly enable the identification of an AGN presence (e.g. Kewley et al. 2001; Kauffmann et al. 2003; Stasińska et al. 2006; Cid Fernandes et al. 2010; Best and Heckman 2012), along with information about its black hole mass and accretion rate (e.g. McLure and Jarvis 2002; Vestergaard and Peterson 2006; Vestergaard and Osmer 2009; Shen et al. 2011; Rakshit et al. 2020). Such properties are derived through empirically constrained or theoretically defined diagnostics. In this discussion, we will specifically focus on diagnostics tailored to distinguish between SFGs and AGN, and their various classes.

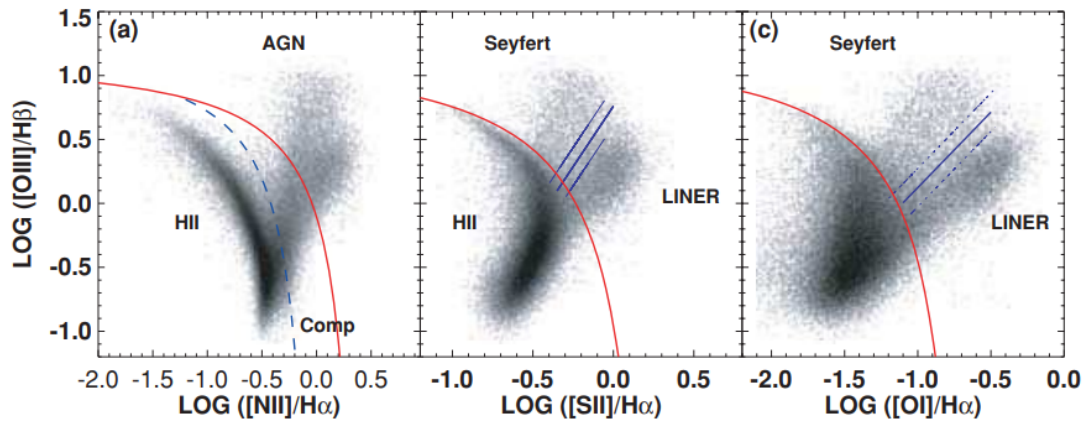


Figure 1.13: The three BPT diagnostic diagrams. The first panel (a) shows the BPT-NII diagram which is commonly used to separate sources into SFGs, composite and AGN by using the demarcation lines proposed by Kauffmann et al. (2003; blue dashed line), and Kewley et al. (2001; red solid line). Panel (b) and (c) show the BPT-SII and BPT-OI, respectively which are used to further separate the AGN class into Seyferts and LINERs by using the demarcation line (blue solid line) proposed by Kewley et al. (2006).

The most widely used tools in separating SFGs and AGN in literature (e.g. Kewley et al. 2006; Cid Fernandes et al. 2010; Best and Heckman 2012; Sabater et al. 2019; Kewley et al. 2019 and references therein) are the BPT diagrams (named after Baldwin, Phillips & Terlevich; Baldwin et al. 1981), which use four optical emission line ratios:  $[OIII] \lambda 5007/H\beta$  versus  $[NII] \lambda 6583/H\alpha$ ,  $[SII] \lambda 6731/H\alpha$ , and  $[OI] \lambda 6300/H\alpha$  (hereafter BPT-NII, BPT-SII and BPT-OI) as seen in Figure 1.13, to determine the dominant mechanism of their excitation. These ratios are an efficient diagnostic since the Balmer lines ( $H\beta$ ,  $H\alpha$ ) are produced from atomic transitions more prevalent in dense regions such as star-forming regions, whereas the higher ionisation forbidden lines ( $[OIII] \lambda 5007$ ,  $[OI] \lambda 6300$ ,  $[NII] \lambda 6583$ ,  $[SII] \lambda 6731$ ) occur in extremely low density environments, and require a much more energetic source of radiation, such as an AGN. Furthermore, the forbidden and Balmer line pairs along each axis are chosen such that they are in close wavelength proximity with each other, such that the effects of dust extinction and imperfect flux calibration are minimal.

A commonly used demarcation line to separate SFGs and AGN across all diagrams is the ‘maximum starburst line’, proposed by Kewley et al. (2001), which is defined using a combination of stellar population synthesis and photoionization models. In addition to this line, the BPT-NII diagram also features additional separation lines, such as the empirically-defined line introduced by Kauffmann et al. (2003), and the less widely used semi-empirical line from Stasińska et al. (2006). These lines delineate a distinct region between them and the maximum starburst line, specifically designated for composite objects where both star formation and AGN activity

contribute. The additional separation between Seyfert galaxies and LINERs, that is between high-ionisation and low-ionisation AGN, was developed by Kewley et al. (2006) by identifying two well separated branches on the BPT-SII and BPT-OI diagrams (see panel (b) and (c) in Figure 1.13). However, requiring a significant detection in all six lines can significantly reduce the sample size. Therefore, since the separation between SFGs and AGN is clearer in the BPT-NII diagram, and the [NII]  $\lambda 6583$  is more prominent than the [OI]  $\lambda 6300$  and extends to higher redshift than [SII]  $\lambda 6731$ , studies have transposed the Seyfert/LINER division to the BPT-NII diagram (e.g. Cid Fernandes et al. 2010), thus making it the main BPT diagram.

Incorporating radio observations in such diagnostics has enhanced our ability to identify different classes of AGN, namely those that possess a ‘radio-excess’ relative to the star-formation (i.e. RL AGN). Amongst many diagrams in the literature is the one proposed by Best et al. (2005), where RL AGN are found to be well distinguished from sources dominated by star-formation on the 4000-Å break strength,  $D_n(4000)$  versus radio luminosity per given stellar mass plane ( $L_{1.4\text{GHz}}/M_*$ ), as demonstrated in the first panel of Figure 1.14. This distinction is possible since both parameters are broadly expected to depend on the specific SFR (SFR per stellar mass) of the galaxy. In a more recent study by Best and Heckman (2012), this diagnostic was applied in conjunction with the BPT diagram and a newly defined  $L_{1.4\text{GHz}}$  vs  $L_{\text{H}\alpha}$  diagram (see second panel of Figure 1.14) to create a ‘cleaner’ RL AGN sample. The latter diagram was created on the basis that  $L_{1.4\text{GHz}}$  and  $L_{\text{H}\alpha}$  in star-forming galaxies should be tightly correlated as both serve as recent SFR indicators, such that sources at higher radio luminosities, outside this correlation, would be associated with RL AGN. Best and Heckman (2012) extended their work by further dividing the RL population into low- and high-excitation systems. They employed a multi-stage approach that involved all six BPT lines, along with the [OIII]  $\lambda 5007$  equivalent width, highlighting the effectiveness of optical spectroscopy in source classification. This discussion will be revisited in Chapter 4.

## 1.5.2 Large Scale Spectroscopic Surveys

Such diagnostic tools are only made possible as a result of large spectroscopic samples, such as those provided by the Sloan Digital Sky Survey (SDSS; York et al. 2000). The SDSS uses the 2.5m wide-angle optical telescope at Apache Point Observatory in New Mexico, USA to conduct

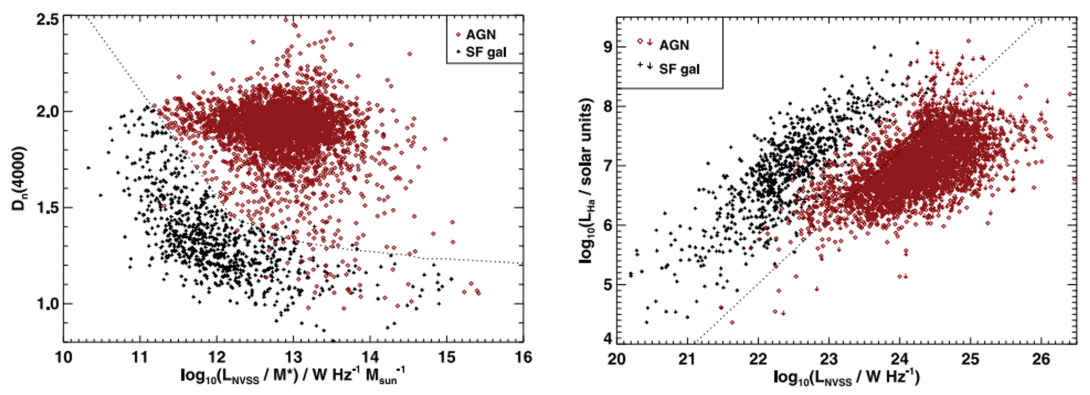


Figure 1.14: Diagnostics diagrams for separating SFGs (black) and RL AGN (red). The first panel presents the  $D_n(4000)$  versus  $L_{1.4\text{GHz}}/M_*$  method, where the demarcation line is taken from Best et al. (2005). The second panel shows the relationship between  $L_{1.4\text{GHz}}$  and  $L_{H\alpha}$ , featuring a separation line derived from Best and Heckman (2012). Image adapted from Best and Heckman (2012).

imaging across five bands ( $u, g, r, i, z$ ) along with spectroscopic follow-up using a pair of multi-object spectrographs<sup>2</sup>, each consisting of 500 fibres with an entrance diameter of  $2''$ , covering the vacuum wavelength range of  $3600 - 10,400\text{\AA}$  at a resolution of  $\lambda/\Delta\lambda \approx 2000$ . To date, its four completed phases have produced over 4 million galactic and extra-galactic spectra (see most recent data release described in Almeida et al. 2023). The most prominent spectroscopic samples produced include: the main-galaxy sample part of the Legacy Survey (SDSS I/II; Strauss et al. 2002; Abazajian et al. 2009), which is fully complete to a magnitude limit of  $r = 17.77$  across  $8,032\text{ deg}^2$ . This low-redshift sample ( $z < 0.2$ ) benefits from the value added catalogues provided by the Max-Planck-Institute for Astrophysics-John Hopkins University group (MPA-JHU; Kauffmann et al. 2003, Brinchmann et al. 2004 and Tremonti et al. 2004), which include emission line, stellar mass, star-formation rate and oxygen abundance estimates, making it a widely used dataset even today (e.g. Gürkan et al. 2018; Pierce et al. 2022; Goubert et al. 2024; Chilufya et al. 2024; Sun et al. 2024; Drake et al. *in prep*). Additionally, there are the LOWZ ( $0.15 < z < 0.4$ ) and CMASS ( $0.4 < z < 0.7$ ) samples from the Baryon Oscillation Spectroscopic Survey (BOSS in SDSS III; Dawson et al. 2013), covering an area of  $9,329\text{ deg}^2$ . These samples are not only magnitude limited ( $16 < r < 19.6$  in the LOWZ and  $17.5 < i < 19.9$  in the CMASS), but also contain a colour-cut to obtain more massive passively evolving galaxies (see Reid et al. 2016 for further details). However, they still contain star-forming galaxies as demonstrated by the value added catalogue provided by the Portsmouth Group (Thomas et al. 2013), which contain emission line and stellar kinematics measurements. Finally, the Emission Line Galaxies

<sup>2</sup>Before the update back in 2008, the spectrographs consisted of a total of 640 fibres with a larger entrance diameter of  $3''$ , and covered the narrower wavelength range of  $3800 < \lambda < 9200\text{\AA}$ .

(ELGs) sample from the extended-Baryon Oscillation Spectroscopic Survey (eBOSS in SDSS-IV; Dawson et al. 2016), selected with photometry from the DECam Legacy Survey (DECaLS; Dey et al. 2019), which is roughly 1.5 mag deeper than that of SDSS (e.g see Jackson et al. 2022b). With this sample, a value added catalogue was created, containing classifications of intermediate redshift ( $0.3 < z < 0.8$ ) galaxies, where machine learning methods were used to separate sources into SFGs, composites, AGN and LINERs (see Zhang et al. 2019 for further details). Apart from the galaxy samples, SDSS also targeted QSOs during its various phases, which will be discussed in Chapter 2.

Following the success of SDSS’s wide-field imaging and spectroscopy, the Dark Energy Survey Instrument (DESI; Desi Collaboration et al. 2016a,b) aims to build upon this foundation, by providing spectroscopy of nearly 14 million bright galaxies (BGS; Hahn et al. 2022), 7.5 million luminous red galaxies (LRG; Zhou et al. 2023), 15.5 million emission line galaxies (ELG; Raichoor et al. 2023), and 3 million quasars (QSO; Chaussidon et al. 2023) over the wide area of 14,000 deg<sup>2</sup>. DESI consists of 10 identical spectrographs, each equipped with 500 fibres, allowing for simultaneous observation of a larger number of targets, and thus faster acquisition of spectra compared to SDSS (for details see DESI Collaboration et al. 2022). Each spectrograph splits the light into three wavelength channels with distinct spectral resolutions ( $\lambda/\Delta\lambda = 2000 - 3000$  in the shortest wavelength channel, and  $\lambda/\Delta\lambda = 4000 - 5000$  in the longest), collectively covering the wavelength range of  $3600 < \lambda < 9800\text{\AA}$ . The photometry needed for these targets is provided by a combination of three surveys (the DESI Legacy Surveys; Dey et al. 2019): DECaLS, which uses the Blanco 4m telescope at Cerro Tololo in Chile, the Beijing-Arizona Sky Survey (BASS) with the 2.3m Bok Telescope and the Mosaic  $z$ -band Legacy (MzLS) with the 4m telescope Mayall telescope, both located at the Kitt Peak National Observatory, Arizona. Together, they provide  $g, r, z$  imaging at a much deeper level than SDSS, which is demonstrated in Figure 1.15, which shows a slice through a 3D map of galaxies up to  $z \sim 1$  from the four completed phases of SDSS and the early data release from DESI (DESI EDR; DESI Collaboration et al. 2023). As can be seen, even in its early stages, DESI’s capabilities to detect fainter and more distant sources provide a denser and more detailed view of the large-scale structure. This dataset contains over 1.2 million extragalactic sources across 1,390 deg<sup>2</sup> area, which will be discussed in Chapter 4.

Both SDSS and DESI have a good overlap with LoTSS, however, due to their selection criteria,

---

<sup>3</sup><https://noirlab.edu/public/images/comparisons/noirlab2203a/>

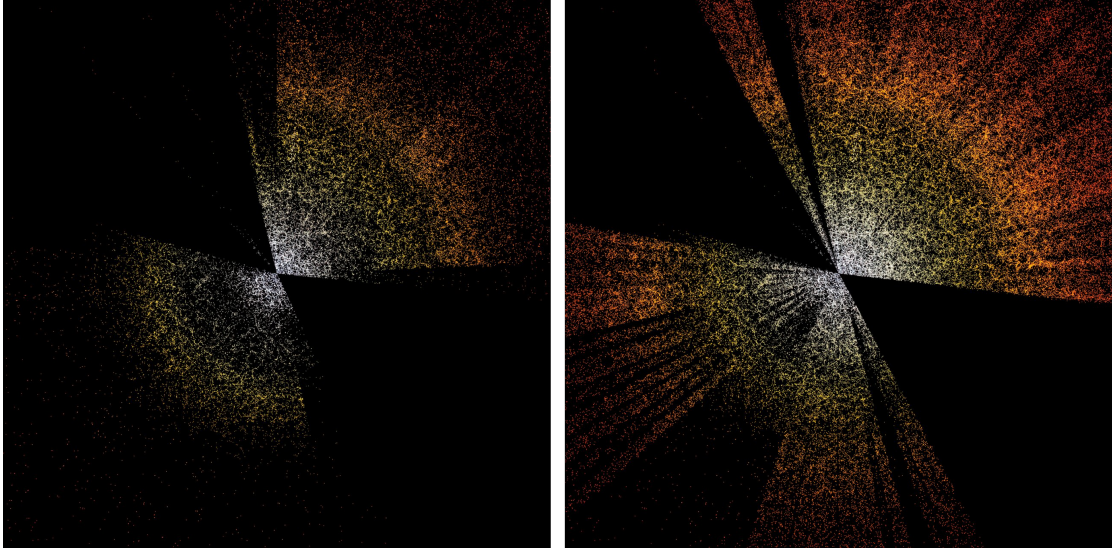


Figure 1.15: A slice through the 3-D map of galaxies from the four completed stages of the Sloan Digital Sky Survey (SDSS; left) and the early data release of the Dark Energy Spectroscopic Instrument (DESI; right). The Sun is at the centre, with the furthest galaxies plotted at  $z \sim 1$ . Image credit: D. Schlegel/Berkeley Lab<sup>3</sup>.

which primarily rely on optical photometry, these surveys do not provide spectroscopic information for all radio sources. For example, the second data release of LoTSS wide area (Shimwell et al. 2022) identified over 4 million radio sources, of which only 272,888 have corresponding SDSS spectroscopic data and merely 33,726 possess DESI spectra (see Hardcastle et al. 2023). Although this will be improved over DESI’s five years of operation, a significant fraction of sources will still be missed. Achieving a comprehensive spectroscopic catalogue of LoTSS targets necessitates a spectroscopic survey employing a radio selection criterion, precisely what the WEAVE-LOFAR survey (Smith et al. 2016) aims to accomplish. This survey will primarily use the multi-object spectrograph (MOS) of the William Herschel Telescope Enhanced Area Velocity Explorer (WEAVE; Dalton et al. 2012; Dalton 2016; Jin et al. 2023), the next generation spectroscopic facility on the 4m William Herschel Telescope in La Palma, to obtain over a million spectra of LoTSS sources. The MOS mode is equipped with 960 fibres, each with a diameter of  $1.3''$ , providing full wavelength coverage across  $3660 < \lambda < 9590\text{\AA}$  at a resolution of  $\lambda/\Delta\lambda \sim 5000$  (‘low-resolution’ mode) and across three distinct wavelength windows within  $4525 < \lambda < 6431\text{\AA}$  at a higher resolution of  $\lambda/\Delta\lambda \sim 20,000$  (‘high-resolution’ mode). Similarly to LoTSS, WEAVE-LOFAR will adopt a tiered strategy consisting of three tiers: Deep ( $S_{150\text{MHz}} > 100\mu\text{Jy}$ ), Mid ( $S_{150\text{MHz}} > 1\text{mJy}$ ), and Wide ( $S_{150\text{MHz}} > 10\text{mJy}$ ), which as seen in Figure 1.16 will efficiently populate the redshift-luminosity plane, and as a result provide large spectroscopic samples of the rarest radio-bright and the more numerous radio-faint sources. In addition to the MOS, WEAVE comprises of 20 individually deployable ‘mini’ integral field

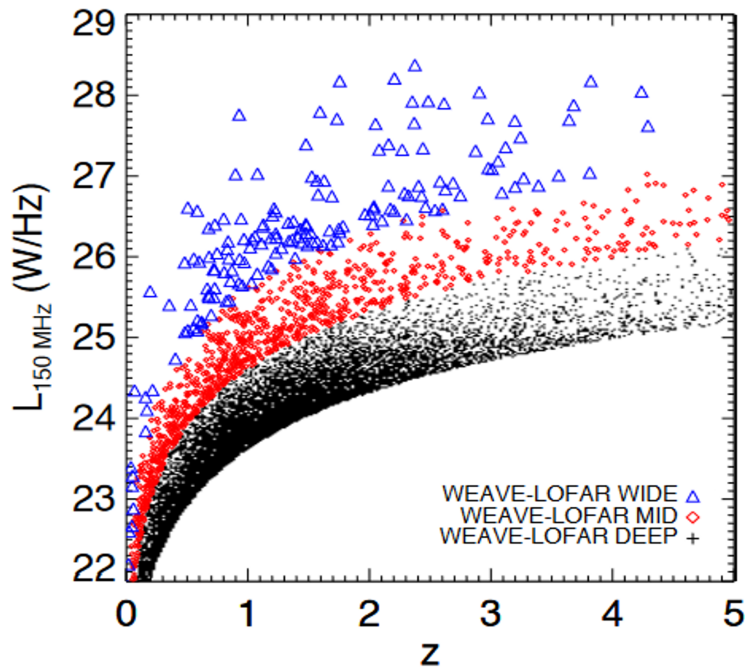


Figure 1.16: The redshift-luminosity plane as sampled by the three tiers of the WEAVE-LOFAR survey: Deep ( $S_{150\text{MHz}} > 100 \mu\text{Jy}$ ), Mid ( $S_{150\text{MHz}} > 1 \text{ mJy}$ ), and Wide ( $S_{150\text{MHz}} > 10 \text{ mJy}$ ), based on realisations of a single WEAVE field of view per tier using the SKA simulated skies (Wilman et al. 2008). Image taken from Smith et al. (2016).

units (IFUs), which share the same spectral resolution as the MOS, and a single large IFU with a factor of two lower resolution in both modes due to the larger fibre size (2.6'' in diameter). These instruments will be used by the survey in relatively poor (as the fibres are larger for the LIFU) or under-subscribed weather condition. They will provide spectra along different spatial locations of nearby, interesting objects, as will be shown in Chapter 3, which will deepen our understanding of the internal dynamics, kinematics, and physical conditions within them.

Another forthcoming spectroscopic survey is the Wide Area VISTA Extra-Galactic Survey (WAVES; Driver et al. 2016), which will use the VISTA/4MOST facility located at the European Southern Observatory's Paranal site in Chile. Similarly to WEAVE, the 4-metre Multi-Object Spectroscopic Telescope (4MOST; de Jong et al. 2022) is a massively-multiplexed facility, which consists of a low-resolution spectrograph (LRS), equipped with 1624 fibres that cover the full wavelength range of  $3700 < \lambda < 9500\text{\AA}$  at a resolution of  $\lambda/\Delta\lambda \sim 6500$ , and a high-resolution spectrograph (HRS) featuring 812 fibres across the narrower range of  $3926 < \lambda < 6790\text{\AA}$  at  $\lambda/\Delta\lambda \sim 20,000$ . Using these instruments, WAVES aims to spectroscopically survey approximately  $\sim 1.6$  million galaxies to  $r < 22$ , achieving a depth four magnitudes deeper than SDSS, but across a smaller area ( $\sim 70 \text{ deg}^2$  in its deep tier, WAVES-DEEP and up to  $1200 \text{ deg}^2$

in its wide tier, WAVES-WIDE). An additional extension to this survey is the Optical, Radio Continuum and HI Deep Spectroscopic Survey (ORCHIDSS; Duncan et al. 2023), which will further provide spectroscopic information for radio continuum and HI selected targets from the deep MeerKAT surveys (MIGHTEE; Heywood et al. 2022, LADUMA; Blyth et al. 2016 and MeerKAT Fornax Surveys; Serra et al. 2016), enabling an in-depth study of the role of neutral hydrogen in the Universe.

Additional next-generation multi-object spectrographs, which will be used by future surveys, include:

- The Prime Focus Instrument (PFS; Tamura et al. 2016) on the 8.2m Subaru telescope with  $\sim 2400$  fibres, covering the wide wavelength range from  $0.38\mu\text{m}$  to  $1.26\mu\text{m}$  at a resolving power of  $\lambda/\Delta\lambda \sim 2300 - 4300$ .
- The Multi-Object Optical and Near-infrared Spectrograph (MOONS; Cirasuolo and MOONS Consortium 2016; Cirasuolo et al. 2020) on ESO's 8.2m Very Large Telescope (VLT), with 1000 fibres covering the wavelength range of  $0.645 < \lambda < 1.8\mu\text{m}$  at low ( $\lambda/\Delta\lambda \sim 4000 - 6000$ ), and high ( $\lambda/\Delta\lambda > 9000$ ) resolution.
- The Maunakea Spectroscopic Explorer (MSE; Hall et al. 2019), an 11.25m optical and near-infrared facility on the summit of Maunakea, which features a total of 4,332 fibers, operating at low ( $\lambda/\Delta\lambda \sim 3000$ ), moderate ( $\lambda/\Delta\lambda \sim 6000$ ) and high ( $\lambda/\Delta\lambda \sim 20,000 - 40,000$ ) spectral resolution across the wavelength range of  $0.37 < \lambda < 1.8\mu\text{m}$ .
- The Wide-field Spectroscopic Telescope (WST; Anderson 2024), a 12.4m telescope consisting of a MOS, fed by  $\sim 20,000$  fibres operating at low-resolution ( $\lambda/\Delta\lambda \sim 4000$ ) and an additional  $\sim 2,000$  fibres operating at high-resolution ( $\lambda/\Delta\lambda \sim 40,000$ ) across the full  $3700 - 9700\text{\AA}$  wavelength range.

## 1.6 Overview

Having outlined our current understanding of galaxy evolution and how the combination of radio observations and optical spectroscopy serves as a powerful tool in this field, we proceed to implement this approach within the framework of the thesis.

In the second chapter, we make use of the available SDSS spectra in the second data release of the LoTSS wide fields (Shimwell et al. 2022), and investigate whether RL and RQ quasars

represent physically distinct populations, which as previously discussed is subject to some debate (e.g. Kellermann et al. 1989; Cirasuolo et al. 2003a,b; Baloković et al. 2012; White et al. 2007; Gürkan et al. 2019; Macfarlane et al. 2021). To address this question, we create a new rest-frame stacking algorithm, designed for future spectroscopic surveys such as WEAVE-LOFAR, and use it to create high signal-to-noise (SNR) composite spectra of RL and RQ quasars, thereby allowing us to study their representative spectral features through cosmic time.

In the third chapter, we use spatially-resolved spectroscopy from the newly-commissioned large IFU of WEAVE in combination with low-frequency LoTSS observations, higher frequency data from the VLA, and additional auxiliary data from the *James Webb Space Telescope (JWST)* to study the large-scale shock front in the nearby compact group, Stephan’s Quintet. This extragalactic shock feature is believed to be the result of an ongoing interaction between NGC 7318b and the system (e.g. Moles et al. 1997; Xu et al. 1999; Iglesias-Páramo et al. 2012; Konstantopoulos et al. 2014; Appleton et al. 2023), making it the ideal laboratory for studying the effects of galaxy mergers and interactions.

In the fourth chapter, we focus on the LoTSS deep fields which contain the most sensitive 150 MHz radio data (see e.g. Tasse et al. 2021; Sabater et al. 2021), where we explore the classification of the faint radio source population. Using the publicly available spectroscopic sample from DESI EDR (DESI Collaboration et al. 2023), we separate sources into four classes: SFGs, RQ AGN, emission-line low-excitation radio galaxies (LINELERGs), and high-excitation radio galaxies (HERGs), and evaluate the performance of photometric classifications, developed for the same sample of radio sources (Best et al. 2023; Das et al. *subm*). This is important as even though spectroscopy is the ‘gold standard’ for source classification (e.g. Best and Heckman 2012), it is not always available. Therefore, optimizing alternative classification methods that rely on photometry is essential.

The main results of these chapters are summarised in Chapter 5, where we discuss their significance in the context of galaxy evolution and how future work will build upon them.

## Chapter 2

# Exploring the radio-loudness of SDSS quasars with spectral stacking

### 2.1 Introduction

The most luminous manifestations of active galactic nuclei (AGN) are quasi-stellar objects (QSOs), also known as quasars, whose bolometric luminosity can reach up to  $10^{47-48}$  erg s<sup>-1</sup> (e.g. Rakshit et al. 2020; Shen et al. 2020). About 5-10% of these optically-selected sources are found to emit strongly in the radio band, likely due to the presence of relativistic jets (Urry and Padovani 1995), while the remaining 90% are only weak radio sources, whose emission could be purely a result of star formation (e.g. Kimball et al. 2011; Condon et al. 2013; Kellermann et al. 2016). This division into radio-loud (RL) and radio-quiet (RQ) quasars raises the question of whether these two types of objects represent physically distinct populations or different evolutionary stages of a single one.

To provide an answer to this question, studies have looked into the distribution of the radio-loudness parameter ( $R$ ; the ratio of radio to optical flux density or luminosity). Some claim that this distribution is bimodal (e.g. Kellermann et al. 1989; Ivezić et al. 2002; White et al. 2007), whilst others present evidence against this bimodality (e.g. Cirasuolo et al. 2003a,b; Baloković et al. 2012; Gürkan et al. 2019; Macfarlane et al. 2021). Part of the reason for these contradictory results could be due to the definition of  $R$ . For example, the use of optical and radio information leads to inhomogeneous samples as a result of different selection effects. In addition, the  $R$  parameter is calculated using different bands, depending on data availability, which may not

give consistent results (Ivezić et al., 2002). Finally, both the optical and radio emission could be contaminated by the host galaxy, while the radio emission could be further complicated by the jet power's dependence on the environment, time and Doppler boosting (e.g. Liu et al. 2006; Gürkan et al. 2019; Radcliffe et al. 2021).

Another debated issue involves the source of radio emission in RQ quasars. In star-forming galaxies, the radio emission is associated with star formation through free-free emission from HII regions and synchrotron radiation from electrons accelerated to relativistic speeds by supernova remnants (Condon, 1992). This leads to the question of whether star formation in the host galaxy is sufficient to account for the observed radio emission from RQ quasars. Some studies find that SF is enough (e.g. Kimball et al. 2011; Condon et al. 2013), whilst others argue that it must come from AGN, in the form of small-scale jets, AGN-driven winds or disc coronal activity (e.g. Laor and Behar 2008; Zakamska et al. 2016; White et al. 2015; Symeonidis et al. 2016; White et al. 2017; Morabito et al. 2022).

The nature of jet production in RL quasars is also not clear. Following the work of Blandford and Znajek (1977), some propose that the black hole (BH) spin plays a vital role in powering radio jets (e.g. Wilson and Colbert 1994; Sikora et al. 2007; Tchekhovskoy et al. 2010). However, due to the extreme difficulty in measuring this quantity, it is challenging to test this model observationally. Another potential physical parameter involved in determining the jet power and thus the distinction between RL/RQ quasars is the BH mass. While some authors find that radio-loudness strongly depends on BH mass (e.g. Gu et al. 2001; Dunlop et al. 2003; McLure and Jarvis 2004; Best et al. 2005; Metcalf and Magliocchetti 2006; Chiaberge and Marconi 2011), others have found only a weak dependence or no dependence at all (e.g. Ho 2002; Shankar et al. 2010; Gürkan et al. 2019; Macfarlane et al. 2021).

To investigate these problems, Gürkan et al. (2019) combined a sample of optically-selected quasars from the fourteenth data release of the Sloan Digital Sky Survey (SDSS; Pâris et al. 2018) with radio observations from the first data release of the LOFAR Two-metre Sky Survey (LoTSS; Shimwell et al. 2017) over the HETDEX spring field (Hill et al., 2008) and the LOFAR H-ATLAS/NGP survey (Hardcastle et al., 2016). With the high sensitivity and wide areal coverage of LoTSS, the authors were able to study the dependence of the radio-loudness parameter on galaxy properties such as redshift, bolometric luminosity, radio luminosity, BH mass and Eddington ratio. They found that quasars exhibit a wide continuum of radio properties, with no clear signatures of a bimodality. Given these results, the authors favoured the scenario where

both AGN jets and SF contribute to the radio emission in quasars such that there is no RL/RQ dichotomy, but rather a smooth transition between the dominance of these two processes.

Recently, Macfarlane et al. (2021) built upon these results by developing a numerical model of the radio flux densities of quasars, in which the radio emission of every quasar consists of two components: AGNs (jets) and SF. This model, coupled with Monte Carlo simulations, allowed the authors to create quasar mock samples and compare them with observations. Their results were found to be in excellent agreement with the observed radio flux distributions of  $\sim 42,000$  SDSS quasars as measured in LoTSS DR1 across several redshift and absolute  $i$ -band magnitude ranges. This is consistent with a model in which jet production is present in all quasars with a different powering efficiency such that it leads to a smooth transition between the RQ and RL quasar regimes.

Our work takes a different approach by developing a spectral stacking algorithm and using it with the much larger LoTSS DR2 sample. With its extensive coverage of 5700 square degrees, LoTSS DR2 provides a much larger observational volume, resulting in a substantial increase of RL quasars. Employing our stacking techniques on this expanded dataset allows us to systematically create composite spectra for each radio class in a given parameter regime (i.e. redshift,  $i$ -band luminosity and black hole mass). This approach enables us to thoroughly explore the continuum and emission line properties of quasars, while also determining the influence of key physical parameters such as black hole mass and Eddington ratio. Therefore, although radio-loudness may not correspond to a physical property of QSOs, it can be useful for identifying sources with powerful jets, and high S/N ratio spectra provide an excellent way to investigate their properties. This stacking algorithm is designed with the upcoming WEAVE-LOFAR survey (Smith et al., 2016) in mind, which as previously discussed will provide over a million spectra of LoTSS targets. Such a tool is necessary as a result of the survey's radio selection criteria, which produces samples dominated by AGN and/or ongoing star formation. The spectra of such sources are rich in emission lines which allow us to robustly determine the redshifts, but a continuum detection is not always available (e.g. for faint star-forming galaxies). Stacking such sources together, however, allows us to statistically detect the continuum and thus recover spectral features otherwise indistinguishable in individual detections. Furthermore, stacking sources of different demographics will enable us to create a large library of high resolution templates that will help improve the WEAVE-LOFAR survey's redshift estimates.

The structure of this chapter is as follows. Section 2.2 provides details of the spectroscopic

and radio data used in this study, along with the methodology for the sample selection and matching process. In section 2.3, we describe the spectral stacking technique employed for comparing the radio classes of QSOs. Subsequently, in sections 2.4 and 2.5, we create high signal-to-noise (S/N) composite spectra of QSOs and investigate potential factors contributing to the observed effects between them. Finally, section 2.6 discusses possible explanations and section 2.7 summarises our main results. Throughout this chapter, we use vacuum wavelengths and a flat  $\Lambda$ CDM cosmology with  $\Omega_\Lambda = 0.7$ ,  $\Omega_M = 0.3$  and  $H_0 = 70 \text{ km s}^{-1} \text{ Mpc}^{-1}$ .

## 2.2 Data

### 2.2.1 Sloan Digital Sky Survey

The spectroscopic data used in this work are taken from the fourteenth data release of the Sloan Digital Sky Survey Quasar Catalogue (SDSS-DR14Q), which is fully described by Pâris et al. (2018). This catalogue includes all spectroscopically confirmed quasars from SDSS-I/II, SDSS-III/BOSS and SDSS-IV/eBOSS programmes, resulting in a sample of 526,356 objects over a region of  $9376 \text{ deg}^2$  as shown in Figure 2.1.

SDSS-I/II contains 79,847 quasars with *i*-band absolute magnitudes brighter than  $M_i[z = 2] = -22.0$  over a wide redshift range of  $0.065 < z < 5.46$ . The targetting algorithm used to obtain these sources has been updated throughout the years and more information about it is provided by Richards et al. (2002) and Schneider et al. (2010). The spectra are produced by a pair of multi-object spectrographs (SDSS) that have a total of 640 fibres with an entrance diameter of  $3''$  and an average resolving power of  $\lambda/\Delta\lambda \approx 2000$  across the vacuum wavelength range from  $3800 \text{ \AA}$  to  $9200 \text{ \AA}$ .

The spectra for SDSS-III/BOSS and SDSS-IV/eBOSS, on the other hand, are produced by the upgraded pair of spectrographs used for the Baryon Oscillation Spectroscopic Survey (BOSS). These spectrographs benefit from having a total of 1000 fibres with a smaller entrance diameter of  $2''$ , an extended vacuum wavelength coverage of  $3600 - 10,400 \text{ \AA}$ , and a resolving power higher in the red channel and lower in the blue channel compared to the SDSS (Smee et al., 2013). These two programs use multiple target selection algorithms to detect much fainter quasars ( $M_i[z = 2] = -20.5$ ) at redshift ranges of  $2.15 < z < 3.5$  and  $0.9 < z < 2.2$ , respectively (for further details see Ross et al. 2012 and Myers et al. 2015). As a result of these differences

and the considerable size of 446,781 for the latter two programs, we use only the BOSS spectra in our analysis.

Complementary to this SDSS-DR14Q catalogue is the value-added catalogue by Rakshit et al. (2020) which includes continuum and line property measurements, including bolometric luminosity ( $L_{\text{bol}}$ ), derived virial black hole mass ( $M_{\text{BH}}$ ) and Eddington ratio ( $R_{\text{edd}}$ ) estimates. This was done using the publicly available spectral fitting code `PYQSOFIT` (Guo et al., 2018), which uses two independent sets of eigenspectra – pure galaxy (Yip et al., 2004b) and pure quasar (Yip et al., 2004a) – to decompose the spectrum into host galaxy and quasar contribution. This decomposition is particularly important in low-redshift quasars ( $z < 0.8$ ), where the stellar contribution can be significant (e.g. Yue et al. 2018; Shen et al. 2019; Rakshit et al. 2020). Briefly, the continuum of the host free spectrum is modelled by a combination of power-law, Fe II and Balmer continuum models, whereas the emission lines are fitted with Gaussian distributions. The bolometric luminosity is computed from  $L_{5100}$  ( $z < 0.7$ ),  $L_{3000}$  ( $0.7 \leq z \leq 1.9$ ) and  $L_{1350}$  ( $z \geq 1.9$ ) using the bolometric corrections from Richards et al. (2006). For the virial black hole mass multiple measurements are included in the catalogue depending on the availability of strong emission lines and various calibrations. In this work, we choose to use the “fiducial” estimate calculated based on the  $H\beta$  line ( $z < 0.8$ ) and the C IV line ( $z \geq 1.9$ ) using the calibrations from Vestergaard and Peterson (2006), and the Mg II line ( $0.8 \leq z < 1.9$ ) using the calibration from Vestergaard and Osmer (2009). These measurements are also used to calculate the Eddington luminosity and thus the Eddington ratio, which is used as a proxy for the accretion rate.

### 2.2.2 LOFAR Two-metre Sky Survey

The radio data used in this work are taken from the second data release of the LOFAR Two-metre Sky Survey (LoTSS DR2; Shimwell et al. 2022). This data release covers 5700 deg<sup>2</sup> of the northern sky (see footprint in Figure 2.1) at a resolution of 6'' and a median rms sensitivity of 83  $\mu\text{Jy beam}^{-1}$ , providing over 4 million radio sources, the vast majority of which have never been detected at radio wavelengths before. In addition to the large area and high sensitivity, LoTSS benefits from using the low radio central frequency of 144 MHz which amongst other advantages reduces the effects from Doppler boosting in jetted sources.

In preparation for the upcoming WEAVE-LOFAR survey, Hardcastle et al. (2023) have created a preliminary cross-matched catalogue containing 296,921 SDSS counterparts by using a combination of statistical methods and visual classification in a similar manner to Kondapally et al.

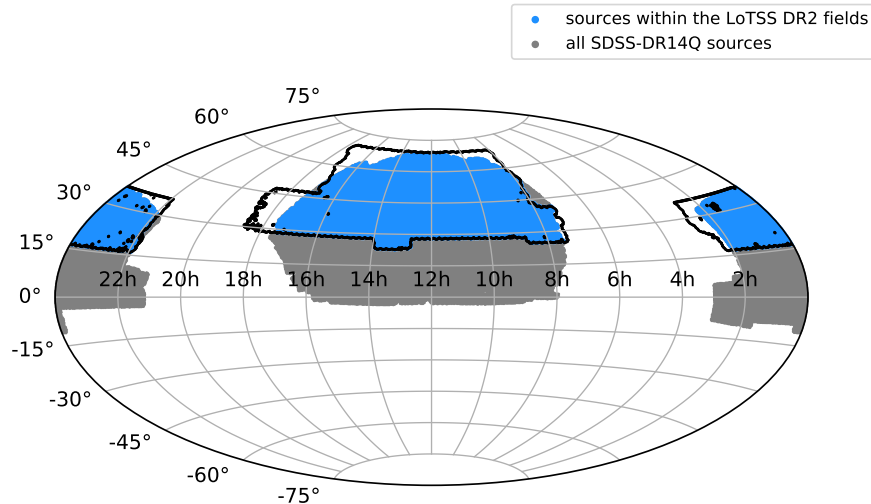


Figure 2.1: Sky coverage of SDSS-DR14Q and LoTSS DR2. The grey region indicates all the sources from the SDSS-DR14Q catalogue, whereas the light blue region - those located in the LoTSS DR2 footprint, where cross-matching has been performed.

(2021). To summarise, for smaller, more compact radio sources, the likelihood ratio method is applied (e.g. Richter 1975; De Ruiter et al. 1977; Sutherland and Saunders 1992). This statistical approach uses both colour and magnitude information as described by Williams et al. (2019) in order to maximise the number of identifications, as well as increase the robustness of the cross-matching. For larger sources with extended radio emission, the web-based interface for visual inspection - the Radio Galaxy Zoo: LOFAR, is needed. Here, the user can perform identification and association for a given radio source by making use of available multi-wavelength images. Finally, for everything in between a decision tree is used to combine the two methods.

### 2.2.3 Sample Selection

Starting with a sample of 446,781 BOSS quasars from the DR14Q catalogue, we identify those located in the LoTSS DR2 area with the use of a Multi-Order Coverage (MOC) map as seen in Figure 2.1. This results in 265,578 objects, out of which 33,968 are part of the LoTSS DR2 optical cross-matched catalogue. Next, we remove spectra with bad plate quality and a non-zero quality flag for  $M_{\text{BH}}$  and  $L_{\text{bol}}$  to ensure reliability of results. Finally, to mitigate selection bias, we use the SDSS selection flags to discard objects targeted for spectroscopy due to their radio/X-ray emission or time variability (we note that this does not necessarily remove time-variable sources, but rather that we do not include QSOs *selected* on the basis of their time variability). The final sample consists of 189,680 quasars, out of which 123,742 are part of the BOSS/eBOSS homogeneously-selected CORE sample. The CORE sample is created by using a

single target selection algorithm, the Extreme Deconvolution (XDQSO; Bovy et al. 2011), which is designed to meet science goals (such as clustering and LF measurements) which require a uniform selection, and so is ideal for our purposes.

To separate quasars into radio-loud and radio-quiet, we adopt the standard definition of the radio-loudness parameter ( $R$ ): the logarithm of the ratio of 1.4 GHz radio luminosity ( $L_{1.4\text{GHz}}$ ) to optical  $i$ -band luminosity ( $L_i$ ), where  $R = 1$  marks the boundary (e.g. Baloković et al. 2012). To calculate the  $k$ -corrected  $L_{1.4\text{GHz}}$  for radio-detected QSOs, we use the integrated 144 MHz flux density ( $S_{144\text{MHz}}$ ) from the LoTSS DR2 catalogue, a radio spectral index of  $\alpha_{\text{rad}} = -0.7$  and the sources' spectroscopic redshifts reported in the DR14Q catalogue. The same calculation is applied to the radio-undetected QSOs in order to obtain a  $5\sigma$  upper limit for  $L_{1.4\text{GHz}}$ , where  $S_{144\text{MHz}}$  is taken to be  $5\times$  the local rms value taken directly from the LoTSS rms maps at the coordinates of the quasars given by SDSS DR14Q.

For the optical luminosity, we take the absolute  $i$ -band magnitude from the DR14Q catalogue which is  $k$ -corrected to  $z = 2$  and use the following conversion given by Richards et al. (2006) to obtain a  $k$ -corrected estimate to  $z = 0$ :

$$M_i[z = 0] = M_i[z = 2] + 2.5(1 + \alpha_{\nu, \text{opt}}) \log(1 + z). \quad (2.1)$$

Here  $z = 2$  and we adopt an optical spectral index of  $\alpha_{\nu, \text{opt}} = -0.5$ . To obtain the  $i$ -band luminosity, we use the simple relationship between luminosity and magnitude, where the solar luminosity ( $3.827 \times 10^{26}$  W) and solar  $i$ -band absolute magnitude (4.58) were used. This gives us a total of 3,697 RL and 111,132 RQ quasars. The remaining sources are discarded as their  $5\sigma$  upper limit puts them in the radio-loud regime, such that we are unable to classify them with confidence.

The radio-loudness distribution of all sources, including a subset of radio detections, is presented in Figure 2.2 (where we have also included a second horizontal axis to show  $R$  in terms of the  $L_{144\text{MHz}}$  for comparison). It is evident that in both cases the conventional demarcation line ( $R = 1$ ) does not represent any particularly significant level for the sample, however we have repeated the analysis considering different values (as denoted in Figure 2.2) finding that our results are qualitatively unchanged. Doing these tests gives additional advantages of further testing whether there is a gradual change between the two populations as found in previous studies (e.g. Gürkan et al. 2019; Macfarlane et al. 2021), as well as avoiding biases that may result from assuming a single radio spectral index.

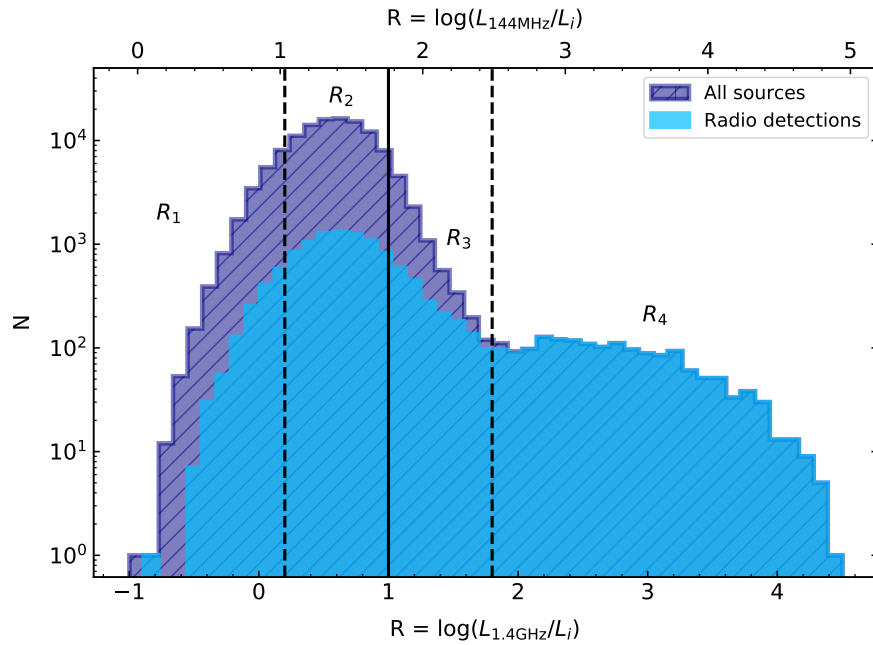


Figure 2.2: The radio-loudness parameter for all sources (dark blue) and only radio-detections (light blue). The solid black line denotes the standard division line for radio-loud and radio-quiet QSOs, whereas the dashed black lines are additional divisions we make to define classes as a function of  $R$  as denoted.

## 2.2.4 The Matching Process

To make a robust comparison between quasar populations, we develop a method to create samples matched in 2D and 3D parameter space. For clarity, in what follows we describe the method for the RL and RQ population, where we create samples matched in  $z$ ,  $M_i$  and  $z$ ,  $M_i$ ,  $M_{\text{BH}}$  to use in sections 2.4.1 and 2.4.2. However, it is important to note that this method can be adapted to various other scenarios, as demonstrated throughout this study.

The 2D matching process involves generating a 2D histogram of the RL QSOs, and identifying the number of RQ that fall within the same  $z$  and  $M_i$  bin. For the one-to-one case, this entails choosing the same number of RQ counts as found for the RL 2D-histogram, such that if one bin is populated by 100 RL sources then we randomly select only 100 RQ counterparts. However, as our RQ sample is considerably larger, we instead choose to normalise the RL 2D-histogram by the total number of RL sources, and multiply the normalised counts by the maximum number of RQ QSOs for which we can say that they are drawn from the same  $z$  and  $M_i$  distribution as the RL population. This is done by employing multiple Kolmogorov–Smirnov (K-S) tests until we accept the null hypothesis that the two samples are drawn from the same distribution if the

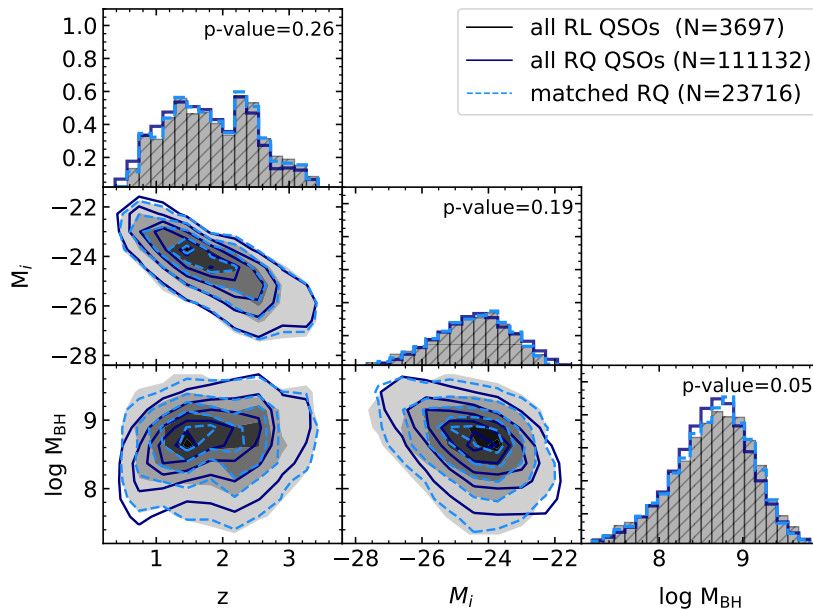


Figure 2.3: A corner plot summary of the redshift, absolute  $i$ -band magnitude and black hole mass distributions for the RL and RQ QSOs. The density contours represent the 10, 30, 50, 70 and 90 per cent of the whole (dark blue) and 3D-matched (dashed, light blue) RQ sample, whereas the density map represents the corresponding percentages for the RL sample. The histograms share a common y-axis and indicate the individual  $z$ ,  $M_i$  and  $M_{\text{BH}}$  distribution, where the quoted  $p$ -values in the upper-right corner are obtained by performing a K-S test on the RL and 3D-matched RQ sample.

$p$ -value is greater than a significance level of  $\alpha = 0.05$ . This results in a sample of 77,532 RQ QSOs matched in  $z$  and  $M_i$  to our RL sample (hereafter the 2D-matched or  $z - M_i$  sample).

Similarly, the 3D matching process to create a sample matched in  $z$ ,  $M_i$  and  $M_{\text{BH}}$  (hereafter the 3D-matched or  $z - M_i - M_{\text{BH}}$  sample) involves creating a normalised 3D-histogram of the RL population, and again using multiple K-S tests to determine the maximum number of RQ sources. The effectiveness of this matching procedure can be seen in Figure 2.3, where we compare the individual  $z$ ,  $M_i$  and  $M_{\text{BH}}$  distributions, along with contours of the 2D-distributions of our 3D-matched sample of 23,716 RQ QSOs with the whole RL and RQ samples.

## 2.3 The Spectral Stacking Method

### 2.3.1 The Stacking Technique

To create high S/N composite spectra of quasars we use the following method. First, we correct for Galactic extinction in the observed-frame by using the re-calibrated reddening data,  $E(B - V)$ ,

from Schlegel, Finkbeiner, and Davis (1998), along with the Milky Way reddening curve from Fitzpatrick (1999) for an extinction-to-reddening ratio of  $R_V = 3.1$ .

Next, we shift the spectra to the rest-frame by using the spectroscopic redshifts from the SDSS-DR14Q catalogue, and resample onto a common wavelength grid, predetermined by the minimum and maximum value of the rest-frame wavelengths sampled, along with the choice of sampling input in the algorithm (e.g.  $1 \text{ \AA}/\text{pixel}$ ). The resampling is performed using the `SPECTRES:Simple Spectral Resampling tool` (Carnall, 2017), where the old wavelength grid is cross-matched with the new one, such that if an old wavelength bin spreads between multiple new ones, the flux density value associated with it is distributed in the new grid based on the fractional coverage. This ensures that the flux density is conserved. To normalise the resampled spectra, we divide through each spectrum by its median, computed at the reddest possible end of the area where all spectra populate the common wavelength grid, where prominent emission lines are masked out. Doing this ensures that the overall spectral shape is preserved, in the sense that we are able to recover stellar population synthesis models once the uncertainties have been estimated and corrected for bias (see next section for details). In addition, by using the reddest possible common wavelength range, we minimize the effects of extinction.

Stacking the de-redshifted, resampled and normalised spectra is generally done in the literature either by taking the weighted average, where the weights are given by the inverse variance of the spectra, or by taking the median (e.g. Rowlands et al. 2012; Zhu et al. 2015; Rigby et al. 2018; Calabrò et al. 2021). The weighted average method is found to produce a higher S/N composite spectrum, however, as explained in Calabrò et al. (2021), this is the result of a bias towards lower redshifts and/or individual spectra with higher S/N. On that account, we have chosen to build a composite spectrum by taking the median of all normalised flux density values that fall within a given wavelength bin. To calculate the uncertainty associated with this stack, we use bootstrapping to randomly resample the spectra at each wavelength bin, creating 1000 realisations with the same size as the original sample. The median method is then performed for each realisation to estimate the flux density distribution at a given bin and thus determine the standard deviation.

Figure 2.4 presents the result of implementing this method on a sample of RQ quasars, where the individual spectra are shown in grey, and the high resolution stack in black. This shows how powerful spectral stacking really is in identifying spectral features otherwise undetected in individual spectra.

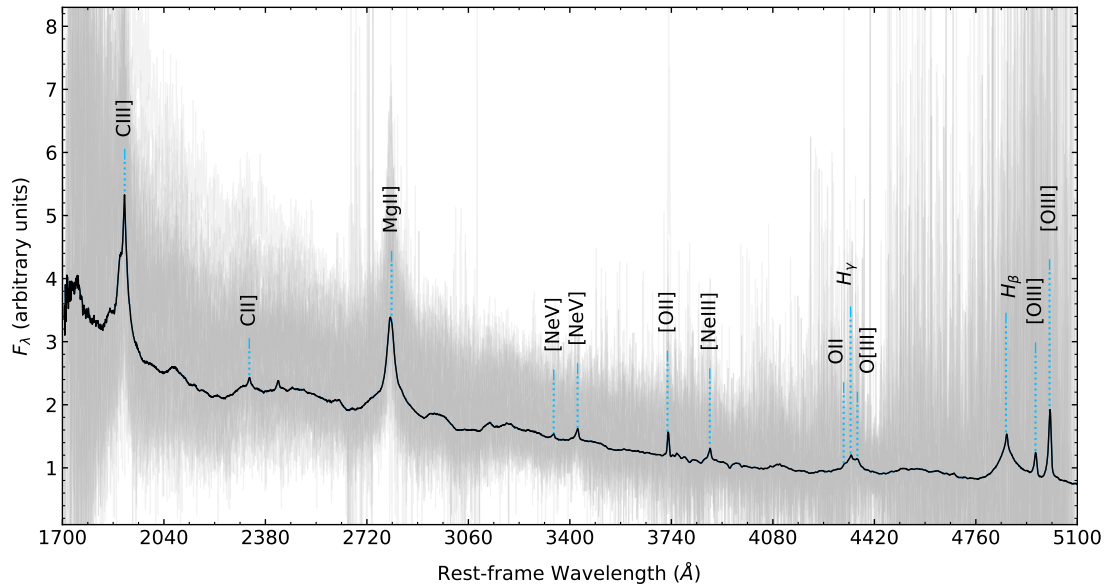


Figure 2.4: An example composite spectrum of RQ QSOs. The average spectrum is indicated by the thick black line, while the grey region indicates the individual normalised, resampled spectra that went in to the stack. The labelled dotted blue lines indicate prominent emission lines visible in the stacked spectrum.

### 2.3.2 The Stacking Corrections

To evaluate the performance of the stacking procedure described in the previous section, we create a model galaxy spectrum by making use of the stellar population synthesis code from Bruzual and Charlot (2003), along with equivalent width measurements of nebular emission lines taken from the value added catalogue produced by the Max-Planck-Institute for Astrophysics-John Hopkins University (MPA-JHU; Brinchmann et al. 2004; Kauffmann et al. 2003 and Tremonti et al. 2004). This galaxy template has a broad wavelength range extending from  $90 \text{ \AA}$  to  $160 \mu\text{m}$ , a resolving power similar to that of SDSS across the range from  $3200$  to  $9500 \text{ \AA}$  and contains the main nebular emission lines targeted by both WEAVE-LOFAR and SDSS. These features enable us to simulate mock samples of galaxy spectra based on SDSS characteristics across a wide range of redshifts, providing us with a robust way of testing the spectral stacking algorithm and further demonstrating its flexibility in handling different type of spectra (see Appendix A for an example of stacking spectra as a function of BPT classes).

Following a range of tests including continuum recovery at low brightness and performance related to different sampling of spectra (the main motivations for implementing it for the WEAVE-LOFAR survey), we have identified two implications of the stacking method. First of all, it is not always possible for the algorithm to choose a normalisation range without strong spectral features, which causes an offset at the blue end of the composite spectrum. Secondly, the spectra

are combined in the rest-frame, where the normalised spectra no longer have the same spectral resolution as a result of the de-redshifting process. This is not accounted for in the bootstrap method, leaving the uncertainties underestimated. To correct for these effects, we include in our stacking algorithm the following procedure.

For a given spectroscopic sample, we create a composite spectrum (hereafter the input composite spectrum) and use it as a template to simulate quasar spectra based on the characteristics of the original sample such as redshift, *i*-band magnitude and inverse variance. Next, we stack the simulated spectra to produce a second spectrum (hereafter the simulated composite spectrum) and obtain the residual in uncertainty units, which is defined as:

$$\chi_{\text{input-sim}} = \frac{F_{\lambda,\text{input}} - F_{\lambda,\text{sim}}}{\sigma_{\lambda,\text{sim}}}, \quad (2.2)$$

where  $F_{\lambda,\text{input}}$  and  $F_{\lambda,\text{sim}}$  are the flux density of the input and simulated composite, respectively and  $\sigma_{\lambda,\text{sim}}$  is the bootstrap uncertainty for the simulated composite. Provided that the issues discussed above are not present, this quantity would be normally distributed with a mean of zero and a standard deviation of one, making it the source of our corrections. To obtain the necessary correction factors, we separate  $\chi_{\text{input-sim}}$  into 30 wavelength slices (or less, depending on pixel availability) and for each one we fit a normal distribution. The best-fit parameters are then interpolated with a spline to produce wavelength dependent corrections as indicated in Figure 2.5. The best-fit of the mean is used to correct for the offset as a result of the normalisation by subtracting a multiple of it and the uncertainty of the simulated composite from the flux density of the input composite. The best-fit of the standard deviation, on the other hand, is used as a multiplication factor for the uncertainty of the input composite spectrum, such that resolution effects are now taken into account.

We note that this procedure does not account for different levels of extinction or diversity of samples. However, spectra of QSOs are reasonably homogeneous and the use of large statistical samples binned in a given parameter space is close to homogeneity.

### 2.3.3 Qualitative Template Comparison

To compare our spectral stacking techniques with the literature, we create RL and RQ composites spanning the broadest possible wavelength coverage. Generating such templates involves using sources at widely different redshifts ( $0.5 < z < 3.5$ ), which affects our method in two ways. First

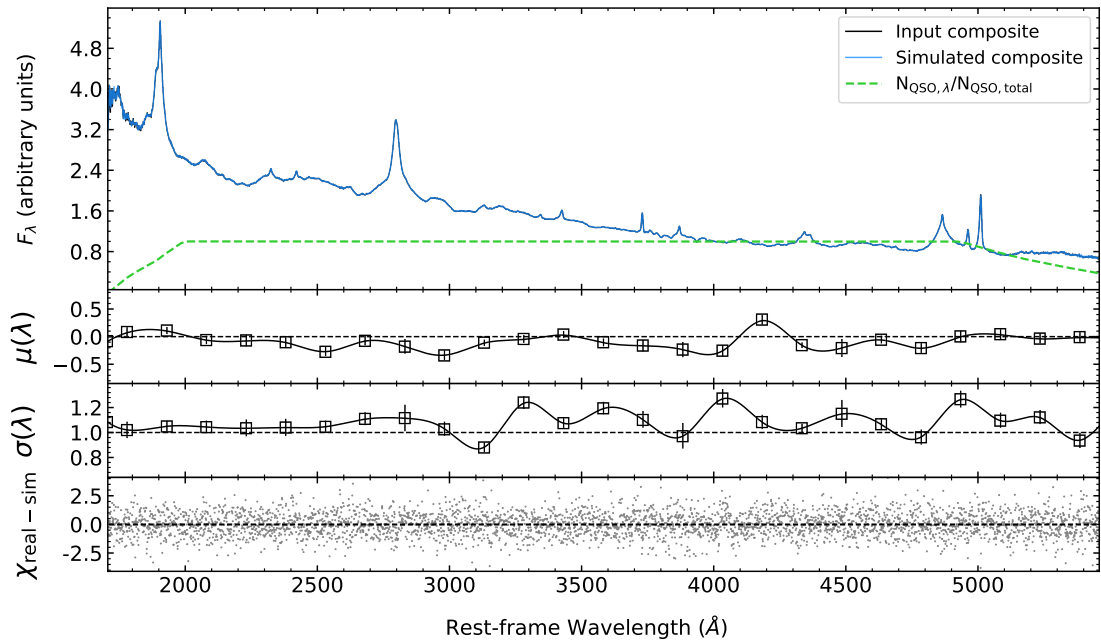


Figure 2.5: A diagnostic plot of an example composite spectrum of RQ QSOs. The upper panel shows the input (dark blue) and simulated (light blue) composite spectra, along with the number of QSOs that went into them at each rest-frame wavelength divided by the total number of QSOs (dashed green line). The second and third panel present the best-fitting parameters for the mean and standard deviation for each wavelength slice, while the lower panel presents the corrected residual in units of the propagated uncertainty.

of all, it has implications for the choice of sources which must be drawn from a similar  $z - M_i$  space in order to reduce the impact of the Malmquist bias. Secondly, the stacking procedure needs to be performed on smaller redshift ranges as a result of the normalisation process, which requires a common wavelength range free from strong spectral features. To account for this, we select all sources with  $-26 < M_i < -24$  and divide them in redshift bins of size  $\Delta z = 0.5$  to create six composite spectra per quasar population using the stacking algorithm and the spectral corrections described in sections 2.3.1 and 2.3.2. These stacks are then re-scaled to the composite at the lowest redshift bin and combined into a single template using the inverse-variance weighted average.

The resulting RL and RQ composites can be seen in Figure 2.6 where they are compared to the SDSS composite from Vanden Berk et al. (2001), the X-Shooter composite from Selsing et al. (2016), the BOSS composite from Harris et al. (2016) and to a new high- $z$  template that we have constructed by applying our algorithm to the sample of 24 radio-bright quasars (21 out of which are classified as radio-loud) at  $4.9 < z < 6.6$ , discovered by Gludemans et al. (2022). Building such a template presents new challenges, since unlike the homogeneous eBOSS spectra used for the RL/RQ templates, the high- $z$  stack requires combining heteroscedastic data obtained from

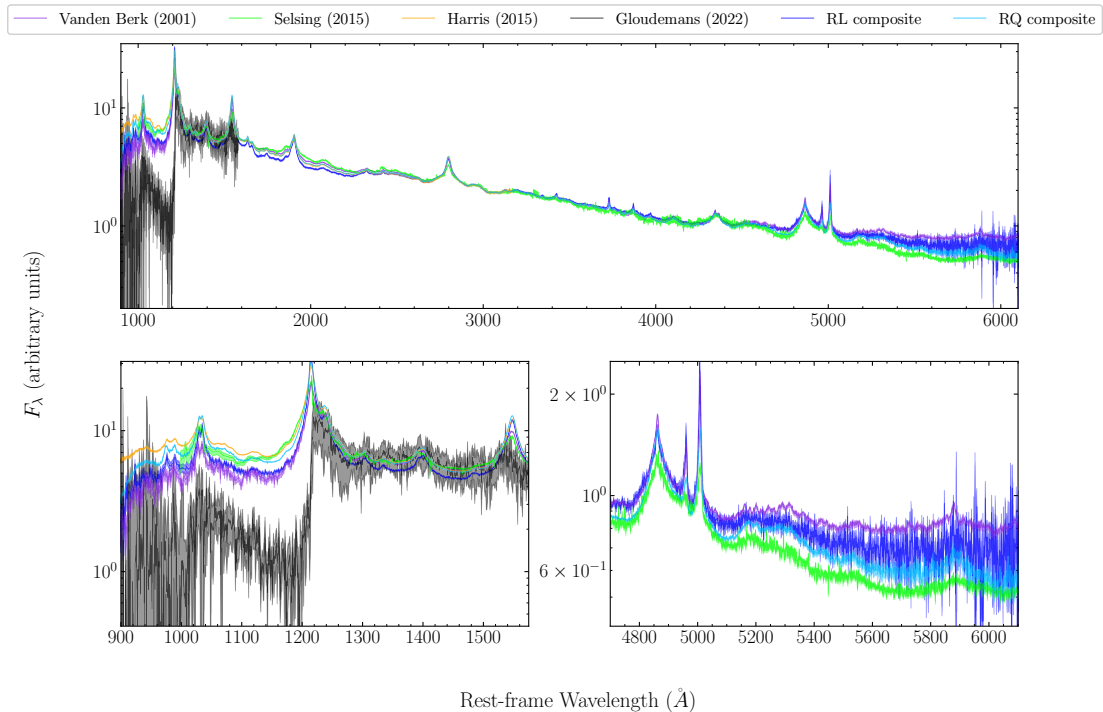


Figure 2.6: A comparison between various composite spectra as indicated by the legend, where the thick lines indicate the flux density, whereas the shaded area corresponds to  $\pm$  the uncertainty. The upper panel presents the full wavelength coverage, where each composite is normalised to the RQ composite at  $3000 - 3600 \text{ \AA}$ . The lower left panel presents a zoom-in window indicating the differences bluewards of  $\text{Ly}\alpha$ , whereas the lower right panel - the discrepancy above  $5000 \text{ \AA}$  which is likely caused by host galaxy contamination.

a range of facilities, including the Faint Object Camera and Spectrograph (FOCAS; Kashikawa et al. 2002) on the Subaru Telescope, the LRS2 instrument (Chonis et al., 2016) on the Hobby-Eberly Telescope and the Low Resolution Imaging Spectrometer (LRIS; Oke et al. 1995) on the Keck telescope. Specifically, and as discussed in section 2.3.2, the simulation component of our stacking algorithm requires photometry with a bandpass that overlaps with the observed spectrum, and given that this was unavailable for the Gloude-mans et al. (2022) sample, we were unable to conduct the simulations and it is therefore likely that the flux density has a normalisation bias with uncertainties systematically underestimated. However, creating and using such a template is beneficial as this is the largest sample of radio-loud quasars at  $z > 4.9$  and its use demonstrates the flexibility of our stacking algorithm in dealing with non-SDSS spectra.

Despite the difference in selection, we find qualitatively a good agreement in the continuum shape with the various templates. The difference observed redwards of  $5000 \text{ \AA}$  amongst the composites is likely caused by various degrees of host galaxy contamination. The SDSS composite from Vanden Berk et al. (2001) includes intrinsically faint sources at low redshifts, making it subject

to significant host contamination (e.g. Glikman et al. 2006; Fynbo et al. 2012). The selection by Selsing et al. (2016), on the other hand, is chosen specifically to circumvent this problem, suggesting that both the RL and RQ composite contain low levels of host galaxy contamination. This will be further investigated in section 2.5.2. The disagreement bluewards of  $\text{Ly}\alpha$ , on the other hand, can be explained by the different IGM absorption corrections applied (or the lack thereof). We have not made any corrections, and so the intense drop in flux density for the high- $z$  template is expected considering the redshift range of the sample. The RL composite appears to agree well with the results of Vanden Berk et al. (2001) as seen in the lower left panel of Figure 2.6, where no IGM correction is applied as well. Interestingly, the RQ composite appears to be less affected by the  $\text{Ly}\alpha$ -forest absorption as it is found to be in better agreement with the X-shooter and BOSS composite where each spectrum within the composites has been individually corrected.

## 2.4 Composite Spectra of Quasars

In this section, we employ our spectral stacking techniques to compare quasars as a function of radio-loudness at different redshift bins. In sections 2.4.1 and 2.4.2, we construct high signal-to-noise (S/N) composite spectra for the classically defined RL and RQ QSOs using the  $z - M_i$  and  $z - M_i - M_{\text{BH}}$  samples to establish whether there are any physical differences between them and investigate the potential influence of the black hole mass. In section 2.4.3, we re-bin our sample into four radio-loudness bins to investigate the presence of a bimodality among the QSOs or a more gradual transition between these populations.

### 2.4.1 High S/N Comparison of RL and RQ QSOs

Starting with our  $z - M_i$  sample, we use the spectral stacking algorithm described in section 2.3.1 and 2.3.2 to define high S/N composite spectra across ten redshift bins for each population. The redshift bins are chosen such that they are consistent with the different redshift ranges used to calculate the “fiducial”  $M_{\text{BH}}$  from Rakshit et al. (2020) and contain comparable numbers of RL sources.

The resulting comparisons for all ten redshift bins are presented in Figure 2.7. For each bin we present an upper panel including the composite spectra representative of the RL (dark blue) and RQ population (light blue) and a lower panel indicating the residual in units of the propagated

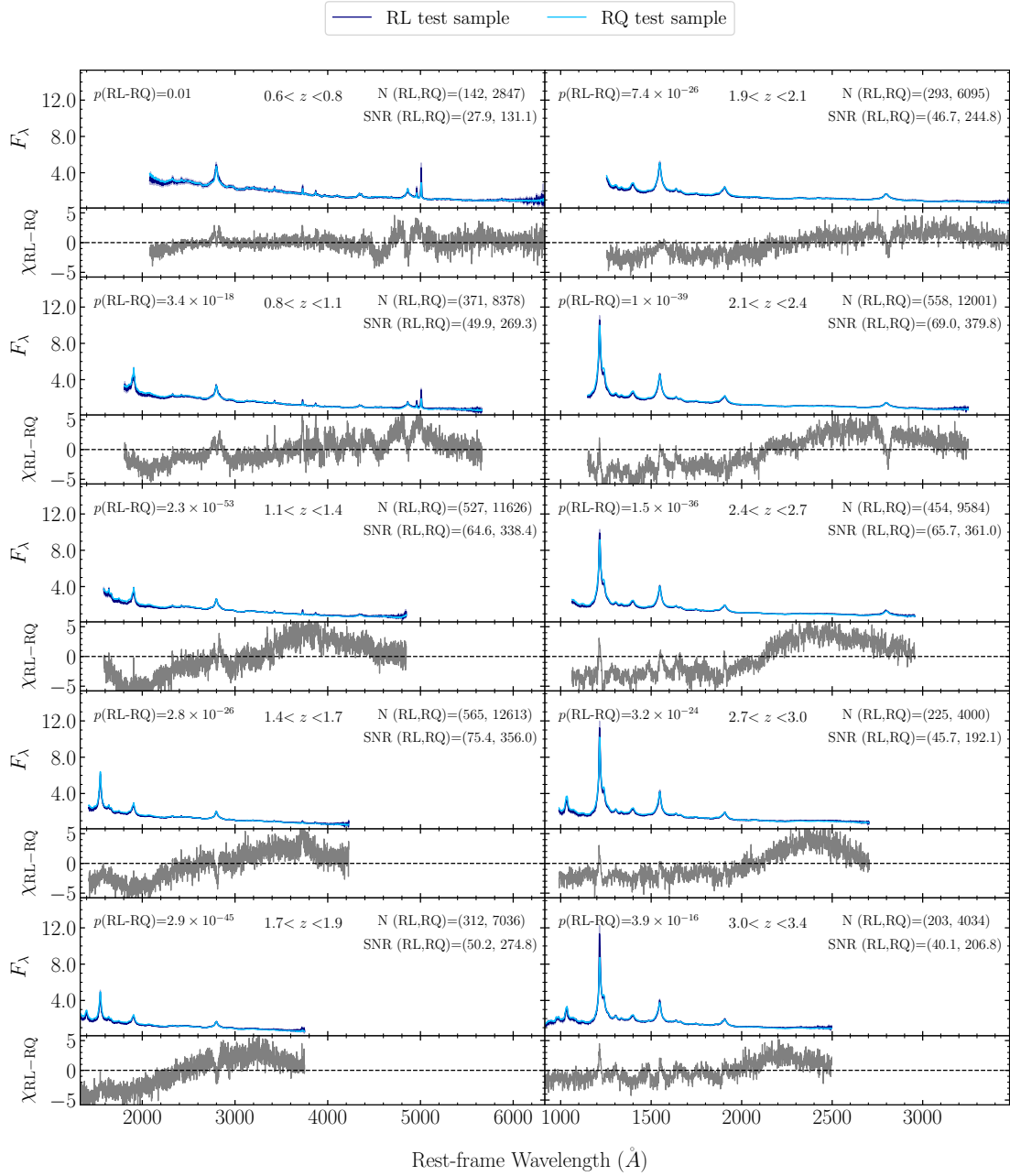


Figure 2.7: A comparison between the RL and RQ population across ten redshift bins. The upper panel of each bin presents the composite spectra of RL QSOs (dark blue) and RQ QSOs (light blue), whereas the lower panel indicates the residual in units of propagated uncertainty (grey). In each panel, the redshift range is indicated in the upper centre of the plot, while the  $p$ -values of the null hypothesis test are presented in the legend in the upper left corner. Finally, the number of sources and median S/N is indicated in the legend in the top right corner.

uncertainties (grey). We can see that there is a consistent picture emerging across all redshift bins considered - the RL QSOs appear to have on average a redder continuum with notable differences in a number of prominent emission lines.

To quantify the significance of the observed results, we perform the same stacking methods using only the RQ population in order to create Monte Carlo simulations under the null hypothesis that the RL sample is consistent with having been randomly drawn from the RQ sample. For each simulation we take the full sample of RQ sources and randomly draw a sub-sample of size equal to the RL population (hereafter referred to as the RL test sample). The remaining RQ sources are then matched in  $z$  and  $M_i$  as described in section 2.2.4 to create a RQ test sample. Finally, the stacking algorithm is applied on the two test samples to create composite spectra across the same ten redshift bins for which we find a “reduced chi-squared value” of

$$\chi_v^2 = \frac{\sum_{i=1}^N \frac{(F_{RL,i} - F_{RQ,i})^2}{(\sigma_{RL,i}^2 + \sigma_{RQ,i}^2)}}{N}, \quad (2.3)$$

where  $N$  is the number of pixels in each stacked spectrum. Having done this 1000 times, we obtain a  $\chi_v^2$  distribution under the null hypothesis for each redshift range. By fitting this distribution with its parametric form, we can estimate the probability of obtaining our observed results under the null hypothesis.

The results of the null hypothesis test for this 2D matched sample are presented in the upper left corner of each panel in Figure 2.7 and in Table 2.1. For all redshift bins, we find  $p$ -values smaller than a significance level of  $\alpha = 0.05$ , indicating that the two samples are not drawn from the same parent population.

## 2.4.2 Black Hole Mass Dependence

As discussed in the introduction, several studies have found the black hole mass to be a defining factor in the radio-loudness dichotomy, where RL QSOs are found to harbour black holes with  $M_{\text{BH}} \gtrsim 10^8$  (e.g. Dunlop et al. 2003, McLure and Jarvis 2004; Chiaberge and Marconi 2011). This, however, does not appear to be the case for our sample. In Figure 2.8 we present the black hole mass distributions for each radio class using the virial black hole mass estimates from Rakshit et al. (2020). We can see that both the RL (dark blue) and RQ QSOs (light blue) are found to span similar  $M_{\text{BH}}$  ranges, irrespective of the different black hole mass calibrations. In addition, the mean black hole masses do not show any systematic trend - the RL appear more

Table 2.1: The  $p$ -values obtained from the null hypothesis test. The columns represent the results obtained from comparing: the RL and RQ populations with the 2D and 3D matched samples, the more radio-loud bins ( $R_2$ ,  $R_3$  and  $R_4$ ) and the radio-quietest sample ( $R_1$ ), and the radio-detected ( $R_{1D}$ ) and the radio-undetected ( $R_{1U}$ ) sample for the radio-quietest bin defined in section 2.4.3 per a given redshift bin.

Redshift Range	(RL - RQ) <sub>2D</sub>	(RL - RQ) <sub>3D</sub>	$R_1 - R_2$	$R_1 - R_3$	$R_1 - R_4$	$R_{1U} - R_{1D}$
0.6–0.8	0.01	0.03				
0.8–1.1	$3.39 \times 10^{-18}$	$1.48 \times 10^{-14}$	$5.51 \times 10^{-41}$	$7.90 \times 10^{-15}$	$2.26 \times 10^{-6}$	0.01
1.1–1.4	$2.31 \times 10^{-53}$	$3.014 \times 10^{-51}$				
1.4–1.7	$2.83 \times 10^{-26}$	$1.88 \times 10^{-25}$	$4.73 \times 10^{-45}$	$1.43 \times 10^{-18}$	$2.16 \times 10^{-18}$	0.31
1.7–1.9	$2.88 \times 10^{-45}$	$3.40 \times 10^{-28}$				
1.9–2.1	$7.43 \times 10^{-26}$	$1.67 \times 10^{-13}$	$2.38 \times 10^{-38}$	$1.92 \times 10^{-23}$	$1.37 \times 10^{-17}$	0.05
2.1–2.4	$1.03 \times 10^{-39}$	$5.15 \times 10^{-24}$				
2.4–2.7	$1.45 \times 10^{-36}$	$2.02 \times 10^{-24}$	$6.61 \times 10^{-30}$	$4.59 \times 10^{-29}$	$1.25 \times 10^{-11}$	0.08
2.7–3.0	$3.21 \times 10^{-24}$	$6.22 \times 10^{-23}$	0.001	$3.28 \times 10^{-9}$	$5.95 \times 10^{-5}$	0.86
2.7–3.4	$3.90 \times 10^{-16}$	$1.38 \times 10^{-10}$				

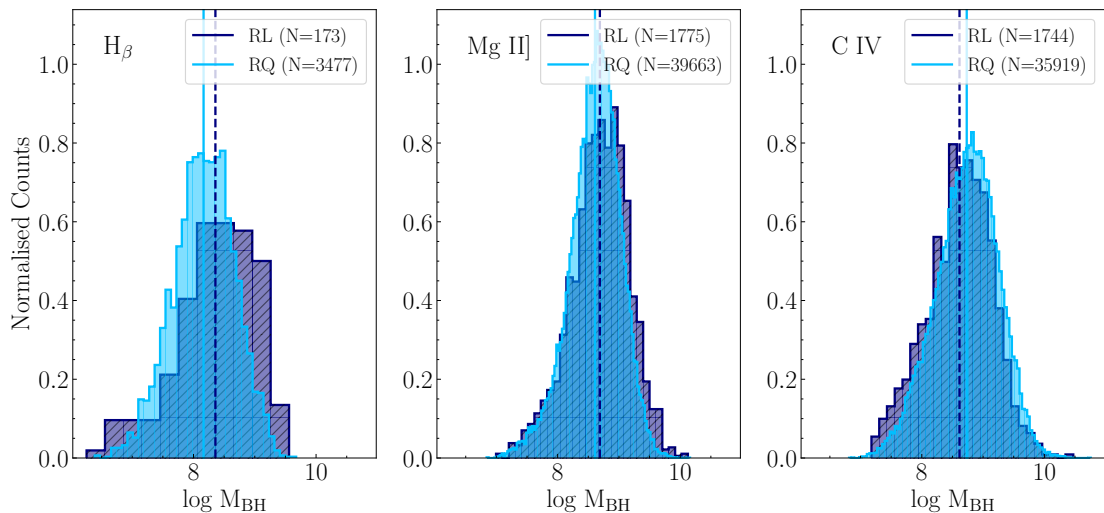


Figure 2.8: The black hole mass estimates provided from Rakshit et al. (2020) for the radio-loud (dark blue) and radio-quiet population matched in redshift and  $i$ -band magnitude (light blue). Each panel corresponds to the three different methods of calculation, which depend on the availability of a given emission line: the  $H\beta$  line ( $z < 0.8$ ), the Mg II line ( $0.8 \leq z < 1.9$ ) and the C IV line ( $z \geq 1.9$ ). The sample means for the RL and RQ QSOs are presented in each panel as dashed dark blue and solid blue lines, respectively.

massive for the  $H\beta$  and Mg II, but less so for the C IV calibration (cf. McLure and Jarvis 2004). However, to determine whether this parameter plays a role in causing the differences observed in Figure 2.7, we re-do the stacking procedure with the  $z - M_i - M_{BH}$  sample, i.e. including the  $M_{BH}$  in the process, even though it reduces the sample size. We note that by matching in  $M_i$  and  $M_{BH}$  that we are also effectively controlling for the Eddington ratio.

The resulting RL/RQ comparison is found to exhibit similar features as for the  $z - M_i$  sample, where both the continuum and the emission lines are found to differ between the two populations

(see Appendix A for the RL/RQ comparison with the  $z - M_i - M_{\text{BH}}$  sample). We use the null hypothesis test as described in the previous section to determine the significance of this result. Similarly to the  $z - M_i$  sample, we are able to rule out the null hypothesis with  $p < 0.05$  for all redshift bins (see results for the 3D matched sample in Table 2.1). Therefore, we conclude that additional information beyond the black-hole mass and accretion rate is required to explain the difference between the RL and RQ population. As matching in  $M_{\text{BH}}$  is on average of little consequence (except for sample size), we proceed with the rest of our analysis using only the  $z - M_i$  sample, since it is about three times larger.

### 2.4.3 Comparison as a Function of Radio-loudness

To investigate whether the differences observed between the RL and RQ population represent a bimodality or a transition between populations, we further separate our sample into four radio-loudness bins as indicated in Figure 2.2. As with our previous approach, we include radio-undetected sources only in the lowest radio-loudness bin ( $R_1$ ) as we cannot confidently assign the rest of the sources to the correct  $R$  bin (i.e when the upper limits fall to the right of the demarcation lines in Figure 2.2). This leads to some challenges when matching in  $z$  and  $M_i$  as demonstrated by Figure 2.9, which presents the redshift-luminosity plane. We can see that the more radio-loud bins ( $R_2$ ,  $R_3$  and  $R_4$ ) in comparison to  $R_1$  span a different parameter space. This means that we need to match to the lowest radio-loudness bin sample, unlike before where the matching was performed to the RL population in order to maximise the radio-loudest sample. As this resulted in a lower number of sources for each radio-loudness bin, we decided to reduce the number of redshift bins by doubling the bin width to maintain comparable signal-to-noise levels of the stacked spectra as before.

The results of applying our spectral stacking algorithm and the null hypothesis test on this sample division for five redshift bins show that all radio-loud bins exhibit statistically significant differences when compared to  $R_1$  (see results for  $R_1$ - $R_2$ / $R_3$ / $R_4$  in Table 2.1 and Appendix A), providing no indication of a smooth transition between populations relative to the null hypothesis test. To address the possibility of a bias arising from our selection process, where only radio-detected sources were included in the more radio-loud bins, we further conducted a comparison between radio-detected ( $R_{1\text{D}}$ ) and radio-undetected sources ( $R_{1\text{U}}$ ) within the lowest radio-loudness bin ( $R_1$ ). We find that we can accept the null hypothesis that the two samples are drawn from the same parent distribution ( $p \geq 0.05$ ) for all, apart from the lowest redshift bin,

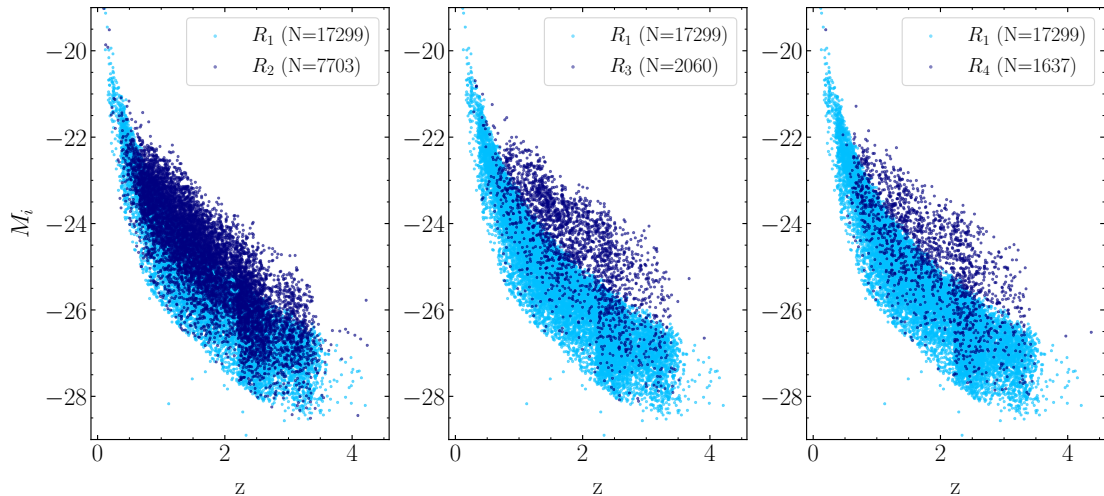


Figure 2.9: The  $z - M_i$  plane for the different radio-loudness bins. The lowest radio-loudness bin ( $R_1$ ) is shown in light blue, whereas the bins with increasing  $R$  are presented in dark blue throughout the three panels.

where  $p = 0.01$  indicating ambiguity. This ambiguous result, however, is not enough to explain  $p$ -values as low as  $10^{-41}$  as found for the  $R_1$ - $R_2$  comparison. Therefore, we conclude that the exclusion of non-detections is not significantly impacting our findings.

We must also consider the possible role of the host galaxy (e.g. Magliocchetti et al. 2020). Given our high S/N, we expect to be able to detect starlight up to redshifts normally inaccessible to SDSS; light from the hosts could therefore be contributing to our results. To test this, we examine the excess region of flux density for each pair per given redshift bin. Our findings indicate that the luminosity of this region is of order  $10^9$ - $10^{10} L_\odot$ , suggesting that the host galaxy might indeed play a significant role in generating the observed effects.

Another possible explanation for the absence of a smooth transition between populations in terms of the hypothesis test results is that we are searching for differences only in the average spectrum in each bin. Since Macfarlane et al. (2021) showed that there exists a significant population of jetted QSOs even at the lowest  $R$  values, it is possible that the differences we see are a result of an increasing fraction of jetted AGN which become numerically dominant in all but the lowest  $R$  bin, and which therefore dominate the median stacked spectra. This hypothesis will become testable in the future as we are increasingly able to morphologically discern the presence of jets in forthcoming wide field sub-arcsecond 144 MHz imaging from the LOFAR international stations.

## 2.5 Spectral Properties of RL and RQ quasars

In this section, we employ the `PYQSOFIT` spectral fitting code to obtain spectral properties from the quasar populations. In section 2.5.2, we analyse the average emission line properties of both RL and RQ quasars, as well as those categorized into different radio-loudness bins, while in section 2.5.3, we focus on investigating the nature of the [O II] excess found for the RL regime.

### 2.5.1 The Spectral Fitting Procedure

To investigate the continuum and emission line properties of the composite spectra of radio-loud and radio-quiet quasars we use the `PYQSOFIT` spectral fitting code in a similar manner to previous works (e.g. Shen et al. 2019, Rakshit et al. 2020, Fawcett et al. 2022), where the continuum is fitted globally (i.e. the regions influenced by the presence of emission lines are masked out), whereas the emission line complexes are fitted separately and locally.

The continuum of each composite spectrum is globally modelled by using a combination of power-law, Balmer continuum, Fe II component and third-order polynomial as:

$$f_{\text{conti}} = f_{\text{pl}} + f_{\text{BC}} + f_{\text{Fe II}} + f_{\text{poly}}. \quad (2.4)$$

The power-law continuum component has been added to represent the emission from the accretion disc and is defined as:

$$f_{\text{pl}} = a_0(\lambda/\lambda_0)^{a_1}, \quad (2.5)$$

where  $a_0$  and  $a_1$  are the normalisation and power-law slope, and  $\lambda_0$  is a reference wavelength at 3000 Å.

The Balmer continuum component represents the sum of blended, higher-order Balmer lines that give rise to the well-known small blue bump at  $\lambda \sim 3000\text{Å}$ . In `PYQSOFIT` it is modelled by the function given by Grandi (1982) for the case of optically thick clouds as:

$$f_{\text{BC}} = F_{\text{BE}} B_{\lambda}(T_e)(1 - e^{-\tau_{\lambda}(\lambda/\lambda_{\text{BE}})^3}), \quad (2.6)$$

where  $\lambda_{\text{BE}}$  is the position of the Balmer edge,  $F_{\text{BE}}$  is the flux at the Balmer edge,  $B_{\lambda}(T_e)$  is the Planck function at the electron temperature  $T_e$  and  $\tau_{\lambda}$  is the optical depth. Here,  $F_{\text{BE}}$ ,  $T_e$  and  $\tau_{\lambda}$  are left as free parameters as in Fawcett et al. (2022).

The Fe II component is another essential part of modelling the continuum. At UV and optical wavelengths, AGN spectra contain numerous iron emission lines that blend together to form a pseudo-continuum. If not properly subtracted, this pseudo-continuum could contaminate the continuum and emission line measurements. Here, `PyQSOFit` models it as:

$$f_{\text{FeII}} = c_0 F_{\text{FeII}}(\lambda, c_1, c_2), \quad (2.7)$$

where  $c_0$  is the normalisation constant,  $c_1$  is a constant describing the Gaussian broadening and  $c_2$  represents the wavelength shift applied to the Fe II templates to match the data. For the UV part of the spectrum, we use the modified UV Fe II template by Shen et al. (2019) that combines the Vestergaard and Wilkes (2001) template for rest-frame wavelengths 1000–2200 Å, the Salviander et al. (2007) template for 2200–3090 Å, and the Tsuzuki et al. (2006) template for 3090–3500 Å. The optical Fe II template, on the other hand, is taken from Véron-Cetty et al. (2004), covering the rest-frame wavelengths of 3535–7534 Å.

Finally, the third-order polynomial is used to account for the bending of the continuum, which is likely caused by the intrinsic dust reddening of the population, and is defined as:

$$f_{\text{poly}} = \sum_{i=0}^{i=3} b_i (\lambda - \lambda_0)^i, \quad (2.8)$$

where  $b_i$  are the model free parameters.

After subtracting the best-fit model of the continuum, we fit the emission line spectrum in log-space. The fitting is performed individually for each emission line complex, where all the emission lines contained within a single complex are fit simultaneously. The narrow components (FWHM < 1200 km s<sup>-1</sup>) are modelled by a single Gaussian, where the velocity offset and line width are tied for each line complex. The broad emission line profiles, however, can be quite complex (e.g., double-peaked, with a flat top, or asymmetric) and thus are not well represented by a single Gaussian. In such cases, we use multiple Gaussian components depending on the line complexity. A full list of the line complexes containing the individual emission lines and number of Gaussian components used in the fit is provided in Table 2.2.

From the best-fitting models, we can obtain emission line fluxes for each line in question. The uncertainties of these measurements are calculated using the Monte Carlo approach embedded within `PyQSOFit`, where we choose to use 100 iterations.

Table 2.2: The emission line fitting information. The columns are as follows: the name of the line complexes, the wavelength range used for the fit, the emission lines present in each line complex and the number of Gaussian components used for each line.

Emission Line Complex Name	Wavelength Range (Å)	Emission Line Name	Number of Gaussian components
H $\beta$	4640-5100	H $\beta$ broad	2
		H $\beta$ narrow	1
		[O III] (4959 Å)	1
		[O III] (5007 Å)	1
H $\gamma$	4200-4440	H $\gamma$ broad	1
		H $\gamma$ narrow	1
		O III (4363 Å)	1
[O II]	3650-3800	[O II] (3728 Å)	1
[Ne v]	3380-3480	[Ne v] (3426 Å)	1
Mg II]	2700-2900	Mg II] broad	2
		Mg II] narrow	1
C III]	1810-1970	C III] broad	2
		C III] narrow	1
C IV	1500-1700	C IV broad	2
		C IV narrow	1
		He II (1640 Å) broad	1
		He II (1640 Å) narrow	1
		O III] (1663 Å) broad	1
		O III] (1663 Å) narrow	1
Si IV + O IV]	1290-1450	Si IV + O IV]	
Ly $\alpha$	1150-1290	Ly $\alpha$ broad	2
		Ly $\alpha$ narrow	1
		N V (1240 Å)	1
O VI	980-1100	O VI	1

## 2.5.2 Average Emission Line Properties

As mentioned in section 2.2.1, `PRQSOFIT` contains an additional feature that separates a given quasar spectrum into host galaxy and pure quasar contribution. However, for this separation to be well represented, the continuum needs to be accurately fitted. Unfortunately, the host and QSO continuum models implemented in `PRQSOFIT` prove inadequate for our objectives, as demonstrated by poor fitting statistics (see example fit in Appendix A). They appear to be strongly dependent on the details of the wavelength range used, indicative of a local minimum problem. Moreover, these high  $\chi^2_{\nu}$  values have additional implications as they prevent us from applying dust-extinction laws to investigate the underlying cause of the continuum differences observed in section 2.4.1. We are, however, able to obtain acceptable fits for the emission lines. To improve their goodness-of-fit, we use an additional localised power-law continuum component for each line complex after subtracting the globally fitted continuum, following the method of Fawcett et al. (2022). In addition, we perform a flux calibration before the fit to obtain non-arbitrary units. This is done by shifting each composite spectrum to the observed-frame by using its

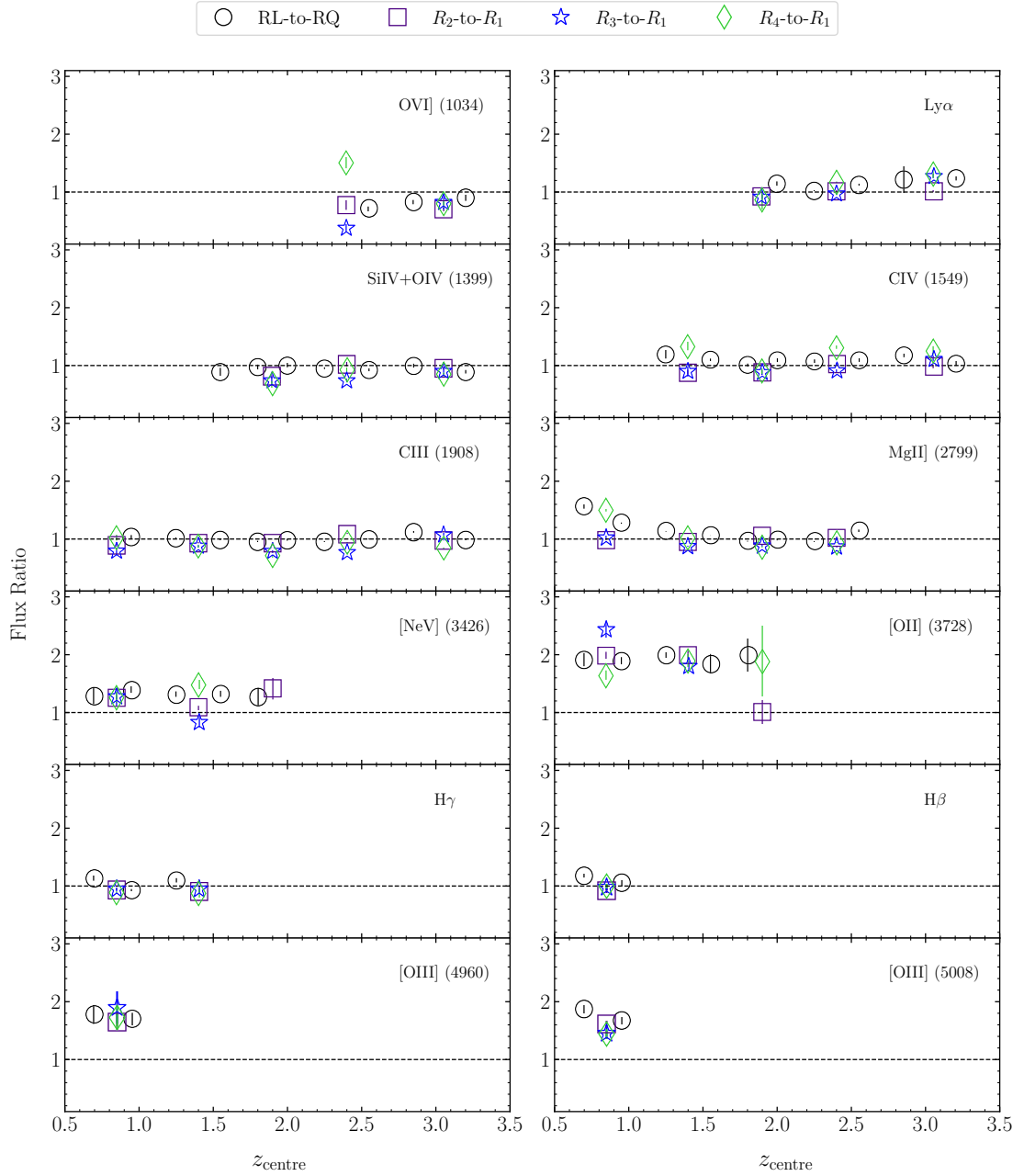


Figure 2.10: The emission line flux ratio of a given pair, as indicated in the legend, as a function of redshift. Each panel represent an emission line under comparison as denoted in the upper right corner, which must be significantly detected ( $> 3\sigma$ ) for inclusion. The dashed line in each panel represents the line of equality, facilitating visual comparison of the emission line flux ratios between the different pairs.

central redshift value ( $z_{\text{centre}}$ ) and the SDSS  $i$ -band filter curve and the median apparent  $i$ -band magnitude of the individual spectra to obtain a flux density in units of  $\text{erg s}^{-1} \text{cm}^{-2} \text{\AA}^{-1}$ .

Figure 2.10 presents the ratio of the emission line flux of the RL to RQ QSOs (RL-RQ), along with the more radio-loud to radio-quietest bin ( $R_2/R_3/R_4-R_1$ ) for the most prominent emission lines. Across all considered pairs, we find that the majority of emission lines exhibit flux ratios

close to unity. However, there is a strong excess for radio-loud objects in the [Ne v] 3426 Å, [O II] 3728 Å and the [O III] 4960/5008 Å (hereafter [Ne v], [O II] and [O III]) emission lines. These lines are of particular interest as [Ne v] is used to trace extended emission line regions (EELR: see discussion in next section), whereas the [O III] emission line is generally associated with the AGN bolometric luminosity (Heckman et al. 2004; Best and Heckman 2012; Kalfountzou et al. 2012), as it is mostly ionised by the continuous radiation coming from the accretion disc. The [O II] emission line, on the other hand, is a well-known star formation tracer in quasar host galaxies (e.g. Ho 2005; Kalfountzou et al. 2012; Matsuoka et al. 2015) as in contrast with the [O III], it is only weakly excited in the narrow line region (NLR). However, as result of the low number of data points for the [O III] emission due to the available redshift range, we focus only on [Ne v] and [O II] in the following section.

### 2.5.3 Star Formation Rates

The [O II] forbidden line is a prominent feature that can be easily detected in moderate resolution spectra, making it a good SF tracer in the absence of  $H\alpha$ . When an AGN is present, however, this emission line can be severely contaminated by excitation from EELR which can span out to several kpc (e.g. Unger et al. 1987; Villar-Martín et al. 2011; Husemann et al. 2014; Maddox 2018). Therefore, to determine whether the elevated levels of [O II] found in section 2.5.2 are due to SF, we employ the AGN correction technique described in Maddox (2018). Briefly, this method involves removing sources from the stacks with a [Ne v] detection and making use of the [O II]-to-[Ne v] emission line flux ratio, which in a typical AGN-dominated galaxy is found to be of order unity as a result of excitation from NLR. The [Ne v] is chosen because of its wavelength proximity to [O II] and its high ionisation potential, making the effects of dust attenuation and star-forming regions negligible.

As the spectral measurements provided by Rakshit et al. (2020) did not contain any information regarding [Ne v], we used `PRQSOFIT` to fit a single Gaussian in a spectral window of 150 Å centered on the [Ne v] central wavelength. The emission line is considered as a non-detection if the measured emission line flux is detected at a  $S/N < 3$ . Although in previous sections we investigated how the optical properties varied in bins of radio-loudness, the need to remove the [Ne v] detections from the stacks (which involves about 20 per cent) reduces the sample size to a point that it is no longer possible to search for evolution in both redshift and radio-loudness. Therefore, we continue the rest of the analysis with the RL and RQ populations. However,

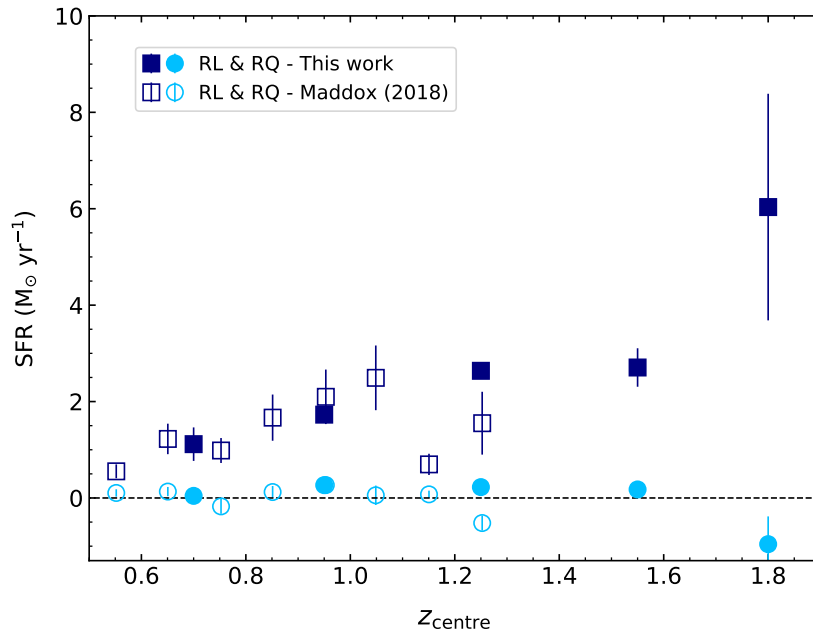


Figure 2.11: The SFR obtained from the doubly corrected  $[\text{O II}]$  emission line flux for the RL (dark blue) and RQ population (light blue) compared against the SFR obtained from Maddox (2018). The black dashed line indicates a SFR of zero.

we also create a new sample matched in  $z$  and  $M_i$ , with the division set at  $R = 0.2$  (i.e. the separation between  $R_1$  and the more radio-loud bins), to check whether using a slightly different classification would yield different results. From the newly computed composite spectra, we obtained emission line measurements for  $[\text{O II}]$  and  $[\text{Ne V}]$  in the same manner as before. A  $[\text{Ne V}]$  detection is still present in the stacks as a result of the high S/N which is sufficient to detect the contribution from the NLR. Using these measurements and the value of  $[\text{O II}] / [\text{Ne V}] = 1.05$  obtained from the SDSS composite spectrum from Vanden Berk et al. (2001), we are able to derive a measure of the  $[\text{O II}]$  emission line flux unaffected by AGN.

Figure 2.11 shows the  $[\text{O II}]$  derived, doubly corrected SFR against redshift obtained for the RL and RQ populations using the  $[\text{O II}]$  - SFR conversion from Kewley et al. (2004). We can see that the SFR of the RQ population is close to zero, indicating that on average star-formation processes in the host galaxy of RQ QSOs are not sufficient to produce a strong  $[\text{O II}]$  emission line. In contrast, the excess of  $[\text{O II}]$  persists for the RL population even when correcting for contamination from EELR and NLR. The alternative classification ( $R > 0.2$ ) also exhibits the same trend, further indicating that the exact value of  $R$  is not important. Our results are consistent with those of Maddox (2018) who used SDSS DR7 with Faint Images of the Radio Sky at Twenty-cm (FIRST; Becker et al. 1995), but we have shown that their findings persist with higher statistical significance and to a further  $\approx 1.4$  Gyr of cosmic history, closer to the peak

epoch of cosmic star formation rate density (Madau and Dickinson, 2014). This is because we benefit not only from the increased sensitivity of LoTSS and the reduced impact of line of sight effects (relative to the 1.4 GHz data), but also the extended wavelength coverage of the BOSS spectrograph (Smee et al., 2013).

## 2.6 Discussion

### 2.6.1 Could our results be caused by starburst galaxies contaminating our RL sample?

As discussed in the introduction, Macfarlane et al. (2021) have shown that the radio flux density of quasars can be modelled by a combination of star formation and radio jets. This naturally leads to the question of whether the [O II] excess found in section 2.5.3 could be caused by having radio-quiet quasars hosted by starburst galaxies in our RL sample. The presence of intense star formation in such hosts can lead to a larger degree of reddening (Gordon et al. 1997), which would further explain the redder continuum observed in section 2.4.1. In addition, this scenario does not require any differences between the black hole mass and accretion rate of the QSOs themselves (i.e.  $R_{\text{edd}}$ ), which is in agreement with our results (see section 2.4.2).

To explore this possibility, we used the main-sequence relation from Schreiber et al. (2015) and an offset of 0.6 dex based on the starburst criterion from Rodighiero et al. (2011) to obtain a SFR value for a typical starburst galaxy with a stellar mass of  $10^{11} M_{\odot}$  at a redshift equal to our central bin values from Figure 2.11. This resulted in SFR values ranging from 127 - 488  $M_{\odot} \text{ yr}^{-1}$  for the redshift range of  $0.6 < z < 1.9$ . These estimates are then converted to a radio luminosity at 150 MHz by using the mass independent SFR- $L_{150\text{MHz}}$  relation from Smith et al. (2021). Comparing these results to the RL sample, we find that up to 5 per cent in any given redshift bin, could have a radio luminosity consistent with contribution from RQ starbursts. However, taking into account the large difference between our doubly corrected [O II] SFR and the values obtained here for the starburst galaxies, it is unlikely that the radio emission is due to such extreme star-forming processes. Furthermore, considering the fact that we are investigating the median stacks of the populations, we believe that if starburst galaxies are present in our samples they will not noticeably impact our results.

### 2.6.2 Could shock excitation be playing a role?

In section 2.5.3, we have used the [Ne v] emission line to remove contamination from EELR and correct for contribution from the AGN NLR. However, shocks in the interstellar medium generated by radio jets or AGN-driven winds could also contribute to the [O II] emission. To assess their potential influence, Maddox (2018) used the MAPPINGS III shock and photoionization modelling code from Allen et al. (2008). The author found that there is a variety of shock conditions capable of exciting [O II], but only high velocity shocks ( $>600 \text{ km s}^{-1}$ ) are able to produce [Ne v]. This suggests that the doubly corrected [O II] could still be contaminated from moderate-velocity shocks. A prevalence of such shocks for the RL population may be able to explain the apparent enhancement of SFR and their redder appearance.

To investigate this scenario, we explore the connection between [O II] emission and 178 MHz luminosity, where we use the low frequency radio emission as a proxy for jet power. Here, we use a radio spectral index of  $\alpha = -0.7$  to convert from 144 MHz to 178 MHz, in order to compare our results with Hardcastle et al. (2009), who have found a positive correlation for a sample of 3CRR radio sources, which is thought to be of nuclear origin. The results for the RL sample from section 2.5.3, which was used to calculate the [O II] SFRs, are presented in Figure 2.12. We can see that the [O II] appears to be independent of the radio emission at any given redshift. However, there is a subset of sources that lie within the region defined by the 3CRR sample. This indicates the presence of some AGN-related influence, which can be as high as 36 per cent for the lowest redshift range ( $0.6 < z < 0.8$ ), and up to 13 per cent for the highest range ( $1.7 < z < 1.9$ ). But, as previously discussed our analysis relies on SFR derived from the median composite spectra of the populations. Furthermore, the correction for the AGN NLR isn't factored into the individual RL sources, which could potentially explain the correlation observed in the 3CRR sources. Therefore, if shocks are present in the RL population, we believe that they alone cannot account for the observed differences between RL and RQ quasars.

### 2.6.3 Possible explanations

To explain the differences between the RL and RQ population, we propose two distinct models: one centered on black hole spin dynamics (Blandford and Znajek 1977; Wilson and Colbert 1994; Sikora et al. 2007) and another on the evolutionary scenario proposed for red and blue

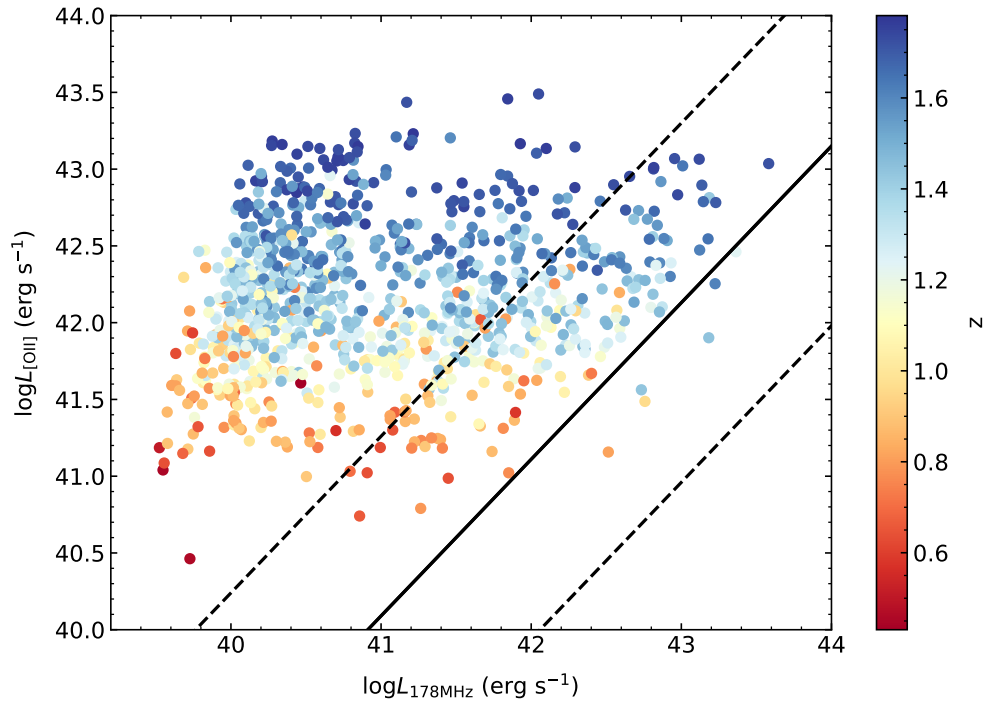


Figure 2.12: The [O II] emission line luminosity as a function of 178MHz total radio luminosity for RL sources without significant [Ne v] detections. The solid and dashed black lines are generated from the regression analysis results for the 3CRR radio sources in Table 6 of Hardcastle et al. (2009), where the solid line indicates the regression line, whereas the dashed lines show  $\pm 3\times$  the obtained scatter.

quasars (e.g. Sanders et al. 1990; Hopkins et al. 2008; Alexander and Hickox 2012; Klindt et al. 2019; Fawcett et al. 2020, 2022).

The first model involves a rapidly spinning black hole, coupled with a rich gas supply required for accretion and jet production (e.g. Hardcastle et al. 2007; Gürkan et al. 2015). Given that the gas needed for accretion, which leads to the radio-loudness of the source, is also essential for fueling star formation, these two processes are inherently interconnected. Therefore, the question becomes how to get a rapidly spinning black hole and a rich gas supply to make a RL quasar. We suggest two plausible scenarios: Firstly, the traditional major merger event which results in a rapid inflow of gas and dust. This material not only transports angular momentum toward the central region, leading to the rapid spin-up of the black hole, but also serves as a trigger for star formation. Secondly, we can consider a scenario in which RL quasars are hosted by massive, gas-rich spiral galaxies. In this setting, a substantial reservoir of cold gas is available, supporting continuous star formation and accretion. Furthermore, due to the ordered rotation characteristic of spiral galaxies, it may give rise to an efficient transfer of angular momentum onto the supermassive black hole, eliminating the necessity for merger events.

The alternative model assumes once more a gas-rich merger triggering an AGN, but here we focus on different stages of evolution, following e.g. Hopkins et al. (2008). The first one is a relatively short-lived phase where the QSO is heavily obscured by high-column gas density and dust. Subsequently, the AGN generates powerful winds and/or outflows, which disperse the obscuring material. In our study, RL quasars could represent the former evolutionary stage, where the redder continuum and enhanced SFR would be explained by the obscuring and dense material, whereas RQ quasars may fall into the latter (unobscured) category. Here we do not require any difference in either the accretion rate or in the BH spins between the two classes. This scheme is related to the one presented for red and blue QSOs discussed in previous studies (e.g. Klindt et al. 2019; Fawcett et al. 2020; Fawcett et al. 2022), where dividing the QSO population according to their optical colours (rather than radio-loudness) gives a red class with a significant radio flux excess relative to the blue class. However, both the red and blue QSO classes contain RL and RQ sources, and the average QSO in both classes is consistent with being radio-quiet (i.e.  $R < 1$ ). It is therefore clear that this association alone cannot explain our results (certainly we cannot equate the RL QSOs with the ‘red QSO’ class, etc).

To make further progress on what controls the radio-loudness of QSOs, we need more information. This could come from the sub-arcsecond 144 MHz imaging that is now becoming possible with LOFAR (and the morphological information that it can provide; e.g. Morabito et al. 2022), along with larger statistical samples from new and forthcoming facilities such as WEAVE (Dalton et al., 2012; Jin et al., 2023), the Dark Energy Spectroscopic Instrument (DESI; Desi Collaboration et al. 2016a,b) and the Multi-object Optical and Near-IR spectrograph (MOONS; Cirasuolo et al. 2014). In addition, improved black hole spin estimates from X-ray observatories such as the European Space Agency’s Athena X-ray observatory (Barcons et al., 2017) and NASA’s Nuclear Spectroscopic Telescope Array (NuSTAR; Harrison et al. 2010) will be crucial in deepening our understanding of this subject.

## 2.7 Summary

In this chapter, we have used the second data release of the LOFAR Two-metre Sky Survey and the fourteenth data release of the Sloan Digital Sky Survey to create the largest, uniformly-selected, spectroscopically-confirmed sample of radio-loud and radio-quiet quasars. To study their spectroscopic properties, we have developed a new spectral stacking code which accounts for a range of biases including those that arise as a result of the redshifting process. Such a

tool not only allows us to robustly compare quasar and galaxy populations, but also enables us to statistically recover the continuum properties of faint sources. This will become particularly important for radio-selected spectroscopic surveys such as the WEAVE-LOFAR survey (Smith et al., 2016), which will generate more than one million optical spectra, with continuum detections absent in a significant fraction. Using this algorithm to investigate the average properties of QSOs as a function of their radio-loudness, we have found the following results:

- (i) The high S/N composite spectra representative of the RL and RQ populations differ. RL QSOs are found to have on average a redder continuum with an [O II] emission line excess across the redshift range of  $0.6 < z < 3.5$ . Such differences highlight the importance of creating high-resolution stacks of both populations to improve the redshift classification of future spectroscopic surveys.
- (ii) The RL and RQ population are found to span similar black hole mass ranges with no systematic trend showing that the mean  $M_{\text{BH}}$  is higher for RL QSOs. Furthermore, using a sample matched in  $z$ ,  $M_i$  and  $M_{\text{BH}}$  to make a comparison between the average spectra of RL and RQ QSOs is found to give similar statistically consistent results as for a sample matched in  $z$  and  $M_i$ . This suggests that neither the BH mass, nor the accretion rate are defining factors in a QSO's radio-loudness.
- (iii) The observed differences between the RL and RQ population are not gradual. Comparing composite spectra as a function of radio-loudness shows that all more radio-loud bins ( $R_2$ ,  $R_3$ ,  $R_4$ ) differ from the radio-quietest ( $R_1$ ), with features consistent with the classical RL and RQ division.
- (iv) These changes cannot be explained by the addition of radio-undetected sources, as we have found that the radio-detected and radio-undetected quasars in  $R_1$  are consistent with being drawn from the same parent distribution.
- (v) We have shown that RL quasars have on average higher SFRs than their RQ counterparts at any given redshift  $0.5 < z < 1.9$ , extending this result to significantly earlier cosmic epochs than previously known. The elevated levels of [O II] emission that we use to infer the SFRs have been corrected for possible influence of AGN contamination (following the procedure of Maddox 2018) and we have shown that our results cannot be explained by contamination from starburst galaxies.

Our results show that there is no clear-cut division in radio-loudness between RL and RQ quasars, and that the differences observed between them is not related to black hole mass or the accretion rate. As a result, we propose two distinct models: one requiring that RL quasars have rapidly spinning black holes in conjunction with abundant gas reservoirs, or are representatives of an earlier obscured phase of QSO evolution.

With the advent of future spectroscopic surveys such as WEAVE-LOFAR, the number of radio-loud QSOs will significantly increase. This will allow to us to investigate their spectral properties in greater detail and with higher significance. With higher S/N, however, we will need more sophisticated theoretical models to fit the composite spectra in order to disentangle their dust and host properties.

## Chapter 3

# WEAVE First Light Observations: Origin and Dynamics of the Shock Front in Stephan's Quintet

### 3.1 Introduction

Galaxy mergers and interactions are a cornerstone of our understanding of Galaxy Formation & Evolution. They are believed to play key roles, not only in the mass build-up and morphological transformation of galaxies, but also for triggering extreme starbursts and active galactic nuclei (AGN; e.g. Barnes and Hernquist, 1996; Hopkins et al., 2006; Smith et al., 2010; Satyapal et al., 2014; Cibinel et al., 2019; Pierce et al., 2023). Mergers and interactions occur predominantly in systems with high galaxy density and low velocity dispersion, making nearby compact galaxy groups ideal laboratories for studying their impact (e.g. Hickson et al. 1992).

One such system is Stephan's Quintet (hereafter SQ), which has been extensively studied across the electromagnetic spectrum ever since its discovery by Stephan (1877). SQ has a systemic redshift of  $z=0.0215$  (Hickson et al., 1992), and consists of three galaxies at its core (NGC 7317, NGC 7318a and NGC 7319 as shown in Figure 3.1), which according to the dynamical scenario proposed by Moles et al. (1997) have experienced several interactions under the gravitational influence of a fourth galaxy with a similar redshift, NGC 7320c (the 'old intruder', to the east of NGC 7319, not shown in Figure 3.1). A fifth nearby galaxy, NGC 7320, is considered to be a foreground source due to its highly discordant redshift (Burbidge and Burbidge, 1961).

Unlike NGC 7317 and NGC 7318a, which have an elliptical morphology, NGC 7319 and the old intruder exhibit spiral structures. However, the process of interaction has stripped almost all of their interstellar medium (ISM; Sulentic et al., 2001) into the intergalactic medium (IGM). The system is currently undergoing a new interaction between the IGM and NGC 7318b, the ‘new intruder’, as it enters the group for the first time at  $\sim 1000 \text{ km s}^{-1}$  towards our line of sight. This has led to the formation of the large-scale shock region (hereafter LSSR), a giant filament of shocked gas,  $\sim 45 \text{ kpc}$  in extent. The LSSR is located to the east of NGC 7318b, and has been studied extensively using X-rays (Trinchieri et al. 2005; O’Sullivan et al. 2009), ionised gas emission (Xu et al. 2003a; Iglesias-Páramo et al. 2012; Konstantopoulos et al. 2014; Rodríguez-Baras et al. 2014; Duarte Puertas et al. 2019, 2021), molecular  $\text{H}_2$  gas (Appleton et al. 2006; Cluver et al. 2010; Appleton et al. 2006) and at radio frequencies (Allen and Hartsuiker 1972; Williams et al. 2002; Xu et al. 2003a; Nikiel-Wroczyński et al. 2013).

Some of the key results from these works can be summarised as follows: X-ray observations of the LSSR by O’Sullivan et al. (2009) revealed the presence of a hot plasma associated with a ‘ridge’ with temperature  $\sim 0.6 \text{ keV}$  and  $Z = 0.3Z_{\odot}$ , embedded within a larger hotter halo with similar metallicity, likely heated by previous dynamical encounters within the system. The hot gas in the ridge is believed to originate from an oblique shock heating a pre-existing  $\text{H I}$  filament, presumably a remnant of a previous interaction. Mid-infrared studies have found that the LSSR is further characterized by dominant warm  $\text{H}_2$  emission, whose luminosity exceeds that of the hot X-ray plasma by a factor of 3 (Cluver et al., 2010), indicating that molecular hydrogen lines play a far greater role in the cooling of the gas than the thermal X-ray emission. By combining *Spitzer Space Telescope* and *James Webb Space Telescope* Mid-Infrared Instrument (hereafter *JWST* MIRI) imaging, with CO (2-1) imaging spectroscopy from the Atacama Large Millimeter/submillimeter Array (ALMA), Appleton et al. (2023) propose that this distinctive emission originates from the fragmentation of cold molecular clouds as they are mixed with post-shocked gas. These clouds were formed during the collision event and were subsequently subjected to ram pressure stripping from the hot X-ray plasma generated by the shock, leading to the formation of smaller fog clouds emitting infrared  $\text{H}_2$  radiation. Radio studies have further revealed a steep non-thermal spectral index along the shock front between 1.43 – 4.86 GHz (observed with the Very Large Array; Thompson et al. 1980) and 4.85 – 8.35 GHz (using the Effelsberg 100-m Radio Telescope; Wielebinski et al. 2011), indicating the presence of old plasma. This suggests that the shock has been active for a significant period, allowing electrons to undergo various stages of interactions.

These works have been complemented by optical IFU observations which have transformed our ability to study the system by enabling us to trace its resolved kinematics and ionised gas properties. Iglesias-Páramo et al. (2012) presented the first IFU observation of the LSSR in SQ using the the Calar Alto 3.5m Telescope with the Potsdam Multi-Aperture Spectro-photometer (PMAS, Roth et al. 2005) to obtain  $16 \times 16$  arcsec<sup>2</sup> field of view (FoV) pointings in three separate regions of the shock with an effective spectral resolution of FWHM =  $3.6 \text{ \AA}$  across the wavelength coverage of  $3810 < \lambda < 6809 \text{ \AA}$ . The authors revealed the presence of three kinematic regimes: H $\text{II}$  regions with recession velocities consistent with the new intruder ( $5400 - 6000 \text{ km s}^{-1}$ ), low-velocity shock-ionised gas with solar metallicity ( $5800 - 6300 \text{ km s}^{-1}$ ) and high-velocity shock-ionised gas with sub-solar metallicity ( $\sim 6600 \text{ km s}^{-1}$ ). They suggested that the high-velocity component is a byproduct of the new intruder colliding with the IGM, whereas the low-velocity component may have existed prior to the collision. These findings were confirmed and complemented by Rodríguez-Baras et al. (2014), who used the same instrument but in PMAS fiber PAcK mode (PPAK; Kelz et al., 2006) which traded lower spectral resolution (FWHM =  $10 \text{ \AA}$ ) for a larger FoV ( $74 \times 65$  arcsec<sup>2</sup>) and extended wavelength coverage ( $3700 - 7100 \text{ \AA}$ ), demonstrating by comparing with theoretical models that the nebular emission in SQ is consistent with a shock origin, with low density pre-existing gas, and velocities between  $200 - 400 \text{ km s}^{-1}$ .

More recently, Duarte Puertas et al. (2019, 2021) observed the entire system, making use of the large  $11 \times 11$  arcmin<sup>2</sup> FoV of the SITELLE instrument (Grandmont et al., 2012), a Fourier transform spectrometer on the Canada France Hawaii Telescope. With three filters (SN1, SN2 and SN3) covering emission lines from [O II]  $3727 \text{ \AA}$  to [S II]  $6716, 6731 \text{ \AA}$  with a mean spectral resolution of  $\lambda/\Delta\lambda \sim 500$ ,  $\lambda/\Delta\lambda \sim 760$  and  $\lambda/\Delta\lambda \sim 1560$ , respectively, the authors were able to study the star formation rates (SFR), oxygen and nitrogen-to-oxygen abundance of 175 H $\alpha$  regions in SQ. They found that the majority of star-formation is present in the starburst region A (SQ-A, the region to the North end of the shock, which appears blue as seen in Figure 3.1 as a result of recent star-formation), suggesting that prior to the collision there was little ongoing star formation in the IGM. Their work also revealed the presence of two chemically different regions, with the low/high metallicity material primarily associated with a relatively low/high radial velocity, suggesting that the metal-rich component comes from the inner part of the new intruder.

In this study, we build upon these results, by combining the first light data from the William Herschel Telescope Enhanced Area Velocity Explorer large integral field unit (WEAVE-LIFU; Dalton et al. 2012) with a range of new and archival multi-wavelength data, including 144 MHz

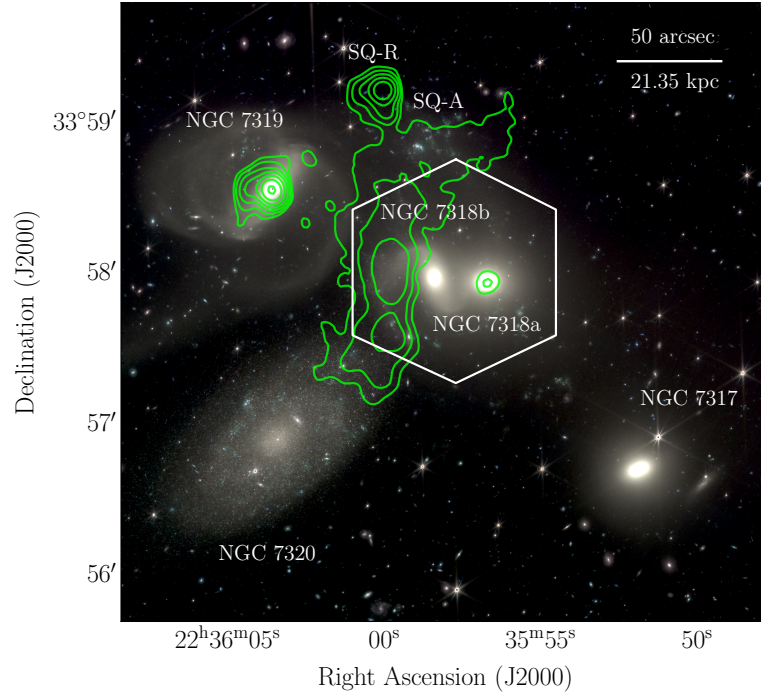


Figure 3.1: A composite image of Stephan's Quintet made with NIRCam's F277W, F356W and F444W bands. The green contours represent the 144 MHz radio flux density from LoTSS in percentage of peak surface brightness, increasing in steps of two. The lowest contour and radio flux density are 1.41 per cent and 1.2 mJy. The hexagon denotes WEAVE's pointing of the system.

radio observations from the second data release of the LOFAR Two-metre Sky survey (LoTSS; Shimwell et al. 2022). The combination of the arcminute-scale FoV ( $90 \times 78 \text{ arcsec}^2$ ) of the WEAVE-LIFU, high spectral resolution ( $\lambda/\Delta\lambda \sim 2500$ ), and virtually-complete wavelength coverage across the optical wavelengths ( $3660 - 9590 \text{ \AA}$ ) allow us to study the shock front in greater detail than previously possible. In addition, we expand the multi-wavelength picture of the system by considering low-frequency radio data, which traces older, more diffuse emission, allowing us to gain new insights into the complex history of Stephan's Quintet.

The structure of this chapter is as follows: Section 3.2 describes the data used in this work, including WEAVE-LIFU and LoTSS observations along with additional auxiliary data from *JWST* and the VLA. Section 3.3 gives an overview of the spectral fitting process used in this work. Section 3.4 presents an overall view of SQ based on the multiwavelength data we have assembled, while section 3.5 investigates the shock region in more detail. Finally, section 3.6 summarises and discusses our findings. Throughout this chapter, we use air wavelengths and a flat  $\Lambda$ CDM cosmology with  $H_0 = 70 \text{ km s}^{-1} \text{ Mpc}^{-1}$ ,  $\Omega_M = 0.3$ , and  $\Omega_\Lambda = 0.7$ .

## 3.2 Data

### 3.2.1 WEAVE First Light Data

Large Integral Field Unit (LIFU) observations of Stephan’s Quintet were taken on 25 October 2022, and released internally on 12 December 2022 as part of WEAVE’s first light data release. The WEAVE LIFU consists of 547 closely-packed optical fibres with a filling factor of 0.55, each 2.6 arcsec in diameter, together providing a field of view of  $90 \times 78$  arcsec<sup>2</sup>. The data were acquired in two observing modes - ‘high-resolution’, which offers a spectral resolution of  $\lambda/\Delta\lambda \sim 10,000$  across the wavelength range of  $4040 < \lambda < 6850$  Å, and ‘low-resolution’, which has  $\lambda/\Delta\lambda \sim 2500$  across  $3660 < \lambda < 9590$  Å. In this work, we focus on the ‘low-resolution’ mode data due to its higher signal-to-noise ratio, which enables us to study the emission lines in the LSSR per spaxel basis.

The observations were taken at a mean airmass of 1.01, in 1.67 arcsec seeing, and at a position angle of  $120^\circ$  centred near  $(\alpha, \delta) = (22^{\text{h}} 35^{\text{m}} 59.3^{\text{s}}, +33^\circ 58' 12.3'')$  between the galaxies NGC 7318a and NGC 7318b (see Figure 3.1 for details, in which the hexagonal WEAVE FoV is outlined in white). The observations consisted of six exposures, each 1020 seconds in duration, using both the blue-(3660 – 6060Å) and red-arms (5790 – 9590Å) with the native  $1\times$  spectral binning giving a scale of  $0.5 \text{ \AA pixel}^{-1}$ . Between exposures, the telescope pointing was adjusted using the default six-point dither pattern, designed to permit complete spatial sampling once the individual observations are combined.

The resulting data were fully reduced using the Core Processing System (CPS; Walton et al., 2014) WEAVE pipeline located at the Cambridge Astronomical Surveys Unit (CASU). More information about the data reduction process is given by Jin et al. (2023), however, the main steps can be summarized as follows. The data are bias- and flat-field corrected, and observations of a quartz-halogen lamp are used to trace out the location of each LIFU fibre’s spectrum along the CCDs, to enable the spectra to be extracted. A wavelength solution is produced based on observations of ThArCr arcs, and a flux scale derived based on observations of white dwarfs. ‘Superstack’ data cubes for each arm are then produced by reconstructing the 3D spectra to a fixed wavelength grid with  $0.5 \text{ \AA}$  pixels. Spectra are produced at each location using the six individual exposures, conserving flux and inverse variance, and accounting for the dithering pattern. Finally, sky subtraction is performed using a principal component analysis.

The resulting data cubes are stored in FITS format, are  $178 \times 188$  0.5 arcsec spaxels on a side, and consist of seven extensions: (i) data, (ii) inverse variance, (iii) data without sky-subtraction, (iv) inverse variance without sky-subtraction, (v) sensitivity function used for flux calibration, (vi) white-light image collapsed in the wavelength direction, (vii) white-light inverse variance. Version 1 of the fully-reduced data can be downloaded from the WEAVE Archive System (WAS<sup>1</sup>).

### 3.2.2 Radio Data

The 144 MHz observations of SQ are included in the second data release of the LOFAR Two-metre Sky survey (LoTSS DR2) and are accessible on the LOFAR surveys website<sup>2</sup>. A comprehensive description of the data processing can be found in Shimwell et al. (2022). To briefly summarise, the 144 MHz data were reduced using the fully automated LoTSS processing pipeline, which corrects for direction-independent instrumental effects, as well as ionospheric distortions that vary with time and direction. The resulting images have a resolution of 6 arcsec and are highly sensitive to emission on both small and large scales, as a result of the range of baselines available in the Dutch LOFAR array.

Additionally, there are publicly available observations of SQ using the Karl G. Jansky Very Large Array (VLA; Perley et al., 2011). Project ID 18B-080 (PI: Blazej Nikiel-Wroczyński) observed the system at 1.7 GHz in C-array configuration, while project ID AS939 (PI: M. Soida) made an observation at 4.86 GHz in the D-array configuration. These datasets are selected for this study, due to their high sensitivity to large-scale extended emission and their comparable angular resolution. We used the Common Astronomy Software Applications (CASA; CASA Team et al., 2022) VLA calibration pipeline to reduce the 1.7 GHz dataset, while the 4.86 GHz dataset was processed using the VLARUN routine within the Astronomical Image Processing System (AIPS; Greisen, 2003). In both cases, we conducted multiple iterations of phase-only and phase+amplitude self-calibration to remove residual errors. More information about individual images can be found in Table 3.1.

---

<sup>1</sup><http://portal.was.tng.iac.es>

<sup>2</sup>[https://lofar-surveys.org/dr2\\_release.html](https://lofar-surveys.org/dr2_release.html)

Table 3.1: Information about the radio images of SQ used in this work, with details of the synthesized beam size, the peak flux densities and rms noise values.

Image	Beam FWHM arcsec <sup>2</sup>	Peak flux mJy	RMS $\mu\text{Jy beam}^{-1}$
LoTSS 144 MHz	$6 \times 6$	662	129.6
VLA C-Array 1.7 GHz	$13.35 \times 11.95$	62	16.3
VLA D-Array 4.86 GHz	$13.63 \times 12.63$	3.5	8.6

### 3.2.3 Additional Auxiliary Data

*JWST* NIRCam and MIRI observations of SQ are available as part of the Early Release Observations (ERO) described in Pontoppidan et al. (2022). To summarise, NIRCam data were obtained using six broad-band filters (F090W, F277W, F150W, F356W, F200W, F444W) covering the wavelength range of  $0.9 - 4.5 \mu\text{m}$ , and using the FULLBOX dither pattern to produce a large  $6.3 \times 7.3 \text{ arcmin}^2$  rectangular mosaic covering all galaxy members, except NGC 7320c. These data are well-suited for providing an overview of the system, effectively highlighting the complexity and intricate details of SQ, as shown in Figure 3.1.

In addition, the MIRI data were obtained in three bands (F770W, F1000W and F1500W with central wavelengths  $7.7 \mu\text{m}$ ,  $10 \mu\text{m}$  and  $15 \mu\text{m}$ , respectively) over a smaller area using four tiles centered on NGC 7318a/b, NGC 7319 and NGC 7320c. The significance of these bands lies in their ability to capture specific features. The F770W band is found to trace the polycyclic aromatic hydrocarbon (PAH) complex when star formation dominates, and the  $0-0 \text{ S}(5) \text{ H}_2$  emission otherwise. The F1000W band, on the other hand, is dominated by emission coming from the  $\text{S}(3)$  mid-IR pure rotational  $\text{H}_2$  line, whereas the F1500W filter captures the faint dust continuum of the IGM (see Appleton et al. 2023 for further details). All these data are publicly available and were downloaded from the Mikulski Archive for Space Telescopes<sup>3</sup>.

## 3.3 Spectral Fitting Method

To study the nebular gas properties of SQ, and the LSSR in particular, we fitted the principal emission line complexes (including the brightest species;  $\text{H}\beta \lambda 4861$ ,  $[\text{OIII}] \lambda \lambda 4959/5007$ ,  $\text{H}\alpha \lambda 6563$ , and  $[\text{NII}] \lambda \lambda 6548, 6583$ ) in all available  $0.5 \text{ arcsec}$  spaxels, using multiple Gaussian components (in a manner similar to Comerón et al., 2021). To determine the optimal number of components required for a given spaxel, we used the Bayesian Information Criteria (BIC), which

<sup>3</sup>doi:10.17909/dfsd-8n65

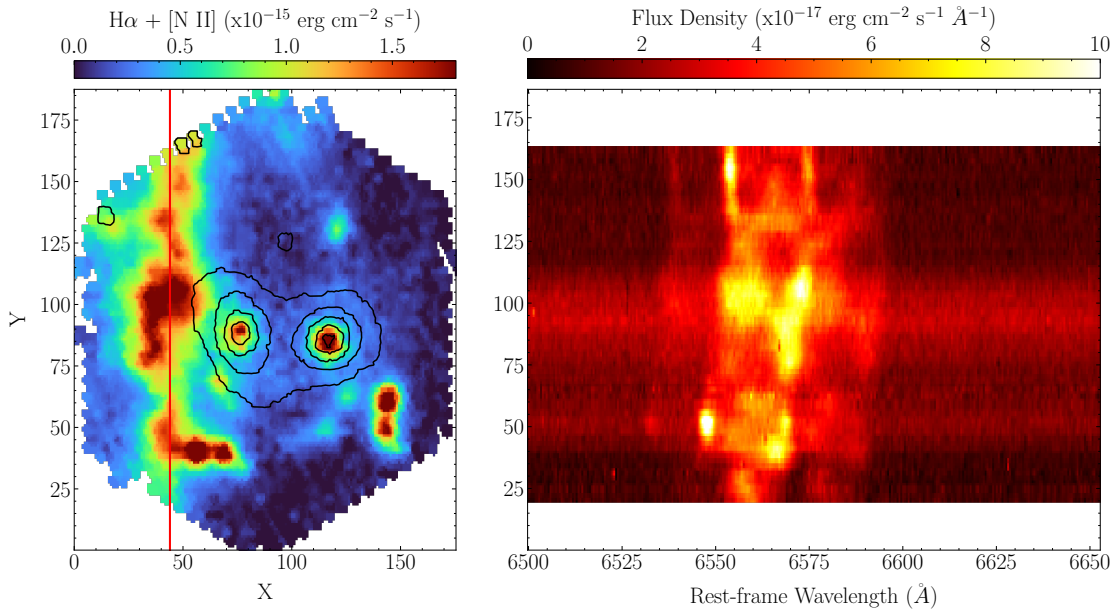


Figure 3.2: The complex velocity structure in the LSSR. The left panel presents the  $H\alpha + [N\text{ II}]$  complex obtained by summing a spectral region of  $150\text{ \AA}$  around  $H\alpha$  for each continuum subtracted spaxel using a linear approximation. The apparent  $H\alpha$  emission associated with the centres of the two galaxies can be attributed to artefacts of the continuum-removal process, as there is no evidence for  $H\alpha$  emission seen in these two regions when visually inspecting those individual spaxels (see Appendix B), unlike in the vicinity of the LSSR. The black contours represent the peak optical flux density from the two data cubes, increasing in steps of two. The lowest black contour and optical flux density are 0.056 per cent and  $3.55 \times 10^{-13}\text{ erg s}^{-1}\text{ cm}^{-2}\text{ \AA}^{-1}$ , respectively. The right panel shows the flux density in the vicinity of the  $H\alpha + [N\text{ II}]$  complex across the region as denoted by the red line in the left panel.

enables us to find a balance between the goodness of fit and the number of free parameters in our model. Such an involved technique is necessary because the velocity structure of the emission lines in SQ is extremely complex. This is evident in Figure 3.2, in which the left-hand panel shows the integrated emission from the  $H\alpha + [N\text{ II}]$  complex, while the right-hand panel shows a position-velocity diagram along the North-South direction of the peak emission (the location is indicated by the red vertical line in the left-hand panel). The  $H\alpha + [N\text{ II}]$  emission has been calculated by summing over a spectral window  $150\text{ \AA}$  wide centered on  $H\alpha$  for each spaxel after subtracting the continuum (approximated using a linear model). We can see that the majority of the  $H\alpha$  emission is concentrated in the region surrounding the shock, located to the East of the two central galaxies (NGC 7318a & b, whose locations are indicated by the contours in the left panel of Figure 3.2).

To summarise our line modelling approach, we first corrected the spectra for Galactic extinction in the observed-frame by using the re-calibrated reddening data,  $E(B - V)$ , from Schlegel, Finkbeiner, and Davis (1998), along with the Milky Way reddening curve from Fitzpatrick (1999)

for an extinction-to-reddening ratio of  $R_V = 3.1$ . For each spaxel, we fitted both the spectral windows of interest from the blue- and red-arms simultaneously, modelling the local continuum near each line complex with a straight line, and each emission line with up to four Gaussian components. Each spectrum was modelled independently of its neighbours. The simplistic, straight-line approach to continuum subtraction was adopted since our primary interest is in the regions away from the galaxies, where the continuum is faint and free from significant structure (see e.g. the right panel of Figure 3.2).

To reduce the number of free parameters in our model and obtain good constraints on the velocity structure of the system, we fixed the relative velocity offsets and line widths for each Gaussian components across all of the lines modelled. In addition, we set the flux ratios for the [OIII]  $\lambda\lambda 4959/5007$  and [NII]  $\lambda\lambda 6548/6583$  doublets to their predicted values (2.98 for [OIII] following Dimitrijević et al. 2007, and 3.05 for [NII] following Dojčinović et al. 2023). As the number of free parameters is still considerable, we employed the Markov Chain Monte Carlo (MCMC) method with 250 walkers running for 5000 steps to determine reliable flux estimates and associated uncertainties for each of the lines modelled. The fit results are visually inspected to ensure that the chains converge and that the results are robust.

Finally, to determine which of the four models to choose from (one for each number of Gaussian components), we used the minimal BIC value which is computed in the following way, assuming that the model errors are independent and identically distributed according to a normal distribution:

$$\text{BIC} = k \ln(n) + \chi^2. \quad (3.1)$$

Here  $n$  is the number of data points,  $k$  is the number of free parameters and  $\chi^2$  is the chi-squared parameter. In Appendix B, we provide examples of fits consisting of all four models identified at different locations within SQ to demonstrate the performance of this method.

From the best-fit models for each emission line species, we obtain the total emission line flux, equivalent width (EW), full width at half maximum (FWHM), and velocity including all of Gaussian components. While determining the line flux and the EW is straightforward, the presence of multiple Gaussian components per emission line makes obtaining representative FWHM and velocity more challenging. The FWHM is calculated using the combined profile fit for each species, irrespective of the line shape. For the velocity, we choose to examine the weighted average velocity, where the weights are given by the emission line flux for each Gaussian component. The uncertainties associated with each spectral property are evaluated

by propagating the values extracted from the MCMC chains. For the entirety of the analysis, we concentrate on spaxels that have a  $\geq 3\sigma$  detection in all four bright lines (i.e.  $H\beta$   $\lambda$ 4861,  $[OIII]$   $\lambda$ 5007,  $H\alpha$   $\lambda$ 6563, and  $[NII]$   $\lambda$ 6583), since these are the spaxels with the best velocity constraints that enable us to confidently deblend  $H\alpha$  from the  $[NII]$  line.

## 3.4 General Overview of Stephan's Quintet

### 3.4.1 Stephan's Quintet as seen with WEAVE

For a general overview of the system, we present the spectral properties of  $H\alpha$  obtained using our spectral fitting method in Figure 3.3, which contains four panels showing the total integrated flux, the weighted-average velocity, the FWHM and the equivalent width (EW), clockwise from the top-left, respectively. In each panel, black contours have been overlaid for reference, indicating the locations of the central galaxies (NGC 7318a & b). What is immediately remarkable upon even a cursory inspection of Figure 3.3 is that the derived line measurements all vary smoothly over the FoV, including on scales larger than the 2.6'' LIFU fibres (which are themselves larger than the seeing at the time of the observations). This is despite each spaxel in the reconstructed WEAVE cube having been fitted independently. The smoothness that is apparent offers great encouragement that our fitting is performing in a robust manner.

The integrated flux in the  $H\alpha$  emission line (top-left panel) is shown after accounting for the  $[NII]$  contribution in the fitting, with the flux in each spaxel indicated by the colour bar to the right. As a result of our selection criteria, which considers only spaxels with a significant detection in  $H\beta$   $\lambda$ 4861,  $[OIII]$   $\lambda$ 5007,  $H\alpha$   $\lambda$ 6563, and  $[NII]$   $\lambda$ 6583, Figure 3.3 does not show any  $H\alpha$  emission associated with the central galaxies (unlike Figure 3.2; visual inspection confirms that all emission lines considered are absent in the cores of NGC 7318a & b). The  $H\alpha$  flux map has been overlaid with grey dashed contours representing the LoTSS 144 MHz flux density. We can see clear spatial association between the  $H\alpha$  intensity and the 144 MHz flux density in the region surrounding the shock, including the regions of maximum 144 MHz intensity near  $(\alpha, \delta) \approx (22^{\text{h}} 36^{\text{m}} 00^{\text{s}}, +33^{\circ} 57' 36'')$  and  $(22^{\text{h}} 36^{\text{m}} 00^{\text{s}}, +33^{\circ} 58' 02'')$  respectively, suggesting a common excitation mechanism.

In the southeastern and southwestern areas, near  $(\alpha, \delta) \approx (22^{\text{h}} 35^{\text{m}} 59^{\text{s}}, +33^{\circ} 57' 34'')$  and  $(22^{\text{h}} 35^{\text{m}} 55^{\text{s}}, +33^{\circ} 57' 44'')$ , however, there are distinct clusters of intense  $H\alpha$  emission with

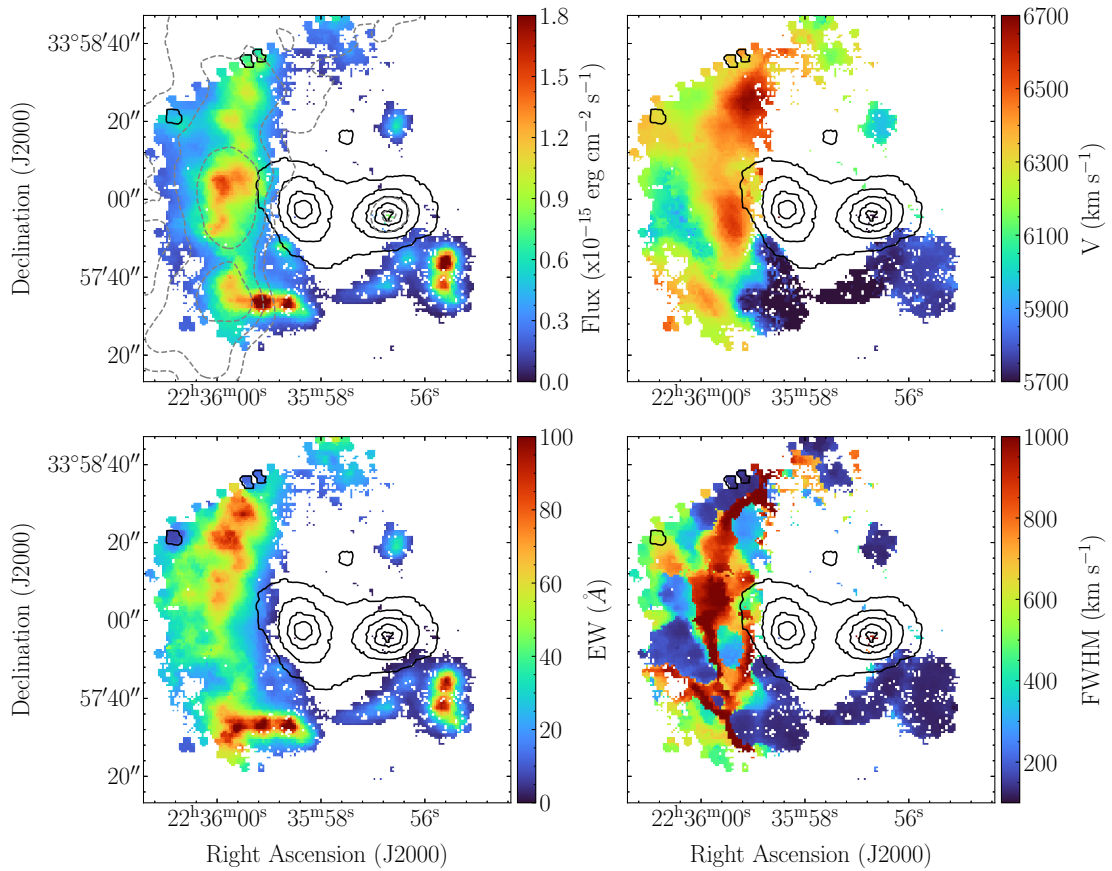


Figure 3.3: The spectral properties of  $H\alpha$  for all spaxels with a  $3\sigma$  detection for all lines of interest. The black contours in each panel show the peak optical flux density as in Figure 3.2. The upper left panel shows the  $H\alpha$  emission line flux, where we have added additional grey contours representing the peak LoTSS 144 MHz flux density as in Figure 3.1. The lower left panel presents the EW, demonstrating a weak continuum throughout the region considered. The upper right panel shows the different velocity structures in the system, whereas the lower right panel demonstrates the complex dynamics occurring in the shock region.

no overlapping contours associated with 144 MHz flux density. These regions exhibit high EW (lower-left panel) and low velocity dispersion (lower-right panel), which correspond to typical attributes of H II regions (e.g. Zaragoza-Cardiel et al., 2015; Lima-Costa et al., 2020). Furthermore, their velocities ( $5600 - 5800 \text{ km s}^{-1}$ , as shown in the upper-right panel) are consistent with those of the new intruder (NGC 7318b), providing strong evidence of their connection. These findings are consistent with previous studies, which suggest that these regions have survived the collision of NC7318b with SQ (e.g. Iglesias-Páramo et al. 2012).

The lower-left panel of Figure 3.3 shows high EW line emission throughout the entire system, which lends support to our decision to use a simple local linear continuum model in our spectral fitting.

Moving to the velocity map (top-right of Figure 3.3), we can see a complex velocity structure. In

the LSSR we can identify both low ( $5800 - 6300 \text{ km s}^{-1}$ ) and high ( $6300 - 6700 \text{ km s}^{-1}$ ) velocity components, which are consistent with the values measured in smaller areas by Iglesias-Páramo et al. (2012) and Konstantopoulos et al. (2014). However, unlike those two works, WEAVE has full spatial coverage providing a virtually complete sampling of the LSSR. The different motions indicate that the components do not share a common origin, as implied by their distinct metallicities (Iglesias-Páramo et al., 2012).

Finally, the map of FWHM (lower-right of Figure 3.3) reveals a broad variety of intriguing and complex structures. Perhaps the principal feature is a prominent strand of high FWHM material ( $> 700 \text{ km s}^{-1}$ , shown as red) spatially coincident with the peak in the  $\text{H}\alpha$  and 144 MHz emission, and surrounded by significantly lower FWHM areas, including several ‘bubble’-like structures with  $\text{FWHM} < 300 \text{ km s}^{-1}$ . Again we note that the individual spaxels are modelled independently, and we therefore believe that the different structures apparent in the FWHM map (which are smoothly varying) are physical. We interpret this  $\text{FWHM} > 700 \text{ km s}^{-1}$  region as our best estimate of the extent of the shock structure, with the high velocity dispersion resulting from the turbulent motion of the gas caused by the collision of NGC 7318b with the detritus deposited in the IGM by previous galaxy interactions. In the rest of this paper, we refer to the region with  $\text{H}\alpha$   $\text{FWHM} > 700 \text{ km s}^{-1}$  as the “dynamically-defined shock region”.

The dynamically calm ‘bubbles’ visible as light blue regions in the LSSR region with lower FWHM ( $< 300 \text{ km s}^{-1}$ ) are also of interest. The relatively calm motion observed in these regions potentially suggests the presence of fainter  $\text{H II}$  regions or small-scale shocks compressing and heating the gas, or perhaps they are simply a result of line-of-sight effects.

### 3.4.2 Extinction, dust and gas with WEAVE and JWST / MIRI

To investigate the dust properties of SQ, we use the Balmer decrement method from Domínguez et al. (2013) to calculate the extinction in the  $V$ -band ( $A_V$ ) across the system for all spaxels with  $\geq 3\sigma$  detections in both  $\text{H}\alpha$  and  $\text{H}\beta$  emission lines. To do this, we make the standard assumption of case B recombination for a typical gas of temperature of  $T = 10^4 \text{ K}$  and an electron number density of  $n_e = 10^2 \text{ cm}^{-3}$ , along with the reddening curve provided by Calzetti et al. (2000) and an extinction-to-reddening ratio of  $R_V = 4.05$ .

The resulting  $A_V$  distribution is shown in the left-hand panel of Figure 3.4, where we can see  $V$ -band extinction values in the range  $0.0 < A_V/\text{mag} < 2.0$ . This range is similar to the values

obtained for a selection of points along the shock region in SQ by Konstantopoulos et al. (2014) and Duarte Puertas et al. (2021), though we find greater extinction in the shock region than was inferred in the immediate environment of NGC 7318a/b by Rodríguez-Baras et al. (2014).

To study this in more detail, we have masked the extinction map by using the *JWST* MIRI images centered at 7.7, 10 and 15  $\mu\text{m}$ , as illustrated in the upper row of Figure 3.4. This was done by defining a colour scale using the  $A_V$  map, and introducing transparency in inverse proportion to the logarithm of the mid-IR flux density in each band. Prior to this, the *JWST* maps were convolved with a Gaussian kernel such that they have the same effective spatial resolution as the WEAVE data (the 1.67 arcsec seeing), and then log-stretched between the maximum likelihood value and the 90th percentile.

As explained in Section 3.2.3, the mid-IR bands trace the PAH complex,  $\text{H}_2$  emission, and hot dust continuum (in increasing order of wavelength, respectively). Weighting the  $A_V$  map in this manner with the shock region outline overlaid enables better comparison between the datasets, since it enables us to compare the apparent locations of the obscuring material (as measured by  $A_V$ ) with the distribution of the hot dust and the  $\text{H}_2$  gas (which is thought to form primarily on dust grains; e.g. Cazaux and Tielens, 2004).

Several effects are immediately obvious. Firstly, regions with the highest dust obscuration are clearly apparent in each of the top-right panels of Figure 3.4 along the innermost regions of the structure (i.e. those that are closest in projection to NGC 7318a/b) highlighting the presence of gas, dust and PAHs associated with the highest extinction areas, as we might expect. However, the shock itself appears anti-correlated with the highest extinction regions (and this is not a signal-to-noise ratio effect, since we show only those spaxels with  $\geq 3\sigma$  in both Balmer lines), as well as with the *JWST* dust images.

This may suggest that the shock has cleared the region of complex molecules and dust grains, either by sweeping them up as the shock propagates through the medium, or heating them to the point of sublimation (thought to happen in the region of  $\sim 1500$  K for carbonaceous grains; e.g. Granato and Danese, 1994). This is an appealing idea, since fast shocks are thought to be the primary means of dust destruction in galaxies (those resulting from supernovae; e.g. Jones et al., 1994; Zhu et al., 2019), although previous works (e.g. Guillard et al., 2009, who studied SQ) have noted that if the shock is weak enough, the dust can survive (and  $\text{H}_2$  can be formed on it). We shall return to this point in Section 3.5.4 when we determine the Mach number of the shocked region.

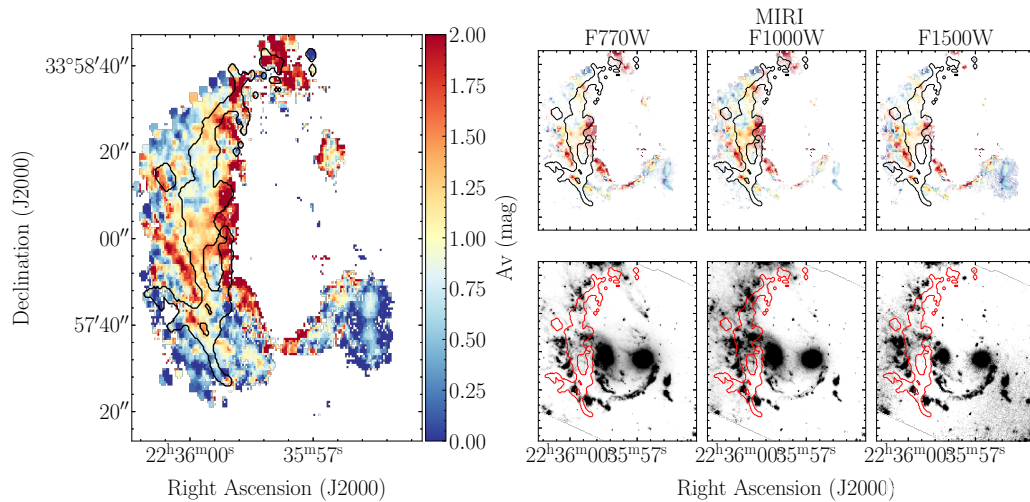


Figure 3.4: The dust properties of the shocked region surrounding NGC 7318a & b. The first panel presents the V-band extinction ( $A_V$ ) obtained with the Balmer decrement method, with the black contours indicating the dynamically-defined shock region as discussed in Section 3.4.1. The top row to the right presents the  $A_V$  measurements masked using the intensity from the *JWST* MIRI observations centred on 7.7, 10 and 15  $\mu\text{m}$  with the shock outline overlaid in black. The bottom row shows the original Mid-IR images (with the shock outline overlaid in red). The three columns are therefore used to compare the V-band extinction with the PAH complex,  $\text{H}_2$  emission and hot dust continuum, respectively.

Other interesting features are apparent: the  $\text{H}\text{II}$  region in the  $A_V$  map toward the North-West in the WEAVE field of view is virtually invisible (or at least significantly less extended) in the resolution-matched *JWST* maps, which reveal only the core; this wider Balmer line emitting region (which Figure 3.2 shows has a low velocity dispersion, but a velocity intermediate between those of the shock and the new intruder) does not appear to be strongly associated with extended mid-IR emission, suggesting that this region is either free from gas and dust or contains dust sufficiently cool that it is not detected at 15  $\mu\text{m}$ . This  $\text{H}\text{II}$  region is not detected in the 70  $\mu\text{m}$  *Spitzer* data from Xu et al. (2008), implying that the region contains  $< 4 \times 10^4 M_\odot$  of dust ( $5\sigma$  limit obtained assuming an isothermal dust model with  $T = 30\text{K}$  and emissivity index  $\beta = 1.82$  typical for galaxies; Smith et al., 2013).

### 3.4.3 Radio morphology of the system

The radio images obtained from LoTSS, VLA C-Array 1.7 GHz, and VLA D-Array 4.86 GHz are presented in Figure 3.5. We can see radio structures consistent with the findings of previous works (e.g., Aoki et al., 1999; Xu et al., 2003b; Xanthopoulos et al., 2004; Nikiel-Wroczyński et al., 2013), but in greater detail as a result of the increased resolution and sensitivity (including

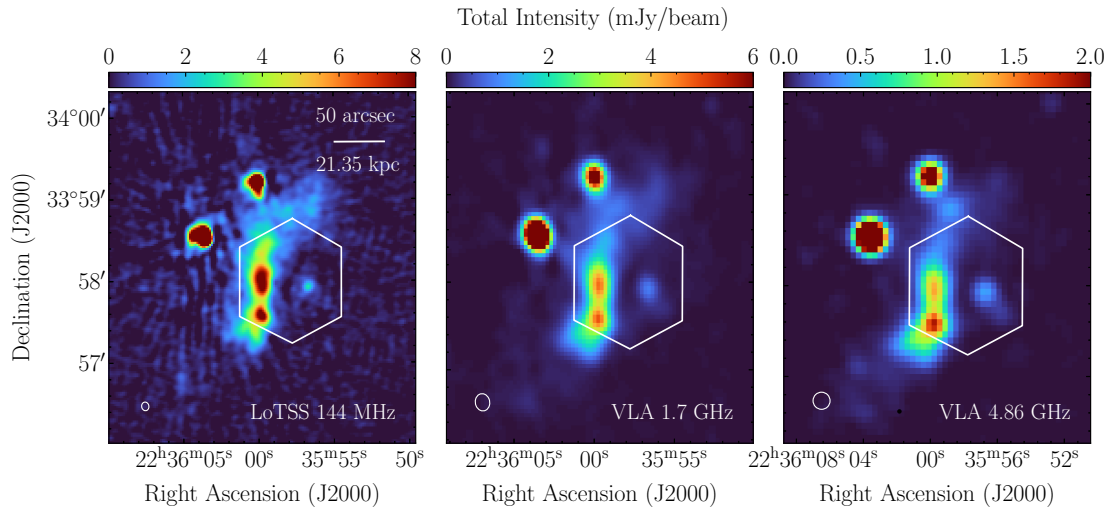


Figure 3.5: Radio observations of Stephan’s Quintet taken by LoTSS at 144 MHz (left panel) and VLA at 1.7 and 4.86 GHz (centre and right panels, taken in C- and D- array, respectively). In each panel, the white hexagon indicates the field covered by the WEAVE first-light LIFU observations. The flux scale for each image is indicated by the colour bar at the top of each panel, while the beam size is indicated by the ellipse visible in the lower left corner of each panel. Further details are available in Table 3.1.

to extended emission) of LoTSS relative to previously published data. The diffuse filament of radio continuum associated with the LSSR is prominent in all three figures and exhibits a ‘boomerang’-like shape, centred near  $(\alpha, \delta) \approx (22^{\text{h}} 36^{\text{m}} 00^{\text{s}}, +33^{\circ} 58' 36'')$ . The upper region extends for at least 25 kpc to the North-West, is fainter and more diffuse than the lower region which is associated with the LSSR, and spans approximately 60 kpc oriented North-South as far as  $(\alpha, \delta) \approx (22^{\text{h}} 36^{\text{m}} 00^{\text{s}}, +33^{\circ} 57' 33'')$  beyond the field of view of WEAVE (as indicated by the hexagon). Further to the south, we observe a rapid decrease in radio brightness and an increase in lateral spread, eventually terminating around the foreground source NGC 7320.

While NGC 7318b is not detected in any of our assembled radio frequency data, we identify three other compact structures in its vicinity. The first of these sources is NGC 7319, which is the brightest source visible in all three images. Xanthopoulos et al. (2004) have suggested that this is a Seyfert galaxy. The very high resolution VLA and MERLIN images (0.15 arcseconds) from Xanthopoulos et al. (2004) have shown an FRII-like structure for this source, potentially hinting at interaction of radio jets with the shocked plasma. However, the resolutions of the radio images chosen for this study are too low to allow us to identify such an FRII-like structure. The second of these sources is the compact radio source SQ-R situated to the north of the diffuse radio filament (as indicated in Figure 3.1), centred near  $(\alpha, \delta) \approx (22^{\text{h}} 36^{\text{m}} 00^{\text{s}}, +33^{\circ} 59' 12'')$ . It is spatially offset from SQ-A (the starburst feature labelled in Figure 3.1) by 26 arcseconds (11 kpc) and lacks optical and IR counterparts, meaning that we cannot determine its relation to the broader

structure. While we are unable to discern the presence of SQ-A itself at 144 MHz given the roughly uniform surface brightness of the extended emission that surrounds it (in projection, at least), it is clearly identifiable as a separate brightness peak in the 4.86 GHz data. This indicates that SQ-A has a spectral index that differs from that of the extended emission. The third source is the galaxy NGC 7318a. Despite being significantly detected in all three images, the radio emission from NGC 7318a is faint in comparison to the other compact sources in the region.

### 3.5 Shock properties

In this section, we now focus on the properties of the shock region, as defined in Section 3.4.1, such that we consider all spaxels where  $H\alpha$  FWHM  $> 700 \text{ km s}^{-1}$  (which corresponds approximately to velocity dispersion  $\sigma \gtrsim 300 \text{ km s}^{-1}$ ).

#### 3.5.1 Thermodynamics

To study the shock properties, we use the  $[\text{O III}]\lambda\lambda (4959+5007)/\lambda 4363\text{\AA}$  line set and  $[\text{S II}]\lambda\lambda 6717/6731\text{\AA}$  doublet as electron temperature ( $T_e$ ) and number density diagnostics ( $n_e$ ), respectively (Osterbrock and Ferland 2006). The  $[\text{O III}] (5007+4959)/4363\text{\AA}$  line intensity ratio serves as an effective temperature diagnostic because the lines originate from energy levels with significantly different excitation energies such that the relative strength between them is strongly dependent on  $T_e$ . For evaluating the number density, on the other hand, the  $[\text{S II}] 6717/6731\text{\AA}$  line ratio is used as the lines arise from energy levels with similar excitation energies, making their relative strength primarily influenced by collision rates and thus the number density.

Since the  $[\text{O III}]\lambda 4364\text{\AA}$  line is not detected in any individual spaxel, we use our dynamical definition of the shock region to create a representative spectrum of this region. This was done by summing all spaxels with FWHM  $> 700 \text{ km s}^{-1}$  in the rest-frame by using the weighted average velocity of  $H\alpha$  to account for the complex velocity structure shown in Figure 3.3. The result is shown in Figure 3.6, where each of the six panels shows regions around the locations of emission lines of interest, with the stacked spectrum shown as the grey line with shaded  $1\sigma$  uncertainties overlaid. The best-fit model obtained from the MCMC fitting (using a method similar to that described in Section 3.4.1, however also modelling additional species;  $[\text{O III}]\lambda 4363\text{\AA}$ , the  $[\text{S II}]$  doublet, and  $H\gamma$  due to its proximity to  $[\text{O III}]\lambda 4363\text{\AA}$ ) is overlaid in red. The complicated broad velocity structure is apparent in each emission line complex, and the fluxes measured in each

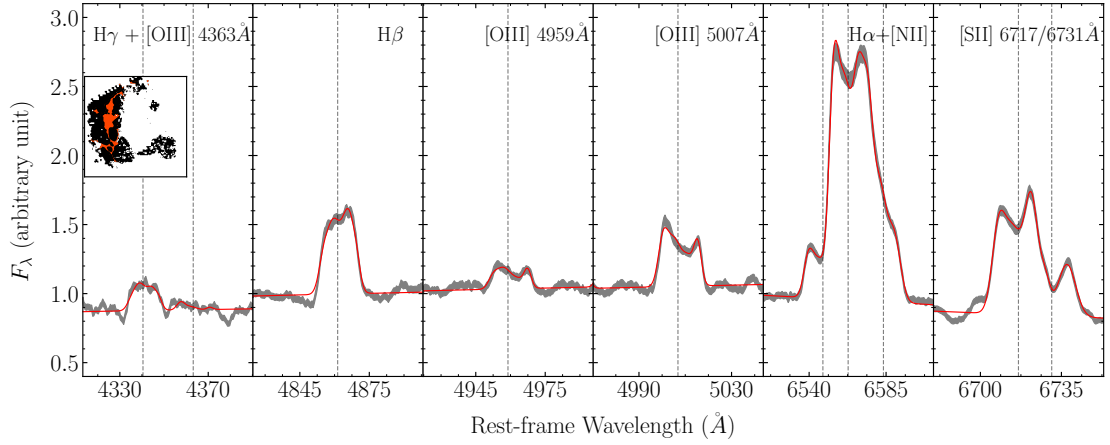


Figure 3.6: Key wavelength ranges of the stacked spectrum of the shock region (as defined by the  $\text{FWHM} > 700 \text{ km s}^{-1}$  spaxels, shown as red in the embedded plot in the first panel). The different panels show the emission line complexes of interest as indicated in the upper right corner, where the data is represented in grey lines with shaded region enclosing the  $1\sigma$  uncertainties, and the best-fit model overlaid in red. The black dotted lines denote the wavelength for each emission line in a given complex. The fluxes measured in each line species are detailed in Table 3.2.

line – integrated over the four individual Gaussian components for each species – are detailed in Table 3.2.

Despite combining the 2,485 spaxels in the shock region, we are unable to detect significant  $[\text{O III}]\lambda 4363\text{\AA}$  flux. Indeed, visual inspection of this region of the stack shows continuum structures in the vicinity of the line with amplitude larger than the local RMS. Our simple continuum model is no longer sufficient, however the situation is not significantly improved when we try replacing it with Bruzual and Charlot (2003) stellar population models. A better estimate of the  $[\text{O III}]\lambda 4363\text{\AA}$  flux (if there is any) requires a more sophisticated analysis which models the stellar population on an even footing with the nebular emission; this is beyond the scope of this thesis.

Nevertheless, to calculate  $T_e$  and  $n_e$ , we have used the empirical relations from Proxauf et al. (2014). Specifically:

$$T_e = 5294(r - 0.848)^{-1} + 19047 - 7769r + 944r^2, \quad (3.2)$$

Table 3.2: Emission line flux measurements obtained by averaging over the FWHM  $> 700 \text{ km s}^{-1}$  shock region. The lines are listed in rest-frame wavelength order, with fluxes and uncertainties derived from the MCMC chains, except for [OIII]  $\lambda 4363$  for which we quote a  $3\sigma$  upper limit based on the uncertainty of the neighbouring H $\gamma$  line.

Line	Flux / $10^{-13} \text{ erg cm}^{-2} \text{ s}^{-1}$
H $\gamma$	$1.28 \pm 0.06$
[OIII] $\lambda 4363$	0.18 ( $3\sigma$ )
H $\beta$	$4.38 \pm 0.13$
[OIII] $\lambda 4959$	$1.18 \pm 0.07$
[OIII] $\lambda 5007$	$3.14 \pm 0.11$
[NII] $\lambda 6548$	$2.05 \pm 0.08$
H $\alpha$	$17.19 \pm 0.44$
[NII] $\lambda 6584$	$8.34 \pm 0.26$
[SII] $\lambda 6717$	$5.52 \pm 0.43$
[SII] $\lambda 6731$	$3.72 \pm 0.32$

where  $r \equiv \log_{10} \left( \frac{F_{4959} + F_{5007}}{F_{4363}} \right)$ , and:

$$\begin{aligned} \log_{10}(n_e [\text{cm}^{-3}]) = & 0.0543 \tan(-3.0553R + 2.8506) \\ & + 6.98 - 10.6905R \\ & + 9.9186R^2 - 3.5442R^3, \end{aligned} \quad (3.3)$$

where  $R \equiv \left( \frac{F_{6717}}{F_{6731}} \right)$ .<sup>4</sup>

Since [OIII] $\lambda 4363\text{\AA}$  is undetected, to estimate  $T_e$  we generate 1000 Monte Carlo realisations of the flux estimates from Table 3.2 in which each flux is modelled as a normal distribution with mean equal to the measured flux, and standard deviation equal to the measured uncertainty. In the absence of a measurement for [OIII] $\lambda 4363\text{\AA}$ , we assume a mean of zero, and standard deviation equal to that measured for the neighbouring (albeit brighter) H $\gamma$  line, along with an additional requirement that the measured flux must be positive. Doing this, we obtain an upper limit of  $T_e < 14,000 \text{ K}$  at 95 per cent confidence (estimated on the basis of the 95th percentile of the  $T_e$  distribution resulting from the Monte Carlo simulations).

For the number density we first calculate the line ratio between the total [SII]  $\lambda 6717$  and [SII]  $\lambda 6731$ , for which we obtain  $R = 1.48 \pm 0.17$ . This value is on the very upper bound of values for which equation 3.3 applies, suggesting that the density is low. Performing a similar Monte Carlo

<sup>4</sup>Equation 3.3 holds for an electron temperature of  $T_e = 10,000 \text{ K}$ , however, as demonstrated by Proxauf et al. (2014) the number density is not strongly dependent on  $T_e$ .

analysis to that used for the  $T_e$  estimation above, we obtain an upper limit on the number density such that  $n_e < 140 \text{ cm}^{-3}$  (at 95 per cent confidence).

It is tempting to compare the product of the number density and temperature we have estimated for the shock with the values obtained from the X-ray analysis in O’Sullivan et al. (2009), however due to the upper limit we have obtained on the number density in the shock we are unable to determine whether the shock is in approximate pressure equilibrium with the surrounding plasma, or otherwise.

### 3.5.2 Comparing WEAVE data with theoretical shock models

To infer additional properties of the shock, we use the line ratios  $[\text{O III}] \lambda 5007\text{\AA}/\text{H}\beta$  and  $[\text{N II}] \lambda 6583\text{\AA}/\text{H}\alpha$  (i.e the BPT diagram; Baldwin et al. 1981) for all spaxels with FWHM  $> 700 \text{ km s}^{-1}$  (the shock region defined in Section 3.4.1). This diagnostic diagram was previously described in more detail, but to summarise it is used to classify sources based on their primary excitation mechanism, often associated with photoionization. In this classification scheme, sources are typically categorized as star-forming (SF) if they fall below the demarcation line provided by Kauffmann et al. (2003), and as AGN if they lie above the maximum starburst line defined in Kewley et al. (2006). The region in between these lines is referred to as composite, indicating the presence of both mechanisms. However, in the context of this study, where we are dealing with shock-excited gas, we are employing the BPT diagram to compare our observations with theoretical models, and thus obtain additional properties of the shock, such as oxygen abundance ( $Z$ ) and magnetic field strengths ( $B$ ). To do this, we consider the fast shock models without a precursor from the MAPPINGS III library (Allen et al., 2008) for a pre-shock density of  $n = 1 \text{ cm}^{-2}$ , shock velocities between  $300 \text{ km s}^{-1}$  and  $1000 \text{ km s}^{-1}$ , and magnetic fields between  $0.5$  and  $10 \mu\text{G}$ . The choice of the shock velocities is motivated by the observed velocity dispersion from Figure 3.3. We do not include shock models with a precursors as the tracks do not occupy the same parameter space as the observed data.

The results are shown in Figure 3.7, where we have overlaid four shock models, each characterised by a different oxygen abundance, which have been normalized relative to the solar value using Table 1 from Allen et al. (2008). In addition, we have included the two demarcation lines (as solid and dotted lines for the Kewley et al. 2006 and Kauffmann et al. 2003 criteria, respectively) for reference. We can see that the spaxels within the shock reside between the models with  $0.26$  and  $0.32Z_{\odot}$ . This metallicity range is in agreement with the value found for the hot X-ray

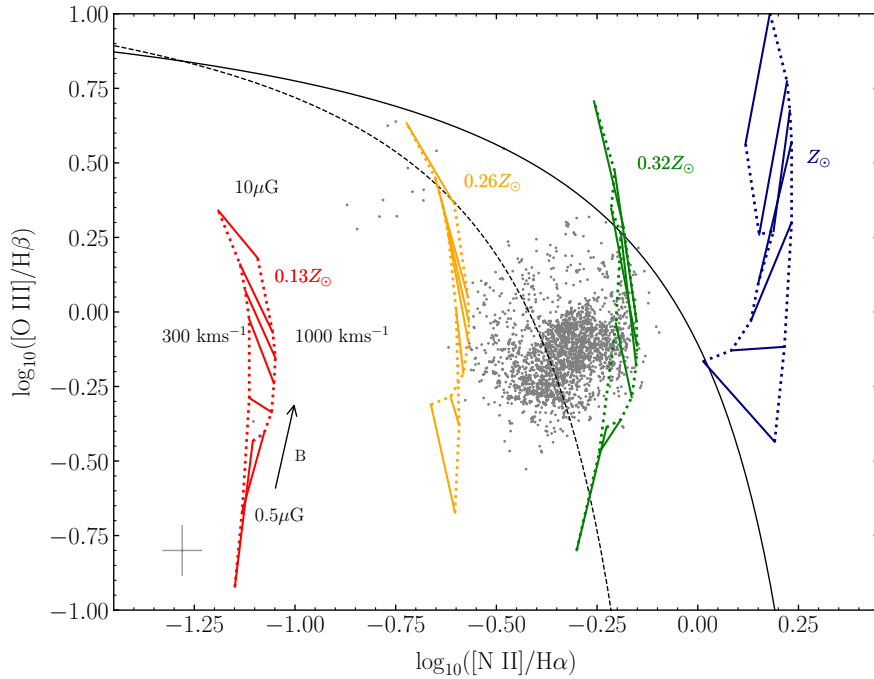


Figure 3.7: The  $[\text{O III}] \lambda 5007 \text{ \AA}/\text{H}\beta$  and  $[\text{N II}] \lambda 6583 \text{ \AA}/\text{H}\alpha$  emission line ratios for all spaxels with  $\text{FWHM} > 700 \text{ km s}^{-1}$ , overlaid with shock models with different metallicities from the MAPPINGS III library. The black solid and dashed lines are the demarcation lines defined by Kauffmann et al. (2003) and Kewley et al. (2006). The coloured dotted lines represent constant tracks of shock velocity, whereas the solid lines show constant tracks of magnetic field strengths (B).

plasma ( $\sim 0.3Z_{\odot}$ ; O’Sullivan et al. 2009), which indicates a common origin for the shock and the surrounding medium. Furthermore, our data points appear to be consistent with the magnetic field tracks for  $1\mu\text{G} < B < 5\mu\text{G}$ . This suggests the presence of internal shocks, as magnitudes of order  $\sim \mu\text{G}$  are typically associated with turbulent flow motions within the intra-cluster medium (ICM), as demonstrated in previous studies (e.g., Ryu et al., 2008; Hong et al., 2015). Such shocks occur within a given system, where the gas has already been heated up by previous interactions, in agreement with the dynamical scenario proposed by Moles et al. (1997).

### 3.5.3 The plasma in the shock

The spectra of sources at radio frequencies are often modelled as a power law in frequency, such that  $S_{\nu} \propto \nu^{\alpha}$ , with  $\alpha$  representing the spectral index. This can be calculated for any two observations with flux densities  $S_{\nu_1}$  and  $S_{\nu_2}$  at frequencies  $\nu_1$  and  $\nu_2$  such that:

$$\alpha = \frac{\log_{10} S_{\nu_1} - \log_{10} S_{\nu_2}}{\log_{10} \nu_1 - \log_{10} \nu_2}. \quad (3.4)$$

Models of the evolving radio frequency spectra for synchrotron emission (e.g. Harwood et al., 2017) account for the fact that the spectral index observed between any two frequencies evolves with time. This happens because higher energy electrons lose energy faster than their lower energy counterparts, causing radio sources to fade more quickly at higher frequencies. As a result, older radio sources exhibit an increase in spectral curvature (i.e. the difference between the spectral index at high- and low-frequencies; see e.g. Calistro Rivera et al. 2017 for a discussion), departing from the spectral index that would have been observed at  $t = 0$  (the so-called ‘injection index’). Therefore, as low frequencies age more slowly, the low frequency spectral index can be used as a good proxy for the injection index which otherwise has to be assumed from models. In this context, measuring the spectral curvature observed across a wide range of radio frequency observations can provide useful constraints on the physical conditions of the plasma, for example within the shock in SQ.

To this end, we have generated two spectral index maps by combining the new LoTSS data at 144 MHz with the VLA data at 1.7 GHz to calculate  $\alpha_{1.7}^{144}$  (our best estimate of the injection index in the SQ shock), and the VLA 1.7 and 4.86 GHz data to derive the high frequency spectral index;  $\alpha_{4.86}^{1.7}$ . To achieve this, we have convolved all three images to a common beam size of  $14 \times 14$  arcsec<sup>2</sup> and have ensured that they are positionally coincident. The spectral indices as a function of position around SQ were then calculated using the AIPS task COMB, where pixels with intensity values below  $3\sigma$  were masked to avoid low signal-to-noise regions.

The results for  $\alpha_{\text{LOW}} \equiv \alpha_{1.7}^{144}$  and  $\alpha_{\text{HIGH}} \equiv \alpha_{4.86}^{1.7}$  are shown in the top and middle panels of Figure 3.8, respectively, with the spectral index at each location and between each pair of frequencies indicated relative to the colour bar to the right. The WEAVE field of view is overlaid as the dark red hexagon, and 144 MHz intensity is indicated as dashed grey contours, while the approximate location of the optical sources in the image have been indicated by the thin black outlines, as taken from *JWST* NIRC*am*’s composite image. In each panel, there is an inset focused on the region that has been observed by WEAVE, and which has the dynamically-defined shock region overlaid as the thick black contours.

The fact that the magnitude of high-frequency indices are generally larger than the low frequency indices is immediately apparent, and consistent with expectations. At low frequencies,  $\alpha_{\text{LOW}}$  varies from  $-0.76 \pm 0.01$  at the southern extent of the shock to  $-0.95 \pm 0.01$  at the northern extent, with an integrated value of  $-0.85 \pm 0.02$  if we sum flux densities across the entire dynamically-defined shock structure. On the other hand, the high frequency indices,  $\alpha_{\text{HIGH}}$ ,

vary from  $-1.11 \pm 0.01$  in the southern end of the shock to  $-1.35 \pm 0.02$  in the northern tip, with an integrated spectral index of  $-1.23 \pm 0.02$  across the entire shock region. These spectral index values are consistent with radio relics (e.g., Botteon et al., 2020, and references therein), giant synchrotron sources that were generated a significant time ago by shocks crossing their intra-cluster medium (e.g. Feretti et al. 2012).

To better put the spectral index information in context, we introduce the spectral-curvature parameter (SCP; Sohn et al., 2003), a proxy for the age of the plasma where higher SCP values indicate older regions, such that:

$$\text{SCP} = \frac{\alpha_{\text{HIGH}} - \alpha_{\text{LOW}}}{\alpha_{\text{HIGH}} + \alpha_{\text{LOW}}}. \quad (3.5)$$

The variation in SCP is presented in the bottom panel of Figure 3.8. We see that the SCP across the shock region is very low and uniform ( $\sim 0.2$ ), which implies the presence of plasma of similar age across the extent of the dynamically-defined shock region. Furthermore, the spectral curvature increases as we move away from the shock, with the red regions indicating older plasma with curved spectrum within which the shock is embedded. Together, these factors offer support for our decision to define the shock region based on the nebular emission line fitting.

Several regions with lower SCP are also apparent, for example the core of NGC 7318a (the central galaxy to the west of the new intruder), NGC 7319 (toward the north east of Figure 3.8) as well as SQ-R and SQ-A, suggesting the presence of younger and more energetic plasma with a flatter spectrum, consistent with ongoing particle acceleration due to either star-formation or AGN activity at these locations.

### 3.5.4 Mach number

To obtain the Mach number ( $\mathcal{M}$ ) of the shock (defined as the ratio of the shock velocity to the sound speed in the medium), we assume a fully ionised gas, mainly composed of hydrogen, such that the sound speed is given by:

$$c_s = \sqrt{\gamma_g k_B T / \mu m_H}. \quad (3.6)$$

Here  $\gamma_g = 5/3$  is the adiabatic index for monatomic gas,  $k_B$  is the Boltzmann constant,  $\mu \approx 0.5$  is the mean molecular weight,  $m_H$  is the mass of a hydrogen atom and  $T = 0.6$  keV is the temperature of the medium through which the shock is propagating (from O’Sullivan et al., 2009). By

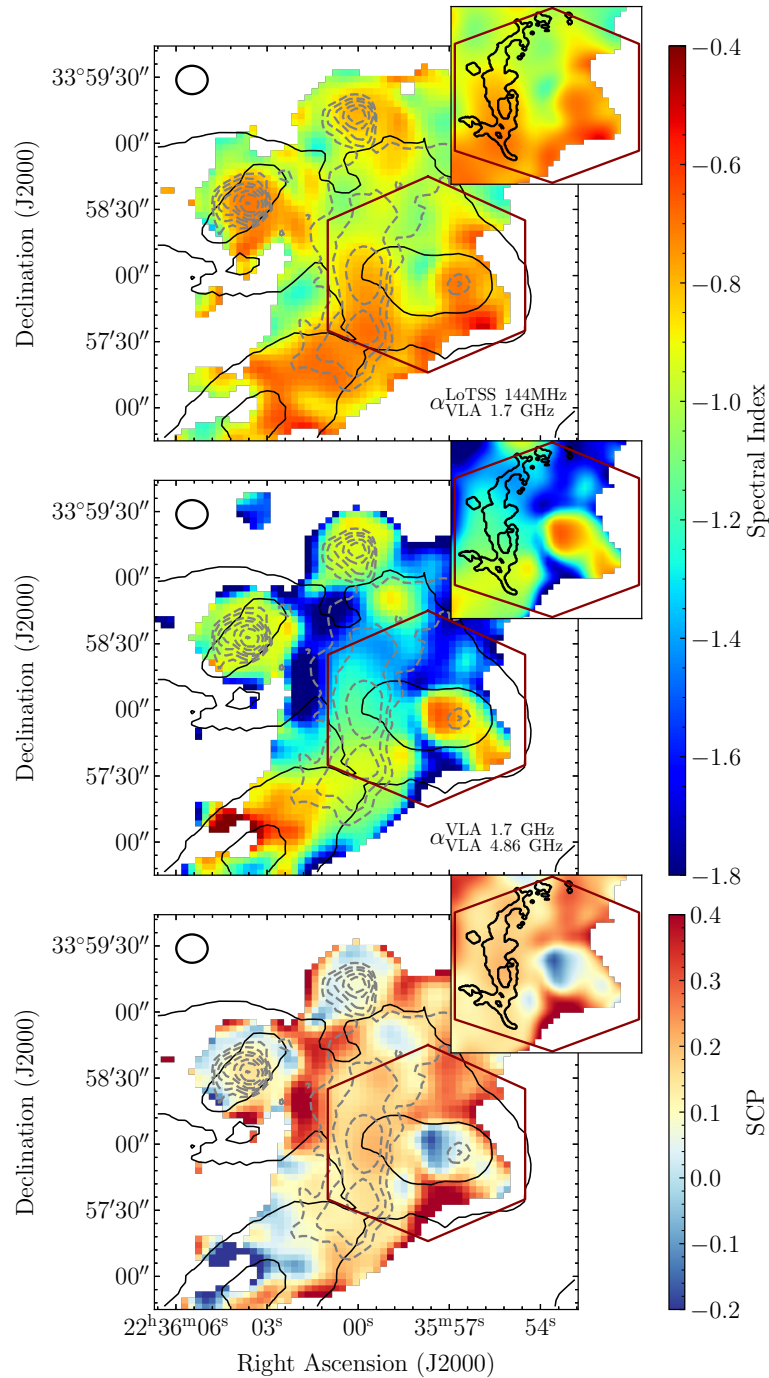


Figure 3.8: Spectral index image obtained using the LoTSS 144 MHz and VLA C-Array 1.7 GHz images (top panel), and VLA C-Array 1.7 GHz and VLA D-Array 4.86 GHz images (middle panel), along with the variation of the SCP (bottom panel) across SQ. For context, we have added LoTSS 144 MHz and *JWST* NIRCcam total intensity contours in gray dashed and solid thin black curves, respectively. The zoomed-in snapshots show the spectral indices and curvature parameter in the shocked region (solid thick black contours) inside the WEAVE field of view as denoted by the red hexagon. The beam size of the radio frequency images (which have been convolved to be consistent across all frequencies) is indicated by the ellipse in the top left corner.

comparing this value to the relative velocity of the shock ( $v$ ), which we define as the difference between the weighted average velocity of  $H\alpha$  derived from the summed spectrum of the shock region ( $v_{H\alpha} = 6268 \text{ km s}^{-1}$ ) and the relative velocity of the new intruder ( $v_{\text{NGC7318b}} = 5774 \text{ km s}^{-1}$ ; Konstantopoulos et al. 2014), we determined a Mach number of  $\mathcal{M} = v/c_s = 1.12 \pm 0.28$ . However, as we are working with radial velocities, and we are uncertain of what the actual geometry of the system is, we treat this value as a lower limit. Previous studies (e.g. Trinchieri et al. 2003; O’Sullivan et al. 2009) have suggested that the shock may be oriented at  $\sim 30^\circ$ , in which case the Mach number would be  $\mathcal{M} \sim 2.2$ .

These Mach number estimates indicate that the shock in SQ is relatively weak, and it is therefore possible that the dust has survived the collision (a possibility that we discussed in Section 3.4.2). The Mach numbers obtained (like the magnetic field strengths, discussed in Section 3.5.2) are consistent with literature values for internal shocks associated with turbulent flow motions in the ICM (e.g., Ryu et al., 2008; Vazza et al., 2012; Brunetti and Jones, 2014), and are far smaller than those typically associated with accretion onto clusters of galaxies (e.g. Skillman et al., 2008). Some works have suggested that shocks with Mach numbers this low are unlikely to be able to accelerate particles (e.g. Vink and Yamazaki 2014). Instead, they are more likely to compress the medium, a possibility we discuss in section 3.5.5.

### 3.5.5 Adiabatic Compression

In the previous section, we found that the Mach number of the shock ( $\mathcal{M} \sim 2.2$ ) is low, suggesting that the collision of NGC 7318b has generated a weak shock. Such shocks are inefficient at accelerating the electrons up to relativistic energies (Enßlin and Gopal-Krishna, 2001; Kang et al., 2007). Instead, the principal driver of the increase in the synchrotron emission associated with the shock is believed to be the adiabatic compression of the pre-existing electron population (Enßlin and Gopal-Krishna, 2001; Enßlin and Brüggen, 2002; Markevitch et al., 2005; Markevitch and Vikhlinin, 2007b; Vink and Yamazaki, 2014). Works led by Enßlin and Gopal-Krishna (2001), Markevitch et al. (2005), Cawthorne (2006), and Colafrancesco et al. (2017) have demonstrated that such an event leads to a boost in the radio emission. To test this scenario, we follow Colafrancesco et al. (2017) and calculate the boosting factor ( $A$ ) at 1.4 GHz as:

$$A \sim C^{(-s+2)/3} \times [C^{2/3}]^{1-\alpha} \times C^{-1}. \quad (3.7)$$

Here  $C$  is the compression ratio of the gas caused by the shock,  $\alpha$  is the radio spectral index (which we take to be  $\alpha \equiv \alpha_{\text{LOW}} = -0.85$ ) and  $s$  is the momentum spectral index, given by  $s = 2\alpha - 1$  (e.g. Longair 2011). The compression ratio is related to  $\mathcal{M}$  and the adiabatic index ( $\gamma_g$ ) by the following expression (e.g. Markevitch and Vikhlinin 2007b, van Weeren et al. 2017):

$$\mathcal{M} = \left[ \frac{2C}{\gamma_g + 1 - C(\gamma_g - 1)} \right]^2 \quad (3.8)$$

By taking  $\gamma_g = 5/3$  (monatomic ideal gas) and  $\gamma_g = 4/3$  (relativistic gas) as the limiting cases for the plasma, we find that  $C$  ranges between 2.5 and 3.2, leading to a boosting factor of  $A \sim 5.2 - 8.1$ . In the absence of 1.4 GHz radio flux measurements, we consider the 1.7 GHz flux density outside the dynamically defined shock region (Section 3.4.1) and inside the boundary to represent the flux density before and after the shock-induced compression. Comparing these values, we find that the observed boost in 1.7 GHz flux density is  $\sim 10$ . This agreement demonstrates that the increase in synchrotron emission can be explained by considering a scenario in which a weak shock adiabatically compresses the existing radio plasma.

### 3.5.6 Magnetic field strength and shock lifetime

Assuming equipartition of energy between the relativistic radiating particles and the magnetic field in which they live, we can establish further constraints on the conditions within the shock region. To do this we use the python package `PySYNCH` (Hardcastle et al., 1998)<sup>5</sup> for calculating the equipartition parameters, which implements the formulae proposed by Myers and Spangler (1985) and later revised by Beck and Krause (2005). Following Hardcastle et al. (1998), we assume that the electron energy distribution follows a power law in Lorentz factor ( $\gamma$ ) between  $\gamma_{\text{min}} = 1$  and  $\gamma_{\text{max}} = 1 \times 10^5$ . The exponent  $p$  is related to the injection index of the synchrotron radio spectra  $\alpha_{\text{inj}}$  as  $p = 2\alpha_{\text{inj}} - 1$ . By considering the lowest measured radio spectral index to represent the injection index, we obtain  $p = -2.7$ . We model the shock region as an isotropic cylinder with a radius of 5 kpc and a height of 30 kpc. The volume filling factor of the radio plasma in the shock is assumed to be unity,  $\sigma = 1$ , and the kinetic energy density of protons is assumed to be negligible when compared to that of the electrons ( $\kappa = 0$ ). We use 144 MHz as the reference frequency in `PySYNCH` as it is the least affected by spectral ageing, and by using the integrated flux density of the shock region ( $= 151$  mJy), we calculate the equipartition magnetic field strength of  $B_{\text{eq}} = 7 \mu\text{G}$ . This estimate is in good agreement with the ranges found from the

<sup>5</sup><https://github.com/mhardcastle/pysynch>

shock models in Section 3.5.2, demonstrating once more the good synergy between the radio and IFU observations.

Additionally, we use the model proposed by van der Laan and Perola (1969) to put an upper limit on the radio emission lifetimes of the relativistic electrons. We assume that the initial interaction of the shock front and the SQ system supplied the relativistic electrons with sufficient energy (the “generation” phase) for a subsequent long-term radio emission phase (the “remnant” phase). During the remnant phase, the energy supply is switched off and the electrons age, undergoing synchrotron and inverse Compton losses (the latter due to interaction with the cosmic microwave background photons). The duration of this remnant phase at frequency  $\nu$  can be calculated using Equation 3.9:

$$\tau \approx 2.6 \times 10^4 \frac{B_{\text{eq}}^{1/2}}{B_{\text{eq}}^2 + B_{\text{R}}^2} [(1+z)\nu]^{-1/2} \text{ yr}, \quad (3.9)$$

where  $B_{\text{R}} = 4(1+z)^2 \mu\text{G}$  is the equivalent magnetic field of the cosmic microwave background (CMB). The tightest constraints on the electron lifetime are provided by the highest-frequency observations (since those frequencies fade the fastest); since the shock is still clearly visible at 4.86 GHz, this analysis suggests that the age of the shock is  $\tau \approx 12 \pm 2 \text{ Myr}$ , similar to our estimate of the dynamical crossing time for NGC 7318b ( $\sim 20 \text{ Myr}$  assuming the same geometry as above, and a relative velocity of  $494 \text{ km s}^{-1}$  – see Section 3.5.4). Since these numbers are comparable, we suggest that the collision is the likely cause of the shock, but it is not possible for us to determine whether the compression phase of the interaction is still under way.

### 3.6 Summary

In this chapter, we have combined IFU observations from the first light data of the new WEAVE facility with low-frequency radio observations from the LOFAR Two-metre Sky Survey to study the large-scale shock front in Stephan’s Quintet. The capabilities of the large IFU focal-plane mode of WEAVE have allowed us to perform robust spectral line fitting of the system. With models involving up to four velocity components, we have been able to deblend prominent emission lines and study the detailed kinematics of SQ. These results have enabled us to dynamically define the shock region based on a velocity dispersion  $> 300 \text{ km s}^{-1}$  and estimate its physical properties by combining the WEAVE first light data cube with the additional auxiliary information.

Our findings can be summarised as follows:

1. The shock region contains low density ( $n_e < 140 \text{ cm}^{-3}$ ) gas at a low temperature ( $T_e < 14,000 \text{ K}$ ).
2. The metallicity of the shock region obtained by comparing the  $[\text{O III}] \lambda 5007\text{\AA}/\text{H}\beta$  and  $[\text{N II}] \lambda 6583\text{\AA}/\text{H}\alpha$  emission line ratios with the fast shock models from Allen et al. (2008) suggests a common origin with the hot X-ray plasma.
3. The 144 MHz LOFAR observations combined with 1.7 and 4.86 GHz VLA observations show that the shock is consistent with containing a homogeneous relativistic particle population with age  $\lesssim 12 \text{ Myr}$ , similar to the crossing time of the new intruder. We conclude that the passage of NGC 7318b is the likely cause of the  $\sim 45 \text{ kpc}$  shock.
4. The kinematics obtained with the IFU allowed us to estimate the Mach number in the shock to be  $\mathcal{M} \sim 2.2$ . This indicates that the shock is relatively weak (e.g. in comparison to the shocks typically found in galaxy clusters), suggesting that it is possible for dust to have survived the collision as further demonstrated by comparing the extinction distribution seen with WEAVE to the molecular gas and hot dust observed with *JWST*.
5. Assuming adiabatic compression (Enßlin and Gopal-Krishna, 2001), we find that the theoretical boost in radio emission (a factor of  $\sim 5.2 - 8.1$ ) is compatible with the observed one. Combining this information with the spectral curvature parameter, we propose that the shock has compressed a pre-existing radio-emitting plasma with a curved radio spectrum, likely the product of previous interactions.

Overall – in addition to the new understanding of SQ, this work highlights the sort of studies that are now becoming possible by combining data from the newly-commissioned WEAVE facility (Dalton et al., 2012) with exciting new and archival data multi-wavelength datasets. This approach is central to many of the WEAVE Surveys, which are described by Jin et al. (2023) and intend to spend an initial period of five years pursuing a range of exciting science (both galactic and extragalactic). The ability of WEAVE observations to unlock the huge diagnostic power of the LOFAR observatory forms a key motivation for the WEAVE-LOFAR survey (Smith et al., 2016) which will obtain  $> 1$  million optical spectra of 144 MHz sources identified in LoTSS (e.g. Shimwell et al., 2022; Hardcastle et al., 2023).

## Chapter 4

# Radio Source Classifications in ELAIS-N1

### 4.1 Introduction

Understanding the co-evolution of galaxies and their supermassive black holes (SMBH;  $M_{\text{BH}} \sim 10^6\text{--}10^8 M_{\odot}$ ) is one of the main drivers of modern astronomy, fueling the development of ground-based and space observatories. Over the past three decades, an avalanche of multi-wavelength data has shed new light on the intricate relation between them: the mass of the SMBH correlates with a number of host galaxy properties (e.g. Ferrarese and Ford 2005; Bernardi et al. 2007; Graham 2016). The evolution of the cosmic star formation (CSFH) history mirrors that of the black hole accretion history (BHAH), where both reach a peak of activity at  $z \sim 2$ , following a decline to the present day (e.g. Boyle and Terlevich 1998; Hopkins et al. 2007; Madau and Dickinson 2014; Cochrane et al. 2023). The feedback from active galactic nuclei (AGN) influences star-formation by either triggering (‘positive’ AGN feedback; e.g. Kalfountzou et al. 2012; Silk 2013; Maiolino et al. 2017) or suppressing it (‘negative’ AGN feedback; e.g. Heckman and Best 2014; Harrison 2017). However, much remains unclear.

The radio band plays a crucial role in such studies, as it can provide a clear view into the dust-obscured phase of activity in the Universe, where it is believed that most of the star formation and AGN activity take place (e.g. Madau and Dickinson 2014; Hickox and Alexander 2018; Zavala et al. 2021). As discussed in section 1.4.1, the primary source of extragalactic radio emission at low frequencies ( $\lesssim$  few GHz) is synchrotron radiation, which is a result of relativistic

particles having been accelerated by either supernova, the end products of short-lived massive stars (e.g. Condon 1992), or jets (e.g. Begelman et al. 1984). This has led to the development of next-generation radio interferometers (e.g. the Low Frequency Array; van Haarlem et al. 2013, MeerKAT; Jonas and MeerKAT Team 2016), which continue to improve their sensitivity and angular resolution, thus allowing us to create large statistical samples of star-forming galaxies (SFGs) and AGN out to high redshifts. At present, the second data release of the LOFAR Two-metre Sky Survey (LoTSS DR2) wide area presents the largest radio catalogue containing 4,396,228 sources across an area of 5,700 deg<sup>2</sup> (see Shimwell et al. 2022 for further details).

Studying these two sources of radio emission also involves investigating the various types of AGN. As discussed in section 1.2.1, AGN can be classified into two fundamental modes, depending on the efficiency of matter accreted onto the SMBH (e.g. see also reviews by Heckman and Best 2014; Hardcastle and Croston 2020). Radiatively-efficient AGN ( $L/L_{\text{Edd}} \gtrsim 0.01$ ) produce electromagnetic radiation from efficiently converting potential energy from cold, accreted gas. This emission ionizes the surrounding gas, resulting in broad permitted and higher excitation forbidden lines compared to those produced by star-forming processes (e.g. Kauffmann et al. 2003; Ho 2008; Best and Heckman 2012; Hardcastle and Croston 2020). This type of AGN is further subdivided into a subset of sources which possess powerful twin radio jets, referred to as high-excitation radio galaxies (HERG), and those that lack (or are associated with weaker) radio jets (e.g., Jarvis et al. 2019; Gürkan et al. 2019; Macfarlane et al. 2021; Morabito et al. 2022), called ‘radio-quiet’ AGN (RQ AGN). Radiatively-inefficient AGN ( $L/L_{\text{Edd}} \lesssim 0.01$ ) produce very little radiation, but are characterized by the presence of two-sided, tightly focused jets of charged particles. Such sources are also referred to as low-excitation radio galaxies (LERGs), as they do not exhibit strong forbidden lines, or any indications of AGN activity at other wavelengths (e.g. Kondapally et al. 2021; Hardcastle and Croston 2020).

Considerable efforts have been made in differentiating between these types of sources (e.g. Best and Heckman 2012; Smolčić et al. 2017; Sabater et al. 2019; Whittam et al. 2022; Best et al. 2023; Das et al. *subm.*; Drake et al. *in prep.*). Recently, Best et al. (2023; hereafter B23) made use of the high-quality radio observations and the available multi-wavelength data spanning from the ultraviolet to far-infrared in the LoTSS Deep Fields (Tasse et al. 2021; Sabater et al. 2021) to classify about 80,000 radio sources, detected at greater depth than the LoTSS wide tier (at a sensitivity of  $\sim 20 - 35 \mu\text{Jy}$  compared to  $\sim 100 \mu\text{Jy}$ ). Employing a combination of four SED fitting codes, they were able to categorise up to 95 per cent as either SFGs, RQ AGN, LERGs, and HERGs. However, using four SED-fitting codes is time-consuming and necessitates substantial

efforts in maintaining consistency and accuracy across the different results. To address these issues, Das et al. *subm.* (hereafter D24) used the SED fitting code `PROSPECTOR` to revisit the classification of radio sources in the European Large Area Infrared Space Observatory Survey-North 1 (ELAIS-N1). They showed that they can achieve comparable results with a single SED fitting code, which would not only expedite efforts in classifying larger statistical samples in future studies, but also simplify the classification process by reducing the complexity and resources required. Nonetheless, relying solely on photometry may not always produce reliable and secure classifications as with SED-fitting you are essentially comparing with models that may not always be applicable (the ‘gold-standard’ involves optical spectroscopy; e.g. Kauffmann et al. 2003; Kewley et al. 2006; Cid Fernandes et al. 2010; Best and Heckman 2012; Drake et al. *in prep.*).

Fortunately, with the advent of new and forthcoming spectroscopic surveys, such as the WEAVE-LOFAR survey (Smith et al. 2016) and the Dark Energy Instrument survey (DESI; Desi Collaboration et al. 2016a,b), it has become possible to obtain spectroscopic information of large statistical samples of faint radio sources, and thus evaluate the performance of photometric classifications needed in their absence. The WEAVE-LOFAR survey will produce a catalogue containing complete spectroscopy of all radio sources in the LOFAR Deep Fields. However, a fraction of these sources have already been observed and are part of the early data release of DESI (DESI EDR; DESI Collaboration et al. 2023). While the redshifts and spectra of these sources are publicly available, derived data products such as emission line fluxes, necessary for spectroscopic classifications, are not provided. Therefore, in this chapter, we perform spectral fitting on a sample of available DESI spectra to provide spectroscopic classifications of radio sources in the ELAIS-N1 field. Following a method similar to Drake et al. *in prep.* (hereafter Dr24), which investigates source classifications in the shallower LoTSS wide area, we divide sources into four classes (SFG, RQ AGN, LINELERG<sup>1</sup> and HERG), and compare our results to B23 and D24.

This chapter is structured as follows: Section 4.2 describes the radio and spectroscopic data used, along with the sample selection process. Section 4.3 describes the fitting technique used to obtain emission lines fluxes, necessary for the source classifications. In section 4.4, we outline the classification method, whereas in section 4.5 we compare our results with B23 and D24, and investigate the physical properties of the different classes. Finally, section 4.6 summarises our

---

<sup>1</sup>LINELERGs = emission line LERGs, a subset of the LERG population, which contain emission lines necessary to be placed on the BPT diagram.

main results. Throughout this chapter, we use air wavelengths and a flat  $\Lambda$ CDM cosmology with  $\Omega_\Lambda = 0.7$ ,  $\Omega_M = 0.3$  and  $H_0 = 70 \text{ km s}^{-1} \text{ Mpc}^{-1}$ .

## 4.2 Data

### 4.2.1 Radio Data

The radio data used in this chapter are taken from the first data release of the LOFAR Two-metre Sky Survey Deep fields (LoTSS Deep DR1; Tasse et al. 2021; Sabater et al. 2021). This dataset includes observations centered on 150 MHz at 6 arcsec resolution of three well-studied extragalactic fields: Lockman Hole ( $10^{\text{h}} 47^{\text{m}} 00^{\text{s}}$ ,  $+58^\circ 05' 00''$ ), Boötes ( $14^{\text{h}} 32^{\text{m}} 00^{\text{s}}$ ,  $+34^\circ 30' 00''$ ), and ELAIS-N1 ( $16^{\text{h}} 11^{\text{m}} 00^{\text{s}}$ ,  $+55^\circ 00' 00''$ ), covering a total area of  $\approx 26 \text{ deg}^2$ . Each field is included in the value-added catalogue by Kondapally et al. (2021), where a combination of the likelihood ratio method (e.g. Sutherland and Saunders 1992; Smith et al. 2011) and visual classification with the LOFAR Galaxy Zoo was used to associate the radio sources with a multi-wavelength counterpart (in a similar fashion to LoTSS DR2 discussed in section 2.2.2), along with the corresponding photometric redshifts and stellar masses catalogue by Duncan et al. (2021).

In this study, we focus only on ELAIS-N1 as it contains the most sensitive 150 MHz data (a root mean square noise level of  $\lesssim 20 \mu\text{Jy beam}^{-1}$  in the central region and below  $30 \mu\text{Jy beam}^{-1}$  over  $10 \text{ deg}^2$ ), the deepest wide-field optical, near-IR and mid-IR data, and is included in both B23 and D24 classifications.

### 4.2.2 Spectroscopic Data

The spectroscopic data used in this chapter are taken from the early data release of the Dark Energy Spectroscopic Instrument survey (DESI EDR; DESI Collaboration et al. 2023). The spectra were taken using the DESI instrument, mounted on the 4m Mayall Telescope at Kitt Peak National Observatory, which consists of 10 identical spectrographs. As previously discussed, each spectrograph is equipped with 500 fibres with a  $1.5''$  entrance diameter, and covers the wavelength range of  $3600 - 9824 \text{ \AA}$  at a resolving power of  $\Delta\lambda/\lambda \approx 2000 - 5500$  (Guy et al. 2023).

The data encompass three stages of survey validation, referred to as “sv1”, “sv2” and “sv3”. Each stage was conducted with a different targeting algorithm, and further subdivided into programs based on observing conditions. The “bright” program targeted sources for the Bright Galaxy Survey and the Milky Way Survey, while the “dark” program focused on fainter objects such as Luminous Red Galaxies (LRG), Emission-Line Galaxies (ELG), and Quasi-Stellar Objects (QSO). In addition, the “backup” program was implemented under bad conditions, and the “other” program was dedicated for secondary targets (see Myers et al. 2023 for further details). This resulted in a total of 1,636,256 unique objects included in the primary surveys, and an additional 137,148 objects as part of a series of secondary programs across 1,390 deg<sup>2</sup>. As we are interested in maximising our spectroscopic sample to obtain the largest possible number of classified sources, we consider all surveys and programs.

### 4.2.3 Sample Selection

Starting with a sample of 31,610 radio sources located in the ELAIS-N1 field and possessing a corresponding multi-wavelength counterpart in the DR1 catalogue (Kondapally et al. 2021), we identify 7,267 with spectroscopic information available from DESI EDR. This was done by using a positional cross-match with a maximum search radius of 1 arcsecond between the multiwavelength counterparts in Kondapally et al. (2021), and those reported as the primary objects in DESI EDR (`'zcat_primary'=True`). The redshift-luminosity plane of all radio sources in ELAIS-EN1, both with and without spectroscopic information from DESI EDR, is shown in Figure 4.1. We can see that DESI probes a different parameter space than the radio source population (lower redshift, less radio bright). However, this will change once WEAVE-LOFAR becomes operational.

Next, we remove sources with a non-zero `'zwarn'` flag to ensure reliability of redshift estimates, and thus emission line identification. This leaves us with a sample of 6,754 sources, out of which 450 are spectroscopically defined as QSOs. We remove such objects from our sample, as the stellar population library from Bruzual and Charlot (2003), which we use in this work, do not account for the various continuum components used for quasars (see section 2.5.1 for details). Finally, we make a redshift cut of  $z = 0.45$  as we are interested in obtaining line information for the  $[\text{S II}]\lambda 6731$  emission line. As discussed in section 1.5.1,  $[\text{S II}]\lambda 6731$  is used in the BPT-SII diagram to divide Seyferts and LINERs (Kewley et al. 2006), which we plan to investigate in the future. This gives us a total sample of 3,251 sources.

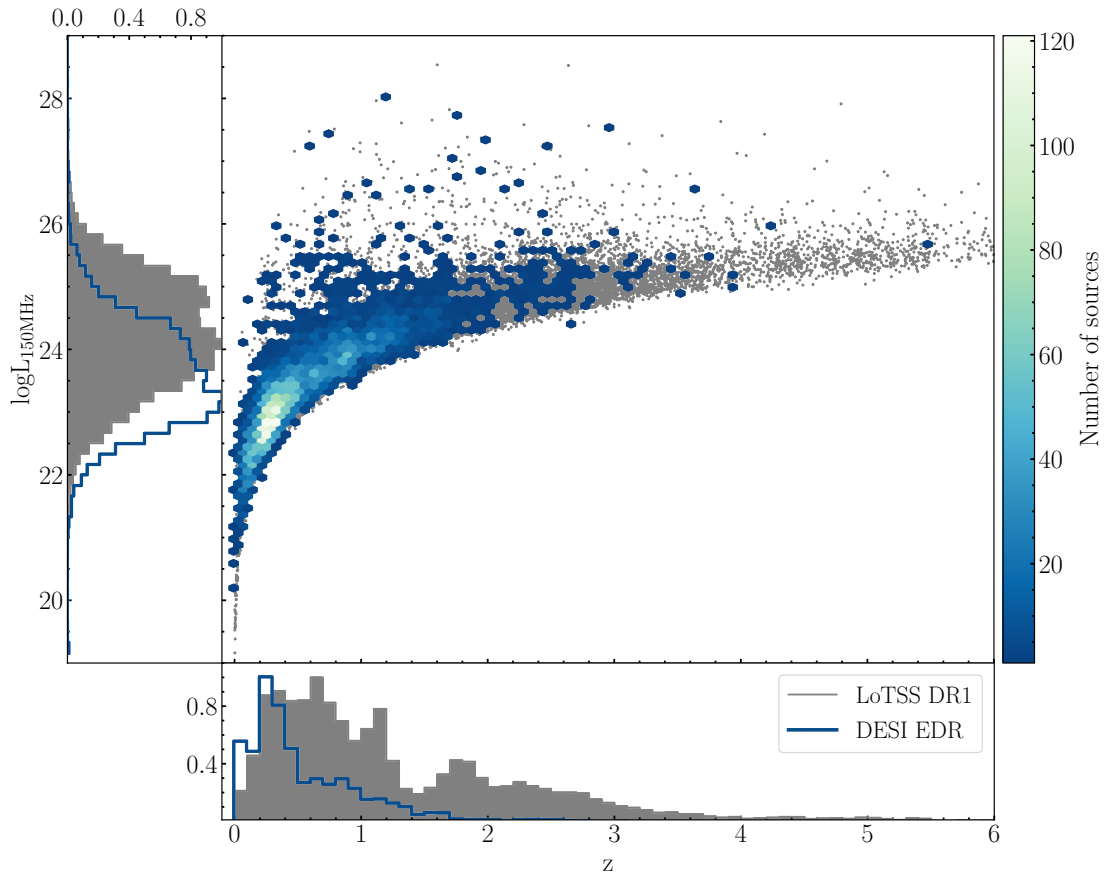


Figure 4.1: The redshift-luminosity plane for all radio sources with a multi-wavelength counterpart in ELAIS-N1 (in grey), and the sources with spectroscopic information from DESI EDR (colour-coded to indicate their number as presented by the colour bar to the right). The additional left and bottom panel indicate the luminosity and redshift distribution, respectively.

### 4.3 Spectral Fitting Method

To obtain emission line fluxes needed for the source classification scheme, we applied an approach similar to the one used in section 3.3, where we modelled the continuum locally to each emission line complex and used multiple Gaussian components for each emission line considered, after correcting all spectra for foreground extinction using the re-calibrated reddening data,  $E(B - V)$ , from Schlegel, Finkbeiner, and Davis (1998) with the Milky Way reddening curve from Fitzpatrick (1999) for an extinction-to-reddening ratio of  $R_V = 3.1$ . However, given the less complex velocity structure of galaxies compared to the shock region in Stephan’s Quintet, we limited the use of Gaussian components to a maximum of two per individual emission line. In addition, since we are no longer dealing with regions where the continuum is faint and featureless, we employed the stellar population library from Bruzual and Charlot (2003), which includes stellar absorption features such as the Balmer absorption lines, instead of a simplistic

linear model to limit the impact of the continuum on our emission line flux estimates.

There are 39 templates included in this library which correspond to three metallicities;  $Z = 0.4$ ,  $1.0$  and  $2.5 Z_{\odot}$ , and 13 star formation history (SFR) models; 10 instantaneous-burst models with ages of 0.005, 0.025, 0.10, 0.29, 0.64, 0.90, 1.4, 2.5, 5 and 11 Gyr, a constant star formation model with an age of 6 Gyr and two models with exponentially declining star formation histories with a timescale of  $\tau_{\text{SFR}} = 5$  Gyr and 9 Gyr and an age of 12 Gyr. All templates were considered in the fits, where they were shifted to the observed frame by using the spectroscopic redshifts from the DESI EDR catalogue and resampled onto the DESI wavelength grid using the `SPECRES` resampling algorithm (Carnall 2017; as in section 2.3.1) to match the data. This resulted in a total of 78 fits for a single galaxy (39 continuum models with one or two Gaussian components per line) using the MCMC method, where the Bayesian Information Criterion (BIC) was used not only to determine the necessary Gaussian components, but also to identify the optimal template for the continuum. For each case, two spectral windows were used: the rest-frame wavelength range  $\lambda = 4790 - 5050\text{\AA}$  covering  $\text{H}\beta$ , and  $[\text{OIII}] \lambda\lambda 4959, 5007$ , and the  $\lambda = 6470 - 6780\text{\AA}$  containing  $\text{H}\alpha$ ,  $[\text{NII}] \lambda\lambda 6548, 6583$  and  $[\text{SII}] \lambda\lambda 6716, 6732$ , where the continuum template normalisation was allowed to differ in the two different wavelength ranges considered for the fitting.

Examples demonstrating the performance of this method are shown in Figure 4.2, where we have chosen a random galaxy, determined to be best modelled with one and two Gaussian components. There are a total of 3,186 galaxies with a reduced chi-square  $\chi_{\nu}^2 < 2$  (which we refer to as ‘good’ fits), out of which 918 required a two-Gaussian component model according to the BIC. Using these good fits, we calculate the total emission line flux per line species, where the uncertainties are evaluated by propagating the values extracted from the MCMC chains.

## 4.4 Spectroscopic Classification Scheme

Following Dr24, we use a combination of the radio excess and BPT-NII (hereafter BPT; Baldwin et al. 1981) diagram diagnostic to classify all objects into four physical classes: star-forming galaxies (SFG), radio-quiet AGN (RQ AGN), emission line low-excitation radio galaxies (LINELERG), and high-excitation radio galaxies (HERG). However, in this work we focus only on the maximum likelihood classifications, as previously done in a number of studies (e.g. Best and Heckman 2012; Sabater et al. 2019). Therefore, we require that  $\text{H}\beta \lambda 4861$ ,  $[\text{OIII}] \lambda 5007$ ,  $\text{H}\alpha \lambda 6563$ , and  $[\text{NII}] \lambda 6583$  emission lines are all significantly detected ( $> 3\sigma$ ), resulting in a

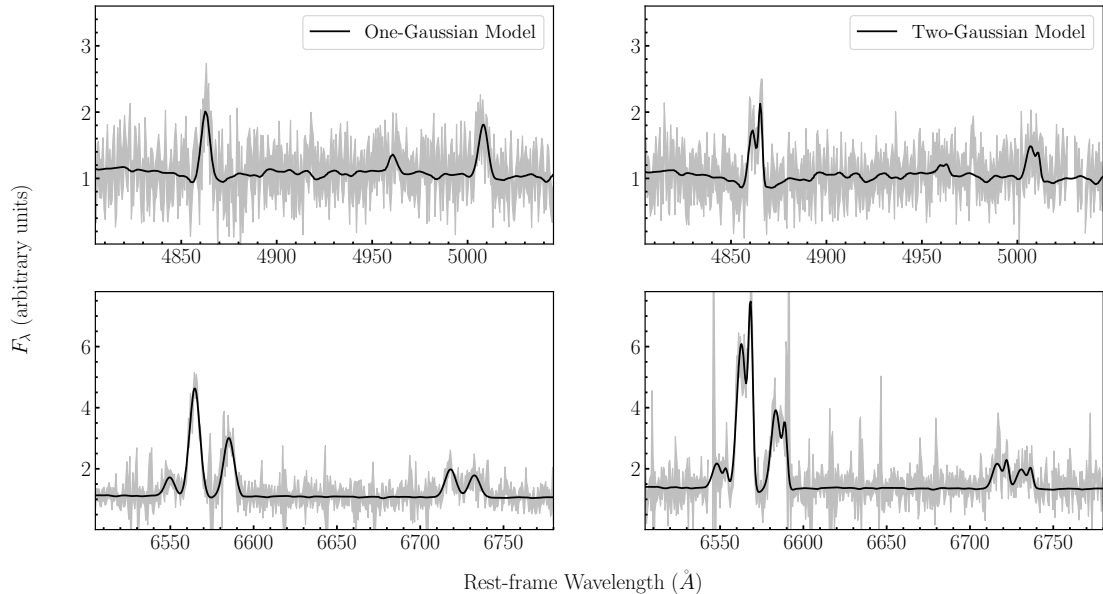


Figure 4.2: Example fits of galaxy spectra using our spectral fitting method, where the data are represented in grey lines with shaded region enclosing the  $1\sigma$  uncertainties, and the best-fit model is overlaid in black. The left panel shows a random galaxy from the sample, where a single Gaussian component has been determined to model the emission line profiles, whereas the right panel presents another example of a galaxy spectrum, whose emission lines are well-fitted with two Gaussian components.

final sample to 2,033 sources. It is worth mentioning that in future work, we intend to employ the comprehensive methodology outlined by Dr24, which employs a probabilistic approach considering the uncertainties in the emission line fluxes and the radio luminosity.

#### 4.4.1 Radio Excess

We use a radio excess diagnostic to examine the correlation between  $H\alpha$  ( $L_{H\alpha}$ ) and the 150 MHz radio luminosity ( $L_{150\text{MHz}}$ ), enabling the identification of AGN with a radio excess compared to star-forming processes (i.e. LINELERGs and HERGs). As explained by Best and Heckman (2012), this diagnostic relies on the expected correlation between  $L_{H\alpha}$  and  $L_{150\text{MHz}}$  in star-forming galaxies (SFGs), where both luminosities serve as direct SFR indicators. Conversely, in radio-excess AGN, the  $L_{150\text{MHz}}$  is significantly higher compared to SFGs, leading to a noticeable deviation from this correlation. The relationship between the  $L_{H\alpha}$  and  $L_{150\text{MHz}}$  is presented in the left panel of Figure 4.3, where we can see that the majority of sources lie in a tight locus, with some scatter in the lower-right quadrant, where radio-excess AGN are situated.

To determine the exact demarcation line for their identification, we replicate the process described Dr24. This is necessary as we are using a much deeper radio sample (with an rms  $\sim 20\text{--}35 \mu\text{Jy}$

as opposed to  $\sim 100\mu\text{Jy}$  in the wide area), as well a different spectroscopic sample (differences in aperture sizes), which is why we cannot adopt the radio-excess demarcation line used in their work. To do this, we examined the  $\log L_{150\text{MHz}} - \log L_{\text{H}\alpha}^{\text{corr}}$  distribution, where  $L_{\text{H}\alpha}^{\text{corr}}$  is the extinction corrected  $\text{H}\alpha$  luminosity. To obtain this parameter, we used the Balmer decrement in  $\text{H}\alpha$  in a similar way as in section 3.4.2, where we assumed case B recombination and a reddening curve provided by Calzetti et al. (2000) with  $R_V = 4.05$ . In cases when we obtain a negative extinction correction, we do not correct the  $\text{H}\alpha$  luminosity. To calculate the radio luminosity, we applied the same calculation as in section 2.2.3, where we used the integrated 150 MHz flux density from the value added catalogue by Kondapally et al. (2021), assumed a radio spectral index of  $\alpha = -0.7$  and used the spectroscopic redshifts as reported in DESI EDR. Next, we used a kernel density distribution (KDE) to find the peak to the left of which we could model the  $\log L_{150\text{MHz}} - \log L_{\text{H}\alpha}^{\text{corr}}$  with a Gaussian distribution. This allowed us to estimate the 99th percentile of the distribution, which allowed us to identify those sources that have a radio excess as:

$$\log_{10}(L_{150\text{MHz}}/\text{WHz}^{-1}) > \log_{10}(L_{\text{H}\alpha}^{\text{corr}}/L_{\odot}) + 15.53 \quad (4.1)$$

#### 4.4.2 The BPT diagram

As discussed in section 1.5.1, the BPT diagram is a widely used tool for distinguishing between SFGs and AGN (more specifically radiatively-efficient or ‘quasar’ mode AGN), which involves the use of the  $[\text{OIII}]\lambda 5007/\text{H}\beta$ , and the  $[\text{NII}]\lambda 6583/\text{H}\alpha$  emission line flux ratios (e.g. Stasińska et al. 2006; Best and Heckman 2012; Cid Fernandes et al. 2010; Sabater et al. 2019; Kewley et al. 2019 and references therein). Depending on the science case, different demarcation lines are employed. Some studies use the empirically defined line by Kauffmann et al. (2003; hereafter Ka03), the theoretically defined maximum starburst line by Kewley et al. (2001; hereafter Ke01), or both to define an additional class where both star-formation and AGN accretion can take place (the ‘composite’ region as previously discussed). While these demarcation lines are appropriate for low-redshift galaxies ( $z \lesssim 0.8$ ) such as those in this work, we note that they are thought to be less applicable at higher redshifts due to extreme ISM conditions, low metallicity, and/or high ionisation fields (e.g., Kewley et al. 2013; Gutkin et al. 2016; Nakajima and Maiolino 2022; Scholtz et al. 2023).

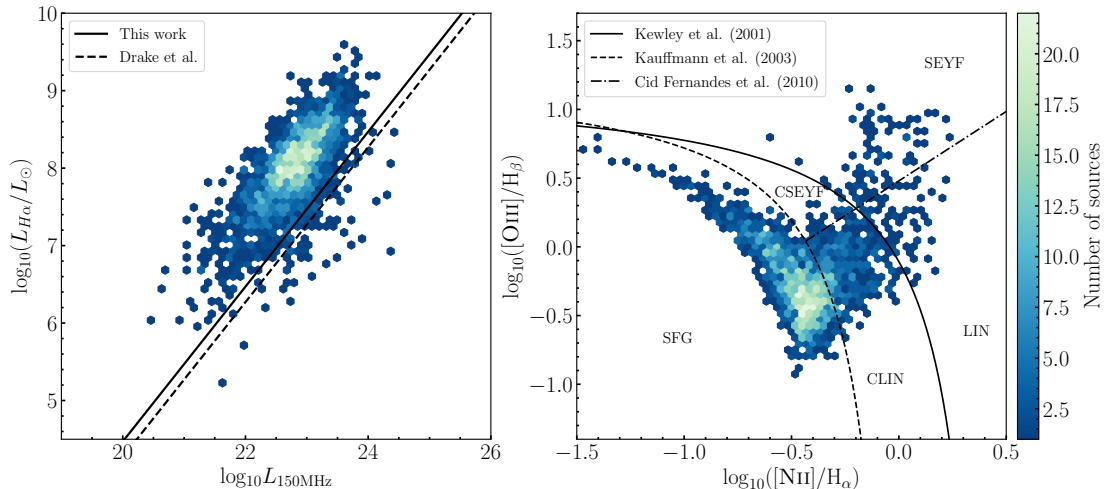


Figure 4.3: The spectroscopic classification scheme. The left panel presents the radio excess diagnostic, where the dashed (Dr24) and solid (this work) lines are used to select sources which have a radio luminosity in excess to what can be explained by star-forming processes alone (i.e radiatively-inefficient AGN). The right panel shows the BPT diagram, used to distinguish between SFGs and radiatively-efficient AGN, further split into low- and high-ionisation, as defined by the Kewley et al. (2001), Kauffmann et al. (2003) and the Cid Fernandes et al. (2010) dividing line. The colour-bar shows the number of sources populating the two diagnostics.

Following Dr24, we use both demarcation lines, along with the additional separation between high-ionisation (Seyferts) and low-ionisation nuclear regions (LINERs) proposed by Cid Fernandes et al. (2010; hereafter C10) to define 5 BPT classes: BPT\_SFG, BPT\_CLIN, BPT\_SEYF, BPT\_LIN and BPT\_SEYF, as shown on the right panel of Figure 4.3. We note that the Seyfert/LINER separation is different from the one used in Dr24, where a demarcation line from Ka03 is adopted. Our selection involves the translated line from the Kewley et al. (2006) scheme from Cid Fernandes et al. (2010), which incorporates additional diagnostics (BPT-SII and BPT-OI) for distinguishing between Seyfert and LINER classes, which we intend to explore in the future. Furthermore, since it is unclear which is the correct line to use to differentiate between SFGs and radiatively-efficient AGN, we will test the impact of using both scenarios (i.e assigning the BPT\_CLIN and BPT\_CSEYF to the SFG or AGN population).

## 4.5 Results

By combining the radio excess and BPT diagnostics discussed in the previous section, we classify sources into the four physical classes in the following way: to identify a source as a SFG, we consider all sources part of the BPT\_SFG class (including the BPT\_CLIN and BPT\_CSEYF for the alternative classification) that lack a radio excess. Those positioned above the Ka03 line (or

Ke01 line) without a radio excess are classified as RQ AGN. Sources exhibiting a radio excess and situated within the BPT\_Seyf (and BPT\_CSeyf) region are categorised as HERGs, while those with a radio excess but not falling within BPT\_Seyf (or BPT\_CSeyf) are classified as LINELERGs. The number of sources in each class resulting from this procedure are shown in Table 4.1. In section 4.5.1, we compare these results with the photometric classifications from B23 and D24, whereas in section 4.5.3 we examine their physical properties.

#### 4.5.1 Comparison with photometric classifications

To evaluate the performance of using photometry alongside SED fitting to classify radio sources, as well as to determine the most suitable spectroscopic classification scheme (i.e. the use of the Ke01 or Ka03 line), we compare our classifications with those provided by B23 and D24 in ELAIS-N1. Since our sample is a subset of those included in B23 and D24, we are able to make a direct comparison. Considering the total number of sources in each class per given classification scheme, as presented in Table 4.1, we can see an overall good agreement between the spectroscopic and photometric classifications, particularly when employing the Ke01 line as the demarcation line between SFG and radiatively-efficient AGN. However, when examining the percentage of sources which are consistently classified in the same class between the different methods, where we have used propagated Poisson errors, the results are not quite straightforward. We find that B23 and D24 successfully identify over 90 per cent of the sources we identify as SFGs, in both the Ke01 and Ka03 classifications. But, when examining the rest of the classes, the recovery rates are noticeably lower. Specifically, using the Ka03 BPT criteria to separate SFGs and radiatively-efficient AGN, B23 and D24 successfully identify only  $9.9 \pm 1.5$  and  $15.0 \pm 1.9$  per cent of our RQ AGN class, although the recovery rate is increased to  $33.6 \pm 6.5$  and  $42.1 \pm 7.7$  per cent, respectively, when considering the Ke01 line instead. For the LINELERG class, B23 and D24 identify  $44.8 \pm 8.2$  and  $34.4 \pm 6.9$  per cent, respectively, while for the HERG class the corresponding percentages are  $12.5 \pm 13.3$  and  $25.0 \pm 19.8$  per cent.

To determine the reasons behind these disparities, we investigate where the B23 and D24 classifications fall within our radio excess and BPT diagnostic, as shown on Figure 4.4. For a statistical comparison, we further calculate the percentage of occupancy for each class in a given region as defined by our criteria (whether showing a radio excess or not, and belonging to a particular BPT class). To provide an uncertainty estimate, we used bootstrapping with replacements to create 10,000 realisations for each classification, identified the percentage of

Table 4.1: The total number of star forming galaxies, radio-quiet AGN, emission line low-excitation radio galaxies, and high-excitation radio galaxies in the ELAIS N1 deep field as identified by the photometric classifications by B23 and D24, along with those generated by our spectroscopic classification method.

	SFG	RQ AGN	LINELERG	HERG	Unclassified
B23	1811	70	87	15	50
D24	1771	114	60	10	78
This work (Ke01)	1822	107	96	8	0
This work (Ka03)	1455	474	96	8	0

occupancy for each one and thus computed a standard deviation from the resultant distribution. The results of this procedure are presented in Table 4.2 and 4.3.

We find that for the radio excess diagnostic, both B23 and D24 classifications perform well in identifying objects with a radio luminosity consistent with star-forming processes, as can be seen in the top panels of Figure 4.4. However, for those objects that exhibit a radio excess, the results are less clear. One potential explanation lies in the methods employed by B23 and D24, which use the  $SFR-L_{150\text{MHz}}$  relation to discern the presence of a radio excess. This relies on the ability of SED fitting codes to successfully recover SFR which may not always be the case, especially for samples exhibiting diverse AGN characteristics. Moving to the BPT diagnostic, we can see an improved behaviour between the physical classes and the BPT regions, showing comparable results for both B23 and D24. A significant portion ( $\sim 77$  per cent in both B23 and D24) of the photometrically identified SFG sources fall within the BPT\_SFG class, and the majority of RQ AGN lie above the Ka03 line, although, there is still a considerable portion ( $\sim 30$  per cent) that are found in the SFG region (see lower panels of Figure 4.4). LINELERGs predominantly occupy the regions outside the BPT\_SEYF, with an interestingly higher percentage found in the BPT\_CLIN region ( $\sim 60$  per cent), while most HERGs are found either in the BPT\_LIN and BPT\_Seyf region (see Table 4.3 for further details). However, it is important to note the low number statistics involved, as well as the fact that we are dealing with maximum likelihood classifications, which do not quantify the uncertainties present in all classes, which we intend to address in the upcoming months.

#### 4.5.2 The influence of redshift and optical source size on classification

As discussed in the previous section, the result of our spectroscopic classification scheme differs from the photometric classifications presented in B23 and D24. Specifically, our radio excess

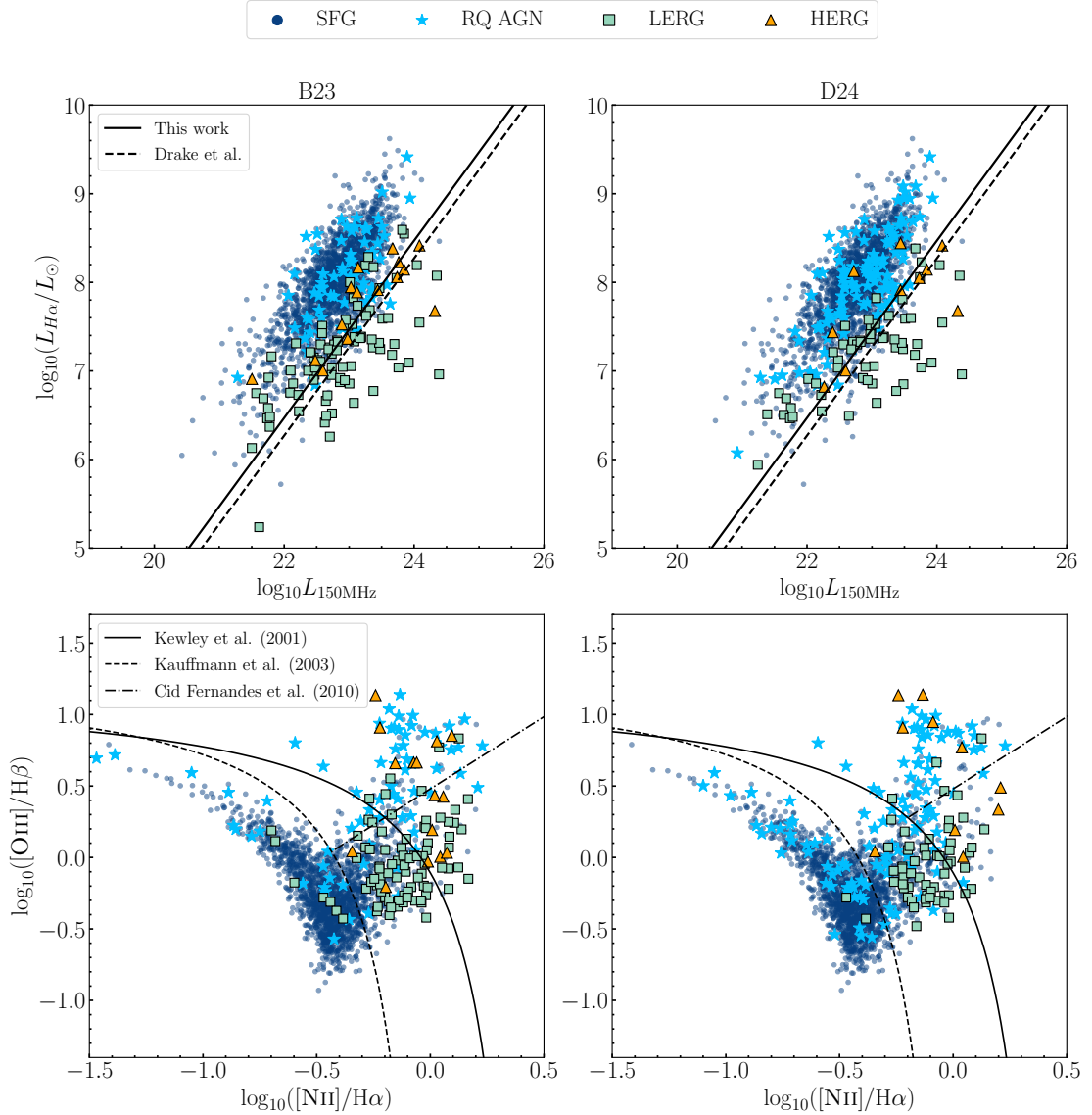


Figure 4.4: The position of the B23 (left) and D24 (right) classifications along the radio excess (top) and BPT (bottom) diagnostics. The solid and dashed lines are the same as in Figure 4.3. The different classes are denoted by various colors and shapes as indicated in the legend.

diagnostic does not agree well with the LINELERG and HERG classes identified in B23 and D24. Furthermore, when employing the BPT diagnostic, we find that  $\sim 30\%$  of their RQ AGN class falls within the SFG region.

Such discrepancies could arise from the redshift estimates used in both works, which primarily rely on photometric redshifts. These redshift estimates are derived from a combination of spectroscopic redshifts obtained from the Sloan Digital Sky Survey Data Release 14 (SDSS DR14; Abolfathi et al. 2018) and photometric redshifts from Duncan et al. (2021). In the absence of spectroscopy for the majority of radio sources, Duncan et al. (2021) created a photometric redshift catalogue combining template fitting and machine learning techniques. The authors

Table 4.2: The radio excess diagnostic. The fraction of sources per classification category exhibiting a radio excess, as identified in the B23 and D24 classifications.

Source Class	Work	Total Number	Radio Excess (%)	
			Yes	No
SFG	B23	1811	$2.5 \pm 0.4$	$97.5 \pm 0.4$
	D24	1771	$3.3 \pm 0.4$	$96.7 \pm 0.4$
RQ AGN	B23	70	$7.1 \pm 3.1$	$92.9 \pm 3.1$
	D24	114	$3.5 \pm 1.7$	$96.5 \pm 1.7$
LINELERG	B23	87	$51.7 \pm 5.3$	$48.3 \pm 5.3$
	D24	60	$56.7 \pm 6.4$	$43.3 \pm 6.4$
HERG	B23	15	$46.7 \pm 12.9$	$53.3 \pm 12.9$
	D24	10	$50.0 \pm 16.0$	$50.0 \pm 16.0$

Table 4.3: The BPT diagnostic. The fraction of sources per classification category in a given BPT class, as identified in the B23 and D24 classifications.

Source Class	Work	Total Number	BPT Classification (%)				
			SFG	CLIN	CSEYF	LIN	SEYF
SFG	B23	1811	$77.4 \pm 1.0$	$18.6 \pm 0.9$	$0.7 \pm 0.2$	$1.4 \pm 0.3$	$1.9 \pm 0.3$
	D24	1771	$77.0 \pm 1.0$	$18.7 \pm 0.9$	$0.7 \pm 0.2$	$1.8 \pm 0.3$	$1.8 \pm 0.3$
RQ AGN	B23	70	$25.7 \pm 5.2$	$8.6 \pm 3.4$	$7.1 \pm 3.1$	$10.0 \pm 3.6$	$48.6 \pm 5.9$
	D24	114	$34.2 \pm 4.5$	$18.4 \pm 3.7$	$4.4 \pm 1.9$	$7.9 \pm 2.6$	$35.1 \pm 4.5$
LINELERG	B23	87	$8.0 \pm 2.9$	$59.8 \pm 5.2$	$2.3 \pm 1.6$	$23.0 \pm 4.5$	$6.9 \pm 2.7$
	D24	60	$3.3 \pm 2.3$	$66.7 \pm 6.0$	$1.7 \pm 1.7$	$21.7 \pm 5.3$	$6.7 \pm 3.2$
HERG	B23	15	0	$13.3 \pm 8.8$	0	$40.0 \pm 12.6$	$46.7 \pm 12.9$
	D24	10	0	$10.0 \pm 9.5$	0	$40.0 \pm 15.5$	$50.0 \pm 15.8$

noted that the outlier fraction (OLF) based on a threshold of  $\delta = (|z_{\text{phot}} - z_{\text{spec}}|)/(1 + z_{\text{spec}}) > 0.15$  is only  $\sim 1.5 - 1.8\%$  for galaxies (or host-dominated sources). However, for sources selected as AGN in the optical, IR and X-rays, the OLF is found to be higher (18 – 20%), which could potentially explain the difference observed between our AGN classes and those classified in B23 and D24. To evaluate the impact of this, we compare the spectroscopic redshifts from DESI EDR ( $z_{\text{spec}}$ ) and those used in B23 and D24 ( $z_{\text{best}}$ ), as shown in the left panel of Figure 4.5. While the majority of sources are not classified as an outlier ( $\sim 99\%$ , as indicated by the dot-dashed lines) according to the criterion from Duncan et al. (2021), there remains a notable scatter between  $z_{\text{best}}$  and  $z_{\text{spec}}$ . However, even when adopting a much more stringent criterion of  $\delta=0.015$  (as denoted by the dashed lines), where about  $\sim 35\%$  of sources are identified as an outlier and thus removed from the sample, we find that the level of agreement between our spectroscopic classifications and the photometric classifications of B23 and D24 do not significantly improve, as can be seen

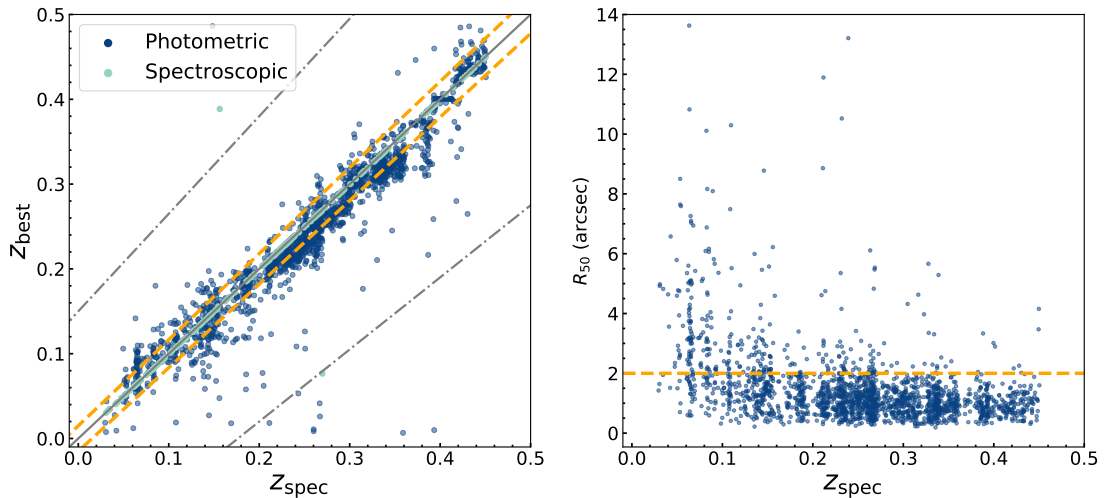


Figure 4.5: The left panel compares the spectroscopic redshifts reported in DESI EDR ( $z_{\text{spec}}$ ), and the redshifts used by B23 and D24 ( $z_{\text{best}}$ ), which include photometric redshifts provided by Duncan et al. (2021) and spectroscopic redshifts from SDSS DR14. The solid line indicates equality, whereas the dot-dashed and dashed lines corresponds to the  $\pm 0.15 \times (1 + z_{\text{spec}})$  criterion from Duncan et al. (2021) and the  $\pm 0.015 \times (1 + z_{\text{spec}})$  used in this work, respectively. The right panel shows the half-light radius ( $R_{50}$ ) distribution as a function of redshift, with the dashed line representing our threshold for excluding sources susceptible to fiber aperture losses.

in Table 4.4.

Another possible factor contributing to the disagreement between classifications is fiber aperture losses. At low redshift, fibers often fail to encompass the entire extent of a galaxy (depending on the size of the fibre and the optical size of the galaxy), leading to significant emission being lost (e.g. Hopkins et al. 2003; Brinchmann et al. 2004; Green et al. 2017). This could impact our measurement of  $H\alpha$  luminosity and thus our radio excess diagnostic. To test this scenario, we use the half-light radius estimates ( $R_{50}$ ) from DESI EDR to identify larger sources, more susceptible to such losses. To establish a reasonable cutoff, we examine the relationship between  $R_{50}$  and redshift, as shown in Figure 4.5. It is evident that at  $z > 0.3$ , the majority of sources have  $R_{50}$  values not exceeding 2 arcsec, therefore we adopt this threshold as our criterion for exclusion, which limits our sample to 1594 sources. However, once again the agreement between both B23 and D24 and our spectroscopic classifications does not significantly improve. This remains to be the case even when applying the combination of redshift and optical size criteria (see Table 4.4 for more details).

Table 4.4: The change of sample size and level of agreement with the redshift and optical size criteria for the photometric classifications by B23 and D24. The first column denotes the type of criterion imposed, the second column shows the resulting total number of sources, whereas the subsequent columns display the percentage of sources consistent with our spectroscopic classifications with the Ke01 line.

Criterion	Samples Size	Work	SFG (%)	RQ AGN (%)	LINELERG (%)	HERG (%)
None	2033	B23	93.9 ± 3.2	33.6 ± 6.5	44.8 ± 8.2	12.5 ± 13.3
		D24	91.4 ± 3.1	42.1 ± 7.5	34.4 ± 6.9	25.0 ± 19.8
$\delta < 0.015$	1293	B23	96.5 ± 4.1	28.8 ± 7.1	45.9 ± 9.5	16.7 ± 18.0
		D24	94.4 ± 4.0	37.0 ± 8.3	37.8 ± 8.4	16.7 ± 18.0
$R_{50} < 2$ arcsec	1594	B23	94.2 ± 3.5	32.9 ± 7.3	55.0 ± 14.6	25.0 ± 28.0
		D24	91.9 ± 3.5	43.9 ± 8.8	40.0 ± 11.8	50.0 ± 43.3
$(\delta < 0.015) \&$ $(R_{50} < 2$ arcsec)	983	B23	97.4 ± 4.6	27.3 ± 7.9	55.6 ± 17.9	33.3 ± 38.5
		D24	95.4 ± 4.6	40.0 ± 10.1	44.4 ± 15.4	33.3 ± 38.5

### 4.5.3 Physical properties of the sources by classification

To investigate the physical properties of the individual classes, as well as to validate our spectral fitting and classification scheme, we make use of the value-added catalogue provided by D24 which includes SFR and stellar mass estimates for all sources in our sample. To ensure reliability of results, we use only sources with acceptable SED fits ( $\chi_{\text{agn}}=0$ ), which include all sources classified in that work (see Table 4.1 for the number of unclassified sources in both B23 and D24). This reduces our sample to 1,955 sources. However, as previously discussed these estimates were performed using a combination ( $z_{\text{best}}$ ) of spectroscopic redshifts from SDSS DR14 and photometric redshifts from Duncan et al. (2021). Therefore, to facilitate an accurate comparison between physical properties, we use the subsample of sources that obey our criterion of  $\delta < 0.015$ , along with the optical source size cut of  $R_{50}$  to ensure that our classifications are not affected by aperture losses. Furthermore, as the Ke01 classification agrees better with the photometric classifications, we move forward with it for the rest of the analysis, such that we have a total of 898 SFG, 55 RQ AGN, 27 LINELERGs and 3 HERGs. This sample size will increase once we include the rest of the LoTSS Deep Fields (namely Lockman Hole and Boötes).

In the left panel of Figure 4.6, we compare the SFR against the  $L_{150\text{MHz}}$  for all classes. We can see that the SFG class lies tightly around the  $L_{150\text{MHz}}$ -SFR relation (denoted by the dotted line which is taken from the mass independent relation in D24) as expected for galaxies whose emission is dominated by star-forming processes. Similarly to the finding by Dr24, the RQ AGN are found to largely overlap with the SFGs. However, both SFGs and RQ AGN exhibit some scatter above

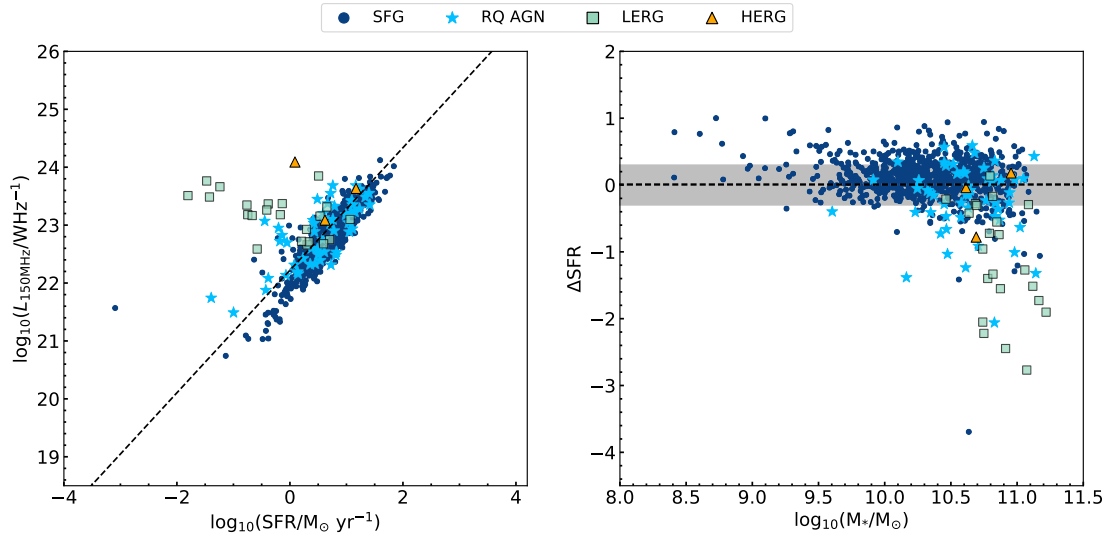


Figure 4.6: The physical properties of the different source classes, as indicated by the legend at the top. The left panel presents the  $L_{150\text{MHz}}$ –SFR plane for each class as indicated in the legend, where the dotted line indicated the stellar mass independent  $L_{150\text{MHz}}$ –SFR relation from D24. Similarly, the right panel shows the SFR relative to those expected for galaxies on the star formation rate stellar mass relation ( $\Delta\text{SFR}$ ), derived from using the redshift dependent relation from Schreiber et al. (2015), as a function of stellar mass. The dashed line indicates the main-sequence, whereas the grey shaded region represents a scatter of  $\pm 0.3$  dex. The SFR and stellar mass estimates are taken from the value-added catalogue from D24.

the  $L_{150\text{MHz}}$ –SFR relation at lower SFRs ( $\log_{10}(\text{SFR}/M_{\odot} \text{ yr}^{-1}) \lesssim 0$ ). This has been observed by previous studies investigating the  $L_{150\text{MHz}}$ –SFR relation (e.g. Gürkan et al. 2018; Smith et al. 2021; D24), which have attributed this behaviour to a stellar mass dependence. The majority of the LINELERGs and HERGs, on the other hand, lie as expected above this relation (albeit with some overlap), which gives us great confidence in our spectral fitting and classification schemes as the SFR are independently estimated.

In the right panel of Figure 4.6, we also examine the difference between the estimated SFR and those expected if the sources lie on the star formation rate–stellar mass relation, also known as the ‘main-sequence’ ( $\Delta\text{SFR}$ ), computed using the redshift dependent relation from Schreiber et al. (2015; converted to the adopted IMF in D24), as a function of stellar mass. We can see once more that the SFG class follow the trend expected for star-forming galaxies, where the majority of sources (above 70 per cent) are found to lie within the typical  $\pm 0.3$  dex of the main-sequence relation (e.g. Tacchella et al. 2016). The AGN classes, on the other hand, have lower SFR to what is expected for main-sequence galaxies at a given stellar mass (again with some overlap) and are found to populate the plane at higher stellar masses ( $\gtrsim 10^{10} M_{\odot}$ ). This is in agreement with previous findings suggesting that the most massive galaxies host a radio AGN, even if it is

at relatively low radio powers (e.g. Sabater et al. 2019), further demonstrating the effectiveness of this work.

These results will be re-evaluated when we extend this analysis to the rest of the LoTSS Deep Fields and employ the probabilistic classification scheme by Dr24. This approach will allow us to achieve a more comprehensive understanding, as a result of the larger sample size and enhanced purity in our classifications.

## 4.6 Summary

In this chapter, we have combined the first data release of the LOFAR Two metre Sky Survey Deep Fields and the early data release of the Dark Energy Spectroscopic Instrument survey to classify sources as star-forming galaxies (SFGs), radio-quiet AGN (RQ AGN), emission line low-excitation radio galaxies (LINELERGs) and high-excitation radio galaxies (HERGs). To do this, we performed spectral fitting of 3,251 sources by making use of the stellar population library from Bruzual and Charlot (2003), combined with a simple model for the emission lines, including one or two Gaussian components per emission line species, in order to extract the emission line information needed for the classification scheme. Following a similar method to that of Dr24, we used a radio excess and BPT diagnostic to produce a maximum likelihood classification, in which we identify 1822 SFGs, 107 RQ AGN, 96 LINELERGs and 8 HERGs, after applying a goodness-of-fit criterion (e.g.  $\chi^2_{\nu} < 2$ ) and requiring that all BPT lines were significantly detected ( $> 3\sigma$ ).

Comparing these results with the photometric classifications provided by B23 and D24, we find a good agreement for the SFG class (above 90 per cent consistency with our classification). However, discrepancies arise among the three AGN classes. Specifically, a fraction of the LINELERG and HERG classes identified in those works do not appear to exhibit a radio excess according to our diagnostic, whereas some RQ AGN are found to populate the SFG region in the BPT diagram. These results persist even when accounting for the differences in redshifts, where the majority of redshifts used in B23 and D24 are from the photometric catalogue provided by Duncan et al. (2021), in contrast to the spectroscopic redshifts from DESI EDR used in this work. Furthermore, these disagreements do not improve when taking into account the effects of fiber aperture losses by examining the half-light radius as a function of redshift.

These findings have significant implications, particularly for our understanding of galaxy populations without spectroscopy, or the numerically dominant sub-population for which the signal to noise in the observed spectra is low. The extent to which low signal-to-noise-ratio spectroscopy can be helpful in classifying sources alongside photometry is a subject of current investigation (Das et al. *in prep*). Alongside high-redshift passive galaxies (which do not exhibit emission lines, and which are therefore all but impossible to detect using spectrographs on 4-metre class telescopes in any reasonable integration time), this is also a concern for dwarf galaxies outside the local Universe due to their low-surface brightness (e.g. Kaviraj 2020). In both cases, photometric redshift estimation, classification and SED fitting will be the primary means to study such sources; it is therefore critical to understand their limitations and work towards improving them.

To investigate the reason behind the discrepancies between the spectroscopic and photometric classifications, we intend to implement the full approach described by Dr24. This method introduces a probabilistic framework that takes into consideration the uncertainties associated with the emission lines and radio properties, which will allow us to identify the subset of sources in each class for which we are most confident in the sources' classification (e.g. > 99 per cent reliability). With this type of classification, we expect to see a better agreement with B23 and D24. At present, we use only the maximum likelihood classifications, which fail to quantify the uncertainties across all classes. Instead, they are based solely on the significant detection of emission lines and radio fluxes ( $> 3\sigma$ ). While widely used in literature (e.g. Best and Heckman 2012; Sabater et al. 2019), such classifications do not reflect the confidence in a given classification, which is why they require further investigation.

Nevertheless, when exploring the distributions of our classes in the SFR and  $L_{150\text{MHz}}$  plane and along the main sequence diagram, we find that our spectroscopic maximum likelihood classifications mostly populate the expected regions: the SFG class lies tightly around the  $L_{150\text{MHz}}$  - SFR relation and aligns well with the main sequence as anticipated for star-forming galaxies. The LINELERGs and HERGs are predominantly hosted by massive galaxies ( $\gtrsim 10^{10} M_{\odot}$ ), that have SFR values below what is expected for main-sequence galaxies at a given stellar mass and exhibit a radio excess. RQ AGN are found to populate the regions in between SFGs and low- and high-excitation radio-galaxies, as expected for sources thought to be fueled by a combination of star-forming processes and small scale radio jets. But as discussed, a more comprehensive classification method is essential to study the nature of these classes, as well as to determine the performance of photometric classifications, which we plan to implement in the future.

## Chapter 5

# Conclusions and Future Work

In this thesis, we have demonstrated that the combination of low-frequency radio observations with optical spectroscopy serve as a valuable tool for understanding the evolution of galaxies and AGN over cosmic time. Making use of the largest, most-sensitive low-frequency radio survey, the Low Frequency Array Two-metre Sky Survey (LoTSS; Shimwell et al. 2017), alongside available optical spectroscopy in its footprint from the Sloan Digital Sky Survey (SDSS; York et al. 2000), the William Herschel Enhanced Area Velocity Explorer (WEAVE; Dalton et al. 2012) and the Dark Energy Instrument (DESI; Desi Collaboration et al. 2016a,b), we conducted the following studies, where for each case we will discuss potential exploration of future avenues that will enhance our understanding of the field.

### 5.1 The radio-loudness of quasars

First, we made a statistical study exploring the radio-loudness of SDSS quasars, in which we created composite spectra of the radio-loud (RL) and radio-quiet (RQ) population across the available redshift range of  $0.6 < z < 3.4$ . Our findings revealed that, on average, RL QSOs display a redder continuum and an enhanced [OIII] emission compared to their RQ counterparts, irrespective of the black hole mass and accretion rate. These differences are also found to persist when probing deeper into the RQ regime (i.e. when making additional cuts at lower values of the radio-loudness parameter,  $R$ ). One possibility for the absence of a smooth transition could be attributed to the dominance of jets, which may drive the radio emission across all quasar populations, with the exception possibly occurring at the lowest  $R$  values, where star-forming

processes could potentially take over. This idea is supported by recent studies (Macfarlane et al. 2021; Yue et al. 2024) which have showed that the radio emission of quasars can be modelled by a combination of jet power and star formation, demonstrating that the jet-launching mechanism operates in all quasars but with different powering efficiency.

The new wide-field sub-arcsecond 144 MHz imaging from the LOFAR international stations (Morabito et al. 2022; Jackson et al. 2022a; Sweijen et al. 2022) presents us with the opportunity to test this scenario. Achieving imaging at sub-arcsecond resolution will allow us to morphologically discern the presence of jets in quasars, thereby facilitating the creation of large statistical samples of both jetted and non-jetted AGN. The follow-up spectroscopy from the WEAVE-LOFAR survey (Smith et al. 2016) will enable us to apply our stacking techniques to these samples, and thus investigate whether the presence of jets influences the observed differences between various quasar populations. Moreover, the continuous advancements of LOFAR and the advent of the Square Kilometer Array (SKA) will significantly enhance our radio sample size in terms of both spatial coverage and sensitivity. This, coupled with spectroscopic surveys such as the WEAVE-LOFAR survey, will provide us with the means to trace the evolutionary pathways of quasars simultaneously across various other parameters. For instance, in Chapter 2, our analysis of the [OII] emission as a function of both radio-loudness and redshift was limited by the sample size. Nevertheless, using only the classical definition of RL and RQ quasars, and employing the [NIV] emission line to correct for potential AGN contribution (following the methodology of Maddox 2018), we discovered that the elevated levels of [OII] represent an excess of star formation in the RL population, at least up  $z = 1.9$ , confirming previous results with higher significance, deeper radio data and at higher redshifts (Maddox 2018). This analysis will be revisited in the future to improve our understanding of the connection between star formation and quasar activity.

## 5.2 Stephan's Quintet and Beyond

The newly commissioned WEAVE large integral field unit (LIFU) further allowed us to explore the large-scale shock front in Stephan's Quintet (SQ) in more detail than previously possible. By harnessing the instrument's large field of view ( $90 \times 78$  arcsec<sup>2</sup>), spectral resolution ( $\Delta\lambda/\lambda \sim 2500$ ) and continuous wavelength coverage across the optical band ( $3660 < \lambda < 9590$  Å), we were able to perform robust spectral fitting of complex emission lines. Using up to four Gaussian components, we were able to deblend prominent emission line such as H $\alpha$  and the

[NII] $\lambda\lambda$  6548,6583 Å doublet, and produce a new, more precise dynamical definition of the shock-dominated region. Combining the emission line information with low-frequency radio observations from LoTSS, high-frequency radio data from the Very Large Array (VLA; Kellermann et al. 1989), and mid-infrared information from early release observations with the *James Webb Space Telescope* (*JWST*; Pontoppidan et al. 2022), we were able to obtain new measurements of physical properties of the shock region. We find that the shock, likely resulting from the collision between NGC 7318b and the intergalactic medium (IGM) of SQ, which is rich in debris from previous encounters, is relatively weak (with a Mach number of  $\mathcal{M} \sim 2.2$ ), such that it adiabatically compresses the medium. This has led to a low density ionised gas ( $n_e < 140\text{cm}^{-3}$ ) at low temperature ( $T_e < 14,000\text{K}$ ) and metallicity ( $Z \sim 0.3 Z_\odot$ ) consistent with the surrounding X-ray plasma, as reported by O’Sullivan et al. (2009) using Chandra observations. Furthermore, it has caused a significant increase in the radio emission, boosting it by a factor  $\sim 10$ . In addition, despite its presence, the shock was not strong enough to destroy the dust present in the IGM (as expected for e.g. fast shocks generated from supernovae; Jones et al. 1994; Zhu et al. 2019). Instead, it appears to have swept the dust away and allowed  $\text{H}_2$  to form on it which was further demonstrated by the comparison between the V-band extinction traced by WEAVE and the molecular gas and hot dust traced by *JWST*.

With this study, we not only gained new insights into SQ, but also demonstrated the power of the newly commissioned WEAVE facility, in conjunction with other multi-wavelength observations, to disentangle the complex nature of such interesting systems, thereby expanding our understanding of the underlying physical processes at play. This trend is expected to continue into the future, in particular for the WEAVE-LOFAR survey, which will use the WEAVE LIFU to target cool-core clusters in the local Universe such as the Perseus Cluster (Abell 426) to study the connection between AGN feedback and the molecular and ionised gas that surrounds the central galaxy (Jin et al. 2023). Another interesting science case that will be explored with the WEAVE LIFU (PI: Gulay Gurkan) is associated with the recently discovered Twin Radio galaxy, TRG J104454+354055 (Gopal-Krishna et al. 2022), located at the center of a galaxy group at  $z \sim 0.16$ . This pair appears to be in the process of merging, with both galaxies hosting a radio-loud AGN and bipolar jets extending for several 100 kpc. This marks the third reported case of such an extremely rare phenomenon, which could provide us with a deeper understanding of galaxy mergers and, by extension, the possibility of supermassive black hole coalescence (e.g. Gualandris et al. 2017). With the WEAVE LIFU, we will be able to obtain detailed kinematics and dynamics of this system, allowing us to shed new light on it.

### 5.3 Classifications of the faint radio source population

Finally, we used the available DESI spectra in the LoTSS Deep Fields (Tasse et al. 2021; Sabater et al. 2021) to classify radio sources as star-forming galaxies (SFGs), radio-quiet AGN (RQ AGN), emission line low-ionisation radio galaxies (LINELERGs), and high-ionisation radio galaxies (HERGs). This was done by employing a similar method to Drake et al. *in prep*, where we used the radio luminosity and the Balmer lines to identify sources with a radio-excess, and the BPT diagram to distinguish between SFGs and radiatively-efficient AGN. Using the maximum likelihood classification (where we required a  $\text{SNR} > 3$  for each BPT emission line), we compared our results to the photometric classifications obtained for the same sample from Best et al. (2023; hereafter B23) and Das et al. *subm* (hereafter D24). We find that both of the photometric classifications successfully identify above 90 per cent of our SFG class, however, the agreement between the three AGN classes is below 40 per cent. These results do not improve when allowing for the impact of the differences between the spectroscopic redshifts used in this work, and those employed by B23 and D24, where the majority of redshifts are taken the photometric redshifts catalogue provided by Duncan et al. (2021), nor when taking into account the effects of fiber aperture losses. A more comprehensive investigation is necessary, which requires using the full probabilistic method described by Drake et al. *in prep*.

This approach incorporates the uncertainties of the emission line and radio flux measurements, which allows for the creation of high purity classifications (with  $> 99$  per cent confidence). To achieve this, Monte Carlo simulations are used to create 1000 realisations of the classification scheme, where in each iteration the radio and emission line fluxes are perturbed by randomly drawing from a normal distribution with a standard deviation equal to their associated uncertainty. With high purity samples identified e.g. on the basis of 99 per cent of realisations of a particular source's lines and radio flux, we will be able to more confidently assess the performance of the photometric classifications, and identify any limitations more confidently. It is important to emphasize the significance of achieving clean classifications and understanding the limitations associated with them. Recent studies (Whittam et al. 2022; Kondapally et al. *in prep.*) have found that LERGs and HERGs have a considerable overlap between their accretion rates at lower radio powers and at higher redshifts. As previously discussed, the primary distinction between LERGs and HERGs is thought to lie precisely in their efficiency to accrete matter (Best et al. 2023). Therefore, further investigation is needed to ascertain whether this observed overlap

accurately reflects the underlying physical properties of these objects or if it is influenced by contamination within the classifications.

In addition to the probabilistic approach, we plan to expand our analysis with DESI across all of the LoTSS Deep Fields (that is including Lockman Hole and Boötes), which will significantly increase our sample size. However, this will be surpassed by WEAVE-LOFAR, which will obtain dedicated spectra of every LoTSS Deep Fields source, allowing us to achieve the most complete and reliable classifications and thus constrain the nature of the faint radio source population in greater detail than previously possible.

## 5.4 Future Contributions to WEAVE-LOFAR

Throughout these studies, we have developed a spectral stacking and spectral fitting code, which will be invaluable for the upcoming WEAVE-LOFAR survey. As previously discussed, the survey is expected to provide over a million spectra of LoTSS targets selected purely on the basis of their 150MHz flux density. Due to this radio selection criterion, we anticipate to obtain spectra primarily from ‘active’ sources (those dominated by star formation or AGN activity), which are rich in emission lines. This will allow us to easily obtain redshift information, in fact using the SKA simulated skies (Wilman et al. 2008), Smith et al. (2016) estimated that the redshift success rate of WEAVE-LOFAR would reach 100 per cent up to  $z = 1$ . However, a continuum detection might not always be available (e.g. for faint star-forming galaxies). Stacking such sources together, however, will allow us to statistically recover their continuum properties, a task for which our spectral stacking code, developed in Chapter 2, is designed. Unlike other spectral stacking codes, this one incorporates a simulation which ensures that the uncertainties are not underestimated and circumvents potential problems arising from normalisation in regions with strong spectral features. Given the large statistical sample, stacking sources as a function of galaxy properties will enable us to study the average spectral properties of various galaxy populations, and thus shed new light on their evolution.

In addition, the WEAVE Advanced Processing System (APS) is tasked with providing derived data products for the large spectroscopic samples expected from WEAVE (see Jin et al. 2023 for further details). This system will use `GALAXY IFU SPECTROSCOPY TOOL` (GIST; Bittner et al. 2019), which obtains stellar kinematics and non-parametric star formation histories using `pPXF`, and emission line kinematics and fluxes using `GANDALF`. Although our spectral fitting code does

not prioritize the continuum, it will serve as an excellent benchmark against which to compare for the **GANDALF** output. This code, similar to ours, is capable of using multiple components to reproduce non-Gaussian profiles, necessary for instance in the presence of an outflow, or in distinguishing between broad and narrow components in AGN. However, its performance in such instances is not yet fully understood. Radio sources are expected to exhibit greater complexity due to the presence of more widespread outflows and feedback mechanisms, leading to more complex line profiles (e.g. Molyneux et al. 2019; Girdhar et al. 2022). As demonstrated in Chapter 3, our code is well equipped to handle such complications. Therefore, it will serve as an effective means to validate the performance of **GANDALF** and thus the overall derived data products underpinning large parts of the WEAVE science case.

These tools can also be applied to upcoming spectroscopic surveys using next-generation facilities such as 4MOST (de Jong et al. 2022), MOONS (Cirasuolo and MOONS Consortium 2016), and WST (Anderson 2024), thereby expanding our understanding of Galaxy Formation & Evolution.

## **5.5 Concluding Remarks**

To conclude, this thesis has highlighted the importance of combining radio observations with optical spectroscopy for advancing our understanding of galaxy and AGN evolution. We have demonstrated that the development of sophisticated data analysis techniques and the use of state-of-the-art observational facilities like WEAVE and LOFAR, have made and will continue to make significant progress in this field, and have hopefully provided the means for further exploration and discovery of previously unexplored territories.



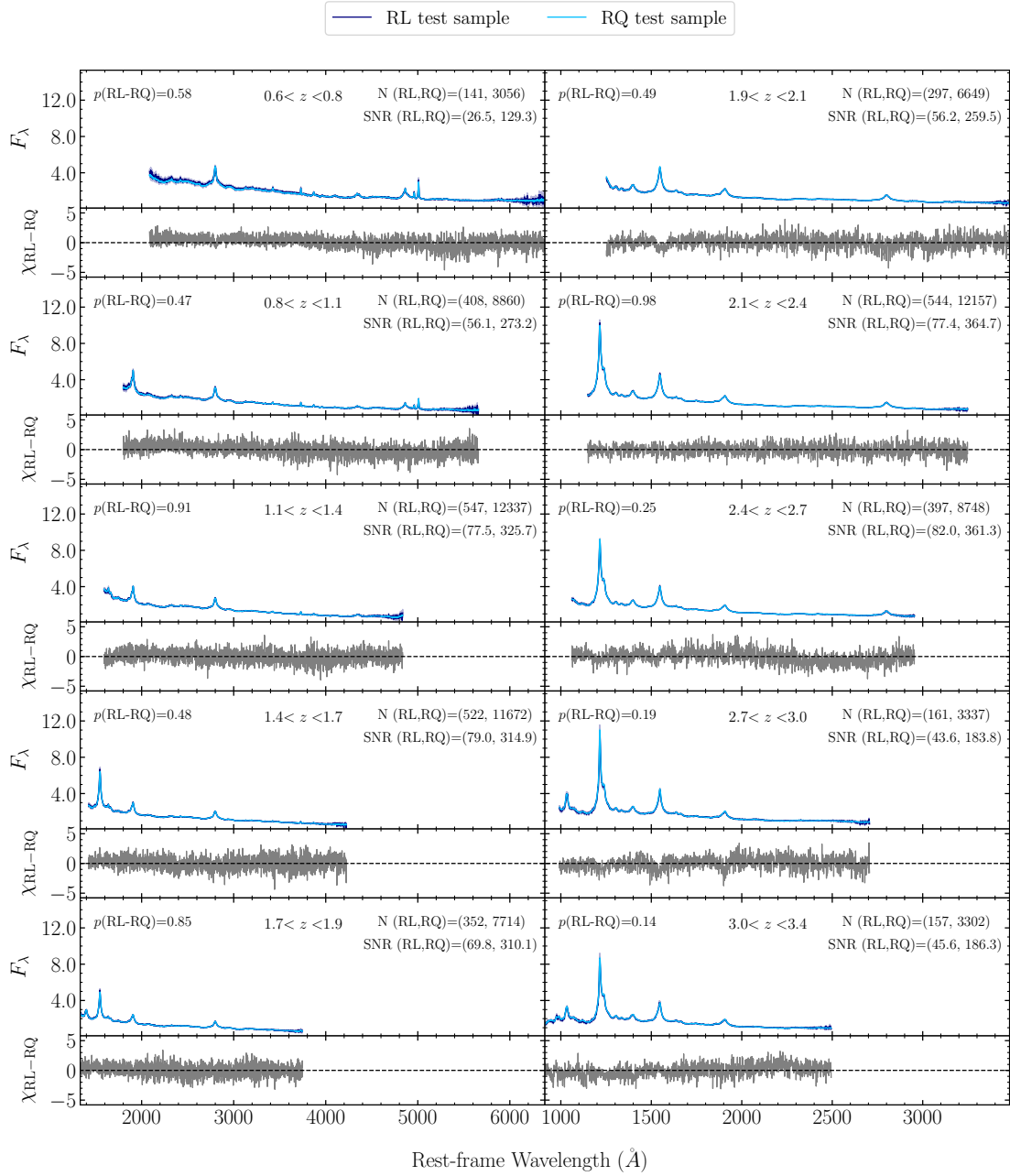


Figure A.2: A Monte Carlo simulation representing the comparison between RL and RQ quasars under the null hypothesis that the RL population is drawn random from the RQ population. The upper panel of each bin presents the composite spectra of the RL test sample (dark blue) and the RQ test sample (light blue), whereas the lower panel indicates the residual in units of propagated uncertainty (grey). The  $p$ -values for each of the null hypothesis tests are presented in the upper left corner, while the number of sources and median S/N are indicated in the top right corner of each panel.

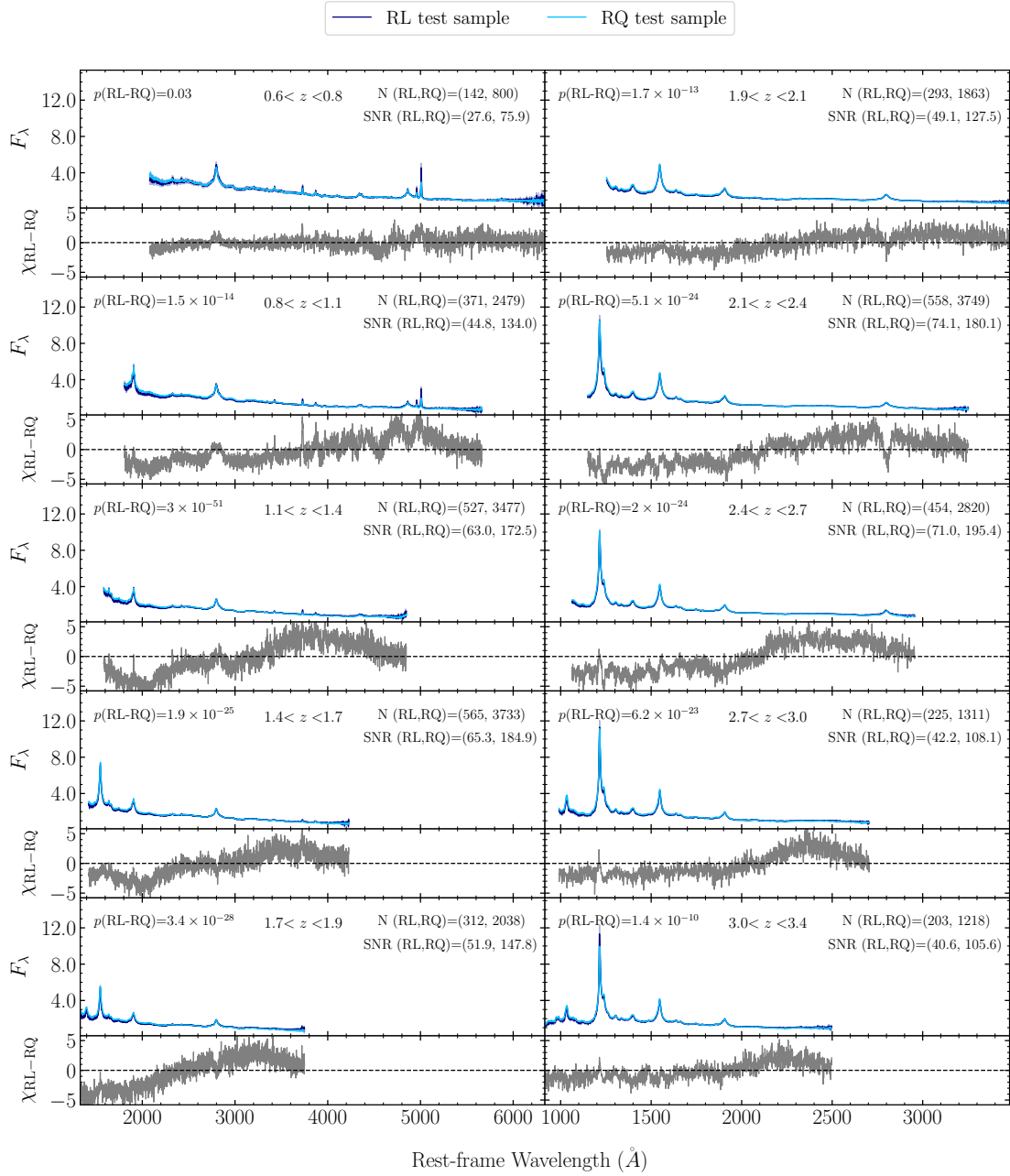


Figure A.3: A high S/N comparison between the RL and RQ population matched in  $z$ ,  $M_i$  and  $M_{BH}$ . As in Figure 2.7, the upper panel of each bin presents the composite spectra of RL QSOs (dark blue) and RQ QSOs (light blue), whereas the lower panel indicates the residual in units of propagated uncertainty (grey). As for figure A.2,  $p$ -values for each of the null hypothesis tests are presented in the upper left corner, while the number of sources and median S/N are indicated in the top right corner of each panel.

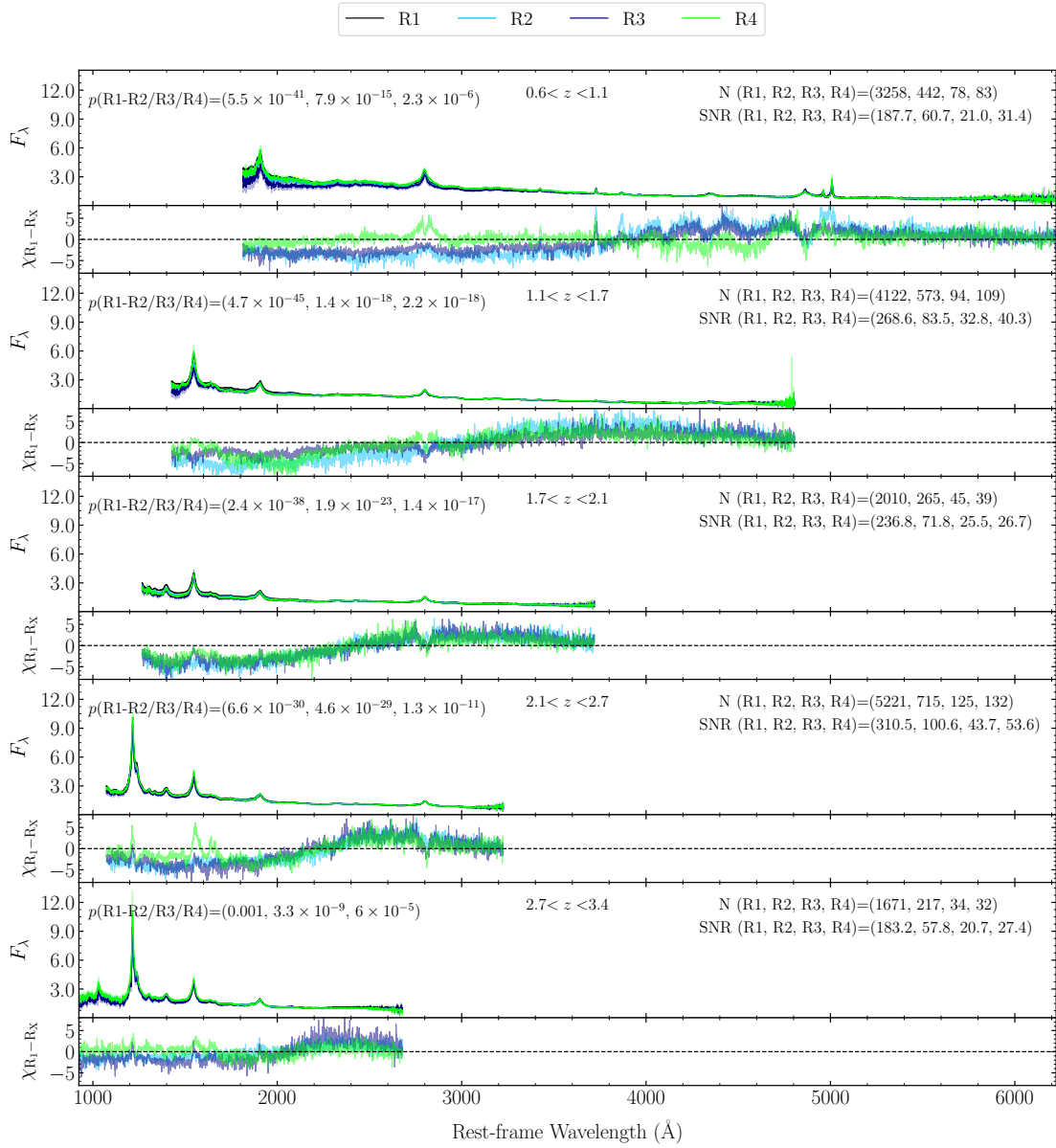


Figure A.4: A high S/N comparison between the radio-quietest ( $R_1$ ) and more radio-loud ( $R_2$ ,  $R_3$  and  $R_4$ ) parts of the QSO population. The upper panel of each bin presents the composite spectra of  $R_1$  (black),  $R_2$  (light blue),  $R_3$  (dark blue) and  $R_4$  (green), whereas the lower panel indicates the residual in units of propagated uncertainty for each comparison. As before, the  $p$ -values for each of the null hypothesis tests are presented in the upper left corner, while the number of sources and median S/N are indicated in the top right corner of each panel.

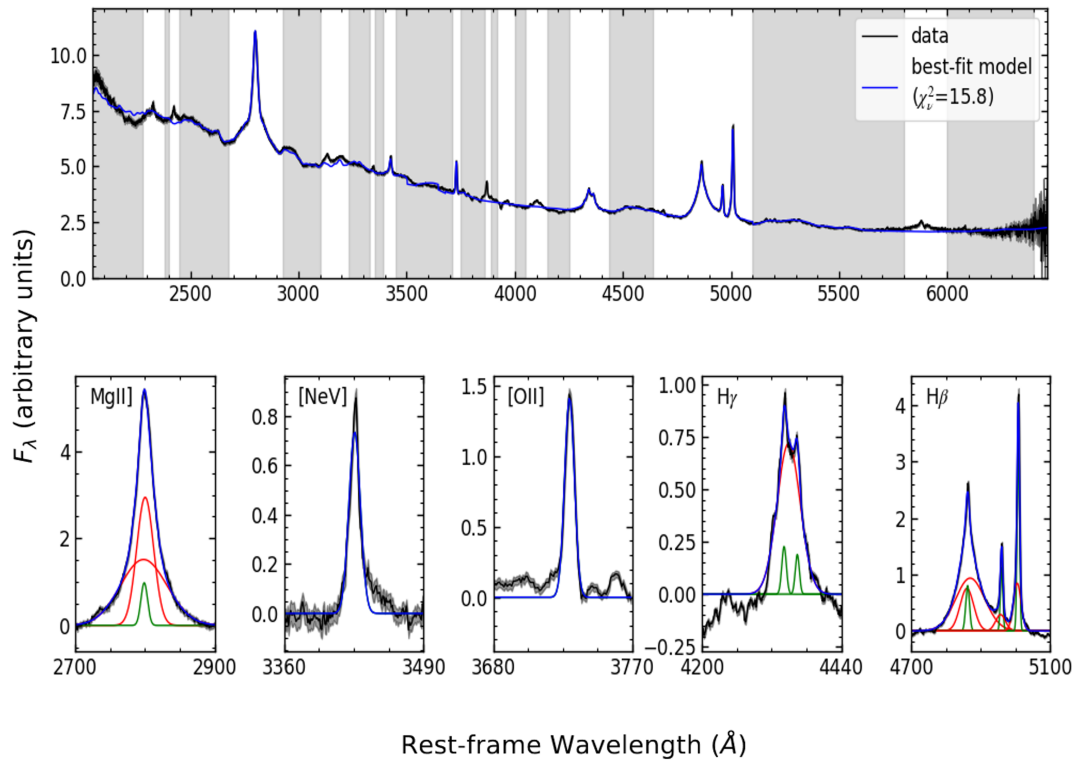


Figure A.5: An example of the spectral fitting procedure with PYSOFIT. The top panel presents the composite spectra of the RQ population in the redshift range of  $0.6 < z < 0.8$  (black) overlaid with the best fit model (blue). The grey shaded region show the wavelength windows used for the continuum fit. The lower panels show the best-fit model of individual line complexes (blue), along with the decomposition into broad (red) and narrow (green) line components.

## Appendix B

### Supplementary Figures for Chapter 3

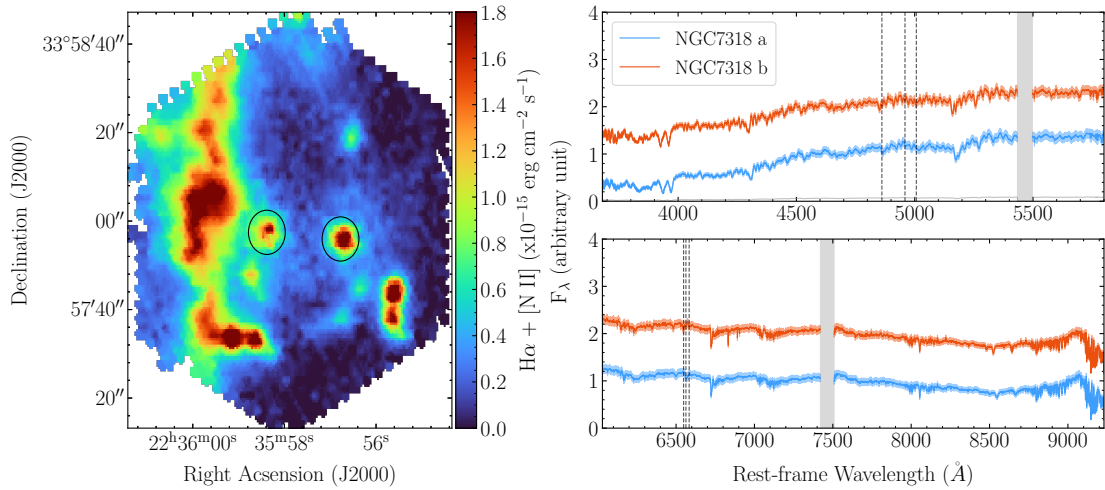


Figure B.1: The left panel shows the H $\alpha$  + [N II] complex as in Figure 3.2. The right panel presents the spectra of NGC 7318a&b from WEAVE, created by summing all spaxels inside the aperture denoted in the H $\alpha$  + [N II] map. These spectra have been arbitrarily normalised and offset from one another for comparison. The grey shaded spectral regions denote the chip gaps, whereas the black dotted lines show the central rest-frame wavelength of the H $\beta$   $\lambda$ 4861, [O III]  $\lambda$ 4959/5007, H $\alpha$   $\lambda$ 6563, and [N II]  $\lambda$ 6548,6583 emission lines, demonstrating their absence in the core of the galaxies.

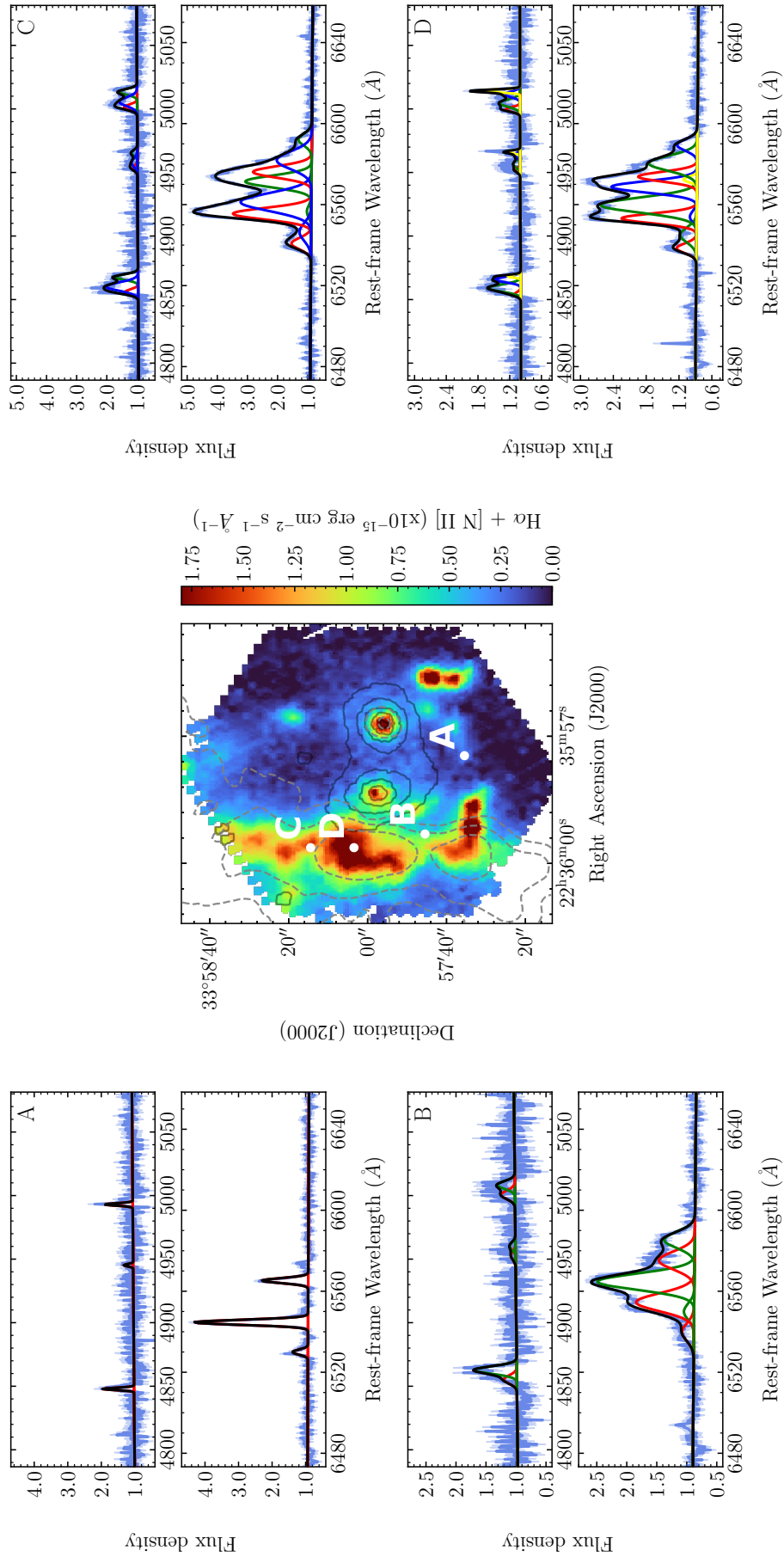


Figure B.2: Example fits of the four Gaussian models at different locations in Stephan's Quintet as denoted in by the letters in the H $\alpha$  map in the middle panel (the same as in Figure 3.2). The flux density  $\pm 1\sigma$  is indicated in blue, whereas the best-fit model is presented in black. The separate Gaussian components are also shown in different colours.

# Bibliography

- Abazajian, K.N., Adelman-McCarthy, J.K., Agüeros, M.A., et al., 2009. The Seventh Data Release of the Sloan Digital Sky Survey. *ApJ*, 182(2):543.
- Abolfathi, B., Aguado, D.S., Aguilar, G., et al., 2018. The Fourteenth Data Release of the Sloan Digital Sky Survey: First Spectroscopic Data from the Extended Baryon Oscillation Spectroscopic Survey and from the Second Phase of the Apache Point Observatory Galactic Evolution Experiment. *ApJ*, 235(2):42.
- Aird, J., Nandra, K., Laird, E.S., et al., 2010. The evolution of the hard X-ray luminosity function of AGN. *MNRAS*, 401(4):2531.
- Alam, S., Ata, M., Bailey, S., et al., 2017. The clustering of galaxies in the completed SDSS-III Baryon Oscillation Spectroscopic Survey: cosmological analysis of the DR12 galaxy sample. *MNRAS*, 470(3):2617.
- Alexander, D.M. and Hickox, R.C., 2012. What drives the growth of black holes? *New Astronomy Reviews*, 56(4):93.
- Algera, H.S.B., van der Vlugt, D., Hodge, J.A., et al., 2020. A Multiwavelength Analysis of the Faint Radio Sky (COSMOS-XS): the Nature of the Ultra-faint Radio Population. *ApJ*, 903(2):139.
- Allen, M.G., Groves, B.A., Dopita, M.A., et al., 2008. The mappings iii library of fast radiative shock models. *The Astrophysical Journal Supplement Series*, 178(1):20.
- Allen, M.G., Groves, B.A., Dopita, M.A., et al., 2008. The MAPPINGS III Library of Fast Radiative Shock Models. *ApJ*, 178(1):20.
- Allen, R.J. and Hartsuiker, J.W., 1972. Radio Continuum Emission at 21 cm near Stephan's Quintet. *Nature*, 239(5371):324.

- Almeida, A., Anderson, S.F., Argudo-Fernández, M., et al., 2023. The Eighteenth Data Release of the Sloan Digital Sky Surveys: Targeting and First Spectra from SDSS-V. *ApJ*, 267(2):44.
- Anderson, R.I., 2024. The Wide-field Spectroscopic Telescope (WST). In *What Was That? - Planning ESO Follow up for Transients*, page 17.
- Antonucci, R., 1993. Unified models for active galactic nuclei and quasars. *Annual Review of Astronomy and Astrophysics*, 31:473.
- Aoki, K., Kosugi, G., Wilson, A.S., et al., 1999. The Radio Emission of the Seyfert Galaxy NGC 7319. *The Astrophysical Journal*, 521(2):565.
- Appleton, P.N., Guillard, P., Emonts, B., et al., 2023. Multiphase Gas Interactions on Subarcsec Scales in the Shocked Intergalactic Medium of Stephan's Quintet with JWST and ALMA. *ApJ*, 951(2):104.
- Appleton, P.N., Xu, K.C., Reach, W., et al., 2006. Powerful High-Velocity Dispersion Molecular Hydrogen Associated with an Intergalactic Shock Wave in Stephan's Quintet. *ApJ*, 639(2):L51.
- Baldwin, J.A., Phillips, M.M., and Terlevich, R., 1981. Classification parameters for the emission-line spectra of extragalactic objects. *PASP*, 93:5.
- Balogh, M., Eke, V., Miller, C., et al., 2004. Galaxy ecology: groups and low-density environments in the SDSS and 2dFGRS. *MNRAS*, 348(4):1355.
- Baloković, M., Smolčić, V., Ivezić, Ž., et al., 2012. Disclosing the radio loudness distribution dichotomy in quasars: An unbiased monte carlo approach applied to the sdss-first quasar sample. *The Astrophysical Journal*, 759(1):30.
- Barcons, X., Barret, D., Decourchelle, A., et al., 2017. Athena: Esa's x-ray observatory for the late 2020s. *Astronomische Nachrichten*, 338(2-3):153.
- Barnes, J.E., 1992. Transformations of Galaxies. I. Mergers of Equal-Mass Stellar Disks. *ApJ*, 393:484.
- Barnes, J.E., 2004. Shock-induced star formation in a model of the Mice. *MNRAS*, 350(3):798.
- Barnes, J.E. and Hernquist, L., 1996. Transformations of Galaxies. II. Gasdynamics in Merging Disk Galaxies. *ApJ*, 471:115.
- Barro, G., Faber, S.M., Dekel, A., et al., 2016. Caught in the Act: Gas and Stellar Velocity Dispersions in a Fast Quenching Compact Star-Forming Galaxy at  $z \sim 1.7$ . *ApJ*, 820(2):120.

- Beck, R. and Krause, M., 2005. Revised equipartition and minimum energy formula for magnetic field strength estimates from radio synchrotron observations. *Astronomische Nachrichten*, 326(6):414.
- Becker, R.H., White, R.L., and Helfand, D.J., 1995. The first survey: faint images of the radio sky at twenty centimeters. *The Astrophysical Journal*, 450:559.
- Beckmann, V. and Shrader, C.R., 2012. *Active Galactic Nuclei*.
- Begelman, M.C., Blandford, R.D., and Rees, M.J., 1984. Theory of extragalactic radio sources. *Reviews of Modern Physics*, 56(2):255.
- Bell, E.F., Wolf, C., Meisenheimer, K., et al., 2004. Nearly 5000 Distant Early-Type Galaxies in COMBO-17: A Red Sequence and Its Evolution since  $z \sim 1$ . *ApJ*, 608(2):752.
- Bennett, C.L., Halpern, M., Hinshaw, G., et al., 2003. First-Year Wilkinson Microwave Anisotropy Probe (WMAP) Observations: Preliminary Maps and Basic Results. *ApJ*, 148(1):1.
- Bernardi, M., Sheth, R.K., Tundo, E., et al., 2007. Selection Bias in the M- $\sigma$  and M-L Correlations and Its Consequences. *ApJ*, 660(1):267.
- Best, P. and Heckman, T., 2012. On the fundamental dichotomy in the local radio-agn population: accretion, evolution and host galaxy properties. *Monthly Notices of the Royal Astronomical Society*, 421(2):1569.
- Best, P., Kauffmann, G., Heckman, T., et al., 2005. The host galaxies of radio-loud active galactic nuclei: mass dependences, gas cooling and active galactic nuclei feedback. *Monthly Notices of the Royal Astronomical Society*, 362(1):25.
- Best, P.N. and Heckman, T.M., 2012. On the fundamental dichotomy in the local radio-AGN population: accretion, evolution and host galaxy properties. *MNRAS*, 421(2):1569.
- Best, P.N., Kauffmann, G., Heckman, T.M., et al., 2005. A sample of radio-loud active galactic nuclei in the Sloan Digital Sky Survey. *MNRAS*, 362(1):9.
- Best, P.N., Kondapally, R., Williams, W.L., et al., 2023. The LOFAR Two-metre Sky Survey: Deep Fields data release 1. V. Survey description, source classifications, and host galaxy properties. *MNRAS*, 523(2):1729.

- Bittner, A., Falcón-Barroso, J., Nedelchev, B., et al., 2019. The GIST pipeline: A multi-purpose tool for the analysis and visualisation of (integral-field) spectroscopic data. *A&A*, 628:A117.
- Blake, C., Pracy, M.B., Couch, W.J., et al., 2004. The 2dF Galaxy Redshift Survey: the local E+A galaxy population. *MNRAS*, 355(329):713.
- Blandford, R. and Eichler, D., 1987. Particle acceleration at astrophysical shocks: A theory of cosmic ray origin. *PhR*, 154(1):1.
- Blandford, R.D. and Znajek, R.L., 1977. Electromagnetic extraction of energy from kerr black holes. *Monthly Notices of the Royal Astronomical Society*, 179(3):433.
- Blanton, M.R., Hogg, D.W., Bahcall, N.A., et al., 2003. The Broadband Optical Properties of Galaxies with Redshifts  $0.02 < z < 0.22$ . *ApJ*, 594(1):186.
- Blyth, S., Baker, A.J., Holwerda, B., et al., 2016. LADUMA: Looking at the Distant Universe with the MeerKAT Array. In *MeerKAT Science: On the Pathway to the SKA*, page 4.
- Borch, A., Meisenheimer, K., Bell, E.F., et al., 2006. The stellar masses of 25 000 galaxies at  $0.2 \leq z \leq 1.0$  estimated by the COMBO-17 survey. *A&A*, 453(3):869.
- Botteon, A., Brunetti, G., Ryu, D., et al., 2020. Shock acceleration efficiency in radio relics. *Astronomy and Astrophysics*, 634:A64.
- Bournaud, F., Jog, C.J., and Combes, F., 2007. Multiple minor mergers: formation of elliptical galaxies and constraints for the growth of spiral disks. *A&A*, 476(3):1179.
- Bouwens, R.J., Oesch, P.A., Stefanon, M., et al., 2021. New Determinations of the UV Luminosity Functions from  $z \approx 9$  to  $z \approx 2$  Show a Remarkable Consistency with Halo Growth and a Constant Star Formation Efficiency. *AJ*, 162(2):47.
- Bouwens, R.J., Stefanon, M., Brammer, G., et al., 2023. Evolution of the UV LF from  $z \approx 15$  to  $z \approx 8$  using new JWST NIRCам medium-band observations over the HUDF/XDF. *MNRAS*, 523(1):1036.
- Bovy, J., Hennawi, J.F., Hogg, D.W., et al., 2011. Think outside the color box: Probabilistic target selection and the sdss-xdqs0 quasar targeting catalog. *The Astrophysical Journal*, 729(2):141.
- Bower, R.G., Benson, A.J., Malbon, R., et al., 2006. Breaking the hierarchy of galaxy formation. *MNRAS*, 370(2):645.

- Boyle, B.J. and Terlevich, R.J., 1998. The cosmological evolution of the QSO luminosity density and of the star formation rate. *MNRAS*, 293(2):L49.
- Brammer, G.B., Whitaker, K.E., van Dokkum, P.G., et al., 2009. The Dead Sequence: A Clear Bimodality in Galaxy Colors from  $z = 0$  to  $z = 2.5$ . *ApJ*, 706(1):L173.
- Brinchmann, J., Charlot, S., White, S., et al., 2004. The physical properties of star-forming galaxies in the low-redshift universe. *Monthly Notices of the Royal Astronomical Society*, 351(4):1151.
- Brunetti, G. and Jones, T.W., 2014. Cosmic Rays in Galaxy Clusters and Their Nonthermal Emission. *International Journal of Modern Physics D*, 23(4):1430007-98.
- Bruno, L., Brunetti, G., Botteon, A., et al., 2023. The Planck clusters in the LOFAR sky. II. LoTSS-DR2: Recovering diffuse extended emission with LOFAR. *A&A*, 672:A41.
- Bruzual, G. and Charlot, S., 2003. Stellar population synthesis at the resolution of 2003. *Monthly Notices of the Royal Astronomical Society*, 344(4):1000.
- Bull, P., Akrami, Y., Adamek, J., et al., 2016. Beyond  $\Lambda$  CDM: Problems, solutions, and the road ahead. *Physics of the Dark Universe*, 12:56.
- Bunker, A.J., Stanway, E.R., Ellis, R.S., et al., 2004. The star formation rate of the Universe at  $z < 6$  from the Hubble Ultra-Deep Field. *MNRAS*, 355(2):374.
- Burbidge, E.M. and Burbidge, G.R., 1961. A Further Investigation of Stephan's Quintet. *ApJ*, 134:244.
- Calabrò, A., Castellano, M., Pentericci, L., et al., 2021. The vandels survey: The relation between the uv continuum slope and stellar metallicity in star-forming galaxies at  $z \sim 3$ . *Astronomy & Astrophysics*, 646:A39.
- Calistro Rivera, G., Williams, W.L., Hardcastle, M.J., et al., 2017. The LOFAR window on star-forming galaxies and AGNs - curved radio SEDs and IR-radio correlation at  $0 < z < 2.5$ . *MNRAS*, 469(3):3468.
- Calzetti, D., Armus, L., Bohlin, R.C., et al., 2000. The Dust Content and Opacity of Actively Star-forming Galaxies. *ApJ*, 533(2):682.
- Caprioli, D., 2012. Cosmic-ray acceleration in supernova remnants: non-linear theory revised. *JCAP*, 2012(7):038.

- Carnall, A., 2017. Spectres: a fast spectral resampling tool in python. *arXiv preprint arXiv:1705.05165*.
- CASA Team, Bean, B., Bhatnagar, S., et al., 2022. CASA, the Common Astronomy Software Applications for Radio Astronomy. *Publications of the Astronomical Society of the Pacific*, 134(1041):114501.
- Cawthorne, T.V., 2006. Polarization of synchrotron radiation from conical shock waves. *Monthly Notices of the Royal Astronomical Society*, 367(2):851.
- Cazaux, S. and Tielens, A.G.G.M., 2004. H<sub>2</sub> Formation on Grain Surfaces. *ApJ*, 604(1):222.
- Chaussidon, E., Yèche, C., Palanque-Delabrouille, N., et al., 2023. Target Selection and Validation of DESI Quasars. *ApJ*, 944(1):107.
- Chiaberge, M. and Marconi, A., 2011. On the origin of radio loudness in active galactic nuclei and its relationship with the properties of the central supermassive black hole. *Monthly Notices of the Royal Astronomical Society*, 416(2):917.
- Chilufya, J., Hardcastle, M.J., Pierce, J.C.S., et al., 2024. The nature of compact radio-loud AGN: A systematic look at the LOFAR AGN population. *MNRAS*.
- Chonis, T.S., Hill, G.J., Lee, H., et al., 2016. Lrs2: design, assembly, testing, and commissioning of the second-generation low-resolution spectrograph for the hobby-ebertly telescope. In *Ground-based and Airborne Instrumentation for Astronomy VI*, volume 9908, pages 1345–1372. SPIE.
- Cibinel, A., Daddi, E., Sargent, M.T., et al., 2019. Early- and late-stage mergers among main sequence and starburst galaxies at  $0.2 \leq z \leq 2$ . *MNRAS*, 485(4):5631.
- Cid Fernandes, R., Stasińska, G., Schlickmann, M.S., et al., 2010. Alternative diagnostic diagrams and the ‘forgotten’ population of weak line galaxies in the SDSS. *MNRAS*, 403(2):1036.
- Cirasuolo, M., Afonso, J., Carollo, M., et al., 2014. Moons: the multi-object optical and near-infrared spectrograph for the vlt. In *Ground-based and airborne instrumentation for astronomy V*, volume 9147, pages 202–214. SPIE.
- Cirasuolo, M., Celotti, A., Magliocchetti, M., et al., 2003a. Is there a dichotomy in the radio loudness distribution of quasars? *Monthly Notices of the Royal Astronomical Society*, 346(2):447.

- Cirasuolo, M., Fairley, A., Rees, P., et al., 2020. MOONS: The New Multi-Object Spectrograph for the VLT. *The Messenger*, 180:10.
- Cirasuolo, M., Magliocchetti, M., Celotti, A., et al., 2003b. The radio-loud/radio-quiet dichotomy: news from the 2df qso redshift survey. *Monthly Notices of the Royal Astronomical Society*, 341(3):993.
- Cirasuolo, M. and MOONS Consortium, 2016. MOONS: A New Powerful Multi-Object Spectrograph for the VLT. In I. Skillen, M. Balcells, and S. Trager, editors, *Multi-Object Spectroscopy in the Next Decade: Big Questions, Large Surveys, and Wide Fields*, volume 507 of *Astronomical Society of the Pacific Conference Series*, page 109.
- Cluver, M.E., Appleton, P.N., Boulanger, F., et al., 2010. Powerful H<sub>2</sub> Line Cooling in Stephan's Quintet. I. Mapping the Significant Cooling Pathways in Group-wide Shocks. *ApJ*, 710(1):248.
- Cochrane, R.K., Kondapally, R., Best, P.N., et al., 2023. The LOFAR Two-metre Sky Survey: the radio view of the cosmic star formation history. *MNRAS*, 523(4):6082.
- Colafrancesco, S., Marchegiani, P., and Paulo, C.M., 2017. The correlation between radio power and Mach number for radio relics in galaxy clusters. *Monthly Notices of the Royal Astronomical Society*, 471(4):4747.
- Colless, M., Peterson, B.A., Jackson, C., et al., 2003. The 2dF Galaxy Redshift Survey: Final Data Release. *arXiv e-prints*, astro-ph/0306581.
- Comerón, S., Knapen, J.H., Ramos Almeida, C., et al., 2021. The complex multi-component outflow of the Seyfert galaxy NGC 7130. *A&A*, 645:A130.
- Condon, J., 1992. Radio emission from normal galaxies. *Annual review of astronomy and astrophysics*, 30(1):575.
- Condon, J., Kellermann, K., Kimball, A.E., et al., 2013. Active galactic nucleus and starburst radio emission from optically selected quasi-stellar objects. *The Astrophysical Journal*, 768(1):37.
- Croton, D.J., Springel, V., White, S.D.M., et al., 2006. The many lives of active galactic nuclei: cooling flows, black holes and the luminosities and colours of galaxies. *MNRAS*, 365(1):11.
- Curti, M., Cresci, G., Mannucci, F., et al., 2017. New fully empirical calibrations of strong-line metallicity indicators in star-forming galaxies. *MNRAS*, 465(2):1384.

- Curtis-Lake, E., Carniani, S., Cameron, A., et al., 2023. Spectroscopic confirmation of four metal-poor galaxies at  $z = 10.3\text{-}13.2$ . *Nature Astronomy*, 7:622.
- Dalton, G., 2016. WEAVE: The Next Generation Spectroscopy Facility for the WHT. In I. Skillen, M. Balcells, and S. Trager, editors, *Multi-Object Spectroscopy in the Next Decade: Big Questions, Large Surveys, and Wide Fields*, volume 507 of *Astronomical Society of the Pacific Conference Series*, page 97.
- Dalton, G., Trager, S.C., Abrams, D.C., et al., 2012. WEAVE: the next generation wide-field spectroscopy facility for the William Herschel Telescope. In I.S. McLean, S.K. Ramsay, and H. Takami, editors, *Ground-based and Airborne Instrumentation for Astronomy IV*, volume 8446 of *Society of Photo-Optical Instrumentation Engineers (SPIE) Conference Series*, page 84460P.
- Dawson, K.S., Kneib, J.P., Percival, W.J., et al., 2016. The SDSS-IV Extended Baryon Oscillation Spectroscopic Survey: Overview and Early Data. *AJ*, 151(2):44.
- Dawson, K.S., Schlegel, D.J., Ahn, C.P., et al., 2013. The Baryon Oscillation Spectroscopic Survey of SDSS-III. *AJ*, 145(1):10.
- de Jong, R.S., Bellido-Tirado, O., Brynnel, J.G., et al., 2022. 4MOST: the 4-metre multi-object spectroscopic telescope project in the assembly, integration, and test phase. In C.J. Evans, J.J. Bryant, and K. Motohara, editors, *Ground-based and Airborne Instrumentation for Astronomy IX*, volume 12184 of *Society of Photo-Optical Instrumentation Engineers (SPIE) Conference Series*, page 1218414.
- de Lapparent, V., Geller, M.J., and Huchra, J.P., 1986. A Slice of the Universe. *ApJ*, 302:L1.
- De Ruiter, H., Willis, A., and Arp, H., 1977. A westerbork 1415 mhz survey of background radio sources. ii-optical identifications with deep iii-a-j plates. *Astronomy and Astrophysics Supplement Series*, 28:211.
- Deeley, S., Drinkwater, M.J., Cunnam, D., et al., 2017. Galaxy and Mass Assembly (GAMA): formation and growth of elliptical galaxies in the group environment. *MNRAS*, 467(4):3934.
- Delvecchio, I., Gruppioni, C., Pozzi, F., et al., 2014. Tracing the cosmic growth of supermassive black holes to  $z \sim 3$  with Herschel. *MNRAS*, 439(3):2736.
- DESI Collaboration, Abareshi, B., Aguilar, J., et al., 2022. Overview of the Instrumentation for the Dark Energy Spectroscopic Instrument. *AJ*, 164(5):207.

- DESI Collaboration, Adame, A.G., Aguilar, J., et al., 2023. The Early Data Release of the Dark Energy Spectroscopic Instrument. *arXiv e-prints*, arXiv:2306.06308.
- Desi Collaboration, Aghamousa, A., Aguilar, J., Ahlen, S., et al., 2016a. The desi experiment part i: science, targeting, and survey design. *arXiv preprint arXiv:1611.00036*.
- Desi Collaboration, Aghamousa, A., Aguilar, J., Ahlen, S., et al., 2016b. The desi experiment part ii: instrument design. *arXiv preprint arXiv:1611.00037*.
- Dey, A., Schlegel, D.J., Lang, D., et al., 2019. Overview of the DESI Legacy Imaging Surveys. *AJ*, 157(5):168.
- Di Matteo, P., Combes, F., Melchior, A.L., et al., 2007. Star formation efficiency in galaxy interactions and mergers: a statistical study. *A&A*, 468(1):61.
- Dimitrijević, M.S., Popović, L.Č., Kovačević, J., et al., 2007. The flux ratio of the [OIII]  $\lambda\lambda$ 5007, 4959 lines in AGN: comparison with theoretical calculations. *MNRAS*, 374(3):1181.
- Dojčinović, I., Kovačević-Dojčinović, J., and Popović, L.Č., 2023. The flux ratio of the [n ii]  $\lambda\lambda$  6548, 6583 Å lines in sample of active galactic nuclei type 2. *Advances in Space Research*, 71(2):1219.
- Domínguez, A., Siana, B., Henry, A.L., et al., 2013. Dust Extinction from Balmer Decrements of Star-forming Galaxies at  $0.75 < z < 1.5$  with Hubble Space Telescope/Wide-Field-Camera 3 Spectroscopy from the WFC3 Infrared Spectroscopic Parallel Survey. *ApJ*, 763(2):145.
- Donnan, C.T., McLeod, D.J., Dunlop, J.S., et al., 2023. The evolution of the galaxy UV luminosity function at redshifts  $z = 8 - 15$  from deep JWST and ground-based near-infrared imaging. *MNRAS*, 518(4):6011.
- Donnan, C.T., McLure, R.J., Dunlop, J.S., et al., 2024. JWST PRIMER: A new multi-field determination of the evolving galaxy UV luminosity function at redshifts  $z \approx 9 - 15$ . *arXiv e-prints*, arXiv:2403.03171.
- Dopita, M.A., Kewley, L.J., Sutherland, R.S., et al., 2016. Chemical abundances in high-redshift galaxies: a powerful new emission line diagnostic. *APSS*, 361:61.
- Dopita, M.A., Sutherland, R.S., Nicholls, D.C., et al., 2013. New Strong-line Abundance Diagnostics for H II Regions: Effects of  $\kappa$ -distributed Electron Energies and New Atomic Data. *ApJ*, 208(1):10.

- Draine, B.T., 2011. *Physics of the Interstellar and Intergalactic Medium*.
- Draine, B.T. and Salpeter, E.E., 1979. On the physics of dust grains in hot gas. *ApJ*, 231:77.
- Drake, A.B., Garel, T., Wisotzki, L., et al., 2017. The MUSE Hubble Ultra Deep Field Survey. VI. The faint-end of the Ly $\alpha$  luminosity function at  $2.91 < z < 6.64$  and implications for reionisation. *A&A*, 608:A6.
- Driver, S.P., Davies, L.J., Meyer, M., et al., 2016. The Wide Area VISTA Extra-Galactic Survey (WAVES). In N.R. Napolitano, G. Longo, M. Marconi, M. Paolillo, and E. Iodice, editors, *The Universe of Digital Sky Surveys*, volume 42 of *Astrophysics and Space Science Proceedings*, page 205.
- Duarte Puertas, S., Iglesias-Páramo, J., Vilchez, J.M., et al., 2019. Searching for intergalactic star forming regions in Stephan's Quintet with SITELLE. I. Ionised gas structures and kinematics. *A&A*, 629:A102.
- Duarte Puertas, S., Vilchez, J.M., Iglesias-Páramo, J., et al., 2021. Searching for intergalactic star forming regions in Stephan's Quintet with SITELLE. II. Physical properties and metallicity. *A&A*, 645:A57.
- Duncan, K., Baker, A., Best, P., et al., 2023. Optical, Radio Continuum and HI Deep Spectroscopic Survey (ORCHIDSS). *The Messenger*, 190:25.
- Duncan, K.J., Kondapally, R., Brown, M.J.I., et al., 2021. The LOFAR Two-meter Sky Survey: Deep Fields Data Release 1. IV. Photometric redshifts and stellar masses. *A&A*, 648:A4.
- Dunlop, J., McLure, R., Kukula, M., et al., 2003. Quasars, their host galaxies and their central black holes. *Monthly Notices of the Royal Astronomical Society*, 340(4):1095.
- Ellison, D.C. and Cassam-Chenai, G., 2005. Radio and X-Ray Profiles in Supernova Remnants Undergoing Efficient Cosmic-Ray Production. *ApJ*, 632(2):920.
- Ellison, D.C., Reynolds, S.P., Borkowski, K., et al., 1994. Supernova Remnants and the Physics of Strong Shock Waves. *PASP*, 106:780.
- Enßlin, T.A. and Brüggen, M., 2002. On the formation of cluster radio relics. *Monthly Notices of the Royal Astronomical Society*, 331(4):1011.
- Enßlin, T.A. and Gopal-Krishna, 2001. Reviving fossil radio plasma in clusters of galaxies by adiabatic compression in environmental shock waves. *Astronomy and Astrophysics*, 366:26.

- Faber, S.M., Willmer, C.N.A., Wolf, C., et al., 2007. Galaxy Luminosity Functions to  $z \sim 1$  from DEEP2 and COMBO-17: Implications for Red Galaxy Formation. *ApJ*, 665(1):265.
- Fabian, A.C., 2012. Observational Evidence of Active Galactic Nuclei Feedback. *Annual Review of Astronomy and Astrophysics*, 50:455.
- Fath, E.A., 1909. The spectra of some spiral nebulae and globular star clusters. *Lick Observatory Bulletin*, 149:71.
- Fawcett, V., Alexander, D., Rosario, D., et al., 2020. Fundamental differences in the radio properties of red and blue quasars: enhanced compact agn emission in red quasars. *Monthly Notices of the Royal Astronomical Society*, 494(4):4802.
- Fawcett, V., Alexander, D., Rosario, D., et al., 2022. Fundamental differences in the properties of red and blue quasars: measuring the reddening and accretion properties with x-shooter. *Monthly Notices of the Royal Astronomical Society*, 513(1):1254.
- Feretti, L., Giovannini, G., Govoni, F., et al., 2012. Clusters of galaxies: observational properties of the diffuse radio emission. *A&ARv*, 20:54.
- Ferrarese, L. and Ford, H., 2005. Supermassive Black Holes in Galactic Nuclei: Past, Present and Future Research. *SSRv*, 116(3-4):523.
- Ferrarese, L. and Merritt, D., 2000. A Fundamental Relation between Supermassive Black Holes and Their Host Galaxies. *ApJ*, 539(1):L9.
- Finkelstein, S.L., D'Aloisio, A., Paardekooper, J.P., et al., 2019. Conditions for Reionizing the Universe with a Low Galaxy Ionizing Photon Escape Fraction. *ApJ*, 879(1):36.
- Fitzpatrick, E.L., 1999. Correcting for the Effects of Interstellar Extinction. *PASP*, 111(755):63.
- Fynbo, J., Krogager, J.K., Venemans, B., et al., 2012. Optical/near-infrared selection of red quasi-stellar objects: evidence for steep extinction curves toward galactic centers? *The Astrophysical Journal Supplement Series*, 204(1):6.
- Gaibler, V., Khochfar, S., Krause, M., et al., 2012. Jet-induced star formation in gas-rich galaxies. *MNRAS*, 425(1):438.
- Gall, C., Hjorth, J., and Andersen, A.C., 2011. Production of dust by massive stars at high redshift. *A&ARv*, 19:43.

- Gardner, J.P., Mather, J.C., Abbott, R., et al., 2023. The James Webb Space Telescope Mission. *PASP*, 135(1048):068001.
- Gebhardt, K., Kormendy, J., Ho, L.C., et al., 2000. Black Hole Mass Estimates from Reverberation Mapping and from Spatially Resolved Kinematics. *ApJ*, 543(1):L5.
- Giallongo, E., Grazian, A., Fiore, F., et al., 2015. Faint AGNs at  $z \lesssim 4$  in the CANDELS GOODS-S field: looking for contributors to the reionization of the Universe. *A&A*, 578:A83.
- Girdhar, A., Harrison, C.M., Mainieri, V., et al., 2022. Quasar feedback survey: multiphase outflows, turbulence, and evidence for feedback caused by low power radio jets inclined into the galaxy disc. *MNRAS*, 512(2):1608.
- Glikman, E., Helfand, D.J., and White, R.L., 2006. A near-infrared spectral template for quasars. *The Astrophysical Journal*, 640(2):579.
- Gludemans, A., Duncan, K., Saxena, A., et al., 2022. Discovery of 24 radio-bright quasars at  $4.9 \leq z \leq 6.6$  using low-frequency radio observations. *Astronomy & Astrophysics*, 668:A27.
- Gopal-Krishna, Joshi, R., Patra, D., et al., 2022. The twin radio galaxy TRG J104454+354055. *MNRAS*, 514(1):L36.
- Gordon, K.D., Calzetti, D., and Witt, A.N., 1997. Dust in starburst galaxies. *The Astrophysical Journal*, 487(2):625.
- Goubert, P.H., Bluck, A.F.L., Piotrowska, J.M., et al., 2024. The role of environment and AGN feedback in quenching local galaxies: comparing cosmological hydrodynamical simulations to the SDSS. *MNRAS*, 528(3):4891.
- Graham, A.W., 2016. Galaxy Bulges and Their Massive Black Holes: A Review. In E. Laurikainen, R. Peletier, and D. Gadotti, editors, *Galactic Bulges*, volume 418 of *Astrophysics and Space Science Library*, page 263.
- Granato, G.L. and Danese, L., 1994. Thick tori around active galactic nuclei: a comparison of model predictions with observations of the infrared continuum and silicate features. *MNRAS*, 268:235.
- Grandi, S., 1982. The 3000 Å bump in quasars. *The Astrophysical Journal*, 255:25.
- Grandmont, F., Drissen, L., Mandar, J., et al., 2012. Final design of SITELE: a wide-field imaging Fourier transform spectrometer for the Canada-France-Hawaii Telescope. In I.S.

- McLean, S.K. Ramsay, and H. Takami, editors, *Ground-based and Airborne Instrumentation for Astronomy IV*, volume 8446 of *Society of Photo-Optical Instrumentation Engineers (SPIE) Conference Series*, page 84460U.
- Green, A.W., Glazebrook, K., Gilbank, D.G., et al., 2017. A test of SDSS aperture corrections using integral-field spectroscopy. *MNRAS*, 470(1):639.
- Greisen, E.W., 2003. AIPS, the VLA, and the VLBA. In A. Heck, editor, *Information Handling in Astronomy - Historical Vistas*, volume 285 of *Astrophysics and Space Science Library*, page 109.
- Gu, M., Cao, X., and Jiang, D., 2001. On the masses of black holes in radio-loud quasars. *Monthly Notices of the Royal Astronomical Society*, 327(4):1111.
- Gualandris, A., Read, J.I., Dehnen, W., et al., 2017. Collisionless loss-cone refilling: there is no final parsec problem. *MNRAS*, 464(2):2301.
- Guillard, P., Boulanger, F., Pineau Des Forêts, G., et al., 2009. H<sub>2</sub> formation and excitation in the Stephan's Quintet galaxy-wide collision. *A&A*, 502(2):515.
- Gultekin, K., 2009. Determination of the intrinsic scatter in the M-sigma and M-L relations. *arXiv e-prints*, arXiv:0912.3898.
- Guo, H., Shen, Y., and Wang, S., 2018. Pyqsofit: Python code to fit the spectrum of quasars. *Astrophysics Source Code Library*, pages ascl-1809.
- Gürkan, G., Hardcastle, M., Best, P., et al., 2019. Lotss/hetdex: Optical quasars-i. low-frequency radio properties of optically selected quasars. *Astronomy & Astrophysics*, 622:A11.
- Gürkan, G., Hardcastle, M., Jarvis, M., et al., 2015. Herschel-atlas: the connection between star formation and agn activity in radio-loud and radio-quiet active galaxies. *Monthly Notices of the Royal Astronomical Society*, 452(4):3776.
- Gürkan, G., Hardcastle, M.J., Smith, D.J.B., et al., 2018. LOFAR/H-ATLAS: the low-frequency radio luminosity-star formation rate relation. *MNRAS*, 475(3):3010.
- Guth, A.H., 1981. Inflationary universe: A possible solution to the horizon and flatness problems. *PhysRevD*, 23(2):347.
- Gutkin, J., Charlot, S., and Bruzual, G., 2016. Modelling the nebular emission from primeval to present-day star-forming galaxies. *MNRAS*, 462(2):1757.

- Guy, J., Bailey, S., Kremin, A., et al., 2023. The Spectroscopic Data Processing Pipeline for the Dark Energy Spectroscopic Instrument. *AJ*, 165(4):144.
- Ha, J.H., Ryu, D., and Kang, H., 2018. Properties of Merger Shocks in Merging Galaxy Clusters. *ApJ*, 857(1):26.
- Haines, C.P., Iovino, A., Krywult, J., et al., 2017. The VIMOS Public Extragalactic Redshift Survey (VIPERS). Downsizing of the blue cloud and the influence of galaxy size on mass quenching over the last eight billion years. *A&A*, 605:A4.
- Hall, P., Balogh, M., Barmby, P., et al., 2019. The Maunakea Spectroscopic Explorer. In *Canadian Long Range Plan for Astronomy and Astrophysics White Papers*, volume 2020, page 30.
- Hardcastle, M., Evans, D., and Croston, J., 2009. The active nuclei of  $z \lesssim 1.0$  3crr radio sources. *Monthly Notices of the Royal Astronomical Society*, 396(4):1929.
- Hardcastle, M., Gürkan, G., van Weeren, R., et al., 2016. Lofar/h-atlas: a deep low-frequency survey of the herschel-atlas north galactic pole field. *Monthly Notices of the Royal Astronomical Society*, 462(2):1910.
- Hardcastle, M., Horton, M., Williams, W., et al., 2023. The lofar two-metre sky survey (lots): Vi. optical identifications for the second data release. *arXiv preprint arXiv:2309.00102*.
- Hardcastle, M.J., Birkinshaw, M., and Worrall, D.M., 1998. Magnetic field strengths in the hotspots of 3C 33 and 111. *Monthly Notices of the Royal Astronomical Society*, 294:615.
- Hardcastle, M.J. and Croston, J.H., 2020. Radio galaxies and feedback from AGN jets. *NewAR*, 88:101539.
- Hardcastle, M.J., Evans, D., and Croston, J., 2007. Hot and cold gas accretion and feedback in radio-loud active galaxies. *Monthly Notices of the Royal Astronomical Society*, 376(4):1849.
- Hardcastle, M.J., Horton, M.A., Williams, W.L., et al., 2023. The LOFAR Two-Metre Sky Survey. VI. Optical identifications for the second data release. *A&A*, 678:A151.
- Harris, D.W., Jensen, T.W., Suzuki, N., et al., 2016. The composite spectrum of boss quasars selected for studies of the  $\text{Ly}\alpha$  forest. *The Astronomical Journal*, 151(6):155.
- Harrison, C.M., 2017. Impact of supermassive black hole growth on star formation. *Nature Astronomy*, 1:0165.

- Harrison, F.A., Boggs, S., Christensen, F., et al., 2010. The nuclear spectroscopic telescope array (nustar). In *Space Telescopes and Instrumentation 2010: Ultraviolet to Gamma Ray*, volume 7732, pages 189–196. SPIE.
- Harwood, J.J., Hardcastle, M.J., Morganti, R., et al., 2017. FR II radio galaxies at low frequencies - II. Spectral ageing and source dynamics. *MNRAS*, 469(1):639.
- Hathi, N.P., Ferreras, I., Pasquali, A., et al., 2009. Stellar Populations of Late-Type Bulges at  $z \sim 1$  in the Hubble Ultra Deep Field. *ApJ*, 690(2):1866.
- Heckman, T.M. and Best, P.N., 2014. The Coevolution of Galaxies and Supermassive Black Holes: Insights from Surveys of the Contemporary Universe. *Annual Review of Astronomy and Astrophysics*, 52:589.
- Heckman, T.M., Kauffmann, G., Brinchmann, J., et al., 2004. Present-day growth of black holes and bulges: The sloan digital sky survey perspective. *The Astrophysical Journal*, 613(1):109.
- Heywood, I., Jarvis, M.J., Hale, C.L., et al., 2022. MIGHTEE: total intensity radio continuum imaging and the COSMOS/XMM-LSS Early Science fields. *MNRAS*, 509(2):2150.
- Hickox, R.C. and Alexander, D.M., 2018. Obscured Active Galactic Nuclei. *Annual Review of Astronomy and Astrophysics*, 56:625.
- Hickson, P., Mendes de Oliveira, C., Huchra, J.P., et al., 1992. Dynamical Properties of Compact Groups of Galaxies. *ApJ*, 399:353.
- Hill, G.J., Gebhardt, K., Komatsu, E., et al., 2008. The hobby-eberly telescope dark energy experiment (hetdex): description and early pilot survey results. *arXiv preprint arXiv:0806.0183*.
- Ho, L.C., 2002. On the relationship between radio emission and black hole mass in galactic nuclei. *The Astrophysical Journal*, 564(1):120.
- Ho, L.C., 2005. [o ii] emission in quasar host galaxies: evidence for a suppressed star formation efficiency. *The Astrophysical Journal*, 629(2):680.
- Ho, L.C., 2008. Nuclear activity in nearby galaxies. *Annual Review of Astronomy and Astrophysics*, 46:475.
- Hong, S.E., Kang, H., and Ryu, D., 2015. Radio and X-Ray Shocks in Clusters of Galaxies. *The Astrophysical Journal*, 812(1):49.

- Hopkins, A.M., Miller, C.J., Nichol, R.C., et al., 2003. Star Formation Rate Indicators in the Sloan Digital Sky Survey. *ApJ*, 599(2):971.
- Hopkins, P.F., Hernquist, L., Cox, T.J., et al., 2005. Black Holes in Galaxy Mergers: Evolution of Quasars. *ApJ*, 630(2):705.
- Hopkins, P.F., Hernquist, L., Cox, T.J., et al., 2006. A Unified, Merger-driven Model of the Origin of Starbursts, Quasars, the Cosmic X-Ray Background, Supermassive Black Holes, and Galaxy Spheroids. *ApJ*, 163(1):1.
- Hopkins, P.F., Hernquist, L., Cox, T.J., et al., 2008. A cosmological framework for the co-evolution of quasars, supermassive black holes, and elliptical galaxies. i. galaxy mergers and quasar activity. *The Astrophysical Journal Supplement Series*, 175(2):356.
- Hopkins, P.F., Richards, G.T., and Hernquist, L., 2007. An Observational Determination of the Bolometric Quasar Luminosity Function. *ApJ*, 654(2):731.
- Hotan, A.W., Bunton, J.D., Chippendale, A.P., et al., 2021. Australian square kilometre array pathfinder: I. system description. *PASA*, 38:e009.
- Hubble, E., 1958. *The realm of the nebulae*.
- Hubble, E.P., 1926. Extragalactic nebulae. *ApJ*, 64:321.
- Husemann, B., Jahnke, K., Sánchez, S., et al., 2014. Integral field spectroscopy of nearby qso*s*—i. enr size–luminosity relation, ongoing star formation and resolved gas-phase metallicities. *Monthly Notices of the Royal Astronomical Society*, 443(1):755.
- Iglesias-Páramo, J., López-Martín, L., Vílchez, J.M., et al., 2012. New insights on Stephan's Quintet: exploring the shock in three dimensions. *A&A*, 539:A127.
- Ignesti, A., Vulcani, B., Poggianti, B.M., et al., 2022. GASP XXXVIII: The LOFAR-MeerKAT-VLA View on the Nonthermal Side of a Jellyfish Galaxy. *ApJ*, 924(2):64.
- Ilbert, O., McCracken, H.J., Le Fèvre, O., et al., 2013. Mass assembly in quiescent and star-forming galaxies since  $z \sim 4$  from UltraVISTA. *A&A*, 556:A55.
- Ilbert, O., Salvato, M., Le Floch, E., et al., 2010. Galaxy Stellar Mass Assembly Between 0.2  $z$   $z \lesssim 2$  from the S-COSMOS Survey. *ApJ*, 709(2):644.

- Ivezić, Ž., Menou, K., Knapp, G.R., et al., 2002. Optical and radio properties of extragalactic sources observed by the first survey and the sloan digital sky survey. *The Astronomical Journal*, 124(5):2364.
- Jackson, N., Badole, S., Morgan, J., et al., 2022a. Sub-arcsecond imaging with the International LOFAR Telescope. II. Completion of the LOFAR Long-Baseline Calibrator Survey. *A&A*, 658:A2.
- Jackson, R.A., Kaviraj, S., Martin, G., et al., 2022b. Extremely massive disc galaxies in the nearby Universe form through gas-rich minor mergers. *MNRAS*, 511(1):607.
- Jarvis, M.E., Harrison, C.M., Thomson, A.P., et al., 2019. Prevalence of radio jets associated with galactic outflows and feedback from quasars. *MNRAS*, 485(2):2710.
- Jin, S., Trager, S.C., Dalton, G.B., et al., 2023. The wide-field, multiplexed, spectroscopic facility WEAVE: Survey design, overview, and simulated implementation. *MNRAS*.
- Jin, S., Trager, S.C., Dalton, G.B., et al., 2023. The wide-field, multiplexed, spectroscopic facility weave: Survey design, overview, and simulated implementation. *Monthly Notices of the Royal Astronomical Society*, page stad557.
- Jonas, J. and MeerKAT Team, 2016. The MeerKAT Radio Telescope. In *MeerKAT Science: On the Pathway to the SKA*, page 1.
- Jones, A., de Gasperin, F., Cuciti, V., et al., 2023. The Planck clusters in the LOFAR sky. VI. LoTSS-DR2: Properties of radio relics. *A&A*, 680:A31.
- Jones, A.P. and Nuth, J.A., 2011. Dust destruction in the ISM: a re-evaluation of dust lifetimes. *A&A*, 530:A44.
- Jones, A.P., Tielens, A.G.G.M., Hollenbach, D.J., et al., 1994. Grain Destruction in Shocks in the Interstellar Medium. *ApJ*, 433:797.
- Kalfountzou, E., Jarvis, M., Bonfield, D., et al., 2012. Star formation in high-redshift quasars: excess [o ii] emission in the radio-loud population. *Monthly Notices of the Royal Astronomical Society*, 427(3):2401.
- Kalfountzou, E., Stevens, J.A., Jarvis, M.J., et al., 2017. Observational evidence that positive and negative AGN feedback depends on galaxy mass and jet power. *MNRAS*, 471(1):28.

- Kang, H. and Ryu, D., 2011. Re-acceleration of Non-thermal Particles at Weak Cosmological Shock Waves. *ApJ*, 734(1):18.
- Kang, H., Ryu, D., Cen, R., et al., 2007. Cosmological Shock Waves in the Large-Scale Structure of the Universe: Nongravitational Effects. *The Astrophysical Journal*, 669(2):729.
- Kashikawa, N., Aoki, K., Asai, R., et al., 2002. Focas: the faint object camera and spectrograph for the subaru telescope. *Publications of the Astronomical Society of Japan*, 54(6):819.
- Kauffmann, G., Heckman, T.M., Tremonti, C., et al., 2003. The host galaxies of active galactic nuclei. *MNRAS*, 346(4):1055.
- Kauffmann, G., Heckman, T.M., White, S.D., et al., 2003. Stellar masses and star formation histories for 105 galaxies from the sloan digital sky survey. *Monthly Notices of the Royal Astronomical Society*, 341(1):33.
- Kauffmann, G., Heckman, T.M., White, S.D.M., et al., 2003. Stellar masses and star formation histories for  $10^5$  galaxies from the Sloan Digital Sky Survey. *MNRAS*, 341(1):33.
- Kaviraj, S., 2020. The low-surface-brightness Universe: a new frontier in the study of galaxy evolution. *arXiv e-prints*, arXiv:2001.01728.
- Kaviraj, S., Peirani, S., Khochfar, S., et al., 2009. The role of minor mergers in the recent star formation history of early-type galaxies. *MNRAS*, 394(4):1713.
- Kaviraj, S., Tan, K.M., Ellis, R.S., et al., 2011. A coincidence of disturbed morphology and blue UV colour: minor-merger-driven star formation in early-type galaxies at  $z \sim 0.6$ . *MNRAS*, 411(4):2148.
- Kellermann, K., Condon, J., Kimball, A., et al., 2016. Radio-loud and radio-quiet qsos. *The Astrophysical Journal*, 831(2):168.
- Kellermann, K., Sramek, R., Schmidt, M., et al., 1989. VLA observations of objects in the palomar bright quasar survey. *The Astronomical Journal*, 98:1195.
- Kelz, A., Verheijen, M.A.W., Roth, M.M., et al., 2006. PMAS: The Potsdam Multi-Aperture Spectrophotometer. II. The Wide Integral Field Unit PPak. *PASP*, 118(839):129.
- Kennel, C.F. and Coroniti, F.V., 1984. Confinement of the Crab pulsar's wind by its supernova remnant. *ApJ*, 283:694.

- Kennicutt, Robert C., J., 1998. Star Formation in Galaxies Along the Hubble Sequence. *Annual Review of Astronomy and Astrophysics*, 36:189.
- Kennicutt, R.C. and Evans, N.J., 2012. Star Formation in the Milky Way and Nearby Galaxies. *Annual Review of Astronomy and Astrophysics*, 50:531.
- Kewley, L.J. and Dopita, M.A., 2002. Using Strong Lines to Estimate Abundances in Extragalactic H II Regions and Starburst Galaxies. *ApJ*, 142(1):35.
- Kewley, L.J., Dopita, M.A., Sutherland, R.S., et al., 2001. Theoretical Modeling of Starburst Galaxies. *ApJ*, 556(1):121.
- Kewley, L.J., Geller, M.J., and Jansen, R.A., 2004. [O II] as a Star Formation Rate Indicator. *AJ*, 127(4):2002.
- Kewley, L.J., Geller, M.J., and Jansen, R.A., 2004. [o ii] as a star formation rate indicator. *The Astronomical Journal*, 127(4):2002.
- Kewley, L.J., Groves, B., Kauffmann, G., et al., 2006. The host galaxies and classification of active galactic nuclei. *MNRAS*, 372(3):961.
- Kewley, L.J., Maier, C., Yabe, K., et al., 2013. The Cosmic BPT Diagram: Confronting Theory with Observations. *ApJ*, 774(1):L10.
- Kewley, L.J., Nicholls, D.C., and Sutherland, R.S., 2019. Understanding Galaxy Evolution Through Emission Lines. *Annual Review of Astronomy and Astrophysics*, 57:511.
- Kim, J.h., Wise, J.H., and Abel, T., 2009. Galaxy Mergers with Adaptive Mesh Refinement: Star Formation and Hot Gas Outflow. *ApJ*, 694(2):L123.
- Kimball, A.E., Kellermann, K.I., Condon, J.J., et al., 2011. The two-component radio luminosity function of quasi-stellar objects: star formation and active galactic nucleus. *The Astrophysical Journal Letters*, 739(1):L29.
- Klindt, L., Alexander, D.M., Rosario, D.J., et al., 2019. Fundamental differences in the radio properties of red and blue quasars: evolution strongly favoured over orientation. *Monthly Notices of the Royal Astronomical Society*, 488(3):3109.
- Kondapally, R., Best, P., Hardcastle, M., et al., 2021. The lofar two-meter sky survey: Deep fields data release 1-iii. host-galaxy identifications and value added catalogues. *Astronomy & Astrophysics*, 648:A3.

- Konstantopoulos, I.S., Appleton, P.N., Guillard, P., et al., 2014. Shocks and Star Formation in Stephan's Quintet. I. Gemini Spectroscopy of H $\alpha$ -bright Knots. *ApJ*, 784(1):1.
- Laor, A. and Behar, E., 2008. On the origin of radio emission in radio-quiet quasars. *Monthly Notices of the Royal Astronomical Society*, 390(2):847.
- Lima-Costa, F., Martins, L.P., Rodríguez-Ardila, A., et al., 2020. Spectroscopic study of the HII regions in the NGC 1232 galaxy. *A&A*, 642:A203.
- Liu, Y., Jiang, D.R., and Gu, M.F., 2006. The jet power, radio loudness, and black hole mass in radio-loud active galactic nuclei. *The Astrophysical Journal*, 637(2):669.
- Longair, M.S., 2011. *High Energy Astrophysics*.
- Lorenzoni, S., Bunker, A.J., Wilkins, S.M., et al., 2011. Star-forming galaxies at  $z \approx 8-9$  from Hubble Space Telescope/WFC3: implications for reionization. *MNRAS*, 414(2):1455.
- Lorenzoni, S., Bunker, A.J., Wilkins, S.M., et al., 2013. Constraining the bright-end of the UV luminosity function for  $z \approx 7-9$  galaxies: results from CANDELS/GOODS-South. *MNRAS*, 429(1):150.
- Luridiana, V., Morisset, C., and Shaw, R.A., 2015. PyNeb: a new tool for analyzing emission lines. I. Code description and validation of results. *A&A*, 573:A42.
- Macfarlane, C., Best, P., Sabater, J., et al., 2021. The radio loudness of sdss quasars from the lofar two-metre sky survey: ubiquitous jet activity and constraints on star formation. *Monthly Notices of the Royal Astronomical Society*, 506(4):5888.
- Madau, P. and Dickinson, M., 2014. Cosmic star-formation history. *Annual Review of Astronomy and Astrophysics*, 52:415.
- Maddox, N., 2018. [o ii] as a proxy for star formation in agn host galaxies: beware of extended emission line regions. *Monthly Notices of the Royal Astronomical Society*, 480(4):5203.
- Magliocchetti, M., Pentericci, L., Cirasuolo, M., et al., 2020. The role of galaxy mass on agn emission: a view from the vandels survey. *Monthly Notices of the Royal Astronomical Society*, 493(3):3838.
- Maiolino, R., Russell, H.R., Fabian, A.C., et al., 2017. Star formation inside a galactic outflow. *Nature*, 544(7649):202.

- Marino, R.A., Rosales-Ortega, F.F., Sánchez, S.F., et al., 2013. The O3N2 and N2 abundance indicators revisited: improved calibrations based on CALIFA and  $T_e$ -based literature data. *A&A*, 559:A114.
- Markevitch, M., Gonzalez, A.H., David, L., et al., 2002. A Textbook Example of a Bow Shock in the Merging Galaxy Cluster 1E 0657-56. *ApJ*, 567(1):L27.
- Markevitch, M., Govoni, F., Brunetti, G., et al., 2005. Bow Shock and Radio Halo in the Merging Cluster A520. *The Astrophysical Journal*, 627(2):733.
- Markevitch, M. and Vikhlinin, A., 2007a. Shocks and cold fronts in galaxy clusters. *PhR*, 443(1):1.
- Markevitch, M. and Vikhlinin, A., 2007b. Shocks and cold fronts in galaxy clusters. *Physics Reports*, 443(1):1.
- Martin, G., Kaviraj, S., Devriendt, J.E.G., et al., 2018. The role of mergers in driving morphological transformation over cosmic time. *MNRAS*, 480(2):2266.
- Matsuoka, Y., Strauss, M.A., Shen, Y., et al., 2015. The sloan digital sky survey reverberation mapping project: Post-starburst signatures in quasar host galaxies at  $z \lesssim 1$ . *The Astrophysical Journal*, 811(2):91.
- McConnell, N.J. and Ma, C.P., 2013. Revisiting the Scaling Relations of Black Hole Masses and Host Galaxy Properties. *ApJ*, 764(2):184.
- McLure, R.J. and Jarvis, M.J., 2002. Measuring the black hole masses of high-redshift quasars. *MNRAS*, 337(1):109.
- McLure, R.J. and Jarvis, M.J., 2004. The relationship between radio luminosity and black hole mass in optically selected quasars. *Monthly Notices of the Royal Astronomical Society*, 353(4):L45.
- Metcalf, R. and Magliocchetti, M., 2006. The role of black hole mass in quasar radio activity. *Monthly Notices of the Royal Astronomical Society*, 365(1):101.
- Miller, P., Rawlings, S., and Saunders, R., 1993. The radio and optical properties of the  $Z \lesssim 0.5$  BQS quasars. *MNRAS*, 263:425.
- Miskolczi, A., Heesen, V., Horellou, C., et al., 2019. CHANG-ES XII. A LOFAR and VLA view of the edge-on star-forming galaxy NGC 3556. *A&A*, 622:A9.

- Moles, M., Sulentic, J.W., and Márquez, I., 1997. The Dynamical Status of Stephan's Quintet. *ApJ*, 485(2):L69.
- Molyneux, S.J., Harrison, C.M., and Jarvis, M.E., 2019. Extreme ionised outflows are more common when the radio emission is compact in AGN host galaxies. *A&A*, 631:A132.
- Momcheva, I.G., Lee, J.C., Ly, C., et al., 2013. Nebular Attenuation in H $\alpha$ -selected Star-forming Galaxies at  $z = 0.8$  from the NewH $\alpha$  Survey. *AJ*, 145(2):47.
- Morabito, L.K., Jackson, N.J., Mooney, S., et al., 2022. Sub-arcsecond imaging with the International LOFAR Telescope. I. Foundational calibration strategy and pipeline. *A&A*, 658:A1.
- Morabito, L.K., Sweijen, F., Radcliffe, J., et al., 2022. Identifying active galactic nuclei via brightness temperature with sub-arcsecond international lofar telescope observations. *Monthly Notices of the Royal Astronomical Society*, 515(4):5758.
- Morganti, R., Frieswijk, W., Oonk, R.J.B., et al., 2013. Tracing the extreme interplay between radio jets and the ISM in IC 5063. *A&A*, 552:L4.
- Morganti, R., Oosterloo, T., Tadhunter, C., et al., 2021. Taking snapshots of the jet-ISM interplay: The case of PKS 0023-26. *A&A*, 656:A55.
- Myers, A.D., Moustakas, J., Bailey, S., et al., 2023. The Target-selection Pipeline for the Dark Energy Spectroscopic Instrument. *AJ*, 165(2):50.
- Myers, A.D., Palanque-Delabrouille, N., Prakash, A., et al., 2015. The sdss-iv extended baryon oscillation spectroscopic survey: Quasar target selection. *The Astrophysical Journal Supplement Series*, 221(2):27.
- Myers, S.T. and Spangler, S.R., 1985. Synchrotron aging in the lobes of luminous radio galaxies. *ApJ*, 291:52.
- Naab, T. and Burkert, A., 2003. Statistical Properties of Collisionless Equal- and Unequal-Mass Merger Remnants of Disk Galaxies. *ApJ*, 597(2):893.
- Nakajima, K. and Maiolino, R., 2022. Diagnostics for PopIII galaxies and direct collapse black holes in the early universe. *MNRAS*, 513(4):5134.
- Netzer, H., 2013. *The Physics and Evolution of Active Galactic Nuclei*.

- Nikiel-Wroczyński, B., Soida, M., Urbanik, M., et al., 2013. Intergalactic magnetic fields in Stephan's Quintet. *MNRAS*, 435(1):149.
- Oesch, P.A., Bouwens, R.J., Illingworth, G.D., et al., 2018. The Dearth of  $z \sim 10$  Galaxies in All HST Legacy Fields—The Rapid Evolution of the Galaxy Population in the First 500 Myr. *ApJ*, 855(2):105.
- Oke, J., Cohen, J., Carr, M., et al., 1995. The keck low-resolution imaging spectrometer. *Publications of the Astronomical Society of the Pacific*, 107(710):375.
- Osterbrock, D.E. and Ferland, G.J., 2006. *Astrophysics of gaseous nebulae and active galactic nuclei*.
- O'Sullivan, E., Giacintucci, S., Vrtilik, J.M., et al., 2009. A Chandra X-ray View of Stephan's Quintet: Shocks and Star Formation. *ApJ*, 701(2):1560.
- Padovani, P., 2016. The faint radio sky: radio astronomy becomes mainstream. *A&ARv*, 24(1):13.
- Padovani, P., Alexander, D.M., Assef, R.J., et al., 2017. Active galactic nuclei: what's in a name? *A&ARv*, 25(1):2.
- Panessa, F., Baldi, R.D., Laor, A., et al., 2019. The origin of radio emission from radio-quiet active galactic nuclei. *Nature Astronomy*, 3:387.
- Pâris, I., Petitjean, P., Aubourg, É., et al., 2018. The sloan digital sky survey quasar catalog: fourteenth data release. *Astronomy & Astrophysics*, 613:A51.
- Penzias, A.A. and Wilson, R.W., 1965. A Measurement of Excess Antenna Temperature at 4080 Mc/s. *ApJ*, 142:419.
- Perley, R.A., Chandler, C.J., Butler, B.J., et al., 2011. The Expanded Very Large Array: A New Telescope for New Science. *The Astrophysical Journal*, 739(1):L1.
- Perlmutter, S., Aldering, G., della Valle, M., et al., 1998. Discovery of a supernova explosion at half the age of the Universe. *Nature*, 391(6662):51.
- Pierce, J.C.S., Tadhunter, C., Ramos Almeida, C., et al., 2023. Galaxy interactions are the dominant trigger for local type 2 quasars. *MNRAS*, 522(2):1736.
- Pierce, J.C.S., Tadhunter, C.N., Gordon, Y., et al., 2022. Do AGN triggering mechanisms vary with radio power? - II. The importance of mergers as a function of radio power and optical luminosity. *MNRAS*, 510(1):1163.

- Planck Collaboration, Ade, P.A.R., Aghanim, N., et al., 2014. Planck 2013 results. XVI. Cosmological parameters. *A&A*, 571:A16.
- Planck Collaboration, Ade, P.A.R., Aghanim, N., et al., 2016. Planck 2015 results. XIII. Cosmological parameters. *A&A*, 594:A13.
- Pontoppidan, K.M., Barrientes, J., Blome, C., et al., 2022. The JWST Early Release Observations. *ApJ*, 936(1):L14.
- Proxauf, B., Öttl, S., and Kimeswenger, S., 2014. Upgrading electron temperature and electron density diagnostic diagrams of forbidden line emission. *A&A*, 561:A10.
- Radcliffe, J.F., Barthel, P., Garrett, M., et al., 2021. The radio emission from active galactic nuclei. *Astronomy & Astrophysics*, 649:L9.
- Raichoor, A., Moustakas, J., Newman, J.A., et al., 2023. Target Selection and Validation of DESI Emission Line Galaxies. *AJ*, 165(3):126.
- Rakshit, S., Stalin, C., and Kotilainen, J., 2020. Spectral properties of quasars from sloan digital sky survey data release 14: the catalog. *The Astrophysical Journal Supplement Series*, 249(1):17.
- Reach, W.T., Tram, L.N., Richter, M., et al., 2019. Supernova Shocks in Molecular Clouds: Velocity Distribution of Molecular Hydrogen. *ApJ*, 884(1):81.
- Reid, B., Ho, S., Padmanabhan, N., et al., 2016. SDSS-III Baryon Oscillation Spectroscopic Survey Data Release 12: galaxy target selection and large-scale structure catalogues. *MNRAS*, 455(2):1553.
- Rich, J.A., Kewley, L.J., and Dopita, M.A., 2011. Galaxy-wide Shocks in Late-merger Stage Luminous Infrared Galaxies. *ApJ*, 734(2):87.
- Rich, J.A., Kewley, L.J., and Dopita, M.A., 2015. Galaxy Mergers Drive Shocks: An Integral Field Study of GOALS Galaxies. *ApJ*, 221(2):28.
- Richards, G.T., Fan, X., Newberg, H.J., et al., 2002. Spectroscopic target selection in the sloan digital sky survey: The quasar sample. *The Astronomical Journal*, 123(6):2945.
- Richards, G.T., Lacy, M., Storrie-Lombardi, L.J., et al., 2006. Spectral energy distributions and multiwavelength selection of type 1 quasars. *The Astrophysical Journal Supplement Series*, 166(2):470.

- Richter, G., 1975. Search for optical identifications in the 5c3-radio survey ii. statistical treatment and results. *Astronomische Nachrichten*, 296(2):65.
- Riess, A.G., Filippenko, A.V., Challis, P., et al., 1998. Observational Evidence from Supernovae for an Accelerating Universe and a Cosmological Constant. *AJ*, 116(3):1009.
- Rigby, J., Bayliss, M.B., Chisholm, J., et al., 2018. The magellan evolution of galaxies spectroscopic and ultraviolet reference atlas (megasaura). ii. stacked spectra. *The Astrophysical Journal*, 853(1):87.
- Robertson, B., Johnson, B.D., Tacchella, S., et al., 2023a. Earliest Galaxies in the JADES Origins Field: Luminosity Function and Cosmic Star-Formation Rate Density 300 Myr after the Big Bang. *arXiv e-prints*, arXiv:2312.10033.
- Robertson, B.E., 2022. Galaxy Formation and Reionization: Key Unknowns and Expected Breakthroughs by the James Webb Space Telescope. *Annual Review of Astronomy and Astrophysics*, 60:121.
- Robertson, B.E., Tacchella, S., Johnson, B.D., et al., 2023b. Identification and properties of intense star-forming galaxies at redshifts  $z \gtrsim 10$ . *Nature Astronomy*, 7:611.
- Rodighiero, G., Daddi, E., Baronchelli, I., et al., 2011. The lesser role of starbursts in star formation at  $z=2$ . *The Astrophysical journal letters*, 739(2):L40.
- Rodrigues, M., Hammer, F., Flores, H., et al., 2017. Morpho-kinematics of  $z \sim 1$  galaxies probe the hierarchical scenario. *MNRAS*, 465(1):1157.
- Rodríguez-Baras, M., Rosales-Ortega, F.F., Díaz, A.I., et al., 2014. A study of the ionized gas in Stephan's Quintet from integral field spectroscopy observations. *MNRAS*, 442(1):495.
- Ross, A.J., Bautista, J., Tojeiro, R., et al., 2020. The Completed SDSS-IV extended Baryon Oscillation Spectroscopic Survey: Large-scale structure catalogues for cosmological analysis. *MNRAS*, 498(2):2354.
- Ross, N.P., Myers, A.D., Sheldon, E.S., et al., 2012. The sdss-iii baryon oscillation spectroscopic survey: quasar target selection for data release nine. *The Astrophysical Journal Supplement Series*, 199(1):3.
- Roth, M.M., Kelz, A., Fechner, T., et al., 2005. PMAS: The Potsdam Multi-Aperture Spectrophotometer. I. Design, Manufacture, and Performance. *PASP*, 117(832):620.

- Rowlands, K., Dunne, L., Maddox, S., et al., 2012. Herschel-atlas/gama: dusty early-type galaxies and passive spirals. *Monthly Notices of the Royal Astronomical Society*, 419(3):2545.
- Russell, H.R., Nulsen, P.E.J., Caprioli, D., et al., 2022. The structure of cluster merger shocks: turbulent width and the electron heating time-scale. *MNRAS*, 514(1):1477.
- Ryu, D., Kang, H., Cho, J., et al., 2008. Turbulence and Magnetic Fields in the Large-Scale Structure of the Universe. *Science*, 320(5878):909.
- Sabater, J., Best, P.N., Hardcastle, M.J., et al., 2019. The LoTSS view of radio AGN in the local Universe. The most massive galaxies are always switched on. *A&A*, 622:A17.
- Sabater, J., Best, P.N., Tasse, C., et al., 2021. The LOFAR Two-meter Sky Survey: Deep Fields Data Release 1. II. The ELAIS-N1 LOFAR deep field. *A&A*, 648:A2.
- Salviander, S., Shields, G.A., Gebhardt, K., et al., 2007. The black hole mass-galaxy bulge relationship for quasars in the Sloan Digital Sky Survey data release 3. *The Astrophysical Journal*, 662(1):131.
- Sanders, D., Soifer, B., and Neugebauer, G., 1990. Ultraluminous infrared galaxies and the origin of quasars. In *Dynamics and Interactions of Galaxies: Proceedings of the International Conference, Heidelberg, 29 May–2 June 1989*, pages 459–464. Springer.
- Satyapal, S., Ellison, S.L., McAlpine, W., et al., 2014. Galaxy pairs in the Sloan Digital Sky Survey - IX. Merger-induced AGN activity as traced by the Wide-field Infrared Survey Explorer. *MNRAS*, 441(2):1297.
- Schawinski, K., Urry, C.M., Simmons, B.D., et al., 2014. The green valley is a red herring: Galaxy Zoo reveals two evolutionary pathways towards quenching of star formation in early- and late-type galaxies. *MNRAS*, 440(1):889.
- Schlegel, D.J., Finkbeiner, D.P., and Davis, M., 1998. Maps of Dust Infrared Emission for Use in Estimation of Reddening and Cosmic Microwave Background Radiation Foregrounds. *ApJ*, 500(2):525.
- Schneider, D.P., Richards, G.T., Hall, P.B., et al., 2010. The Sloan Digital Sky Survey Quasar Catalog. v. Seventh Data Release. *The Astronomical Journal*, 139(6):2360.
- Scholtz, J., Maiolino, R., D'Eugenio, F., et al., 2023. JADES: A large population of obscured, narrow line AGN at high redshift. *arXiv e-prints*, arXiv:2311.18731.

- Schreiber, C., Pannella, M., Elbaz, D., et al., 2015. The herchel view of the dominant mode of galaxy growth from  $z=4$  to the present day. *Astronomy & Astrophysics*, 575:A74.
- Selsing, J., Fynbo, J.P., Christensen, L., et al., 2016. An x-shooter composite of bright  $1 < z < 2$  quasars from uv to infrared. *Astronomy & Astrophysics*, 585:A87.
- Serra, P., de Blok, W.J.G., Bryan, G.L., et al., 2016. The MeerKAT Fornax Survey. In *MeerKAT Science: On the Pathway to the SKA*, page 8.
- Seyfert, C.K., 1943. Nuclear Emission in Spiral Nebulae. *ApJ*, 97:28.
- Shankar, F., Bernardi, M., Richardson, K., et al., 2019. Black hole scaling relations of active and quiescent galaxies: Addressing selection effects and constraining virial factors. *MNRAS*, 485(1):1278.
- Shankar, F., Sivakoff, G.R., Vestergaard, M., et al., 2010. The relative growth of optical and radio quasars in sdss. *Monthly Notices of the Royal Astronomical Society*, 401(3):1869.
- Shankar, F., Weinberg, D.H., and Miralda-Escudé, J., 2009. Self-Consistent Models of the AGN and Black Hole Populations: Duty Cycles, Accretion Rates, and the Mean Radiative Efficiency. *ApJ*, 690(1):20.
- Shectman, S.A., Landy, S.D., Oemler, A., et al., 1996. The Las Campanas Redshift Survey. *ApJ*, 470:172.
- Shen, X., Hopkins, P.F., Faucher-Giguère, C.A., et al., 2020. The bolometric quasar luminosity function at  $z=0-7$ . *Monthly Notices of the Royal Astronomical Society*, 495(3):3252.
- Shen, Y., Greene, J.E., Ho, L.C., et al., 2015. The Sloan Digital Sky Survey Reverberation Mapping Project: No Evidence for Evolution in the  $M_{\bullet} - \sigma_{*}$  Relation to  $z \sim 1$ . *ApJ*, 805(2):96.
- Shen, Y., Hall, P.B., Horne, K., et al., 2019. The sloan digital sky survey reverberation mapping project: sample characterization. *The Astrophysical Journal Supplement Series*, 241(2):34.
- Shen, Y., Richards, G.T., Strauss, M.A., et al., 2011. A catalog of quasar properties from sloan digital sky survey data release 7. *The Astrophysical Journal Supplement Series*, 194(2):45.
- Shields, G.A., 1999. A Brief History of Active Galactic Nuclei. *PASP*, 111(760):661.
- Shimwell, T., Röttgering, H., Best, P.N., et al., 2017. The lofar two-metre sky survey-i. survey description and preliminary data release. *Astronomy & Astrophysics*, 598:A104.

- Shimwell, T.W., Hardcastle, M.J., Tasse, C., et al., 2022. The LOFAR Two-metre Sky Survey. V. Second data release. *A&A*, 659:A1.
- Sikora, M., Stawarz, L., and Lasota, J.P., 2007. Radio loudness of active galactic nuclei: observational facts and theoretical implications. *The Astrophysical Journal*, 658(2):815.
- Silk, J., 2005. Ultraluminous starbursts from supermassive black hole-induced outflows. *MNRAS*, 364(4):1337.
- Silk, J., 2011. Feedback in Galaxy Formation. In C. Carignan, F. Combes, and K.C. Freeman, editors, *Tracing the Ancestry of Galaxies*, volume 277, pages 273–281.
- Silk, J., 2013. Unleashing Positive Feedback: Linking the Rates of Star Formation, Supermassive Black Hole Accretion, and Outflows in Distant Galaxies. *ApJ*, 772(2):112.
- Skillman, S.W., O’Shea, B.W., Hallman, E.J., et al., 2008. Cosmological Shocks in Adaptive Mesh Refinement Simulations and the Acceleration of Cosmic Rays. *ApJ*, 689(2):1063.
- Smee, S.A., Gunn, J.E., Uomoto, A., et al., 2013. The multi-object, fiber-fed spectrographs for the sloan digital sky survey and the baryon oscillation spectroscopic survey. *The Astronomical Journal*, 146(2):32.
- Smith, D., Best, P., Duncan, K., et al., 2016. The weave-lofar survey. *arXiv preprint arXiv:1611.02706*.
- Smith, D., Haskell, P., Gürkan, G., et al., 2021. The lofar two-metre sky survey deep fields—the star-formation rate–radio luminosity relation at low frequencies. *Astronomy & Astrophysics*, 648:A6.
- Smith, D.J.B., Best, P.N., Duncan, K.J., et al., 2016. The WEAVE-LOFAR Survey. In C. Reylé, J. Richard, L. Cambrésy, M. Deleuil, E. Pécontal, L. Tresse, and I. Vauglin, editors, *SF2A-2016: Proceedings of the Annual meeting of the French Society of Astronomy and Astrophysics*, pages 271–280.
- Smith, D.J.B., Dunne, L., Maddox, S.J., et al., 2011. Herschel-ATLAS: counterparts from the ultraviolet-near-infrared in the science demonstration phase catalogue. *MNRAS*, 416(2):857.
- Smith, D.J.B., Hardcastle, M.J., Jarvis, M.J., et al., 2013. Isothermal dust models of Herschel-ATLAS galaxies. *MNRAS*, 436(3):2435.

- Smith, D.J.B., Simpson, C., Swinbank, A.M., et al., 2010. When galaxies collide: understanding the broad absorption-line radio galaxy 4C +72.26. *MNRAS*, 404(3):1089.
- Smolčić, V., Delvecchio, I., Zamorani, G., et al., 2017. The VLA-COSMOS 3 GHz Large Project: Multiwavelength counterparts and the composition of the faint radio population. *A&A*, 602:A2.
- Sohn, B.W., Klein, U., and Mack, K.H., 2003. The spectral-curvature parameter: An alternative tool for the analysis of synchrotron spectra. *Astronomy and Astrophysics*, 404:133.
- Spergel, D.N., Verde, L., Peiris, H.V., et al., 2003. First-Year Wilkinson Microwave Anisotropy Probe (WMAP) Observations: Determination of Cosmological Parameters. *ApJ*, 148(1):175.
- Stasińska, G., Cid Fernandes, R., Mateus, A., et al., 2006. Semi-empirical analysis of Sloan Digital Sky Survey galaxies - III. How to distinguish AGN hosts. *MNRAS*, 371(2):972.
- Stephan, M., 1877. Nebulae (new) discovered and observed at the observatory of Marseilles, 1876 and 1877, M. Stephan. *MNRAS*, 37:334.
- Strateva, I., Ivezić, Ž., Knapp, G.R., et al., 2001. Color Separation of Galaxy Types in the Sloan Digital Sky Survey Imaging Data. *AJ*, 122(4):1861.
- Strauss, M.A., Weinberg, D.H., Lupton, R.H., et al., 2002. Spectroscopic Target Selection in the Sloan Digital Sky Survey: The Main Galaxy Sample. *AJ*, 124(3):1810.
- Sulentic, J.W., Rosado, M., Dultzin-Hacyan, D., et al., 2001. A Multiwavelength Study of Stephan's Quintet. *AJ*, 122(6):2993.
- Sun, Y., Lee, G.H., Zabludoff, A.I., et al., 2024. Evolution of gas flows along the starburst to post-starburst to quiescent galaxy sequence. *MNRAS*, 528(4):5783.
- Sutherland, W. and Saunders, W., 1992. On the likelihood ratio for source identification. *Monthly Notices of the Royal Astronomical Society*, 259(3):413.
- Sweijen, F., van Weeren, R.J., Röttgering, H.J.A., et al., 2022. Deep sub-arcsecond wide-field imaging of the Lockman Hole field at 144 MHz. *Nature Astronomy*, 6:350.
- Symeonidis, M., Giblin, B., Page, M., et al., 2016. Agn are cooler than you think: the intrinsic far-ir emission from qos. *Monthly Notices of the Royal Astronomical Society*, 459(1):257.

- Tacchella, S., Dekel, A., Carollo, C.M., et al., 2016. The confinement of star-forming galaxies into a main sequence through episodes of gas compaction, depletion and replenishment. *MNRAS*, 457(3):2790.
- Tacconi, L.J., Genzel, R., Smail, I., et al., 2008. Submillimeter Galaxies at  $z \sim 2$ : Evidence for Major Mergers and Constraints on Lifetimes, IMF, and CO-H<sub>2</sub> Conversion Factor. *ApJ*, 680(1):246.
- Tamhane, P.D., McNamara, B.R., Russell, H.R., et al., 2023. Radio jet-ISM interaction and positive radio-mechanical feedback in Abell 1795. *MNRAS*, 519(3):3338.
- Tamura, N., Takato, N., Shimono, A., et al., 2016. Prime Focus Spectrograph (PFS) for the Subaru telescope: overview, recent progress, and future perspectives. In C.J. Evans, L. Simard, and H. Takami, editors, *Ground-based and Airborne Instrumentation for Astronomy VI*, volume 9908 of *Society of Photo-Optical Instrumentation Engineers (SPIE) Conference Series*, page 99081M.
- Tasse, C., Shimwell, T., Hardcastle, M.J., et al., 2021. The LOFAR Two-meter Sky Survey: Deep Fields Data Release 1. I. Direction-dependent calibration and imaging. *A&A*, 648:A1.
- Tchekhovskoy, A., Narayan, R., and McKinney, J.C., 2010. Black hole spin and the radio loud/quiet dichotomy of active galactic nuclei. *The Astrophysical Journal*, 711(1):50.
- Thomas, D., Steele, O., Maraston, C., et al., 2013. Stellar velocity dispersions and emission line properties of SDSS-III/BOSS galaxies. *MNRAS*, 431(2):1383.
- Thompson, A.R., Clark, B.G., Wade, C.M., et al., 1980. The Very Large Array. *ApJ*, 44:151.
- Tremonti, C.A., Heckman, T.M., Kauffmann, G., et al., 2004. The origin of the mass-metallicity relation: insights from 53,000 star-forming galaxies in the sloan digital sky survey. *The Astrophysical Journal*, 613(2):898.
- Trinchieri, G., Sulentic, J., Breitschwerdt, D., et al., 2003. Stephan's Quintet: The X-ray anatomy of a multiple galaxy collision. *A&A*, 401:173.
- Trinchieri, G., Sulentic, J., Pietsch, W., et al., 2005. Stephan's Quintet with XMM-Newton. *A&A*, 444(3):697.
- Tsuzuki, Y., Kawara, K., Yoshii, Y., et al., 2006. Fe ii emission in 14 low-redshift quasars. i. observations. *The Astrophysical Journal*, 650(1):57.

- Unger, S., Pedlar, A., Axon, D.J., et al., 1987. The extended narrow-line region in radio seyferts: evidence for a collimated nuclear uv field? *Monthly Notices of the Royal Astronomical Society*, 228(3):671.
- Urry, C.M. and Padovani, P., 1995. Unified Schemes for Radio-Loud Active Galactic Nuclei. *PASP*, 107:803.
- van den Bergh, S. and Tammann, G.A., 1991. Galactic and extragalactic supernova rates. *Annual Review of Astronomy and Astrophysics*, 29:363.
- van der Laan, H. and Perola, G.C., 1969. Aspects of Radio Galaxy Evolution. *A&A*, 3:468.
- van Haarlem, M.P., Wise, M.W., Gunst, A.W., et al., 2013. LOFAR: The LOw-Frequency ARray. *A&A*, 556:A2.
- van Weeren, R.J., Andrade-Santos, F., Dawson, W.A., et al., 2017. The case for electron re-acceleration at galaxy cluster shocks. *Nature Astronomy*, 1:0005.
- Vanden Berk, D.E., Richards, G.T., Bauer, A., et al., 2001. Composite quasar spectra from the sloan digital sky survey. *The Astronomical Journal*, 122(2):549.
- Vazza, F., Roediger, E., and Brüggén, M., 2012. Turbulence in the ICM from mergers, cool-core sloshing, and jets: results from a new multi-scale filtering approach. *Astronomy and Astrophysics*, 544:A103.
- Véron-Cetty, M.P., Joly, M., and Véron, P., 2004. The unusual emission line spectrum of i zw 1. *Astronomy & Astrophysics*, 417(2):515.
- Vestergaard, M. and Osmer, P.S., 2009. Mass functions of the active black holes in distant quasars from the large bright quasar survey, the bright quasar survey, and the color-selected sample of the sdss fall equatorial stripe. *The Astrophysical Journal*, 699(1):800.
- Vestergaard, M. and Peterson, B.M., 2006. Determining central black hole masses in distant active galaxies and quasars. ii. improved optical and uv scaling relationships. *The Astrophysical Journal*, 641(2):689.
- Vestergaard, M. and Wilkes, B.J., 2001. An empirical ultraviolet template for iron emission in quasars as derived from i zwicky 1. *The Astrophysical Journal Supplement Series*, 134(1):1.

- Villar-Martín, M., Tadhunter, C., Humphrey, A., et al., 2011. Interactions, star formation and extended nebulae in sdss type 2 quasars at  $0.3 < z < 0.6$ . *Monthly Notices of the Royal Astronomical Society*, 416(1):262.
- Vink, J. and Yamazaki, R., 2014. A Critical Shock Mach Number for Particle Acceleration in the Absence of Pre-existing Cosmic Rays. *ApJ*, 780(2):125.
- Wagner, A.Y. and Bicknell, G.V., 2011. Relativistic Jet Feedback in Evolving Galaxies. *ApJ*, 728(1):29.
- Walton, N.A., Irwin, M., Lewis, J.R., et al., 2014. WEAVE core processing system. In G. Chiozzi and N.M. Radziwill, editors, *Software and Cyberinfrastructure for Astronomy III*, volume 9152 of *Society of Photo-Optical Instrumentation Engineers (SPIE) Conference Series*, page 91520R.
- Wang, B., Fujimoto, S., Labbé, I., et al., 2023. UNCOVER: Illuminating the Early Universe—JWST/NIRSpec Confirmation of  $z \lesssim 12$  Galaxies. *ApJ*, 957(2):L34.
- White, R.L., Helfand, D.J., Becker, R.H., et al., 2007. Signals from the noise: image stacking for quasars in the first survey. *The Astrophysical Journal*, 654(1):99.
- White, S.D.M. and Rees, M.J., 1978. Core condensation in heavy halos: a two-stage theory for galaxy formation and clustering. *MNRAS*, 183:341.
- White, S.V., Jarvis, M.J., Häußler, B., et al., 2015. Radio-quiet quasars in the video survey: evidence for agn-powered radio emission at  $s \approx 1.4 \text{ GHz}$ ;  $1 \text{ mJy}$ . *Monthly Notices of the Royal Astronomical Society*, 448(3):2665.
- White, S.V., Jarvis, M.J., Kalfountzou, E., et al., 2017. Evidence that the agn dominates the radio emission in  $z \approx 1$  radio-quiet quasars. *Monthly Notices of the Royal Astronomical Society*, 468(1):217.
- Whittam, I.H., Jarvis, M.J., Hale, C.L., et al., 2022. MIGHTEE: the nature of the radio-loud AGN population. *MNRAS*, 516(1):245.
- Wielebinski, R., Junkes, N., and Grahl, B.H., 2011. The Effelsberg 100-m Radio Telescope: Construction and Forty Years of Radio Astronomy. *Journal of Astronomical History and Heritage*, 14(1):3.

- Wild, V., Almaini, O., Dunlop, J., et al., 2016. The evolution of post-starburst galaxies from  $z=2$  to 0.5. *MNRAS*, 463(1):832.
- Wild, V., Taj Aldeen, L., Carnall, A., et al., 2020. The star formation histories of  $z \sim 1$  post-starburst galaxies. *MNRAS*, 494(1):529.
- Williams, B.A., Yun, M.S., and Verdes-Montenegro, L., 2002. The VLA H I Observations of Stephan's Quintet (HCG 92). *AJ*, 123(5):2417.
- Williams, R.J., Quadri, R.F., Franx, M., et al., 2009. Detection of Quiescent Galaxies in a Bicolor Sequence from  $Z = 0-2$ . *ApJ*, 691(2):1879.
- Williams, W., Hardcastle, M., Best, P., et al., 2019. The lofar two-metre sky survey-iii. first data release: Optical/infrared identifications and value-added catalogue. *Astronomy & Astrophysics*, 622:A2.
- Willmer, C.N.A., Faber, S.M., Koo, D.C., et al., 2006. The Deep Evolutionary Exploratory Probe 2 Galaxy Redshift Survey: The Galaxy Luminosity Function to  $z \sim 1$ . *ApJ*, 647(2):853.
- Wilman, R.J., Miller, L., Jarvis, M.J., et al., 2008. A semi-empirical simulation of the extragalactic radio continuum sky for next generation radio telescopes. *MNRAS*, 388(3):1335.
- Wilson, A.S. and Colbert, E.J., 1994. The difference between radio-loud and radio-quiet active galaxies. *arXiv preprint astro-ph/9408005*.
- Woo, J.H., Schulze, A., Park, D., et al., 2013. Do Quiescent and Active Galaxies Have Different  $M_{BH}-\sigma_*$  Relations? *ApJ*, 772(1):49.
- Xanthopoulos, E., Muxlow, T.W.B., Thomasson, P., et al., 2004. MERLIN observations of Stephan's Quintet. *Monthly Notices of the Royal Astronomical Society*, 353(4):1117.
- Xu, C., Sulentic, J.W., and Tuffs, R., 1999. Starburst in the Intragroup Medium of Stephan's Quintet. *ApJ*, 512(1):178.
- Xu, C.K., Appleton, P.N., Dopita, M., et al., 2008. Spitzer Observations of Stephan's Quintet – IGM Dust and Gas in a Multi-galaxy Collision. In R.R. Chary, H.I. Teplitz, and K. Sheth, editors, *Infrared Diagnostics of Galaxy Evolution*, volume 381 of *Astronomical Society of the Pacific Conference Series*, page 88.
- Xu, C.K., Lisenfeld, U., Gao, Y., et al., 2021. NOEMA Observations of CO Emission in Arp 142 and Arp 238. *ApJ*, 918(2):55.

- Xu, C.K., Lu, N., Condon, J.J., et al., 2003a. Physical Conditions and Star Formation Activity in the Intragroup Medium of Stephan's Quintet. *ApJ*, 595(2):665.
- Xu, C.K., Lu, N., Condon, J.J., et al., 2003b. Physical Conditions and Star Formation Activity in the Intragroup Medium of Stephan's Quintet. *The Astrophysical Journal*, 595(2):665.
- Yang, G., Caputi, K.I., Papovich, C., et al., 2023. CEERS Key Paper. VI. JWST/MIRI Uncovers a Large Population of Obscured AGN at High Redshifts. *ApJ*, 950(1):L5.
- Yip, C., Connolly, A., Berk, D.V., et al., 2004a. Spectral classification of quasars in the sloan digital sky survey: Eigenspectra, redshift, and luminosity effects. *The Astronomical Journal*, 128(6):2603.
- Yip, C.W., Connolly, A., Szalay, A., et al., 2004b. Distributions of galaxy spectral types in the sloan digital sky survey. *The Astronomical Journal*, 128(2):585.
- York, D.G., Adelman, J., Anderson, John E., J., et al., 2000. The Sloan Digital Sky Survey: Technical Summary. *AJ*, 120(3):1579.
- Yue, B.H., Best, P.N., Duncan, K.J., et al., 2024. A novel Bayesian approach for decomposing the radio emission of quasars: I. Modelling the radio excess in red quasars. *MNRAS*.
- Yue, M., Jiang, L., Shen, Y., et al., 2018. The sloan digital sky survey reverberation mapping project: Quasar host galaxies at  $z \lesssim 0.8$  from image decomposition. *The Astrophysical Journal*, 863(1):21.
- Yun, M.S., Reddy, N.A., and Condon, J.J., 2001. Radio Properties of Infrared-selected Galaxies in the IRAS 2 Jy Sample. *ApJ*, 554(2):803.
- Zakamska, N.L., Lampayan, K., Petric, A., et al., 2016. Star formation in quasar hosts and the origin of radio emission in radio-quiet quasars. *Monthly Notices of the Royal Astronomical Society*, 455(4):4191.
- Zaragoza-Cardiel, J., Beckman, J.E., Font, J., et al., 2015. Comparative internal kinematics of the H II regions in interacting and isolated galaxies: implications for massive star formation modes. *MNRAS*, 451(2):1307.
- Zavala, J.A., Casey, C.M., Manning, S.M., et al., 2021. The Evolution of the IR Luminosity Function and Dust-obscured Star Formation over the Past 13 Billion Years. *ApJ*, 909(2):165.

- Zhang, K., Schlegel, D.J., Andrews, B.H., et al., 2019. Machine-learning Classifiers for Intermediate Redshift Emission-line Galaxies. *ApJ*, 883(1):63.
- Zhou, R., Dey, B., Newman, J.A., et al., 2023. Target Selection and Validation of DESI Luminous Red Galaxies. *AJ*, 165(2):58.
- Zhu, G.B., Comparat, J., Kneib, J.P., et al., 2015. Near-ultraviolet spectroscopy of star-forming galaxies from eboss: signatures of ubiquitous galactic-scale outflows. *The Astrophysical Journal*, 815(1):48.
- Zhu, H., Slane, P., Raymond, J., et al., 2019. Dust Destruction in Nonradiative Shocks. *ApJ*, 882(2):135.
- Zolotov, A., Dekel, A., Mandelker, N., et al., 2015. Compaction and quenching of high-z galaxies in cosmological simulations: blue and red nuggets. *MNRAS*, 450(3):2327.